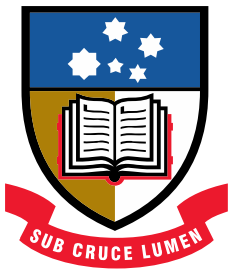

THE UNIVERSITY of ADELAIDE

Faculty of Sciences
School of Physical Sciences

High Frequency Surface Backscatter Coefficients

Danielle Jade Edwards

Supervisors:
Assoc. Prof. Andrew MacKinnon
Assoc. Prof. Manuel Cervera

Thesis submitted for the degree of
Master of Philosophy

November 2020

Table of Contents

Abstract

Over-the-horizon radar is a class of high frequency (HF) radar used for long range (1000-3000 km) wide area surveillance. These radars utilise the refractive properties of the ionosphere to illuminate targets beyond the Earth's horizon, and consequently their performance is highly dependent on the ionosphere. Accurate models of the radar ground backscatter are required to accurately assess the ionospheric propagation conditions and thus the expected performance of over-the-horizon radars for operational purposes.

The ground backscatter coefficient characterises the amount of radiation scattered back from a surface towards a receiver per unit area. While the backscatter coefficient of the sea is well understood and may be calculated from theory if the sea state is known, the backscatter coefficient of land at high frequencies is not well understood. To calculate the land backscatter coefficients over Northern Australia, a methodology which compares observed backscatter ionograms to those synthesised using HF radio wave ray tracing techniques through model ionospheres was developed. The results from this ionogram comparison method were compared to sea backscatter coefficients calculated from theory using sea state data.

Data from the Jindalee Operational Radar Network (JORN) frequency management system's backscatter sounders from September 2015 and March 2016 were analysed and maps of the backscatter coefficients across Northern Australia were developed. The effects of the ray propagation and surface properties, including radar frequency, topography, soil moisture and vegetation cover on the backscatter coefficients were investigated. It was found that desert-like regions had a much lower backscatter coefficient than mountainous/tropical regions. A weak positive correlation between the backscatter coefficient and the soil moisture and surface roughness was observed; however, it was found that the vegetation structure had the largest effect on the backscatter coefficient.

Declaration of Originality

I certify that this work contains no material which has been accepted for the award of any other degree or diploma in my name, in any university or other tertiary institution and, to the best of my knowledge and belief, contains no material previously published or written by another person, except where due reference has been made in the text. In addition, I certify that no part of this work will, in the future, be used in a submission in my name, for any other degree or diploma in any university or other tertiary institution without the prior approval of the University of Adelaide and where applicable, any partner institution responsible for the joint-award of this degree.

I give permission for the digital version of my thesis to be made available on the web, via the University's digital research repository, the Library Search and also through web search engines, unless permission has been granted by the University to restrict access for a period of time.

I acknowledge the support I have received for my research through the provision of an Australian Government Research Training Program Scholarship.

Signed: Date: 27/11/2020

Acknowledgements

I am extremely grateful to my supervisors, Andrew MacKinnon and Manuel Cervera, for their valuable guidance and feedback throughout this project. To Andrew MacKinnon, thank you for the opportunities you have provided, for your insights and suggestions regarding the presentation of this work along with your encouragement and support throughout. To Manuel Cervera, thank you for all of the technical support you have provided along the way, for the many discussions and all of the feedback you have provided, and for your enthusiasm about this work.

I would like to thank my friends and colleagues from the Space and Atmospheric Physics Group at the University of Adelaide; Thomas Chambers, Baden Gilbert, Daniel Field, Simon Curtis, Andrew Heitmann, Andrew Spargo, Lenard Pederick, Murray Hamilton, Bob Vincent and Mike Hatch for their insights and for making this a thoroughly enjoyable experience. I would also like to thank the members of the DST Group HF Radar Branch, including Trevor Harris, David Netherway, David Neudegg, David Holdsworth, David Francis, Robert Gardiner-Garden, Chris Crouch and Bruce Ward for their technical expertise and advice. Finally, I would like to thank my family for all of their support throughout this project.

This research is supported by the Defence Science and Technology Group. Results were obtained using the HF propagation toolbox, PHaRLAP, created by Dr Manuel Cervera, Defence Science and Technology Group, Australia (manuel.cervera@dsto.defence.gov.au). This toolbox is available by request from its author.

The Centre for Australian Weather and Climate Research is acknowledged for providing wave hindcast data. Geoscience Australia is acknowledged for providing the SRTM derived 1 arc-second digital elevation model (DEM-H). NOAA is acknowledged for providing ETOPO1, a 1 arc-minute global relief model. The Joint Remote Sensing Research Programs is acknowledged for providing vegetation height and structure data. The NASA National Snow and Ice Data Centre is acknowledged for providing 3 hourly soil moisture data.

List of Figures

List of Tables

Chapter 1 Introduction

1.1 Overview and Motivation

Over-the-horizon radar is a class of high frequency (HF) radar used for long range (1000-3000 km) wide area surveillance. These radars utilise the refractive properties of the ionosphere to illuminate targets beyond the Earth's horizon, and consequently their performance is highly dependent on the ionosphere. Under the right conditions, HF radio waves may propagate over the horizon via the ionosphere where they are refracted down towards the surface of the Earth again. They may then scatter from the ground back towards a receiver. Typically backscatter sounders (BSS), a type of over-the-horizon environmental radar, measure the power returned from ground backscatter in order to assess the ionospheric propagation conditions. The main surveillance radar is then tasked accordingly. However, low/high power noted by a BSS may be due to either poor/good ionospheric propagation or low/high ground backscatter. Consequently, accurate models of the radar ground backscatter are required at HF to accurately assess the propagation conditions and thus the expected performance of over-the-horizon radars for operational purposes.

The ground backscatter coefficient characterises the amount of radiation scattered back from a surface towards a receiver per unit area. While the backscatter coefficient of the sea/ocean is well understood and may be calculated from theory if the sea state is known, the backscatter coefficient of land at high frequencies is not well understood. To calculate the land backscatter coefficients over Northern Australia, a methodology which compares observed backscatter ionograms to those synthesised using HF radio wave ray tracing techniques through model ionospheres has been developed. The numerical ray tracing toolbox PHaRLAP [1] developed by the Defence Science and Technology Group was used together with a near real time data-driven model of the ionosphere. Propagation losses such as focussing/defocussing and ionospheric absorption were accounted for appropriately and the transmit and receive antenna gains were modelled using a method-of-moments electromagnetic solver. Sea backscatter coefficients were calculated from theory using a wave height spectrum obtained from sea state data. These backscatter coefficient results were compared with those from the ionogram comparison methodology.

Data from the Jindalee Operational Radar Network (JORN) [2] frequency management system (FMS) [3] backscatter sounders from September 2015 and March 2016 were analysed to develop maps of the backscatter coefficient across Northern Australia. The effects of the ray propagation and surface properties, including radio wave frequency, topography, soil moisture and vegetation structure, on the backscatter coefficient were investigated.

Chapter 2 Background

2.1 Overview of chapter

In this chapter, the background theory of radio wave propagation through the ionosphere will be outlined, along with a description of backscatter sounders and backscatter ionograms. A review of previous work done on calculating and measuring high frequency surface backscatter coefficients is presented.

2.2 Radio wave propagation through the ionosphere

High frequency (HF) radio wave signals are used for long distance surveillance and communication. This is possible because high frequency radio waves, around 3 to 30 MHz [4], are able to propagate via the ionosphere, where they are refracted back towards the surface of the Earth [5]. Over-the-horizon (OTH) radars utilise the propagation of high frequency radio waves via the Earth's ionosphere to detect objects of interest at large distances, from 1000 to 3000 kilometres away [6].

The ionosphere is an ionised layer of the Earth's atmosphere, extending from altitudes of around 60 km to 600 km [5]. The ionosphere is formed when ultra-violet solar radiation ionises neutral atoms and molecules in the atmosphere, removing electrons and creating positively charged ions in the process; known as photoionization. Recombination of electrons and ions to produce neutral species occurs at all times, whereas photoionization occurs only during the day. This results in maximum electron densities occurring in the middle of the day. During the day, the ionosphere consists of four layers; the D, E, F_1 and F_2 layers (listed in order of increasing altitudes) governed by chemistry of the atomic and molecular species in those regions. Sporadic E layers may also form at times; this is a reflecting layer that forms intermittently at E region heights.

The existence of free electrons within the ionosphere changes the refractive index, as is shown in the Appleton-Hartree formula [7], which causes HF rays to refract and hence allows propagation of radio waves via the ionosphere to distant locations. The refractive index decreases with increasing electron density and decreasing radio wave frequency. There are many modes of propagation that a ray may take through the ionosphere (Figure 2.1). The ray may travel via a single hop propagation path or propagate along multiple hops, where the ray is reflected between the ionosphere and the ground multiple times. The ray may also propagate via different layers of the ionosphere. For HF propagation the E, sporadic E and F_2 layer propagation modes are the most important [2, 5]. High and low modes of propagation may occur through the F_2 layer depending on the angle of elevation of the ray. A ray may also propagate via different modes when travelling away from the transmitter compared to when travelling back towards the receiver. Thus, the mode structure of available propagation paths for HF radar may be very complicated.

Propagation modes with more hops will have a lower signal strength, as they lose energy when travelling through the ionosphere due to absorption and when scattered by the ground. Most of the absorption of radio waves within the ionosphere occurs in the D and lower E regions [5]. Finally, rays may penetrate the ionosphere rather than being reflected back towards Earth if the elevation angle is too large or the radio wave frequency is too large for reflection to occur. When the vertical component of the radio wave propagation frequency exceeds the maximum plasma frequency of the ionospheric layer (known as the critical frequency), the radio wave will penetrate the ionospheric layer.

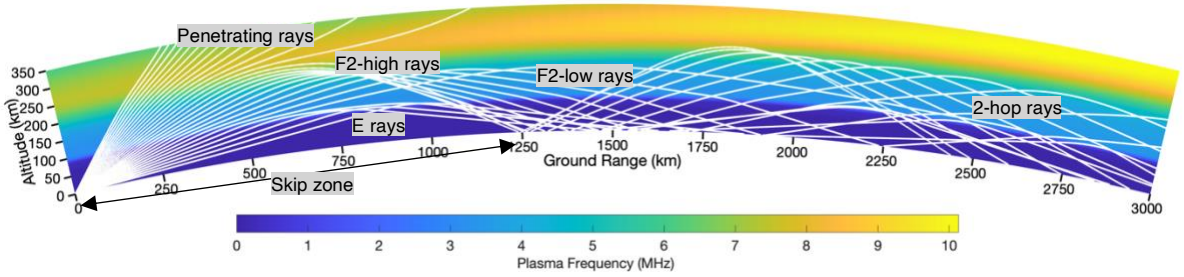

Figure 2.1: Propagation modes of a 15 MHz ray calculated from numerical ray tracing. Rays were transmitted at 0600 UT on 2015/09/03 from -28.3˚ N, 122.8˚ E in the direction -3.5˚ East of North.

2.3 Backscatter sounders and ionograms

A backscatter sounder is a quasi-monostatic radar system; the transmitter and receiver are separated for site isolation requirements. In the case of JORN, the transmitter and receiver sites are separated by around 100 km [2]. Backscatter sounders are used to observe backscattered signals that have propagated via the ionosphere to and from distant ground scatterers [4]. They are used in the JORN frequency management system to obtain an overall assessment of the propagation conditions [3]. A backscatter sounder operates by transmitting a signal swept through the HF band. The signal propagates via the ionosphere, is backscattered from the surface and is received by a receiver array. The backscatter sounders from the JORN frequency management system use a vertically polarised log-periodic transmit antenna to illuminate the area to be observed by the backscatter sounder. By introducing appropriate phasing between receive array antenna elements, the receiver array is able to form beams in the direction of the area floodlit by the transmitter [3]. In the case of the JORN backscatter sounders, eight receiver beams are simultaneously formed within the area of regard and are used to create eight backscatter ionograms. The JORN backscatter sounders are described in detail in Section 3.1.

Backscatter ionograms display the power returned from a radio wave transmitted through the ionosphere and scattered back from the Earth's surface to the receiver, as a function of group range and frequency. The group range is defined as the distance a signal travelling at the speed of light in a vacuum would cover in half of the time delay between the transmission and reception of a backscatter signal [8]. This distance will be greater than the actual distance travelled by the radio waves as the radio waves are retarded by the ionosphere. Within a backscatter ionogram, certain features can be noted such as the leading edge, areas of multiple

hop propagation, effects of sporadic E-layer propagation and power returned via backscatter from meteors (Figure 2.2). The leading edge of a backscatter ionogram is the minimum group range at which power is received for each frequency. Group ranges less than the leading edge are inside the skip zone; signals are not able to be received from this region as the ionosphere is unable to support the high elevation angles required for these radio waves to be refracted back to the receiver and will instead penetrate the ionosphere. At the transition from low to high rays the change in propagation distance with elevation is small so the power of rays with these elevations are focused at the edge of the skip zone [7] (see Figure 2.1); hence the power returned along the leading edge is stronger than for lower frequencies at the same group range [5]. The power returned from multiple propagation hops can also be seen in a backscatter ionogram. Multiple hops occur when a ray is refracted from the ionosphere multiple times and is forward scattered from the ground in between. The presence of a sporadic E layer can be seen in a backscatter ionogram as a region of power returned from group ranges closer than the leading edge at higher frequencies than typically expected. Sporadic-E can also exist within the bulk of the power in the backscatter ionogram; it does not always protrude out beyond the frequencies of the leading edge. Power returned from meteors may also be seen in a backscatter ionogram, as spots of power returned at low group ranges.

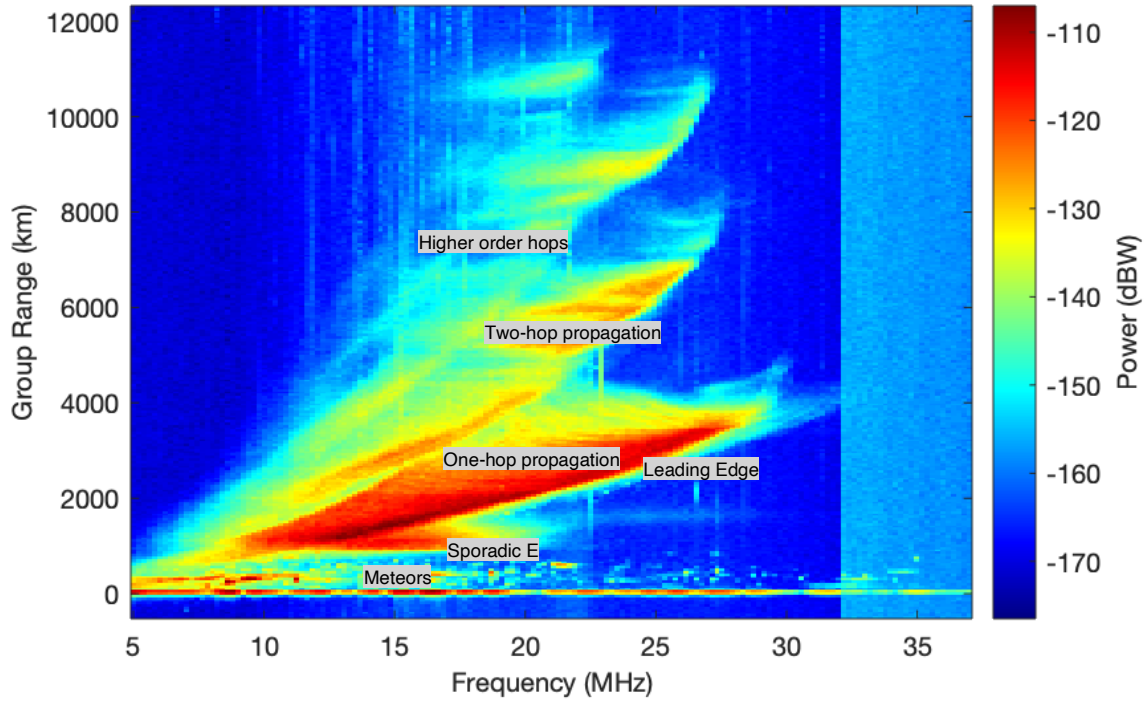

Figure 2.2: Features of a backscatter ionogram. Ionogram collected by the Laverton East JORN BSS Beam 3 at 0400 UT 2016/03/26.

2.4 Synthesising backscatter ionograms

Synthesised backscatter ionograms may be used to aid the interpretation of observed backscatter ionograms [9] and give a better understanding on how changes in ionospheric

conditions affect backscatter ionograms [10, 11]. Backscatter ionograms can be simulated using a model of the ionosphere and a suitable way of determining the propagation of waves through the ionosphere, such as ray tracing [12]. To simulate a backscatter ionogram, a fan of rays is generated for the required elevations at each frequency of interest. The power returned for each group range cell is calculated as the sum of the power returned by all of the propagation paths that contributed to that particular range [12]. This is repeated for all relevant frequencies and a grid of the power returned from each group range for each frequency is constructed; a model backscatter ionogram.

The synthesis of backscatter ionograms has been shown to be relatively straight forward when certain assumptions are made [4, 10, 12-15]. If it is assumed that the ionosphere is spherically symmetric and constructed from quasi-parabolic layers, analytical ray tracing can be used to quickly determine the path of rays travelling through the model ionosphere to synthesise a backscatter ionogram [10]. However, if the ionospheric model is more complicated, numerical ray tracing must be used to determine the path of a ray through the model ionosphere. The Haselgrove ray tracing equations [1, 9, 16-18] and the Jones and Stephenson formulation [19] are two widely used formulations of the canonical equations for the ray path. The complexity of the ray tracing is dependent upon which characteristics of the ionosphere and the rays are being modelled. For many applications, two-dimensional ray tracing is sufficient; however, if out of plane propagation due to the effects of the Earth's magnetic field and ionospheric tilts are to be included in the model then three-dimensional ray tracing is required [12]. The power returned by an area of the ground may then be calculated by considering the loss due to the distance the rays have travelled, the gain of the transmit and receive antennas, the ionospheric absorption losses, the focusing and defocusing gains and losses and the backscatter coefficient of the surface. These are discussed in detail in Section 4.2.

2.5 Backscatter coefficients

The backscatter coefficient, otherwise known as the scattering cross section per unit area, describes the amount of radiation scattered back from a surface towards a receiver per unit area. Backscatter coefficients are expressed in decibels (dB) and hence are given on a logarithmic scale [20]. While much work has been done on calculating backscatter coefficients from theory [21-23], many parameters about the scattering surface and the radio waves must be known, making this difficult to do in practise. From observations, the backscatter coefficient of the sea is well understood [24]. Calculations of the sea backscatter coefficient from theory have also been successful. However, much less work has been done on calculating the backscatter coefficients of land areas.

2.5.1 Theoretical Backscatter Coefficients

The backscatter coefficient depends on the roughness of the surface, the conductivity of the surface, the polarisation of the incident and scattered rays, the angle of incidence of the rays and the frequency of the radio waves [22]. In order to theoretically model the backscatter

coefficient of a surface, the surface properties must be characterised and the electromagnetic scattering problem must be solved [21]. Two main methods of doing this have been developed in the past; (1) using perturbation theory to calculate the electromagnetic properties of a surface with a specified roughness, and (2) constructing a surface out of objects with known scattering properties such as spheres or cylinders [21]. For a slightly rough surface, defined as $k_0\zeta \cos\theta_i < 1.0$ where k_0 is the signal wavenumber, ζ is the mean height of surface variations and θ_i is the angle of incidence of the signal from the mean surface normal, the electromagnetic properties may be calculated using a perturbation method [21, 22, 24, 25]. For a very rough surface, defined as $k_0\zeta \cos\theta_i > 1.0$, a physical optics approach to calculating the backscatter coefficient can be used [26]. In the high frequency limit for a very rough surface backscattering occurs from areas of the surface which are oriented normal to the ray [22]. For radio waves near grazing over a rough surface, the physical optics approach is less accurate due to shadowing. A model that takes this into account was presented by Barrick [27]. It was found that there were large differences between vertically and horizontally polarised waves and that the backscatter power depended on the grazing angle to the fourth power [23].

2.5.2 Sea Backscatter Coefficients

The sea backscatter coefficient has been well researched over many years, as there has been a strong interest in the backscatter from the sea for applications in the detection of near surface military targets and for remote sensing of the sea state [27, 28]. The sea backscatter coefficient is dependent on the depth of the water, the wind speed, the wave heights and the ocean surface currents [29]. From measurements, it has been found that the backscatter coefficient of a fully developed sea (where the waves have reached an equilibrium with the wind) is around -23 dB [30]. Since the sea backscatter coefficient is likely to be uniform over large areas of fully developed sea, the sea may be used as a reference for the calibration of HF radars [31]. Radio waves scattered back from the sea also have a characteristic doppler shift caused by the coherent Bragg scattering of the signal from components of the sea wave height spectrum that are moving towards or away from the radar with wavelengths half the length of the radio wavelength [28, 32].

The sea backscatter coefficient can be theoretically modelled using a directional wave height spectrum. Equations for the sea backscatter coefficient from a directional wave height spectrum in deep and shallow water were derived by Barrick using a boundary perturbation approach [24, 29]. Directional sea spectra were assumed to be separable into the wave number component and the directional factor [33, 34]. The model of the backscatter coefficient is dependent on the wave height spectrum that is used. The Pierson-Moskowitz spectrum is one of the simplest spectra; it is a non-directional spectrum that defines a fully developed sea. The JONSWAP spectrum is based on the Pierson-Moskowitz spectrum, with an extra factor included to adjust for the sea never becoming fully developed [35]. These two sea spectra accompanied by a direction factor, along with high resolution wind speed, swell height and swell period data were used by Neller [36] to model sea backscatter coefficients. It was found

that the sea backscatter coefficient varied with location and time and increased with increasing radio wave frequency.

2.5.3 Land Backscatter Coefficients

Unlike the sea, there is a limited understanding of the backscatter coefficient of land at HF. It has been found that topographic and geographic features such as mountains, islands and cities produce enhanced backscatter coefficients compared to surrounding terrain [6, 37, 38].

Early work on calculating the theoretical land backscatter was done by constructing the terrain out of objects with known scattering properties [21]. Steele [39] suggested that the HF land backscatter coefficient may be affected by trees behaving as antennas, receiving and reradiating energy. The land backscatter coefficient would then depend on both the density of the trees and their individual radar cross sections. A study of the HF radar cross section of an oak tree found that for radio waves with elevations below 15 degrees, the radar cross section was much larger for vertical polarisations than for horizontal polarisations and that the tree acted like a dipole [39]. A similar study was done to measure the HF radar cross section of cement walls, such as may be found in a city. It was found that the radar cross section of wet walls was larger than for dry walls [40]. Balser and Scott [38] investigated the ground backscatter using high resolution oblique sounders and found that the backscatter was highly nonuniform due to the presence of localised surface features such as large cities, mountains and islands with greater radar cross sections than the surrounding terrain. Li [41] used a transponder to measure the backscatter coefficient in a desert region and a mountainous region of China. They found that the average backscatter coefficients of the desert region and mountain region were about -25 dB and -20 dB respectively. An empirical formula for the land backscatter coefficient over different terrains was given as a function of elevation; however, few samples went into this formula and the method of generating and validating this formula was not described [41]. Slimming and Cervera [42] investigated another method of calculating land backscatter coefficients. In this method model backscatter ionograms in which the backscatter coefficient was set to zero were synthesised using a ray tracing algorithm and ionospheric models. These synthesised ionograms were then compared with observed backscatter ionograms to determine the backscatter coefficient for specific land areas. It was found that the backscatter coefficient of an area of land near Daly River in the Northern Territory, Australia was different when viewed from different directions, and that desert regions had lower backscatter than hilly terrain.

The differences between the scatter from different land features and sea has been investigated as a way to improve the location accuracy in coordinate registration [43, 44]. Coordinate registration is the process of transforming from the group range to the ground range to get the geographic coordinates of an object observed by a radar [5]. Jin et al. [44] investigated a method of using the backscatter coefficient and doppler from land and sea to determine the land/sea boundaries. Values for the land backscatter coefficients from -10 dB for mountains or cities to -45 dB for dry flat ground and values for the sea backscatter coefficient within -23 dB to -30 dB were used; however, it was not stated where these values came from. Turley et al.

[43] used a high spatial resolution radar to obtain the difference in the doppler shifts of a signal backscattered from the land or sea to determine land/sea boundaries for the purpose of coordinate registration. A map of the land/sea classifications was produced which clearly showed the coordinate registration corrections required for target location registration. The difference in backscatter from different terrain features was investigated as a way to do coordinate registration by Barnum and Simpson [37]. Backscatter ionograms were synthesised and fit to the observed ionograms by changing the critical frequency as a function of range. Contour maps of the relative backscatter were then created with 3 dB contour spacing. These contour maps were fit to terrain features, concluding that differences in the backscatter from terrain features can be used for coordinate registration. Holdsworth [6] investigated the use of a wind turbine farm and a mountain range that produced strong backscatter as known reference points for coordinate registration. Transponders were placed near these features and the signals returned from the mountain range and wind turbine farm provided similar azimuth-range information to the nearby transponders, suggesting these features could be used as known reference points.

2.6 Summary

The propagation of radio waves through the ionosphere allows over-the-horizon radars to detect objects at large distances. Backscatter sounders are a quasi-monostatic radar system used to observe backscattered signals that have propagated via the ionosphere to and from distant ground scatterers. Backscatter ionograms are produced from backscatter sounders; these display the power returned from a radio wave transmitted through the ionosphere and scattered back from the Earth's surface to the receiver, as a function of group range and frequency. The backscatter coefficient describes the amount of radiation scattered back from a surface towards a receiver. A review of previous work done on calculating surface backscatter coefficients was presented; the sea backscatter coefficients are relatively well understood, but there is only a limited understanding of land backscatter coefficients. In the next chapter, the backscatter ionograms and other sources of data and software that were used in this project are described.

Chapter 3 Data and Software

3.1 Overview of chapter

This chapter describes the data and software that were used for this project including the backscatter ionograms, ray tracing software, ionospheric models, sea state data, topographic data, soil moisture data and vegetation data.

3.2 Backscatter ionograms

Backscatter ionograms observed by four backscatter sounders across Australia from the JORN frequency management system (FMS) were provided by Defence Science and Technology Group. These sounders were located at Longreach (LO), Laverton East (LAE), Laverton West (LAW) and Alice Springs (AS). Data collected in September 2015 [45] and March 2016 with a temporal resolution of 5.5 minutes was analysed. The group range resolution of this data was 50 km, the frequency resolution was 0.2 MHz and the power resolution was 0.5 dBW. The ionograms were scaled to a transmit power of 20 kW.

3.2.1 Backscatter sounder sites

The locations and orientations of the backscatter sounders are shown in Table 3.1. Each sounder can be electronically steered to create 8 receiving beams (labelled clockwise from 1 to 8), spanning around 90 degrees in azimuth. The field of view covered by these beams is shown in Figure 3.1. The beam centres relative to bore for the Longreach and Laverton sounders were -38.5, -27.5, -16.5, -5.5, 5.5, 16.5, 27.5, 38.5 degrees. For the Alice Springs sounder the beam centres relative to bore were -38.2, -26.2, -15.4, -5.1, 5.1, 15.4, 26.2, 38.2 degrees.

The backscatter sounders operate over the frequency range 5 to 45 MHz. To support this large frequency range two sets of antenna arrays (low band and high band) are used. The cross over frequency between the low and high band antennas is 32 MHz for the Longreach and Laverton sounders and 30 MHz for the Alice Springs sounder. Each backscatter sounder transmits using a single log-periodic antenna. The transmit power was nominally 15 kW for the Laverton and Longreach low band transmitters and 10 kW for Alice Springs low band transmitter. The high band transmit power was 1 kW for all systems. Reception is on linear arrays of 6.5 m high doublet monopoles with a doublet spacing of 3.5 m for the Longreach and Laverton sounders [2] and a linear array of 5.5 m high dual fan monopoles with a spacing of 3 m for the Alice Springs sounder [3]. Each doublet is considered an element. A ground mat is used for elevation control. Figure 3.2 is an image of the Alice Springs log-periodic transmit antenna, Figure 3.3 is an image of the Longreach receiver arrays and Figure 3.4 is an image of the Alice Springs receiver array. The low band receive array for the Laverton and Longreach sounders consists of 32 elements with a spacing of 6.2 m, and the high band array consists of 16 elements with a spacing of 3.7 m. The Alice Springs sounder low band array consists of 28 elements at a spacing of 6.0 m, and the high band array consists of 12 elements at a spacing of 3.9 m.

Table 3.1: Backscatter sounder locations and orientations.

Sounder	Latitude (˚)	Longitude (˚)	Bore (East)	Bore (West)
Longreach Transmitter	-23.66	144.14	323.00	-
Longreach Receiver	-24.29	143.19	325.00	-
Laverton Transmitter	-28.32	122.84	33.10	304.65
Laverton Receiver	-28.32	122.02	35.00	305.00
Alice Springs Transmitter	-22.97	134.45	324.2	-
Alice Spring Receiver	-23.52	133.68	324.2	-

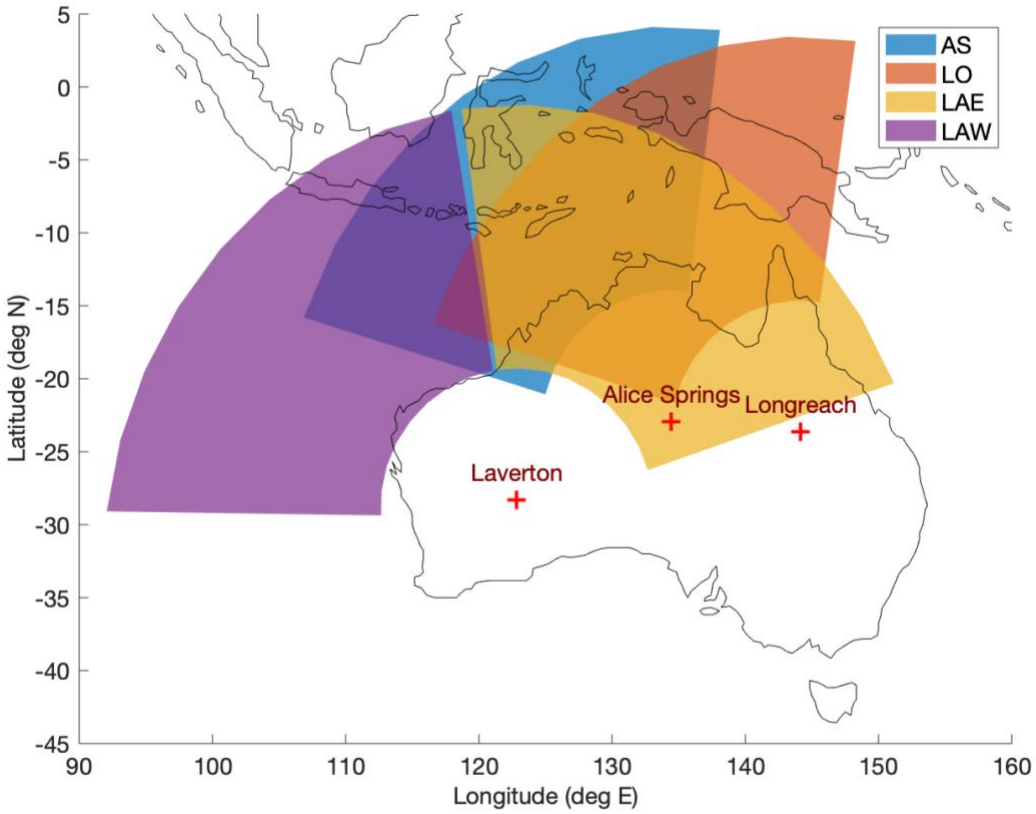

Figure 3.1: Backscatter sounder locations and fields of view. The inner arcs are 1000 km from the sounders and the outer arcs are 3000 km from the sounders.

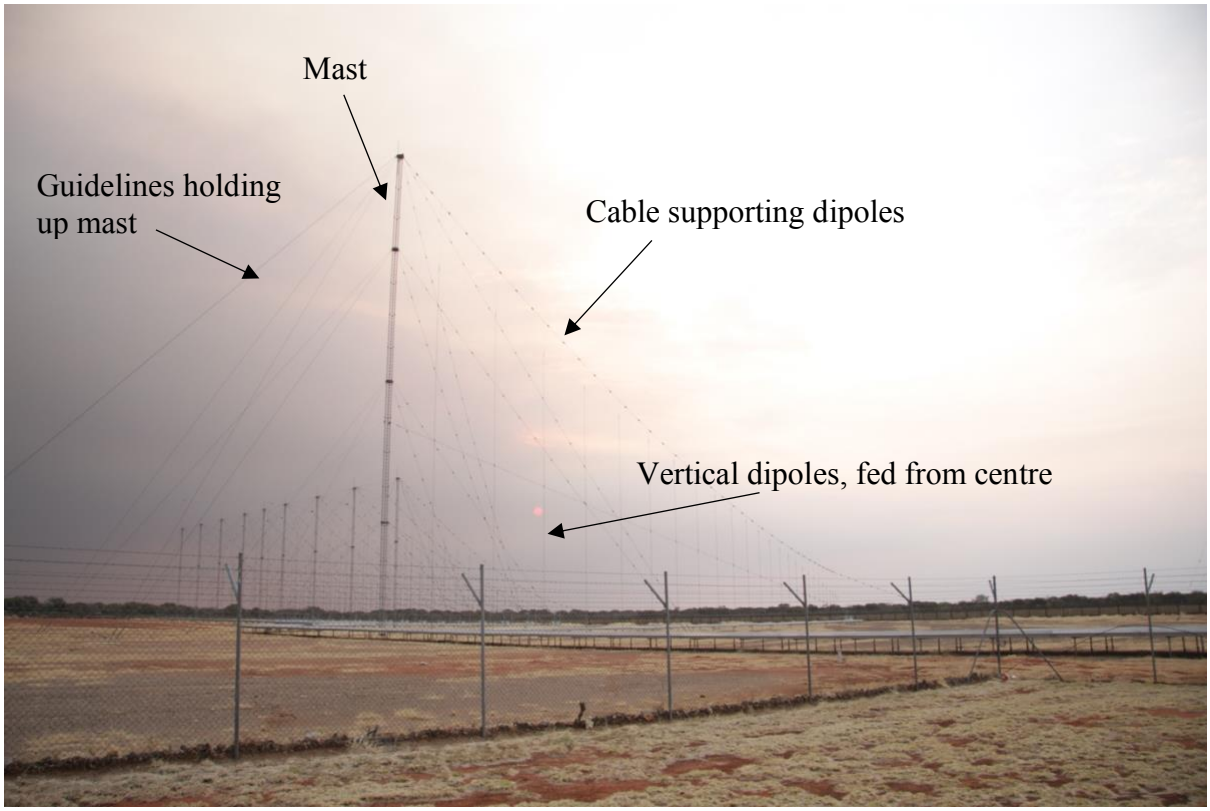

Figure 3.2: The Alice Springs FMS low band single log-periodic transmit antenna. Image provided by DST Group.

Figure 3.3: The Longreach FMS doublet monopole receiver antenna array. The low band antenna is in the foreground, the high band antenna is in the background. Image provided by DST Group.

Figure 3.4: The Alice Springs dual fan monopole receiver antenna array. Image provided by DST Group.

3.3 PHaRLAP ray tracing software

The 2D numerical ray tracing functionality of PHaRLAP was used to synthesise backscatter ionograms. PHaRLAP is a MATLAB toolbox developed by Defence Science and Technology Group [1] for modelling the propagation of high frequency radio waves through the Earth's ionosphere. Within PHaRLAP, 2D and 3D numerical ray tracing and analytical ray tracing engines are provided along with the International Reference Ionosphere and International Geomagnetic Reference Field models. The ray tracing algorithms account for many different effects including geometric gains and losses via the focussing and defocussing of rays, ionospheric absorption, ground forward and backscatter losses, ordinary (O) and extraordinary (X) polarisation mode splitting and Doppler shift and spread.

3.4 Real Time Ionospheric Model

The real time ionospheric model (RTIM) is a data driven model, generated using data from the Australian Defence Force's (ADF) network of oblique and vertical incidence sounders [46] (Figure 3.5). These sounders constantly monitor the ionosphere for the purpose of generating a near real time ionospheric model, which is required for the JORN coordinate registration system [47]. The RTIM is built from quasi-parabolic layers [48, 49] that parameterise the electron density profile. A 3D grid of ionospheric electron densities was provided by Defence Science and Technology Group for use in this work.

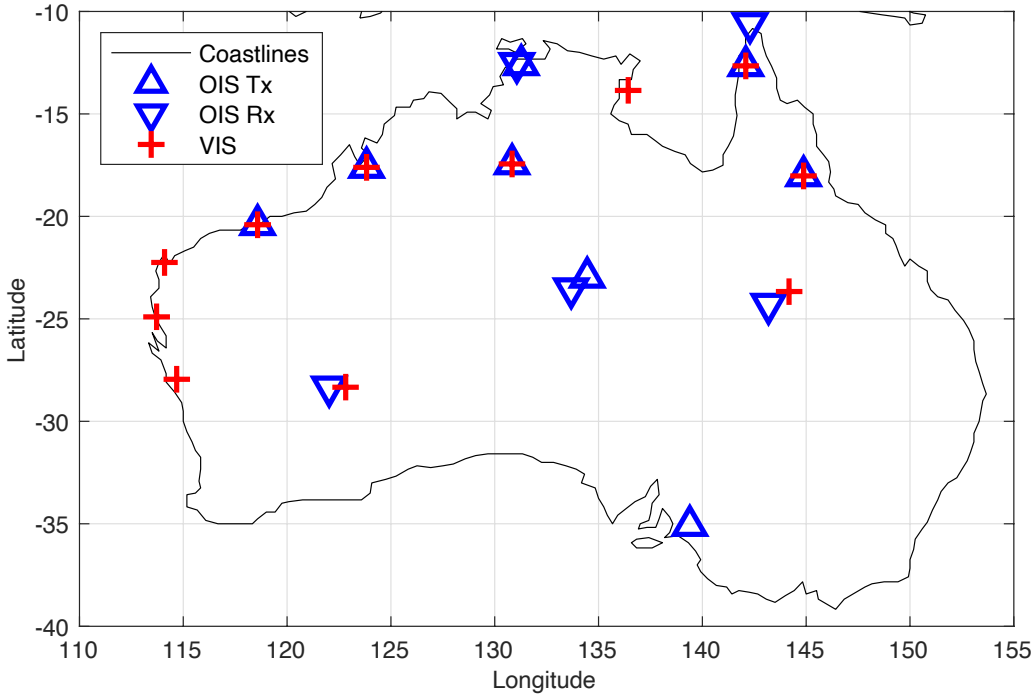

Figure 3.5: Network of the ADF oblique incidence sounder (OIS) transmit (Tx) and receive (Rx) sites and the vertical incidence sounder (VIS) sites.

This data was supplied at a temporal resolution of 5 minutes for September 2015 and March 2016. The spatial resolution of this data was one degree in latitude and longitude and one-kilometre height steps. The coverage of the ionospheric model provided was from -32 to -10 degrees in latitude, 100 to 155 degrees in longitude and from 80 to 600 km in altitude. Figure 3.6 shows the critical frequencies of the F2 layer (foF2) from the RTIM data at 0400 UT on 1/9/2015.

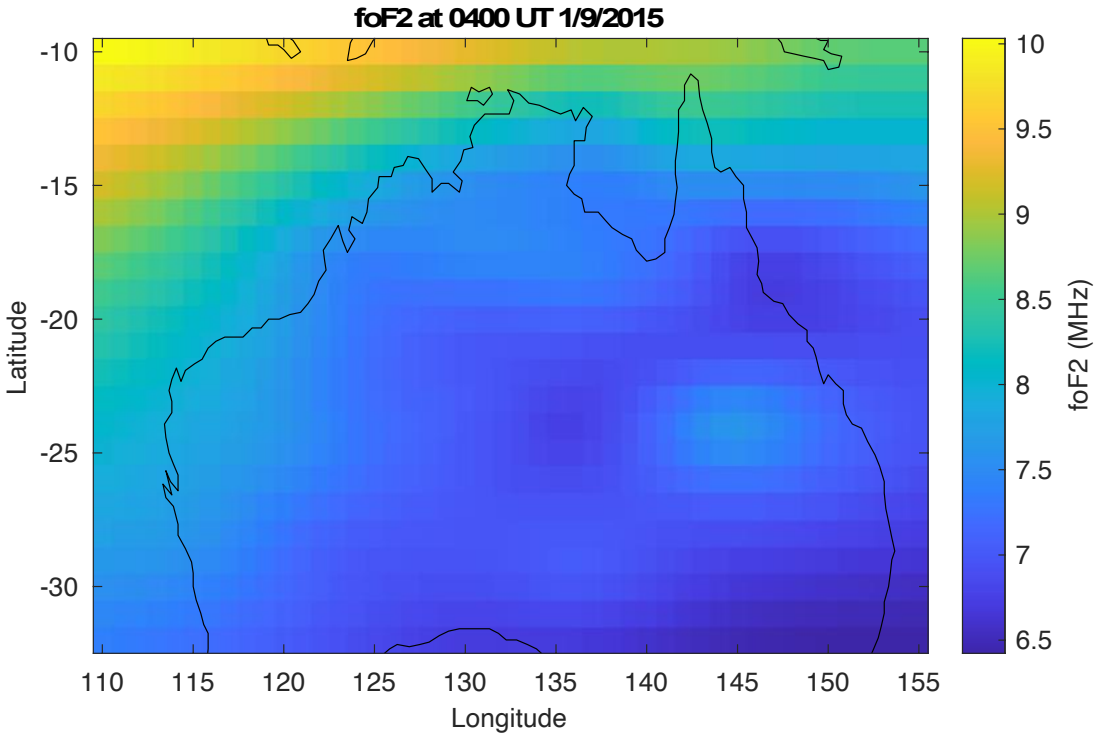

Figure 3.6: foF2 values from the RTIM at 0400 UT on 2015/09/01.

3.5 Sea state data

Sea hindcast data for September 2015 and March 2016 was accessed from the Centre for Australian Weather and Climate Research [50]. The hindcast data was produced using the WAVEWATCH III model forced by the reanalysed winds. It was available hourly over the globe at 0.4˚ resolutions and available at high resolution down to 4’ over the South Pacific and the Australian coast. Many parameters were available from this data set, but for this project only the significant wave height (m) and peak period (s) of the primary, secondary and tertiary swells and the wind sea were used along with the northward and eastward components of the wind (m/s). A plot of the peak period of the primary swell from the 0.4˚ resolution hind cast data is shown in Figure 3.7.

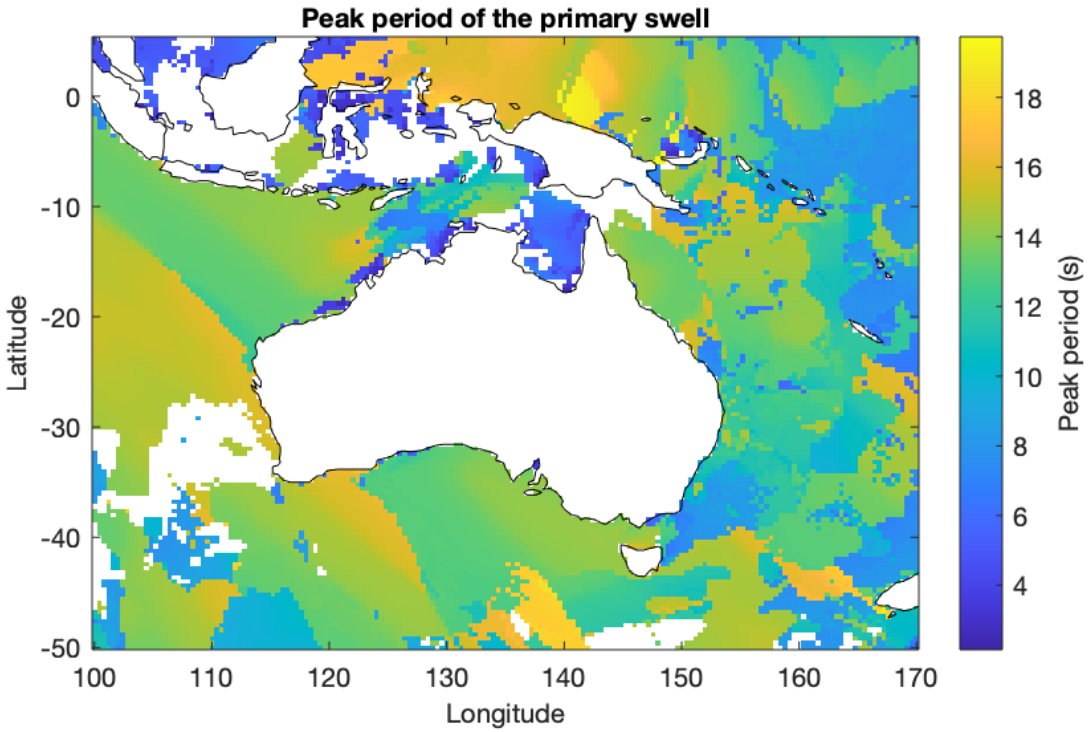

Figure 3.7: Peak period of the primary swell at 0400 UT on 2015/09/10 from the 0.4˚ resolution sea hindcast data.

3.6 Australian topographic data

3.6.1 ETOPO1 Global Relief Model

A topographic map of Australia was accessed from the National Geophysical Data Center, NOAA [51]. This model was built from global and regional data sets and includes the land topography and the ocean bathymetry. The spatial resolution is 1 arc-minute (around 2 kilometres) and the resolution of the elevation data is 1 metre.

3.6.2 SRTM Smoothed Digital Elevation Model

A hydrologically enforced smoothed digital elevation model (DEM-H) derived from data from the Shuttle Radar Topography Mission (SRTM) was accessed from Geoscience Australia [52]. The DEM-H was based on a smoothed bare-earth digital elevation model, where features such as vegetation and man-made structures were removed when possible to represent the ground surface topography. This data has a spatial resolution of 1 arc-second (around 30 metres). The extent of the data was over mainland Australia, covering latitudes from -10˚N to -44˚N and longitudes from 113˚E to 154˚E.

3.7 Soil moisture data

Global soil moisture data was accessed from the NASA National Snow and Ice Data Centre [53]. This data was available from the 31st March 2015 to the present and spans the globe. The temporal resolution of this data is 3 hours, and the spatial resolution is 9 by 9 km. The soil moisture data describes the volumetric water content and is in units of cubic metres of water per cubic metres of soil (m^3m^{-3}). Data from Australian local day times (0130 UT, 0430

UT and 0730 UT) for September 2015 and March 2016 was used in this project. The top layer soil moisture (0-5 cm) from this data set on 15/9/2015 is shown in Figure 3.8.

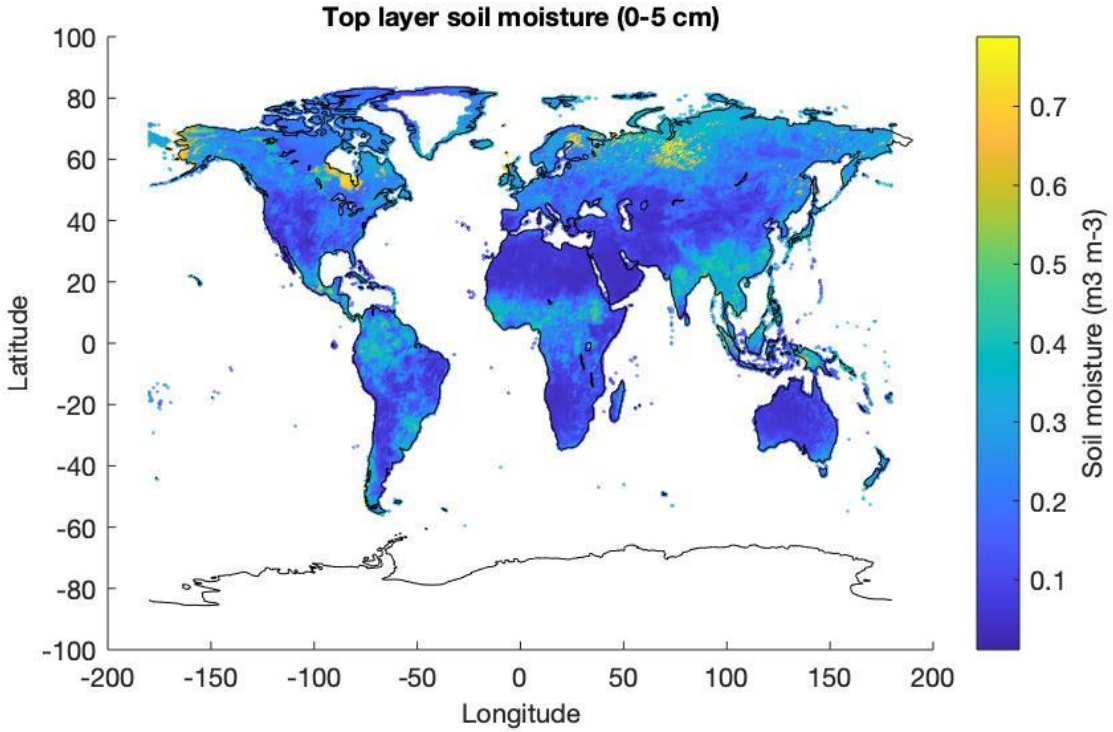

Figure 3.8: Global top layer soil moisture on 2015/09/15 at 0130 UT.

3.8 Vegetation height and structure data

A map of the vegetation height and structure across Australia (Figure 3.9) was accessed from the Joint Remote Sensing and Research Project [54]. This data contained forest structure codes which are dependent on the plant coverage and height (Table 3.2). The data covered latitudes from -6 to -45 degrees and longitudes from 108 to 160 degrees, with a spatial resolution of 30 metres. A 30-metre spatial resolution was much finer than required for this work, so the data was decimated in both directions, resulting in a decrease in size by a factor of 100. The vegetation data obtained was for a single snapshot of the vegetation coverage of Australia in 2009. However, it was assumed that the vegetation structure at the spatial scales of interest had not changed significantly, so was used to compare to the backscatter coefficients calculated for 2015 and 2016.

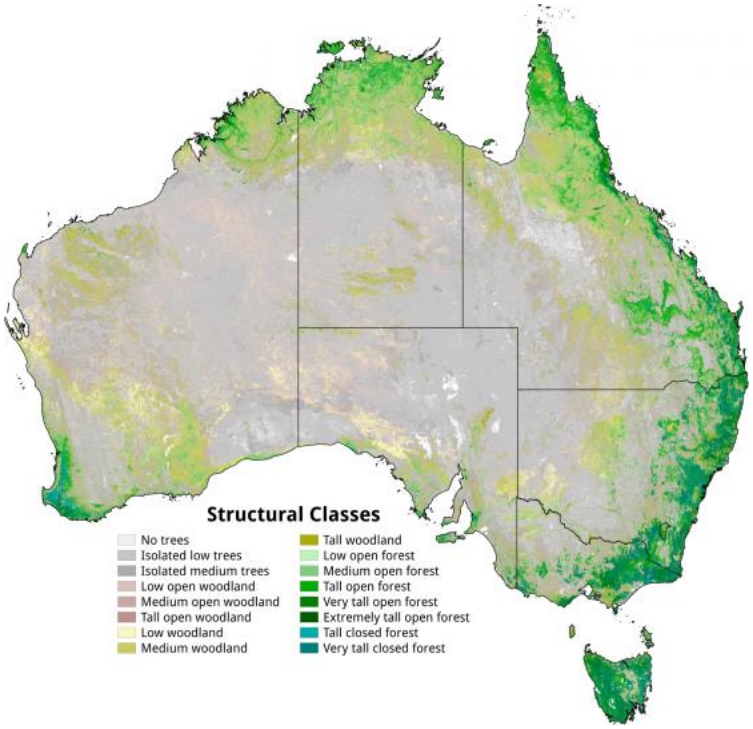

Figure 3.9: Vegetation structural classes across Australia. Image from [54].

Table 3.2: Definition of the forest structure codes.

Code	Structural Formation	Total plant cover fraction (%)	95th Percentile Height (m)
0	No Data	-	-
10	No trees	0	-
21	Low scattered trees	0 to 6	< 9
22	Medium scattered trees	0 to 6	9 to 17
31	Low open woodland	6 to 11	< 9
32	Medium open woodland	6 to 11	9 to 17
33	Tall open woodland	6 to 11	17 to 27
41	Low woodland	11 to 30	< 9
42	Medium woodland	11 to 30	9 to 17
43	Tall woodland	11 to 30	17 to 27
44	Very tall woodland	11 to 30	27 to 57
51	Low open forest	30 to 70	< 9
52	Medium open forest	30 to 70	9 to 17
53	Tall open forest	30 to 70	17 to 27
54	Very tall open forest	30 to 70	27 to 57
55	Extremely tall open forest	30 to 70	> 57
63	Tall closed forest	> 70	17 to 27
64	Very tall closed forest	> 70	27 to 57

3.9 MATLAB

MATLAB version 2019b [55] was used along with the PHaRLAP ray tracing software to synthesise backscatter ionograms. This code is included in Appendix A. The MATLAB mapping and statistics toolboxes were used in the analysis of the results.

3.10 Summary

A range of data sources and software are required for calculating surface backscatter coefficients using the methods described in the next chapter, including backscatter ionograms, ionospheric models, sea state data and ray tracing software. Topographic data, soil moisture data and vegetation data were required to investigate how different surface parameters affect the backscatter coefficient. Two methods of calculating surface backscatter coefficients are presented in Chapter 4, along with a description of how the effects of surface parameters were investigated.

Chapter 4 Method

4.1 Overview of chapter

This chapter describes two methods of calculating surface backscatter coefficients; a method of comparing synthesised and observed ionograms and a method of calculating the sea backscatter coefficient from sea state data. A process of comparing these two methods is described, along with a method of investigating the effects of ray and surface parameters on the backscatter coefficient.

4.2 Calculating the backscatter coefficient using observed backscatter ionograms

A method of determining the backscatter coefficient by comparing an observed backscatter ionogram to a backscatter ionogram synthesised using numerical ray tracing was developed. The backscatter coefficient was calculated by investigating the difference in power between the synthesised and observed ionograms when all other losses were accounted for. In order for the backscatter coefficient calculated from the comparison of the synthesised backscatter ionograms and observed backscatter ionograms to be valid, the environmental conditions at that time must be accurately represented in the model.

4.2.1 Synthesising a backscatter ionogram

Backscatter ionograms in which the backscatter coefficient was set to 0 dB were synthesised using a model of the environmental conditions at the same time and locations as observed backscatter ionograms were available. The ionospheric conditions, antenna patterns, ray paths and ionospheric absorption were modelled.

Backscatter ionograms were synthesised by modelling the propagation of a fan of rays over a large number of elevations, as described by [12, 56]. Ray tracing was used to determine the path of these rays through the ionosphere, if they penetrated the ionosphere or where they returned to the ground. The received power P_r was calculated using a modified form of the two-way radar equation appropriate for HF propagation through the ionosphere

$$P_r = \frac{P_t G_t G_r \lambda^2 \Delta A \sigma_o}{(4\pi)^3 d_{e,o}^2 d_{e,i}^2} L_o L_i L_{pol} L_{scatt} \tag{4.1}$$

where P_t is the transmitted power, G_t is the transmit antenna gain, G_r is the receive antenna gain, λ is the signal wavelength, ΔA is the area of the ground illuminated by the flux tube, σ_o is the backscatter coefficient, $d_{e,o}$ is the out-bound effective range, $d_{e,i}$ is the in-bound effective range, L_o is the out-bound ionospheric absorption loss, L_i is the in-bound ionospheric absorption loss, L_{pol} is the polarisation mismatch loss and L_{scatt} is the forward scattering losses (which only applies for 2nd and higher order hops) [12]. The effective range accounts for propagation effects such as ray focussing and is given by the equation

$$d_e^2 = R_e \sin\left(\frac{D}{R_e}\right) \frac{\sin(\beta_f)}{\cos(\beta_i)} \left|\frac{dD}{d\beta_i}\right| \tag{4.2}$$

where β_i is the launch elevation of the ray and β_f is the ray elevation at the landing point [12]. The ionospheric absorption of the rays was calculated using the George and Bradley absorption model [57]. The antenna gain patterns were calculated using a numerical electromagnetics code (NEC) model of the transmitter and receiver arrays and were provided by DST Group. As with Coleman [12], it was assumed that polarisation mismatch caused by the difference in the polarisation of the signal with respect to the receiver antenna results in a 3 dB loss in power. A synthesised backscatter ionogram was then produced by finding the inbound and outbound ray paths that matched according to the ground range. The area of the ground illuminated by the flux tube of each ray was calculated. The area of the ground illuminated was given by [42]

$$\Delta A = R_e \sin\left(\frac{D}{R_e}\right)\left(\frac{dD}{d\beta}\right)\Delta\beta\Delta\phi \qquad (4.3)$$

where R_e is the radius of the Earth, D is the ground range, β is the elevation angle of the transmitted ray, $\Delta\beta$ is the elevation step used in the fan of rays, and $\Delta\phi$ is the azimuthal beam width. The azimuthal beam width is given by $\Delta\phi = \frac{\lambda}{l\cos\theta}$ where θ is the steer angle away from bore, λ is the wavelength of the signal and l is the length of the receiver array. The modelled received power was then distributed across the group range bins encompassed by the flux tube of the ray. This was done by determining which group bins the flux tube of each mode contributed energy to by calculating the group range extent of the flux tube using the change in group range with elevation and multiplying this by the elevation step. The power contributed to each group bin was then scaled based on the number of bins encompassed by the flux tube. This was repeated for each of the frequencies swept over by the backscatter sounders to populate the group-range versus frequency grid of the model backscatter ionogram (Figure 4.1).

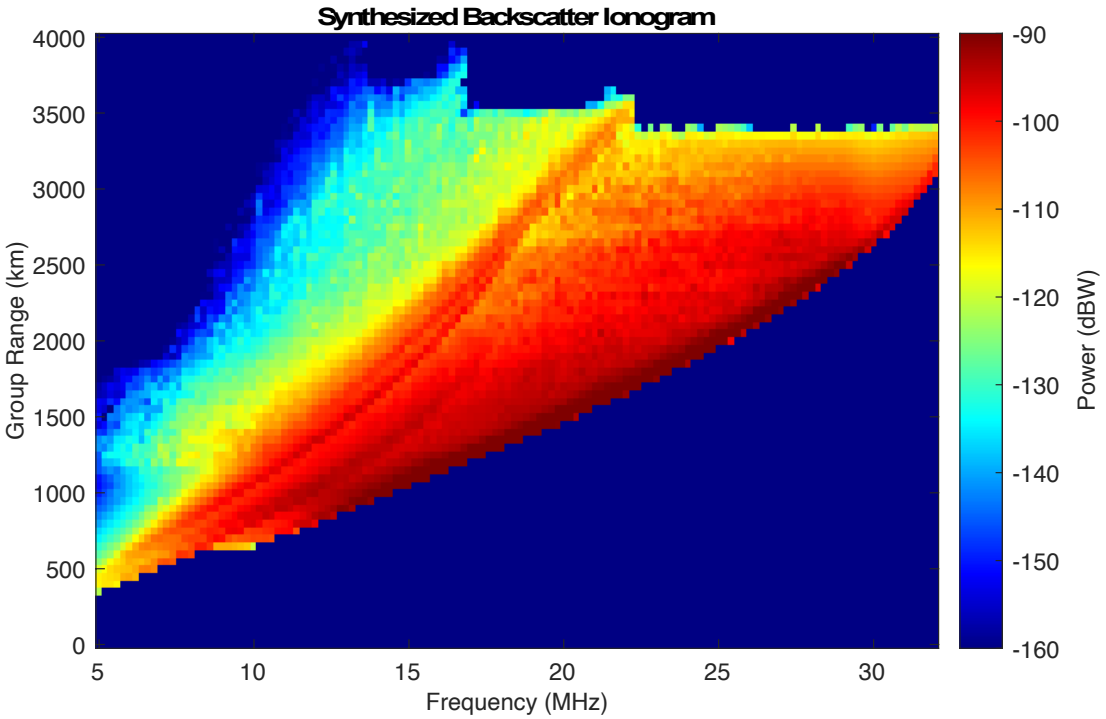

Figure 4.1: A synthesised backscatter ionogram.

Backscatter ionograms were synthesised for times between 0000 UT and 1000 UT, as these times corresponded with local times during the day when ionospheric propagation conditions were strongest. In central Australia 0000 UT corresponds with 0930 local time. During the night the electrons in the ionosphere recombine with the ions, reducing the ability for the ionosphere to support radio wave propagation. This results in propagation being constrained to low frequencies and thus a much less useable area of the backscatter ionograms for calculating backscatter coefficients (Figure 4.2).

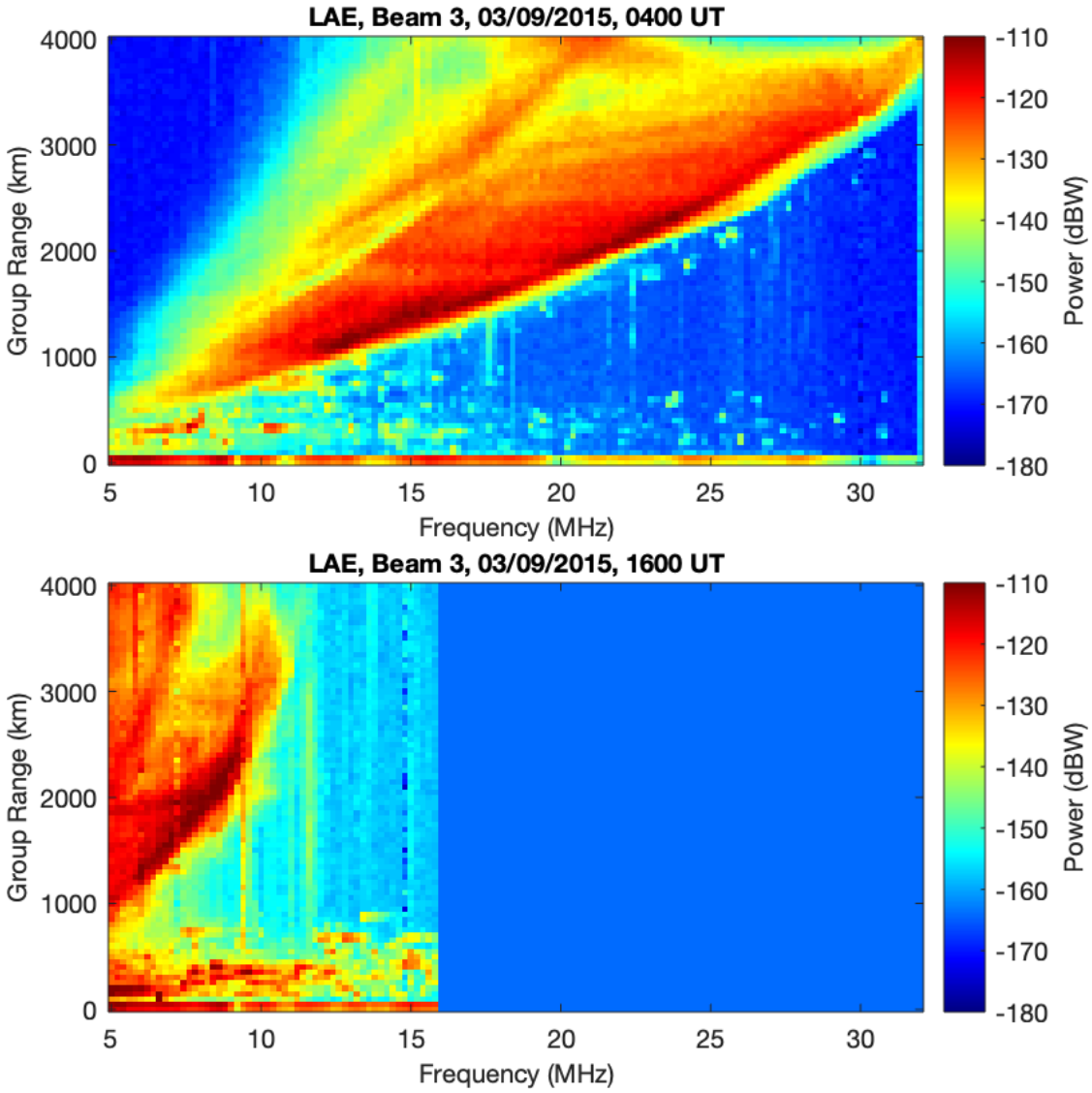

Figure 4.2: Top: Backscatter ionogram observed at 0400 UT during the day. Bottom: Backscatter ionogram observed at 1600 UT during the night. Note that in the night-time ionogram propagation at higher frequencies is no longer supported.

4.2.1.1 Ray tracing

PHaRLAP's 2D numerical ray tracing algorithm was used to model the paths of the transmitted radio waves through a model ionosphere (see Section 4.2.1.2). This ray tracing algorithm is based on the 2D ray tracing equations developed by Coleman [9, 12], and are numerically solved using a Runge-Kutta method [1]. While a 2D model of the ray paths does not include effects of the Earth's magnetic field i.e. the splitting of rays into ordinary and extraordinary modes [7] or out of plane propagation due to ionospheric tilts, it is much less computationally intensive than using a full 3D model, and has been shown to be sufficient for many simulations [12, 16]. 2D ray tracing was chosen for its speed, as many ionograms were required to be synthesised for this method of calculating the backscatter coefficient to build up a large database of results.

The surface of constant phase for a linear array is the shape of a cone. To take into account the coning effect of the backscatter sounder's linear receiver array, a correction was

applied to the azimuth of each ray for each off-boresight steer angle. As this correction factor is dependent upon the elevation of the ray, it was calculated for each ray in the fan separately. The correction to the azimuth of the ray is given by

$$\phi_{ray} = \sin^{-1}\left(\frac{\sin\phi_{steer}}{\cos\beta_{ray}}\right) \tag{4.4}$$

where ϕ_{ray} is the corrected azimuth of the ray, ϕ_{steer} is the angle the beam was steered off boresight and β_{ray} is the elevation of the ray.

Rays were modelled for frequencies from 5-32 MHz with frequency steps of 0.2 MHz. For each of these frequencies a fan of rays at elevations from 2 to 50 degrees at steps of 0.2 degrees were traced through the model ionosphere (Figure 4.3). The ray tracing software was used to model up to four hops for each of these rays. The software then determined whether the ray reached the ground, penetrated the ionosphere or exceeded the maximum ground range. The ground range, group range, elevation, apogee, absorption and path information of the rays were recorded. Using this information, the E-layer rays and F2-high layer rays were flagged, and the power contributed to each cell by these rays was calculated during the synthesis. The E-layer and F2-high rays were flagged so that regions of the ionogram where their contribution was significant could be discarded. It was important to calculate the backscatter coefficient using a region of the ionogram where only one main propagation mode contributed. E-layer rays were identified as rays with an apogee less than 110 km and F2-high rays were identified as rays with a change in ground range with respect to elevation greater than zero.

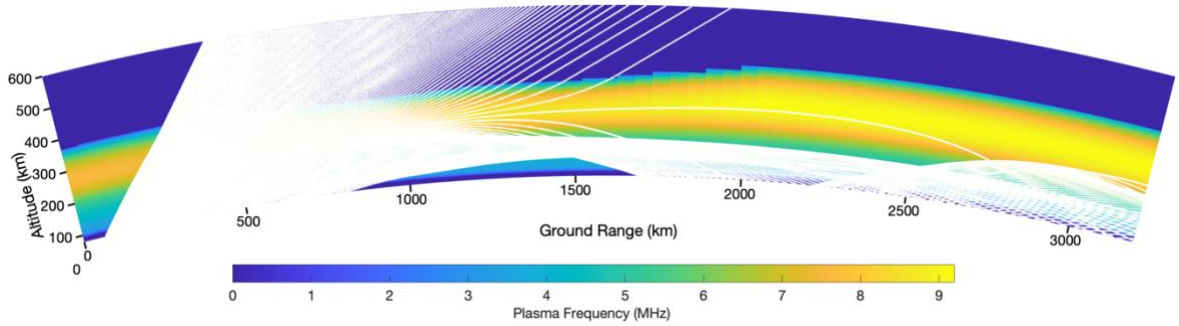

Figure 4.3: An example of ray tracing through the RTIM for a fan of rays.

4.2.1.2 Ionospheric models

A model of the ionospheric electron densities at the times and locations of interest was required for the ray tracing. Two different empirical models of the ionosphere were investigated for use in synthesising the backscatter ionograms; the international reference ionosphere (IRI-2016) and the real time ionospheric model (RTIM).

4.2.1.2.1 IRI-2016

The International Reference Ionosphere (IRI-2016) is a climatological model developed by the Committee on Space Research (COSPAR) and the International Union of Radio Science (URSI). It produces monthly median electron densities at altitudes of 50-2000 km [58]. The PHaRLAP toolbox includes the ability to generate an ionospheric grid from IRI-

2016 for a given location and time for use with the ray tracing. Figure 4.4 displays an example of a slice though the ionosphere generated by IRI. As this model produces a monthly median of the electron densities, the day-to-day variation in the ionosphere was not captured. Hence it was not expected that IRI-2016 would provide an accurate representation of the ionosphere at a given time of interest.

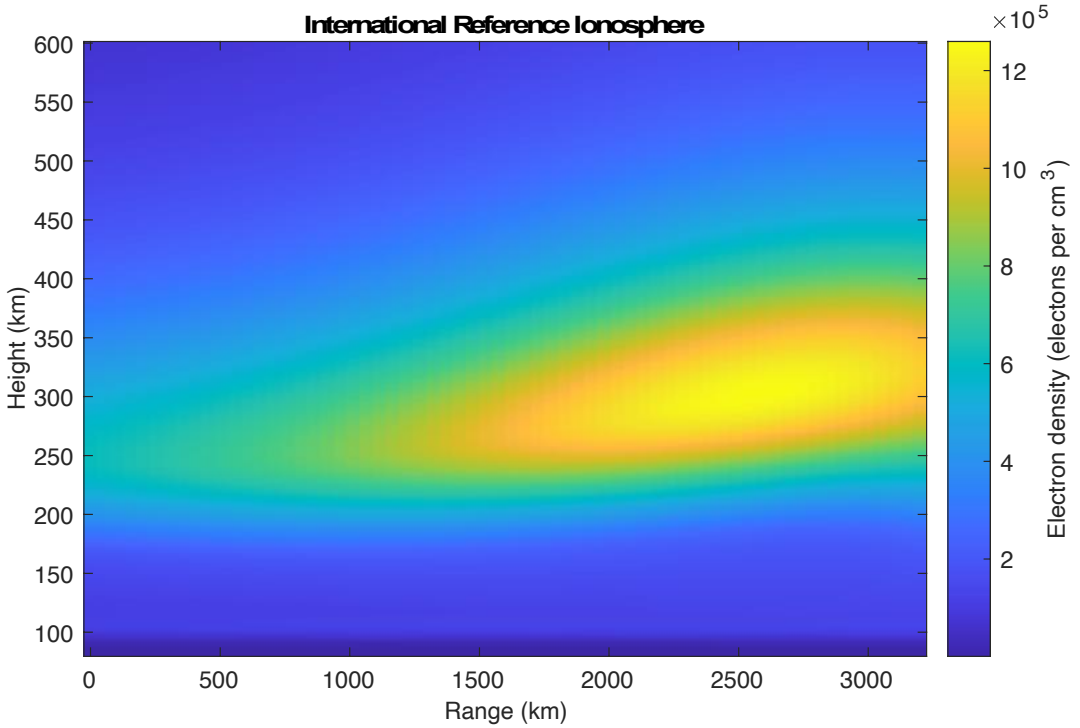

Figure 4.4: A slice of the IRI-2016 at 0100 UT on 2015/09/03 in the direction of beam 1 from Laverton East.

4.2.1.2.2 RTIM

Slices through the JORN real time ionospheric model (RTIM) were also used for the ray tracing in the backscatter ionogram synthesis. As this ionospheric model is produced near real time, it is expected to capture day-to-day variability better than IRI-2016 and hence provide a more accurate representation of the ionosphere at each time of interest. However, the accuracy of the RTIM depends on the number of sounders available in the area of interest.

Ionospheric slices starting from the location of the backscatter sounder and extending 3200 km in range in the required direction were created using the RTIM. Linear interpolation was used to determine the electron densities along each slice at range steps of 50 km and heights from 80 to 600 km with height steps of 1 km. If the RTIM did not extend the entire 3200 km away from the sounder location, the electron density values from the last available range of the RTIM were replicated for the remainder of the slice. Rays that passed through a replicated area of the ionospheric model in the ray tracing were flagged for subsequent treatment. If a ray was above 80 km when it reached the replicated region of the ionosphere it was rejected for future analysis. Rays below 80 km were kept as these rays only propagated through the neutral atmosphere and the ray path would not undergo any appreciable ray bending.

To smooth the transition from the neutral atmosphere to the ionosphere at the bottom of the ionospheric model, a small number of electrons were added to the ionospheric grid immediately below the first non-zero cell. An electron density equal to the first non-zero value divided by 8 and divided by 64, were added to the cells one height step and two heights steps below the first non-zero value respectively. The quasi-parabolic layers of the ionospheric model are discontinuous in the second derivative, so the addition of these small electron density values improved the transition into the ionosphere while having an insignificant effect on the ray path. Section 4.3.1.1 describes the effect of adding these small electron densities in more detail. An example of one of the slices of the RTIM is shown in Figure 4.5. Note that the RTIM does not model the topside ionosphere and so at altitudes above the peak electron density the RTIM is not realistic. This has no impact on the synthesis of the model backscatter ionograms as only propagation via the bottom side ionosphere is important.

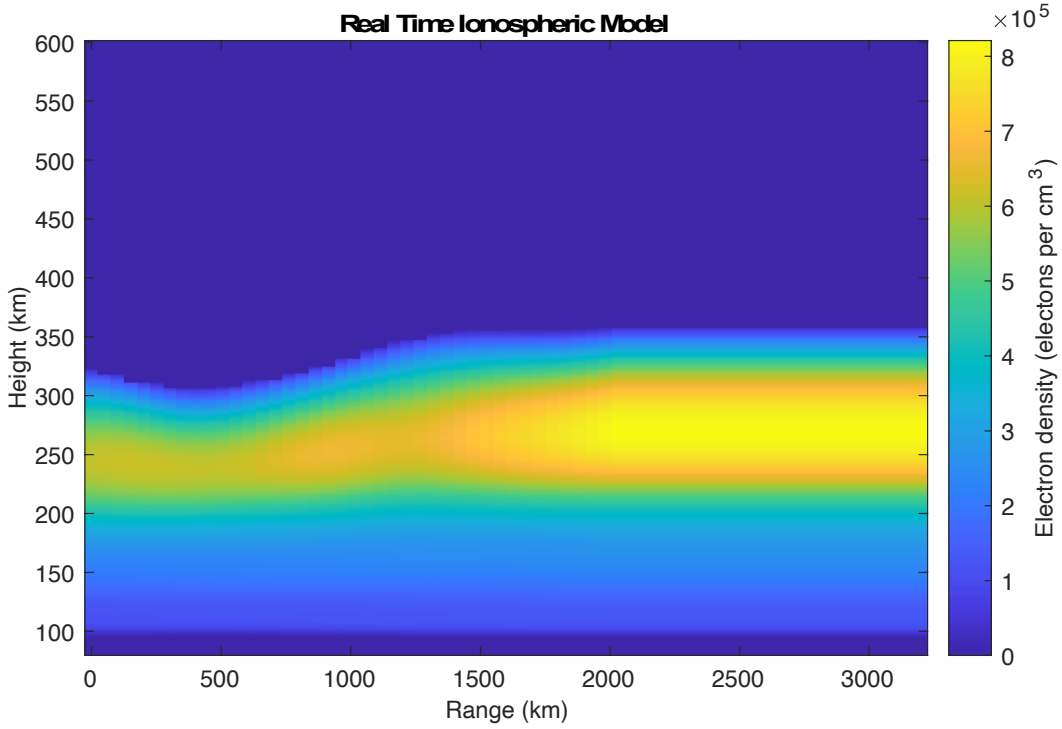

Figure 4.5: A slice of the RTIM at 0100 UT on 2015/09/03 in the direction of beam 1 from Laverton East.

4.2.1.3 Ionospheric absorption

As radio waves travel through the ionosphere, they undergo absorption by the ionosphere dependent on the electron density, electron collision frequency and radio wave frequency. Most of the absorption occurs in the lower regions of the ionosphere; in the D region and lower part of the E region [5]. Absorption in this region of the ionosphere is often referred to as non-deviative absorption [7] as the ionosphere is weak and does not affect the path of the radio waves. Strong absorption occurs in this region of the ionosphere due to the relatively high neutral density resulting in high electron collision frequencies. The non-deviative absorption is inversely proportional to the square of the frequency of the wave [7]. Absorption also occurs when the radio waves experience appreciable amounts of deviation to their path (e.g., at the

apogee of the path) and is usually referred to as deviative absorption [7]. The total absorption can be calculated by integrating the imaginary component of the complex refractive index along the path of the ray [59]. However, as the RTIM does not include a model of the D region of the ionosphere, this method of calculating the absorption would lead to the absorption being underestimated. Hence, the George and Bradley model of absorption [57, 60] was used in the backscatter ionogram synthesis. This model of absorption is an empirical model based around measurements of absorption at vertical incidence and translating these to oblique paths. As such it is not expected to be accurate for unusual non-typical paths (e.g., chordal or ducted paths). The George and Bradley model of absorption does not capture any day-to-day variation in absorption. The deviative absorption at the F1-F2 cusp or for F2 high rays (where the rays experience significant bending) is not included in the George and Bradley model. However, it is estimated by the PHaRLAP ray tracing routines. Hence, the total absorption experienced by the radio waves was given by the George and Bradley absorption plus the deviative absorption estimated by PHaRLAP.

4.2.1.4 Antenna patterns

The antenna patterns were provided by Defence Science and Technology Group. These patterns were calculated using a method-of-moments electromagnetic solver; Numerical Electromagnetics Code (NEC) [61]. The transmit antenna gains and the receiver gains, including the power loss due to antenna impedance mismatch were used for the given direction and frequencies required for each of the beams. The transmitter gain and receiver gain for a JORN sounder steered towards beam 3 are shown in Figure 4.6 and Figure 4.7 respectively.

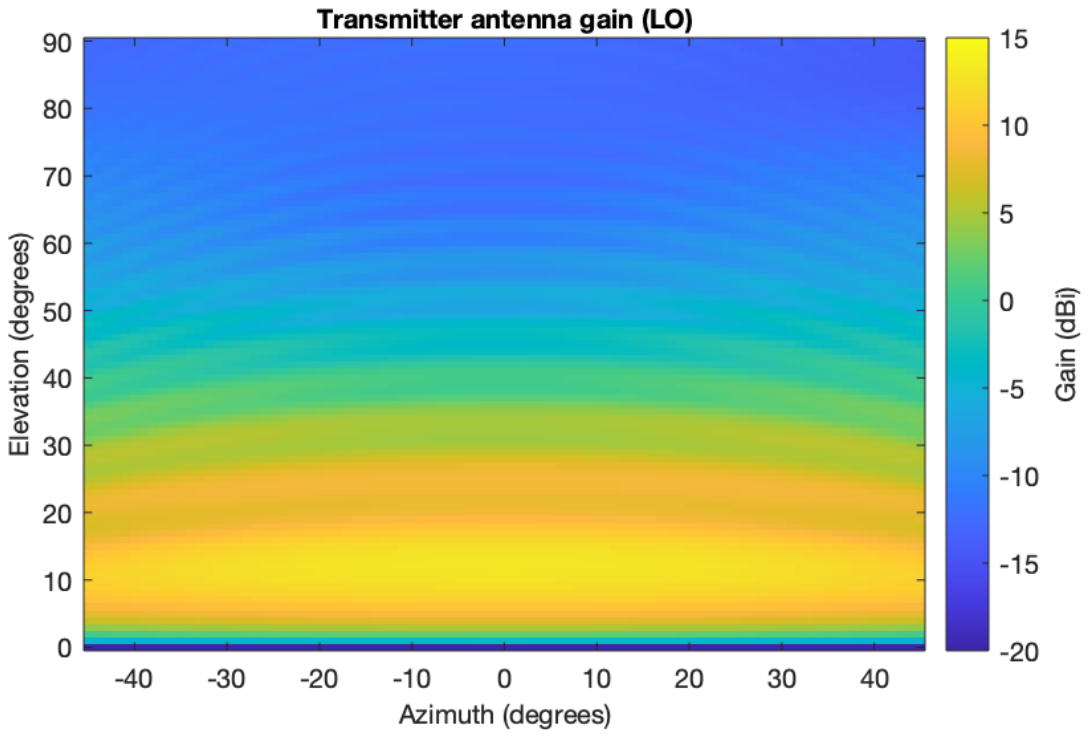

Figure 4.6: Transmitter gain for a JORN sounder, calculated using NEC.

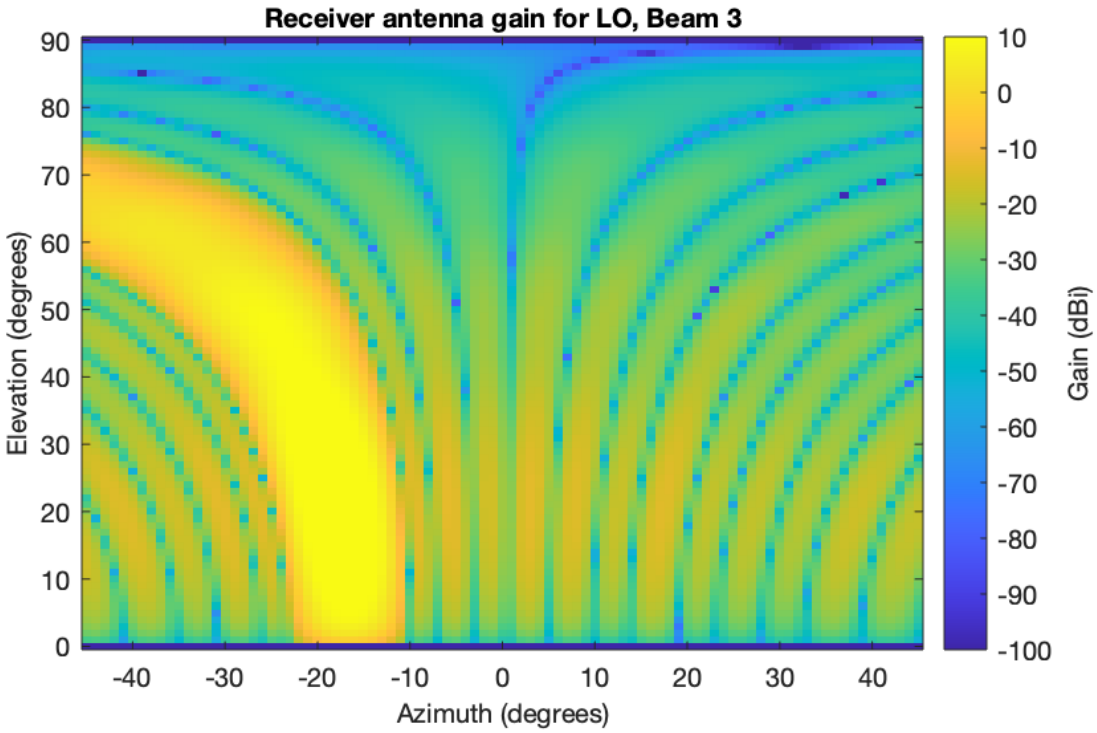

Figure 4.7: Receiver gain for Beam 3 of a JORN sounder (steered -16.5 degrees off bore), calculated using NEC.

4.2.2 Comparing an observed ionogram to a synthesised ionogram

To calculate the backscatter coefficient, a suitable area of the observed and synthesised ionograms for comparison is required to be identified. An area of the ionogram containing only one significant mode of propagation was desired. This is because different modes of propagation have different elevations and may have different ground ranges, and the backscatter coefficient is expected to be elevation dependent and dependent on the surface properties of the ground. This also meant that only the first hop area of the backscatter ionogram was desired, as rays from this region had only scattered off one patch of ground. The area of the backscatter ionogram predominantly comprised of contributions from one-hop F2-low rays was selected for the calculation of the backscatter coefficients.

A method of automatically selecting this region of the backscatter ionograms was developed. First, the amount of power in the observed ionogram was examined to ensure the ionosphere was adequately supporting propagation at that time. The method of examining the power in the observed ionograms is described in Section 4.2.2.1.1. If the observed ionogram was suitable, a backscatter ionogram was synthesised using the modelled conditions from the time and location of the observed ionogram. Next, the observed and synthesised ionograms were compared by checking how well the leading edges matched, as described in Section 4.2.2.1.2. If the leading edges were significantly different, the synthesis model was deemed not sufficiently accurate at that time and the ionograms were not used. If the ionograms were considered suitable, the area corresponding to one-hop F2 low propagation was selected, based on the results from the ray tracing.

4.2.2.1 Selecting suitable ionograms

4.2.2.1.1 Power check

The power in the observed ionogram was checked to identify if it was suitable. This was done by ensuring that at least 75 cells contained a power value greater than -125 dBW. The conditions of this check were somewhat arbitrary; however, from observation of many ionograms it was found that this criterion worked well. Ionograms recorded when the sounder was not operating normally, or when the ionosphere was not supporting much propagation were removed by this check. An example of ionograms rejected due to the sounder not operating normally and due to poor ionospheric propagation are shown in Figure 4.8 and Figure 4.9 respectively. An example of an ionogram considered to be suitable is shown in Figure 4.10.

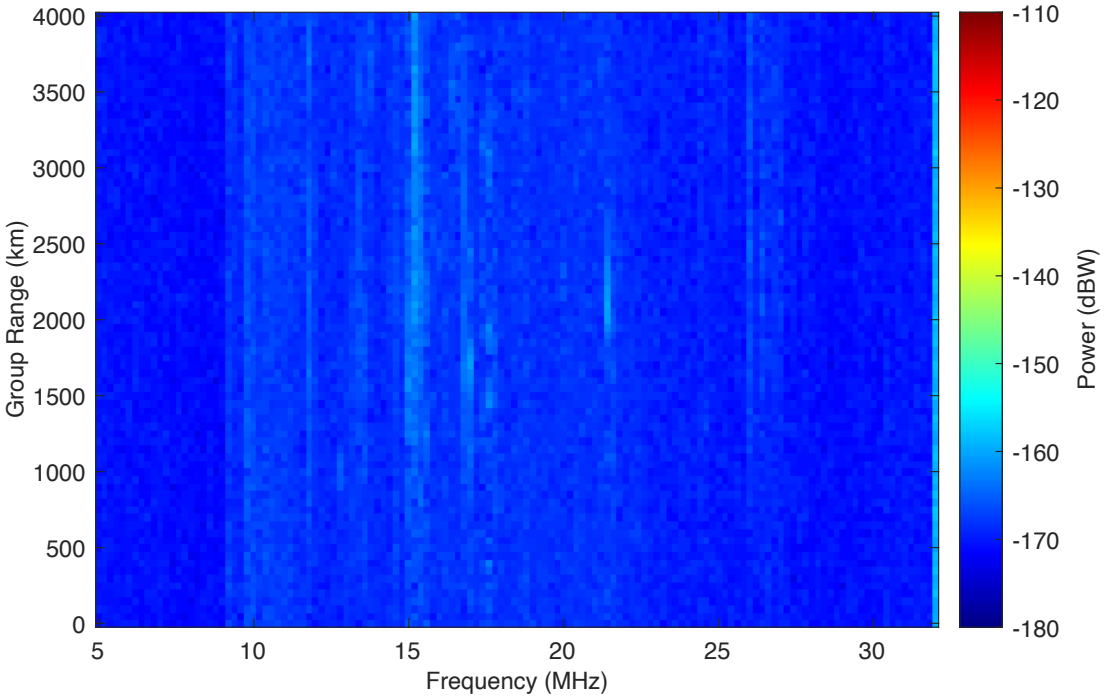

Figure 4.8: An ionogram rejected by the observed power check due to the sounder not operating normally. Here only background noise is display suggesting that the transmitter was not operating.

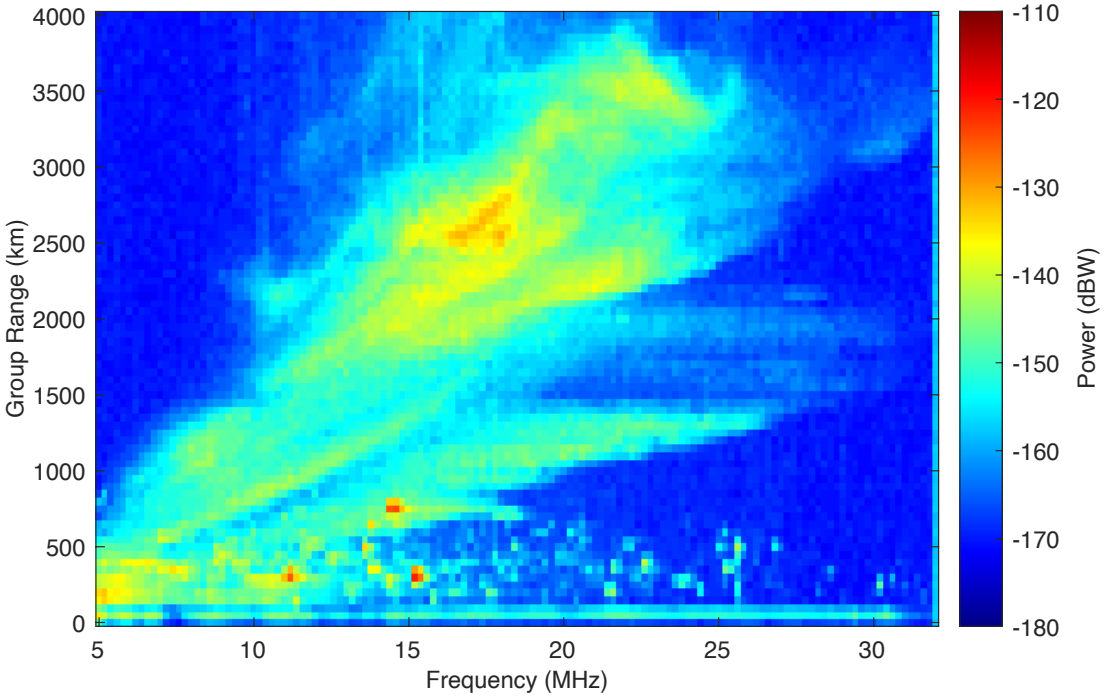

Figure 4.9: An ionogram rejected by the observed power check because the ionospheric propagation was poor. Although propagation was supported at frequencies up to 26 MHz, it can be seen by the low power of the ionogram that propagation was poor.

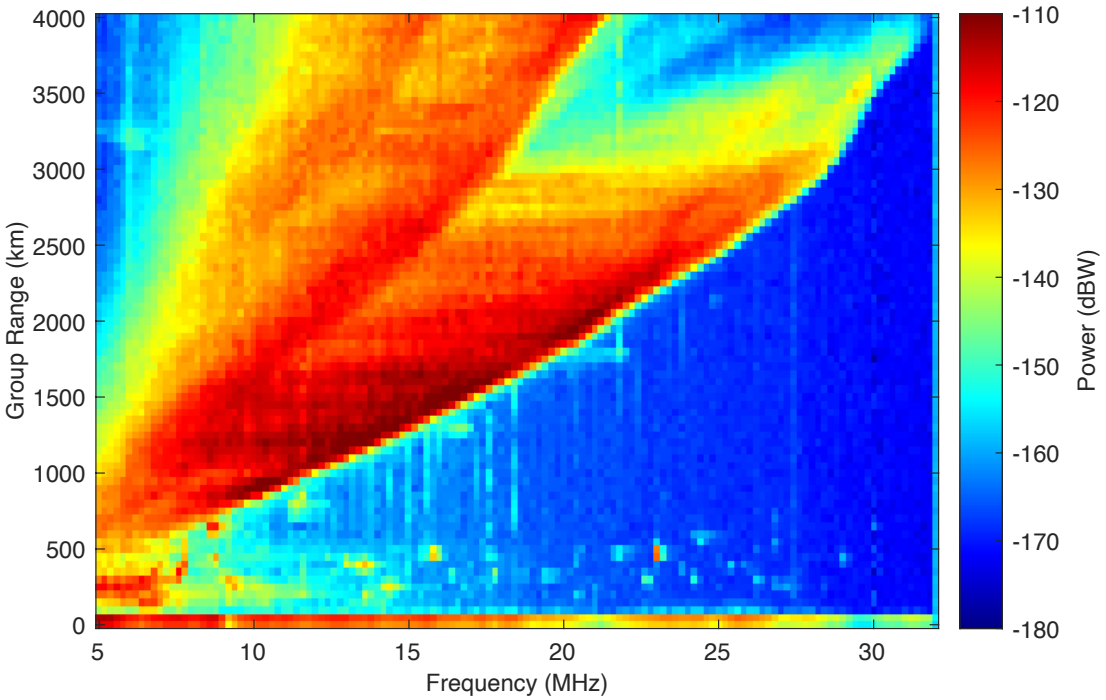

Figure 4.10: An ionogram that passed the observed power check so was considered suitable for subsequent analysis.

4.2.2.1.2 Leading edge check

The leading edges of the observed and synthesised ionograms were compared to test how well the ionospheric model used to synthesise the ionograms captured the true conditions. If the leading edges were too dissimilar the ionograms were discarded. The leading edges of the synthesised ionograms were straight forward to find, as it was simply the locus of the points of the first non-zero element for each frequency in the group-range versus frequency grid of the backscatter ionogram (Figure 4.11). The leading edges of the observed ionograms were more difficult to determine. An algorithm written in MATLAB to find the leading edge of backscatter ionograms was provided by Defence Science and Technology Group for this task. A side lobe canceller was applied to the backscatter ionograms to improve the ability of this algorithm to locate the leading edge [62]. Beyond the range where E mode propagation was expected, an initial slope of the F2 mode leading edge was estimated. A Kalman filter was then used to follow this slope along the leading edge of the ionogram out to the furthest group ranges. The slope from this section of the leading edge was then used to initialise the Kalman filter to follow the downward track to the nearest group ranges and so obtain the complete location of the leading edge of the observed ionogram. An example of the leading edge of an observed ionogram detected using this method is shown in Figure 4.12.

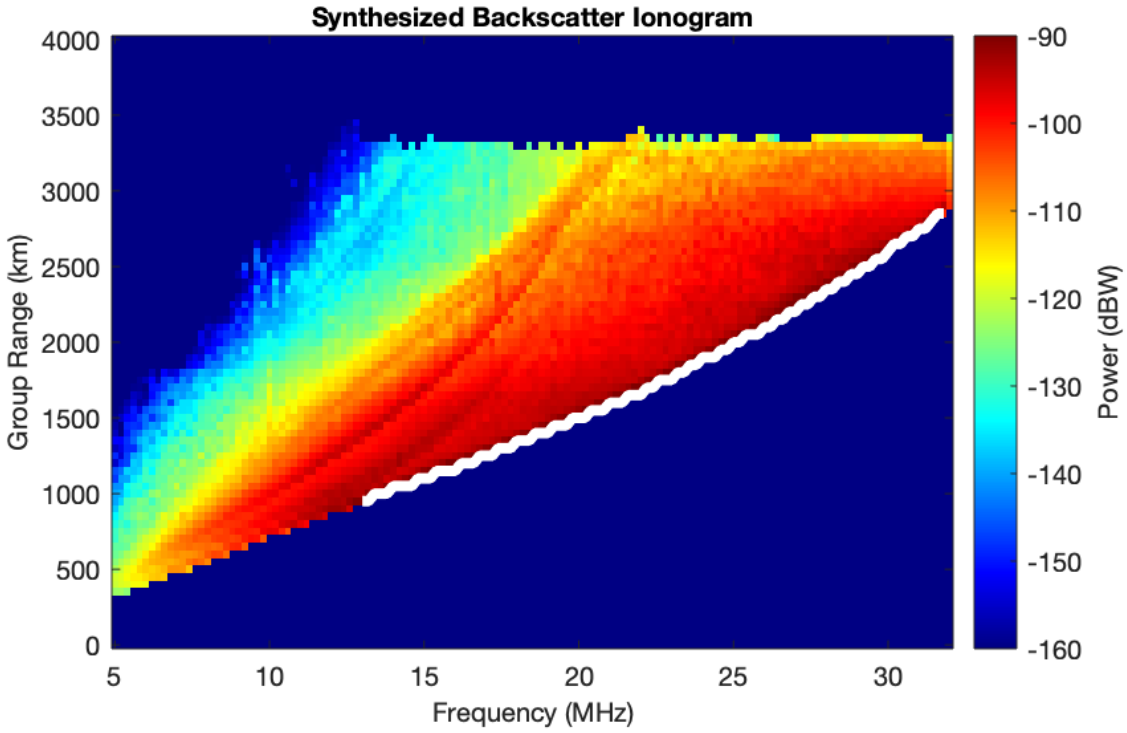

Figure 4.11: The leading edge (shown as a white line) of a synthesised ionogram. This synthesised ionograms is for Longreach beam 2 at 0200 UT on the 2015/09/03.

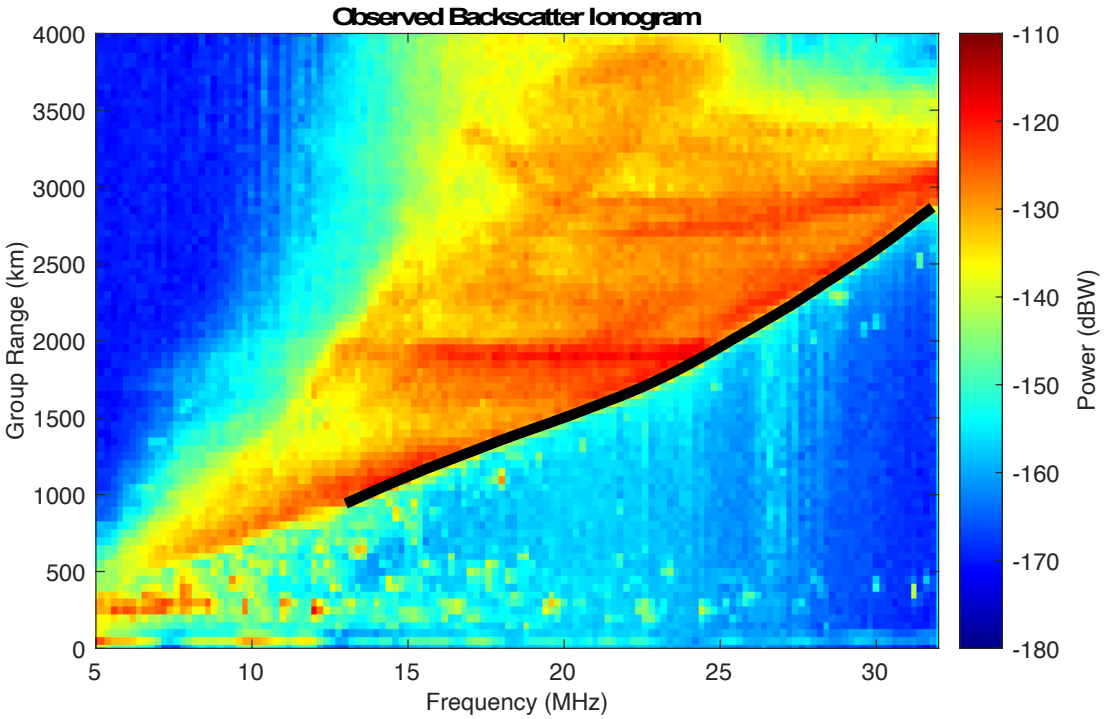

Figure 4.12: The leading edge (shown as a black line) of an observed ionogram, detected using the Kalman filter method. This ionogram was observed from Longreach beam 2 at 0200 UT on the 2015/09/03.

Once both the synthesised and observed leading edges had been found, the root mean square (RMS) difference of the group range between the two curves was calculated. If the RMS difference in the group ranges of the leading-edge curves was less than 300 km the ionograms were considered similar enough to be useful. If this difference was greater than 300 km the ionograms were rejected. The Longreach Beam 2 ionograms from 2015/09/03 at 0200 UT are an example of a time when the leading edges of the synthesised (Figure 4.11) and observed ionograms (Figure 4.12) agreed well. The RMS group range difference of the leading edges at this time was 22 km. The comparison of the two leading edges is displayed in Figure 4.13.

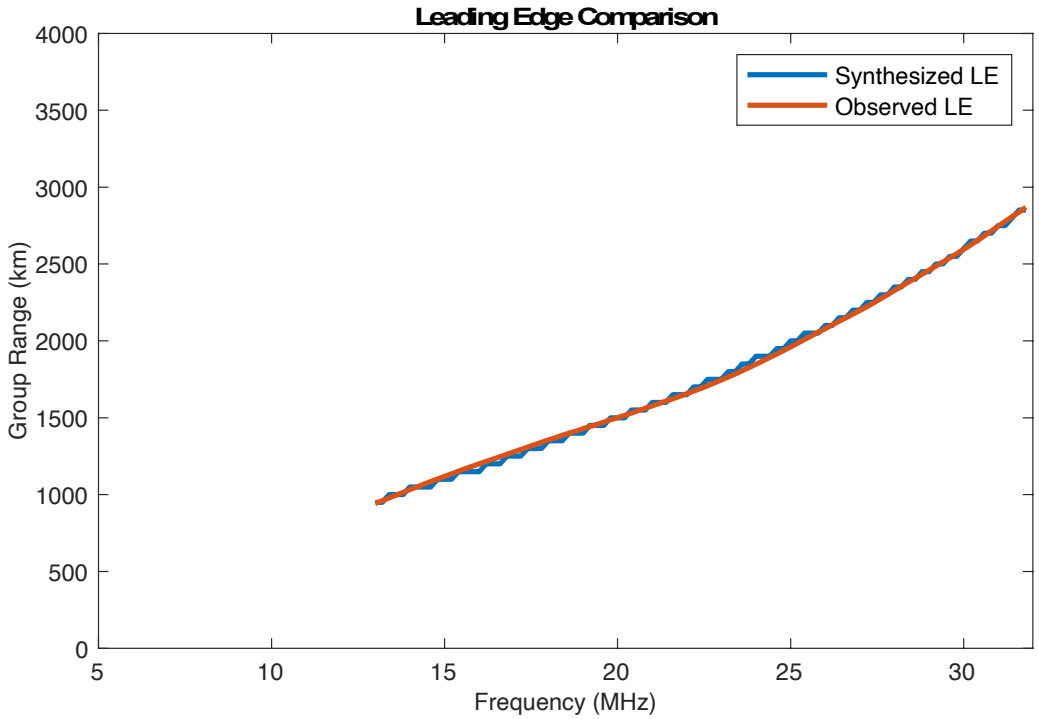

Figure 4.13: Synthesised and observed ionograms leading edges for Longreach beam 2 at 0200 UT on the 2015/09/03. The RMS group range difference of the leading edges is 22 km.

An example of a time where the ionograms were rejected as being too different is shown in Figure 4.14. At this time the RMS group range difference of the leading edges was 588 km.

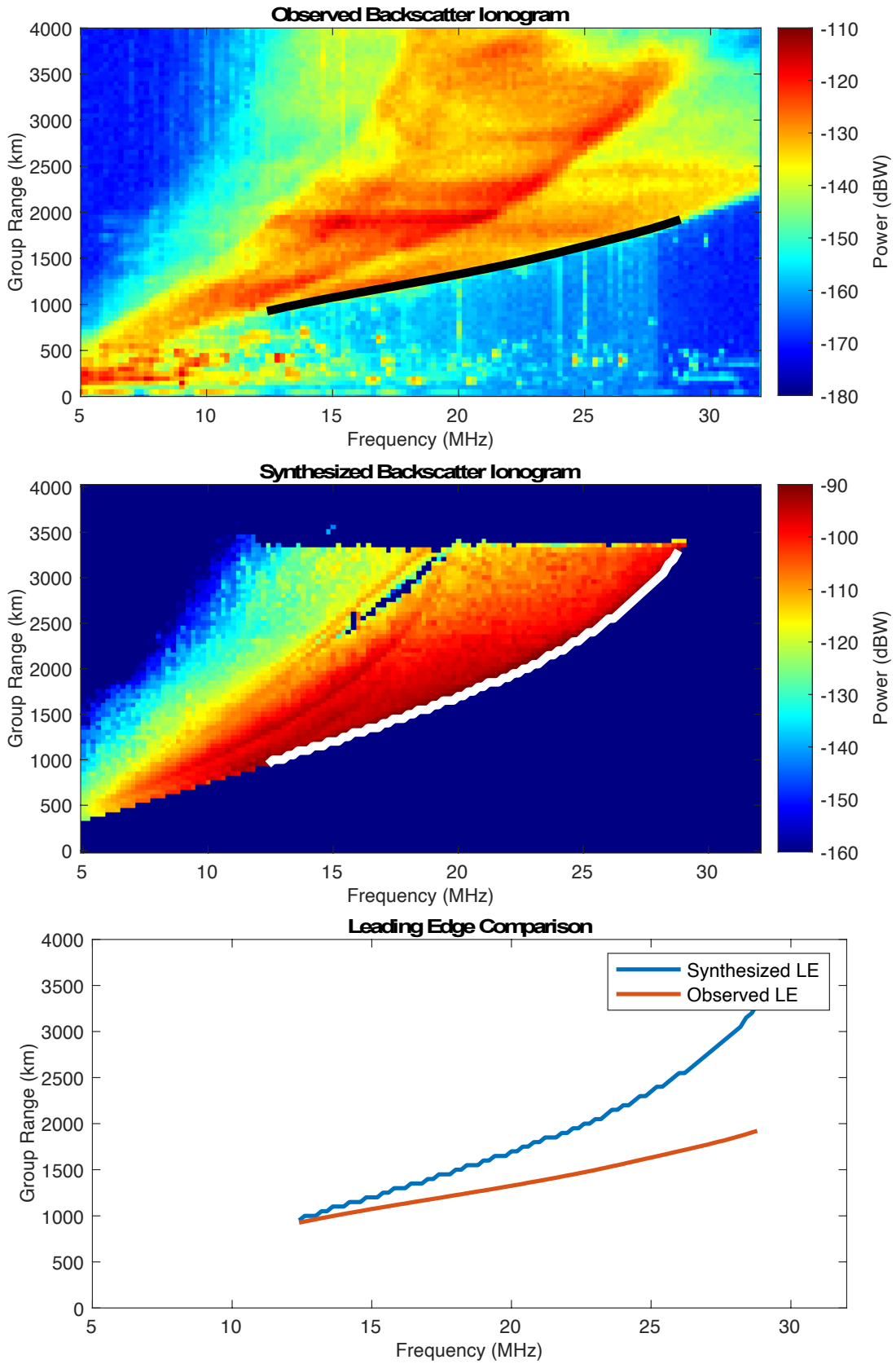

Figure 4.14: Leading edge comparison of Longreach beam 2 at 0100 UT on the 2015/09/06. Top: Observed ionogram. Middle: Synthesised ionogram. Bottom: Leading edge comparison. The RMS group range difference of the leading edges is 588 km.

4.2.2.2 Selecting the area of ionograms to compare

Once a pair of suitable observed and synthesised ionograms had been identified, the one-hop F2 low region of the ionogram was selected using the results from the ray tracing. The region dominated by one-hop propagation was selected based on the ray tracing results. Areas where the difference between the total power and the power contributed from E or F2 high propagation was less than 10 dB were removed. This was done to ensure the area selected consisted of predominantly one mode of propagation: the F2 low mode. The power contributed by these E and F2 high rays was calculated during the synthesis of the ionogram. Rays that propagated via the E layer were identified as the rays with an apogee less than 110 km (around 1 scale height above the peak of the E layer). Rays that underwent F2 high propagation were those rays with a change in ground range with respect to elevation greater than zero.

To account for any small differences in the location of the one-hop region of the observed and synthesised ionograms, the areas close to the leading and trailing edges were not selected for comparison. The trailing edge is the maximum group range of the one-hop region at which power is received for each frequency. The 3 group range cells nearest to the synthesised leading edge were excluded, i.e., the selected area was moved in 150 km from the synthesised leading edge. Cells within 100 km of the observed leading edge were also excluded, i.e., the 2 nearest group range cells. The nearest 10 cells to the trailing edge of the one-hop region of the synthesised ionogram in the frequency dimension were also removed to reduce the likelihood of areas outside of the one-hop region of the observed ionogram from being selected.

Once all these criteria had been applied, the region of one-hop F2 low propagation was left; this area was used to calculate the backscatter coefficient. An example of this selected region is shown in Figure 4.15.

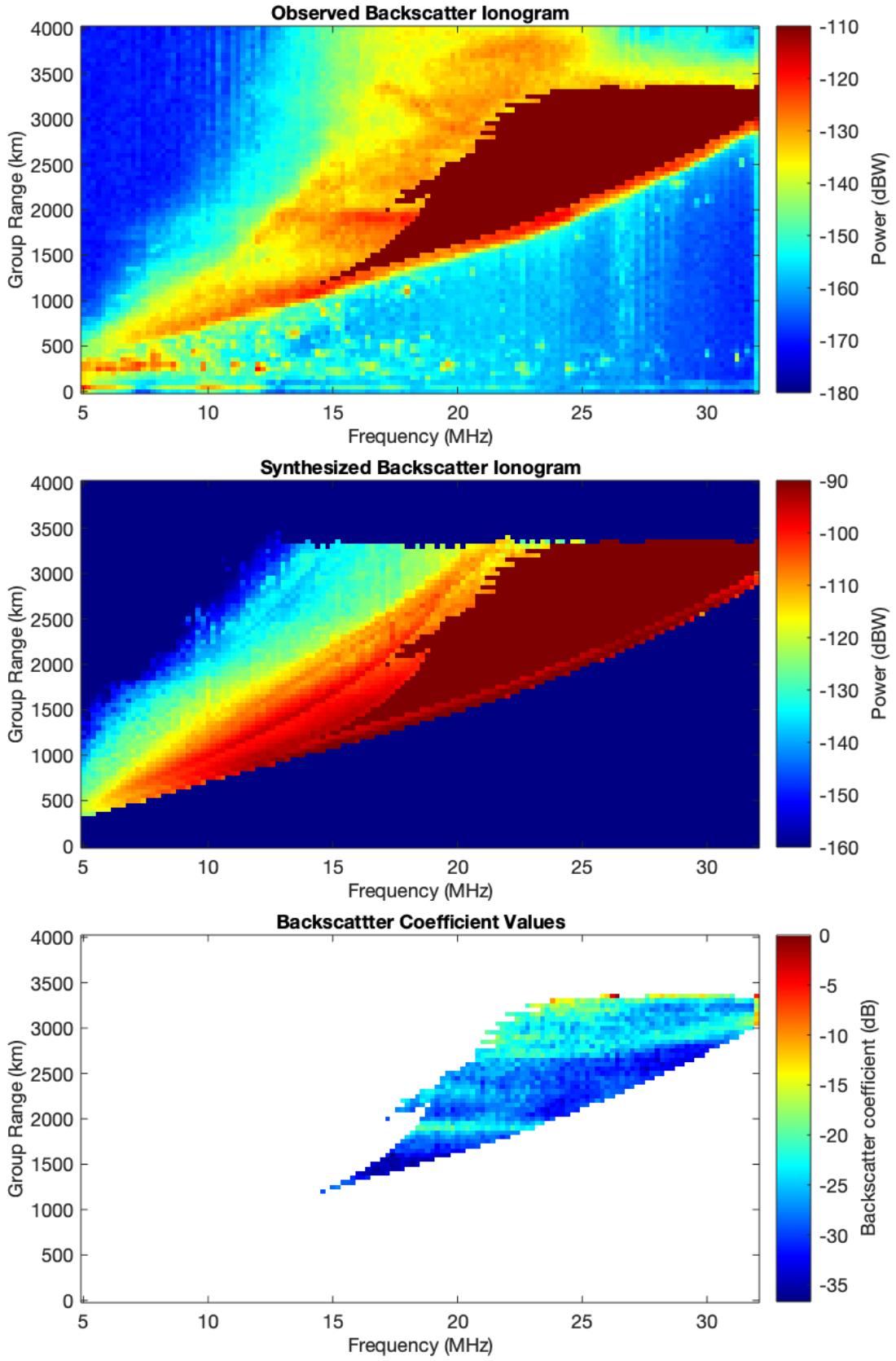

Figure 4.15: Area of one-hop F2 low propagation selected for use in calculating the backscatter coefficients (Longreach beam 2, 0200 UT 2015/09/03). Top: Area selected shown in maroon, overlayed on the observed ionogram. Middle: Area selected shown in maroon, overlayed on the synthesised ionogram. Bottom: The backscatter coefficients calculated from this area by taking the difference in power between the observed and synthesised ionograms.

4.2.3 Calculating the backscatter coefficient

Once a suitable area of an ionogram had been found, the difference in power between the observed and synthesised ionograms for each suitable cell was calculated. As the synthesised ionograms were produced with the backscatter coefficient set to zero, this difference is the backscatter coefficient for that location. The ground range, frequency and dominant elevation of the rays contributing to each cell were also saved for subsequent analysis. This was done for many ionograms to build up a large data set of backscatter coefficient values for each location.

A map of the backscatter coefficients calculated from each sounder was created using the ground ranges calculated by the ray tracing. Each of the 8 beams for each sounder were divided into equal range bins, and the backscatter coefficient for each range bin of each beam was calculated by taking the median value of all of the data points available in that location. These results are displayed in Chapter 5.

4.3 Assumptions and limitations of the backscatter ionogram method of calculating the backscatter coefficient

It is expected that the method of synthesising the backscatter ionograms and comparing these with the observed backscatter ionograms will introduce variance into the backscatter coefficient results due to the assumptions that were made and the limitations of this method. The assumptions and limitations of the ionospheric model, absorption model, gain and antenna models, ray tracing and the selection of the one-hop F2 low area of the ionograms are discussed in this section.

4.3.1 Assumptions and limitations of the ionogram synthesis method

4.3.1.1 Ionospheric models

The RTIM was used as the ionospheric model because it was based on real time data. As such it was able to represent the daily variations in the ionosphere whereas the IRI-2016 could not (discussed further in Section 5.2.1). Differences between the modelled ionosphere and the true ionosphere could cause differences between the modelled ray paths and the true ray paths, leading to errors in the calculated backscatter coefficient.

The RTIM does not include a model of the D region at the bottom of the ionosphere; it models the E, F1 and F2 regions. The first derivative of the electron density is not smooth at the boundary of the RTIM and at the boundaries between the quasi-parabolic layers, which can introduce error in the numerical ray tracing. An example of this introduced error is shown in Figure 4.16; this shows the ground and group range errors in the numerical ray tracing when compared to analytical ray tracing through a spherically symmetric ionosphere. The largest errors occurred for low elevation rays or when the ray apogee was at an altitude where there was a join in the quasi-parabolic layers and hence a slight discontinuity. While the RTIM attempts to smooth the interface between the neutral atoms and the ions, it was found that this was not sufficient to fully suppress numerical errors in the numerical raytracing solution for low elevation rays (see Figure 4.16 top panel at elevations from 5 to 10 degrees). This was

reduced by the addition of small electron density values below the start height of the model ionosphere to aid in the smoothness of the transition. One height step below the first electron density, a value of that density divided by 8 was added and the next height step below the first modelled electron density divided by 64 was added. Figure 4.16 (bottom panel) shows the suppression of the numerical error for the low elevation rays when the small electron density values were added.

While PHaRLAP includes analytical raytracing (ART) routines which can very quickly calculate the path of a ray, ART was not used to synthesise the backscatter ionograms in this work as ART requires a spherically symmetric ionosphere. The ionospheric model that was used (the JORN RTIM) is not spherically symmetric; it includes downrange gradients and other variations in the ionosphere at different scales so as to accurately represent the true ionospheric conditions.

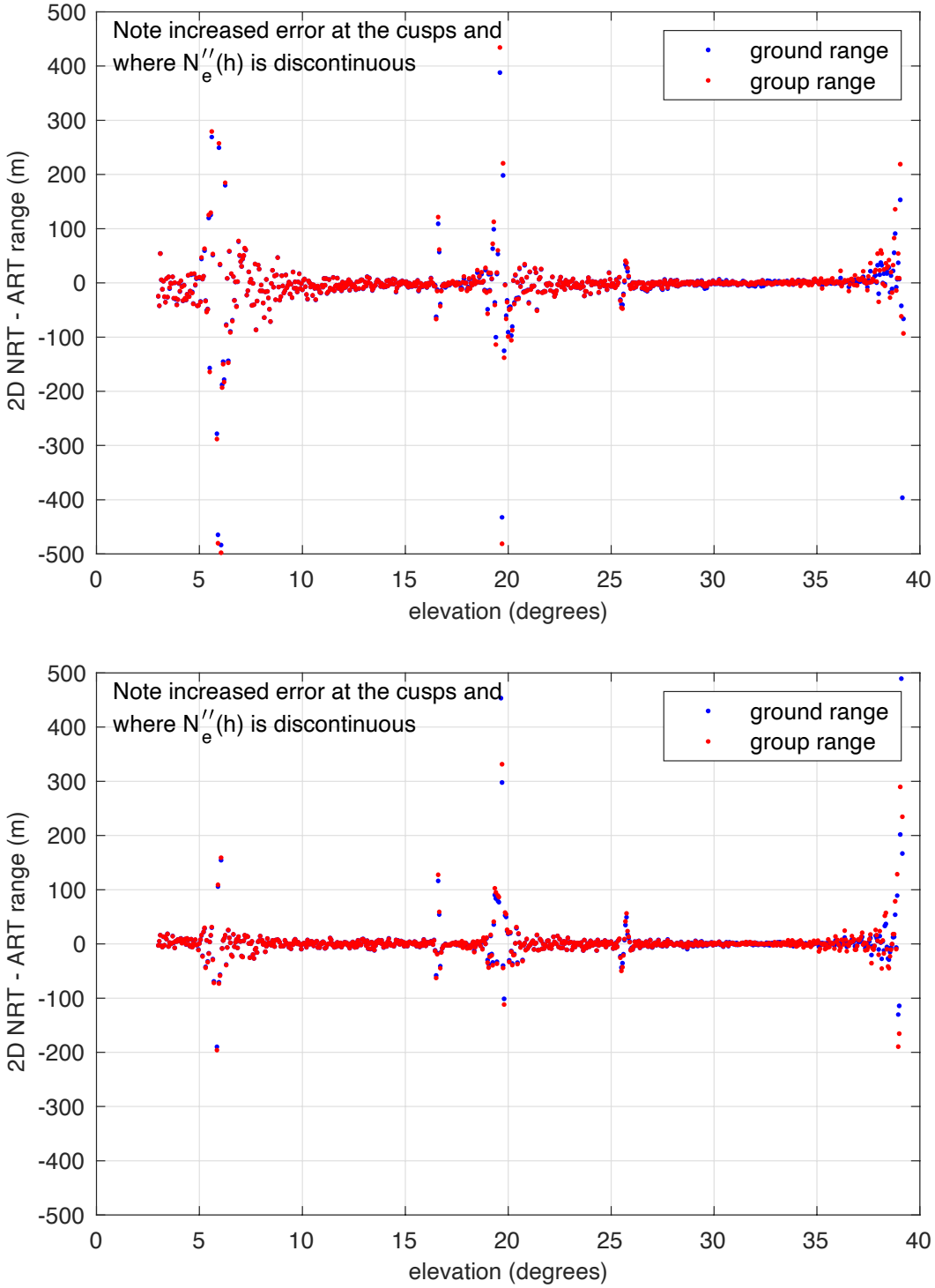

Figure 4.16: The ground and group range error between 2D numerical ray tracing and analytic ray tracing through a spherically symmetric ionosphere. Top: Ray traced through an ionospheric model where no values were added to smooth the transition to a neutral atmosphere. Bottom: Ray traced through an ionospheric model where small electron density values were added below the E layer to smooth the transition to the neutral atmosphere.

4.3.1.2 Absorption model

The George and Bradley model [57] was used to calculate the ionospheric absorption loss of radio waves due to passing through the D region. However, the George and Bradley

model does not include deviative absorption for the F layer. The deviative absorption was estimated in the PHaRLAP raytracing routine and was added for rays above the E layer. The use of the George and Bradley model for calculating the absorption will introduce some error in the results as this model does not take into account day to day variations in the ionosphere. The George and Bradley model is a monthly median climatological model where the calculation of the absorption is based on the sunspot number, the time and the location of the ray. The George and Bradley model estimates the absorption along an oblique path based on the absorption from vertical incidence data, so was not expected to be accurate for "non-typical" ray paths such as ducted or chordal paths [59]. However, most rays that contribute to the backscatter ionograms do not travel along these non-typical paths. Furthermore, the rejection criteria (see Section 4.2.2.2) removes these cases.

In order to account for daily changes in the ionosphere a method of calculating the absorption by modelling individual ray paths may be used, such as the model known as SiMIAN [59]. The ionospheric absorption experienced by a ray may be calculated by integrating the imaginary component of the refractive index along the ray path. However, to use this method a D layer is required in the ionospheric model, which was not present in the RTIM. Hence, the SiMIAN model was not used.

4.3.1.3 Gain and antenna pattern assumptions

A NEC model of the antenna gains was used for the ionogram synthesis. The gain across the width of the main receiver beam varies within this beam; however, the raytracing was done only in the direction of maximum gain. Ideally, multiple samples at different directions within the width of the beam would be used. However, the computational expense of additional ray tracing in multiple directions would be large. Hence, raytracing was done only in the direction of maximum gain, i.e., it was assumed that the gain across the width of the beam was equal to the maximum gain of that beam. This assumption had a minor effect on the synthesised ionograms and hence the calculated backscatter coefficients. Figure 4.17 shows the extent of this effect; this assumption meant that the beam gain used in the ionogram synthesis was slightly larger than what it was in reality, which caused the calculated backscatter coefficients to be slightly larger (although the effect was less than 1 dB). The difference between the gain in the centre of the beam and the mean gain across the width of the beam was greatest for lower frequencies. At higher frequencies the beam width narrows, so the difference between the mean gain and the maximum gain is less.

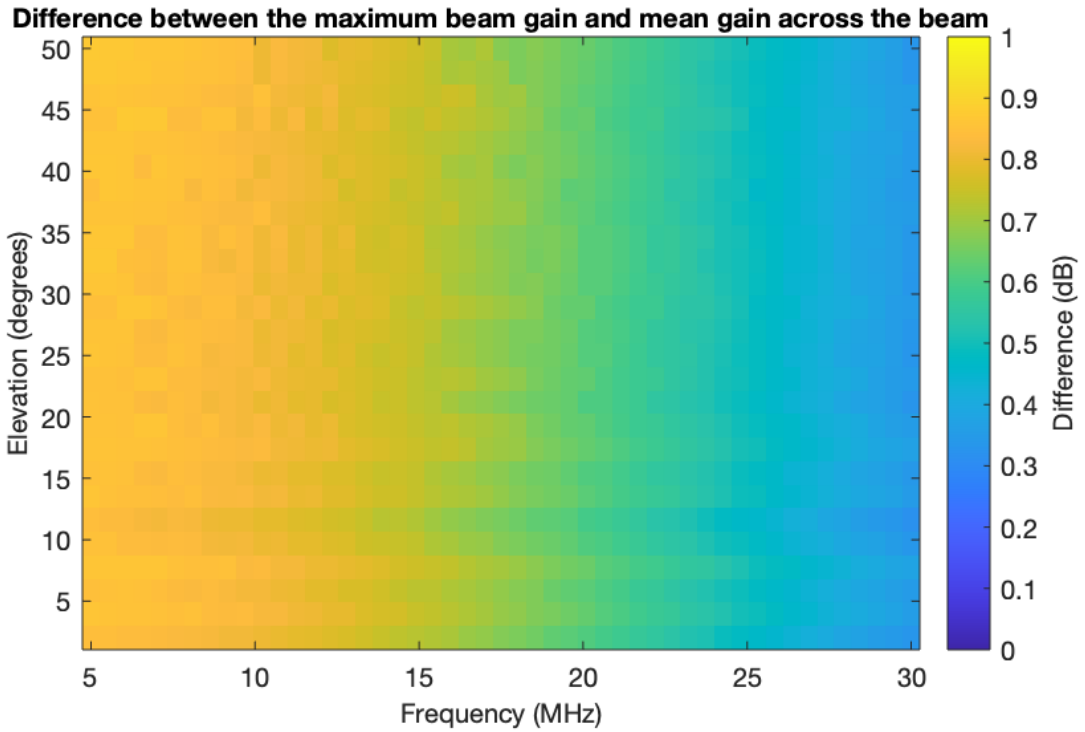

Figure 4.17: The effect of the assumption that the gain was the same across the entire beam width on the calculated backscatter coefficient. Figure calculated for beam 4.

4.3.1.4 Use of 2D rather than 3D numerical ray tracing

Two-dimensional numerical ray tracing is much less computationally intense than three-dimensional numerical ray tracing. Over-the-horizon radar modelling work done by Cervera et al. found that two-dimensional numerical raytracing was sufficient to characterise the performance of an OTH radar [15]. Hence, 2D numerical raytracing was used to synthesise backscatter ionograms as it was deemed adequate for this work. However, due to the limitations of 2D ray tracing, certain assumptions were made. The ray paths were limited to a plane, so out of plane propagation such as that introduced by a tilted ionosphere, or the effect of the geomagnetic field splitting the radio waves into ordinary (O) and extraordinary (X) propagation modes could not be modelled [1]. This introduces errors in the location of the region of ground backscatter. Out of plane propagation due to coning, caused by the cone shaped surface of constant phase for linear receiver arrays, was not modelled in the 2D ray tracing. Instead, a correction was applied to the azimuth of each ray when steered off boresight based on the elevation of the ray as described in the Section 4.2.1.1. This assumed that the ionosphere along the centre of the beam was similar to the ionosphere along the corrected ray azimuth. This assumption is valid for the spatial resolution of the RTIM. The use of 3D ray tracing would account for these effects, and hence could improve the accuracy, to some degree, of the ray path through the ionospheric models and the modelled location of where each ray scattered from the ground.

4.3.1.5 *Effect of the elevation step on the ionogram synthesis*

When modelling a fan of rays, artefacts in the synthesised ionogram may be introduced if the choice of elevation step is too large. A larger step in the elevation between each ray in the fan decreased the quality of the synthesised ionogram. However, when the elevation step was halved the time taken to synthesise an ionogram is doubled. Reducing the elevation step is desirable, but it can significantly increase the computation time. Through inspection, it was found that when an elevation step greater than 0.5 degrees was used, the quality of the synthesised ionograms noticeably decreased, especially at the leading edge which is not as sharp (Figure 4.18). An elevation step of 0.2 degrees was used to synthesise the backscatter ionograms, as this produced a reasonable ionogram while the time required to synthesise an ionogram remained practical.

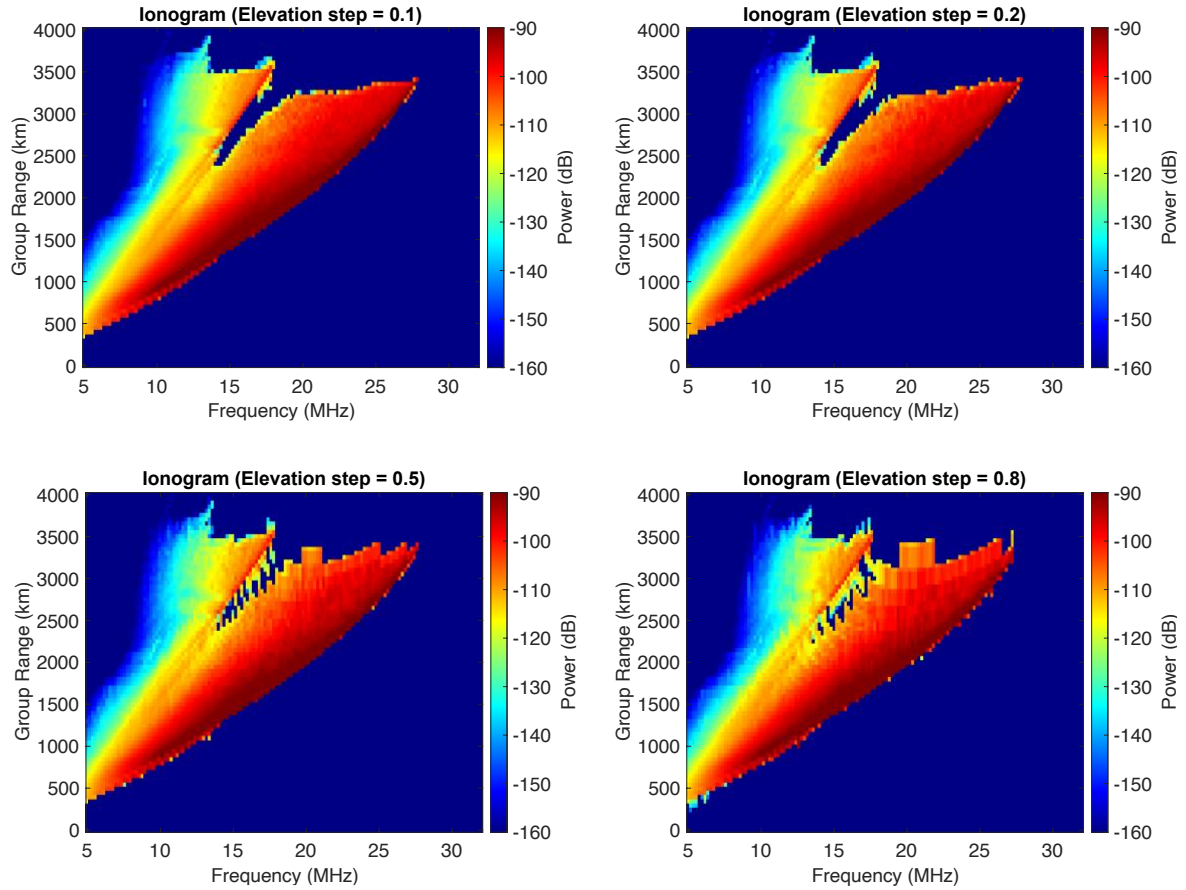

Figure 4.18: The effect of different modelled elevation steps on a synthesised ionogram.

4.3.2 Assumptions and limitations of the ionogram comparison method

An automated method of comparing the synthesised and observed backscatter ionograms was developed, as the large number of ionograms to compare meant that a manual method of comparison was not viable. The automatic method of comparison also removed the human bias that may have been introduced when choosing the areas of the ionograms to compare. However, in order to automate this process several assumptions needed to be made. To determine the similarity of the synthetic and observed ionograms the leading edges were used; if the RMS range difference between the leading edges was greater than 300 km the

ionograms were rejected from further analysis. This criterion was a balance between removing the data when the model had not accurately depicted the ionospheric conditions and keeping enough ionograms for analysis. While calculating the leading edge of the synthesised ionograms was simple, finding the leading edge of the observed ionogram was more difficult. At times, received power from the side lobes of the antenna array obscured the leading edge, causing the otherwise useful ionograms to be rejected.

The ray tracing results used to synthesise the model ionograms were used to select the area of the ionograms that consisted of rays with an F2 low mode of propagation. However, if the shape of the observed ionogram was slightly different to that of the synthesised ionogram, other areas that may have been nearer the leading edge than desired or outside of the one-hop region of the observed ionograms were erroneously selected. This effect was minimised by reducing the size of the F2 low mode region selected for analysis. This was done by removing areas near the leading edges of both synthesised and observed ionograms and near the trailing edge of the synthesised ionogram. Again, this was a balance of selecting a good area without reducing the size of the data set too much.

4.4 Calculating the sea backscatter coefficient from sea state data

The sea backscatter coefficient can be calculated from theory if the wave height spectrum of the ocean is known [36]. This alternative method for calculating the backscatter coefficients was compared with the ionogram comparison method of calculating the sea backscatter coefficients. This provided a way to assess the similarities and difference between the results of these two methods. The wave height spectrum was calculated using sea state data accessed from the Centre for Australian Weather and Climate Research [50].

4.4.1 Calculating the backscatter coefficient with a wave height spectrum

Barrick showed that for deep water in the absence of a surface current the first-order backscatter coefficient can be calculated using the perturbation approximation as the heights of the ocean waves are small compared to the radar wavelength [24, 31]. The equation for the first-order backscatter coefficient, dependent on the frequency of the radio wave, is given by

$$\sigma(\omega) = 2^6 \pi k_0^4 \sum_{m=\pm 1} S(-2mK_0)\delta(\omega - m\omega_B) \tag{4.5}$$

where $m = \pm 1$ denotes the sign of the doppler shift, k_0 is the magnitude of the incoming radio wavenumber, $K_0 = (k_x, k_y) = (k_0, 0)$ is the radar wave vector (of magnitude k_0) in the radar direction, $S(K)$ is the directional wave height spectrum, and ω_B is the ocean wave frequency (Bragg line frequency) associated with $2K_0$ [29, 63]. For deep water $\omega = \sqrt{gk}$, hence $\omega_B = \sqrt{2gk_0}$ where g is the gravitational acceleration [29].

Gardiner-Garden and Pincombe [63] showed that using the separable form of the wave height spectrum $S(k_x, k_y) = f(k)g(\theta)$ and the averaged radar cross section of the sea

$$\sigma_0 = \frac{1}{2}\int_{-\infty}^{\infty} \sigma(\omega) d\omega \tag{4.6}$$

the backscatter coefficient could be given by

$$\sigma_0 = 2^6 \pi k_0^4 f(-2k_0)\big(g(\theta) + g(\theta + \pi)\big) \tag{4.7}$$

where $2k_0$ is the wavenumber of the Bragg lines and $g(\theta)$ is the directionality factor. The directionality factor is given by

$$g(\theta) = \frac{4}{3\pi}\cos^4\left(\frac{\theta - \alpha^*}{2}\right) \tag{4.8}$$

where θ is the local angle of the wind (principal wave direction) and α^* is the wind direction with respect to the radar beam (i.e., $\theta - \alpha^*$ is given by the sum of the radar angle and the wind direction).

As the power from both the Bragg lines must be included, the backscatter coefficient is defined as

$$\sigma_0 = 2^6\pi k_0^4 f(-2k_0)h(\theta) \tag{4.9}$$

where

$$h(\theta) = g(\theta) + g(\theta + \pi) = \frac{4}{3\pi}\left(\cos^4\left(\frac{\theta - \alpha^*}{2}\right) + \cos^4\left(\frac{\theta - \alpha^*}{2} + \frac{\pi}{2}\right)\right). \tag{4.10}$$

For the non-directional wave height spectrum, $f(k)$, the JONSWAP spectrum [35] (described below) was used.

In the sea state data accessed from the Centre for Australian Weather and Climate Research there were values for the significant wave height (H_m) and the peak period (T_p) of the wind swell along with the primary, secondary and tertiary swells. Thus, the backscatter coefficient was calculated by finding the wave height spectrum and backscatter coefficient for each of these swells and then summing the results [36]

$$\sigma_{total} = \sigma_{wind} + \sigma_{primary} + \sigma_{secondary} + \sigma_{tertiary}. \tag{4.11}$$

Only the first order Bragg scatter is considered in this calculation of the sea backscatter coefficient, higher order scatter is ignored.

4.4.2 JONSWAP spectrum

The JONSWAP spectrum is a non-directional wave height spectrum, based on the Pierson-Moskowitz spectrum for a fully developed sea [35]. An extra peakedness factor (calculated empirically) is included to adjust for the sea never becoming fully developed. The JONSWAP spectrum [35, 64] is given by the equation

$$f(\omega) = \frac{\alpha g^2}{\omega^5}\exp\left(-\frac{5}{4}\left(\frac{\omega_p}{\omega}\right)^4\right)\gamma^{\exp\left(-\frac{(\omega-\omega_p)^2}{2\sigma_j^2\omega_p{}^2}\right)} \tag{4.12}$$

where

$$\sigma_j = \begin{cases} 0.07 & \omega < \omega_p \\ 0.09 & \omega \geq \omega_p \end{cases} \tag{4.13}$$

Here α is a normalisation constant, g is the gravitational acceleration, ω is the wave angular frequency (rad/s), ω_p is the wave angular peak frequency (rad/s) and γ is the JONSWAP peakedness parameter. The normalisation constant is defined as

$$\alpha = 5.061\frac{H_m^2}{T_p^4}(1 - 0.287\ln\gamma) \tag{4.14}$$

The peakedness parameter γ is given by

$$\gamma = \exp\left(3.484\left(1 - 0.1975\left(0.036 - \frac{0.0056T_p}{\sqrt{H_m}}\right)\frac{T_p^4}{H_m^2}\right)\right) \tag{4.15}$$

where T_p is the peak period (s) of the wind swell and H_m is the significant wave height (m). The peakedness parameter is limited by $1 \leq \gamma \leq 7$ from qualitative considerations of deep water wave data from the North Sea [64]. When $\gamma = 1$, the JONSWAP spectrum reduces to the Pierson-Moskowitz spectrum of a fully developed sea. The JONSWAP spectrum can be written in terms of the wave number [36].

$$\begin{aligned} f(k) &= f(\omega)\frac{d\omega}{dk} \\ &= f\left(\sqrt{gk}\right)\left(\frac{g}{2\sqrt{gk}}\right) \\ &= \frac{\alpha g^2}{(gk)^{\frac{5}{2}}}\exp\left(-\frac{5}{4}\left(\frac{\sqrt{gk_p}}{\sqrt{gk}}\right)^4\right)\gamma^{-\frac{\left(\sqrt{gk}-\sqrt{gk_p}\right)^2}{2\sigma_j^2 gk_p}}\left(\frac{g}{2\sqrt{gk}}\right) \\ &= \frac{\alpha}{2k^3}\exp\left(-\frac{5}{4}\left(\frac{k_p}{k}\right)^2\right)\gamma^{-\frac{\left(\sqrt{k}-\sqrt{k_p}\right)^2}{2\sigma_j^2 k_p}} \end{aligned} \tag{4.16}$$

The directionality of the wind is included in the manner described in Section 4.4.1. Hence, the backscatter coefficient when using the JONSWAP spectrum is given by

$$\begin{aligned} \sigma = 2^6\pi k^4 \frac{\alpha}{2(2k)^3}\exp\left(-\frac{5}{4}\left(\frac{k_p}{2k}\right)^2\right)\gamma^{-\frac{\left(\sqrt{2k}-\sqrt{k_p}\right)^2}{2\sigma_j^2 k_p}}\frac{4}{3\pi}\Bigg(\cos^4\left(\frac{\theta-a^*}{2}\right) \\ + \cos^4\left(\frac{\theta-a^*}{2}+\frac{\pi}{2}\right)\Bigg) \end{aligned} \tag{4.17}$$

An example of the backscatter coefficients calculated using this method is shown in Figure 4.19.

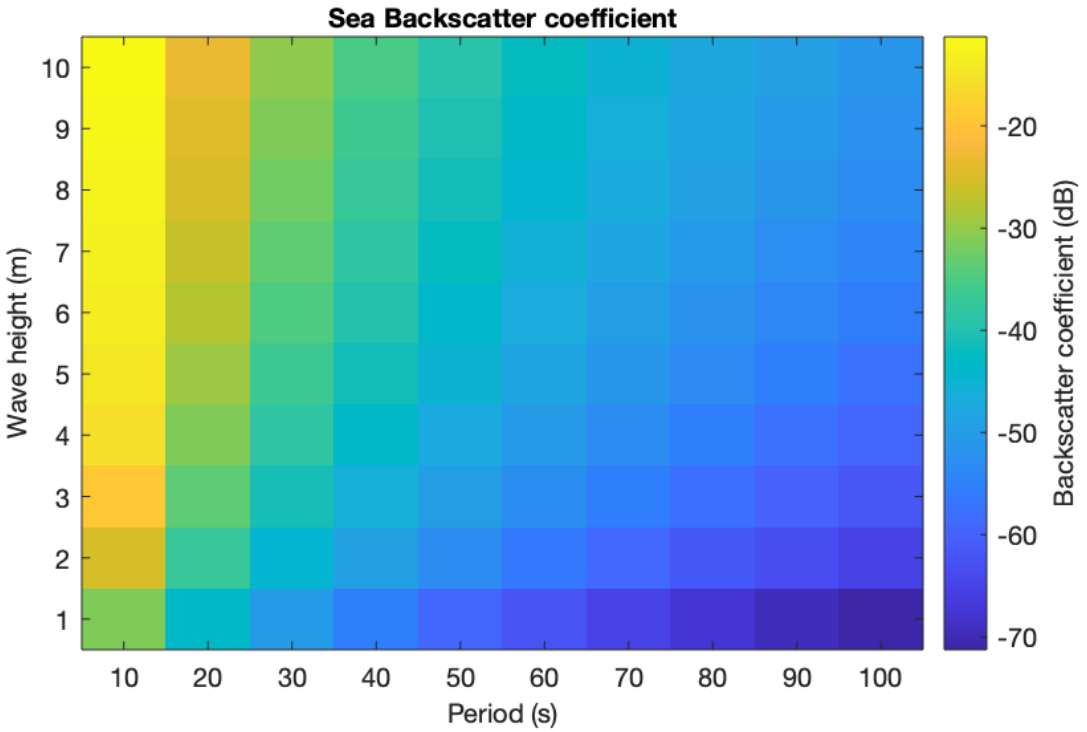

Figure 4.19: The backscatter coefficient calculated for a range of wave heights and periods using the JONSWAP wave spectrum method described above for a radar operating at 15 MHz. The radar beam steer angle and wind were in the same direction.

4.5 Comparing the two methods of calculating the sea backscatter coefficient

The backscatter coefficient results from the ionogram comparison method were compared to the sea backscatter results from the sea wave height spectrum method, to investigate the similarities and differences between these methods. The sea backscatter coefficients were calculated using the sea wave height spectrum for a selection of radar frequencies (6, 8, 10, 12, 14, 16, 18, 20, 22, 24, 26 MHz) twice each day at 0300 UT and 0700 UT for the months of September 2015 and March 2016. Due to the computational time required to calculate these sea backscatter coefficients, only two times each day were considered. The median backscatter coefficient from the ionogram comparison method was calculated in the morning using results from 0000UT to 0600 UT and in the afternoon using results from 0400 UT to 1000 UT. These larger time periods that overlapped with the time backscatter coefficients were calculated using the wave spectrum method were chosen to increase the number of data points for each location and thus improve the statistics when calculating the median backscatter coefficient.

Data from each of the eight receive beams of each sounder were divided into 100-kilometre range bins, and the mean frequency of the rays contributing to these locations was calculated. The mean backscatter coefficient for each range bin was calculated from the sea wave height spectrum data using a radar frequency closest to the mean frequency of the rays reaching that location. This was compared to the ionogram comparison method result twice daily throughout the months of interest. The similarities and differences in the backscatter

coefficient results using these two methods of calculation were investigated by plotting how the backscatter coefficient changed over time for each location using the two methods, calculating the mean difference between the results from each method for these locations and testing the correlation between the results from the two methods.

4.6 Investigating the effects of different parameters on the backscatter coefficient

It was expected that certain surface properties and ray parameters could affect the backscatter coefficient, such as the radio wave frequency, time of day and year, angle of incidence, aspect, roughness, soil moisture and vegetation. The effects of each of these parameters were investigated (see Section 5.4). Daily changes in the backscatter coefficient were inspected by looking at the backscatter coefficient throughout a month for locations over the sea and land. Diurnal patterns in the backscatter coefficient were investigated by looking at how the backscatter coefficient varied with the time of the day for each month of data. Seasonal variations in the backscatter coefficients were explored by comparing the results from September 2015 and March 2016. However, data over several years would be required to develop a better understanding of the seasonal variation. The effect of radio wave frequency on the backscatter coefficient was also investigated. However, the propagation via the ionosphere limits the range of frequencies. The relationship between the topography of the land and the backscatter coefficient was investigated by calculating the angle of incidence of rays using the gradient of the land from land elevation data and the elevation of the rays. Aspect dependence in the backscatter coefficient was investigated by comparing the results for a particular location when viewed from multiple directions. This was done by comparing the results between different backscatter sounders located across Australia. The effect of the surface roughness was investigated using the RMS height of the land as a measure of the roughness. Soil moisture data was used to analyse the correlation between the soil moisture and backscatter coefficient. Vegetation structure data across Australia was used to investigate the relationship between the backscatter coefficient and the vegetation.

4.7 Summary

In this chapter a method of calculating the backscatter coefficient by comparing a synthesised backscatter ionogram to an observed ionogram was described. A discussion of the assumptions and limitations of the ionogram comparison method of calculating the backscatter coefficient followed. A method of calculating the sea backscatter coefficient from the sea state defined by a wave height spectrum was reviewed and the process used to compare the two methods of calculating the backscatter coefficients was presented. The process of investigating the effects of certain ray and surface properties on the backscatter coefficient was then described. The backscatter coefficient results from the methods described are presented and discussed in the next chapter.

Chapter 5 Results and Discussion

5.1 Overview of chapter

This chapter first provides a broad overview of the backscatter coefficient maps over Northern Australia that were produced. A comparison between the sea backscatter coefficient when calculated using the ionogram comparison method and the wave spectrum method is then presented. In later sections a more detailed analysis on the effects of different ray parameters and surface properties on the backscatter coefficient is presented.

5.2 Backscatter coefficient maps – ionogram method

Maps of the backscatter coefficient across Australia were constructed to investigate how the backscatter coefficient varied across different regions. The backscatter coefficients for the areas observed by the Longreach, Laverton and Alice Springs backscatter sounders were calculated for September 2015 and March 2016. Data from both September and March was used to investigate any seasonal dependence in the backscatter coefficient. The sea state and the soil moisture were noticeably different between March and September, as the Northern Australia dry season is generally from May to October while the wet season is from November to April. Backscatter ionograms synthesised at ten-minute intervals from 0000 UT to 1000 UT (around 0930 to 1930 local time) for days when observed data was available over these months were used to generate the backscatter coefficient data. The median backscatter coefficient was then calculated for each 50 km range bin for each of the 8 receive beams of the sounders.

Backscatter coefficient maps were constructed from the results generated using the IRI-2016 climatological ionospheric model and the JORN near real time ionospheric model (RTIM). The beam width was set to a constant width of 11.25 degrees for simplicity in displaying and interpreting these maps. However, it should be noted that the beam width is dependent on the beam azimuth and the radio wave frequency. The azimuthal beam width in radians can be approximated by the equation $\phi = \frac{\lambda}{l \cos\theta}$ where λ is the wavelength, l is the array length and θ is the angle the beam was steered off boresight. Hence, at the further ranges where the mean frequency of the radio waves needed to obtain returns is higher at around 18 MHz (see Figure 5.19) the beam width is around 5 degrees for the central beams and 6 degrees for the edge beams. For the closer ranges where the mean frequency of the radio waves was lower at around 9 MHz the beam width is around 10 degrees for the central beams and 13 degrees for the edge beams. The use of the constant beamwidth of 11.25 degrees in the maps is effectively displaying a nearest neighbour interpolation of the backscatter coefficient. The backscatter coefficient maps for Northern Australia in September 2015 calculated using IRI-2016 and the RTIM are shown in Figures 5.1 to 5.4 and Figures 5.5 to 5.8 respectively. In general, the backscatter coefficients calculated using IRI-2016 were around 2 dB less than those calculated using the RTIM. This was possibly due to the RTIM supporting propagation of higher frequency rays to the relevant ground areas, as higher frequency rays experience less

absorption. Figure 5.13 shows the difference in the mean frequency of the rays contributing to each range-azimuth cells when the ray tracing was done through the RTIM and IRI-2016; the mean frequency of the rays reaching each range-azimuth bin was larger when the RTIM was used (except at the boundaries of the ionospheric model where additional ray criteria were applied). The maps calculated when the RTIM was used are more restricted in extent because the geographic region covered by the RTIM was limited. Maps of the backscatter coefficients for Northern Australia in March 2016 calculated using the RTIM are shown in Figures 5.9 to 5.12.

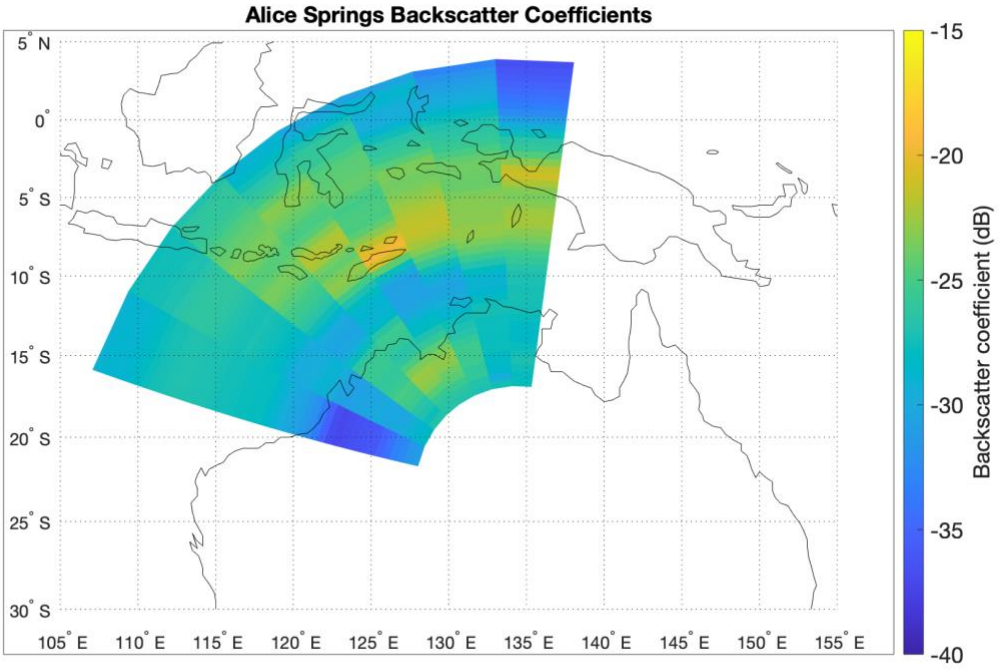

Figure 5.1: Backscatter coefficient map for Alice Springs in September 2015 calculated using the International Reference Ionosphere (IRI-2016).

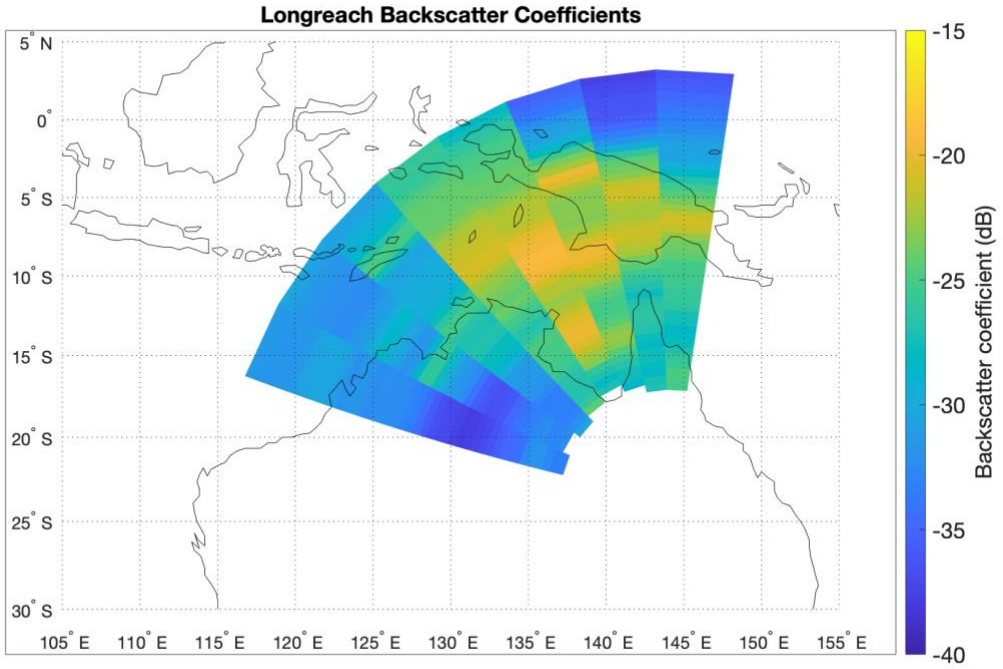

Figure 5.2: Backscatter coefficient map for Longreach in September 2015 calculated using the International Reference Ionosphere (IRI-2016).

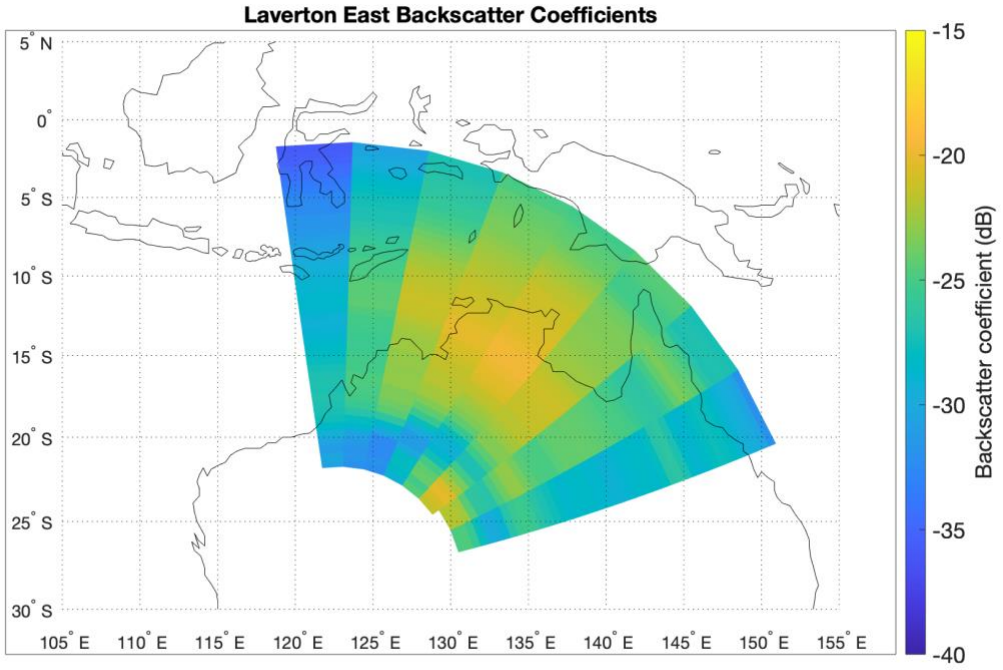

Figure 5.3: Backscatter coefficient map for Laverton East in September 2015 calculated using the International Reference Ionosphere (IRI-2016).

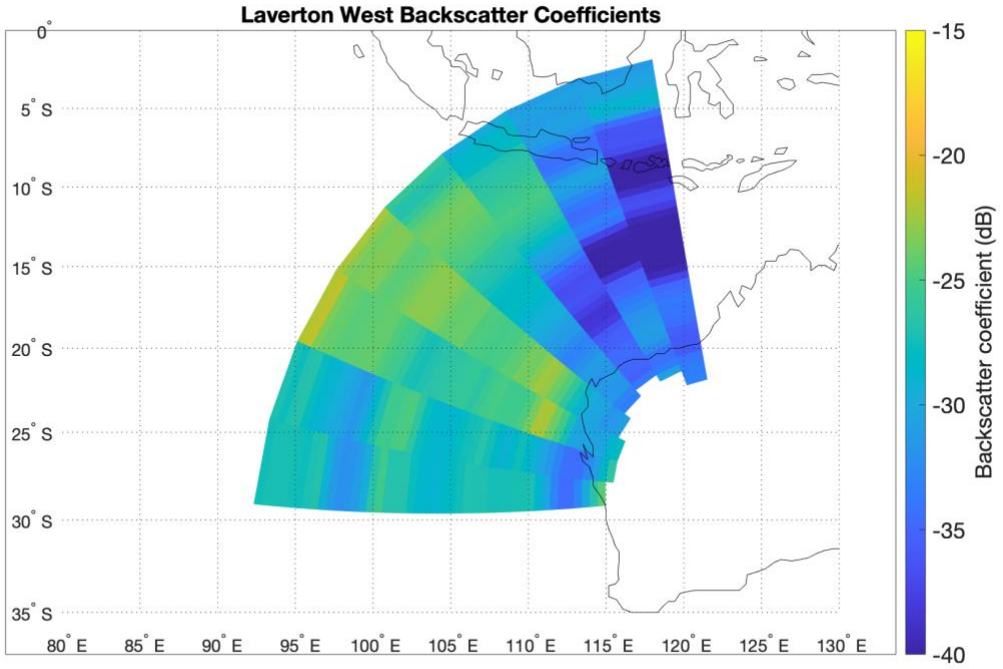

Figure 5.4: Backscatter coefficient map for Laverton West in September 2015 calculated using the International Reference Ionosphere (IRI-2016).

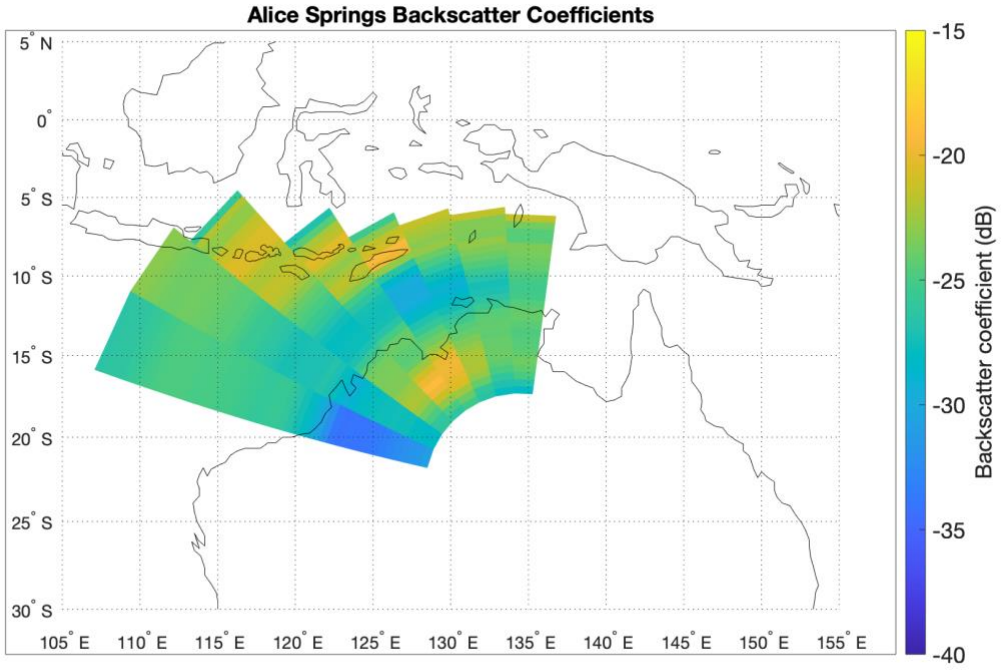

Figure 5.5: Backscatter coefficient map for Alice Springs in September 2015 calculated using the Real Time Ionospheric Model (RTIM).

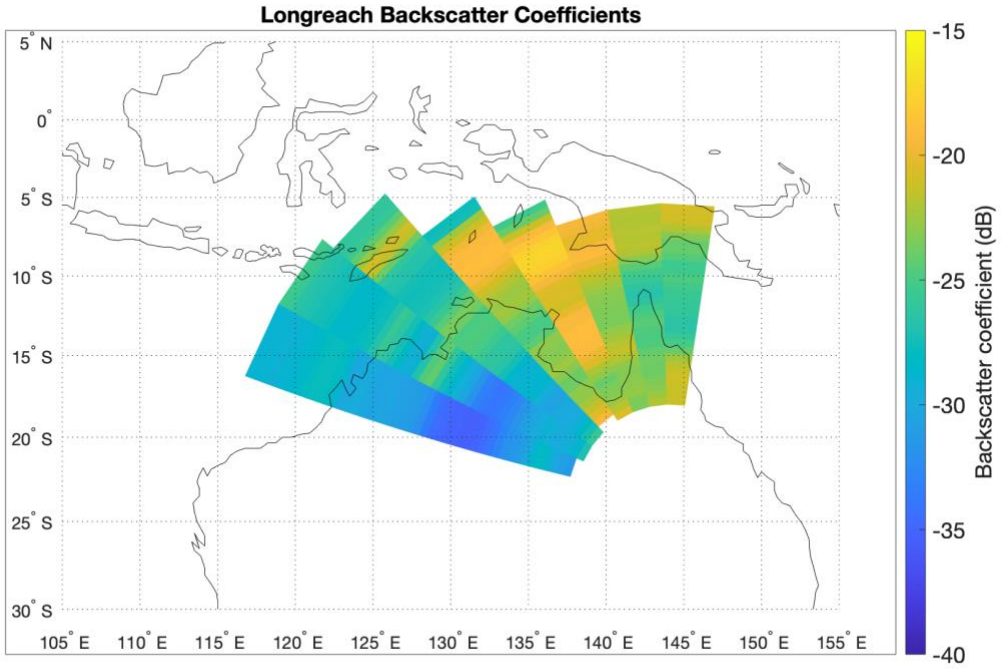

Figure 5.6: Backscatter coefficient map for Longreach in September 2015 calculated using the Real Time Ionospheric Model (RTIM).

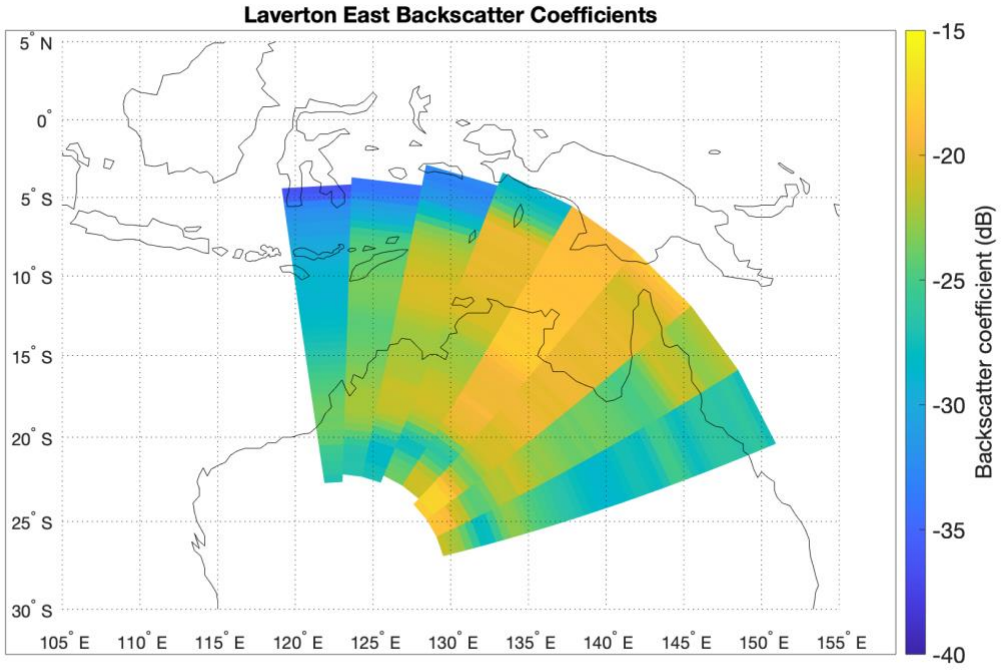

Figure 5.7: Backscatter coefficient map for Laverton East in September 2015 calculated using the Real Time Ionospheric Model (RTIM).

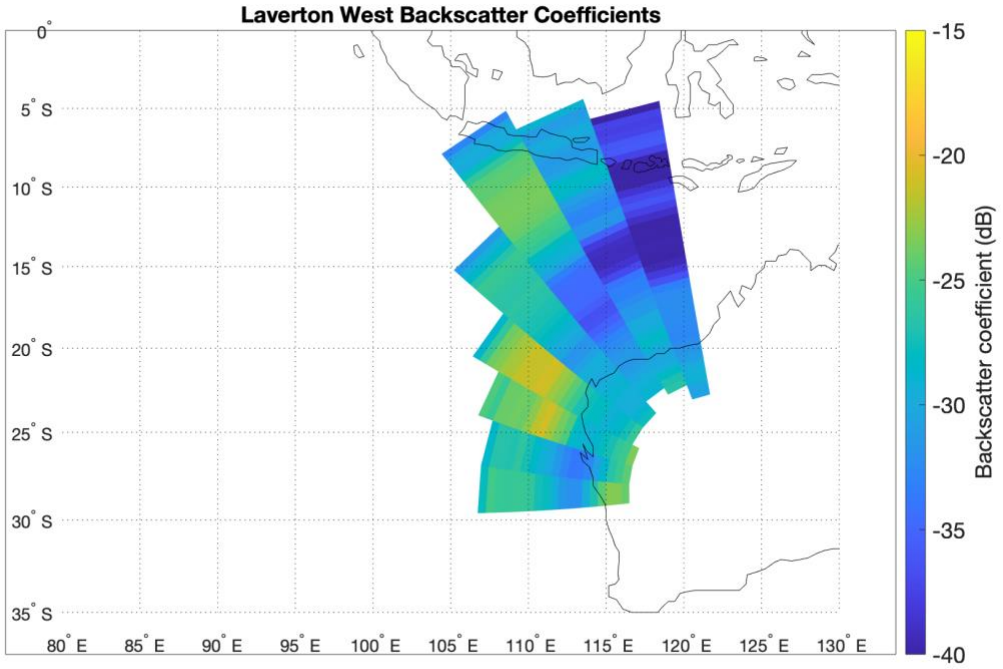

Figure 5.8: Backscatter coefficient map for Laverton West in September 2015 calculated using the Real Time Ionospheric Model (RTIM).

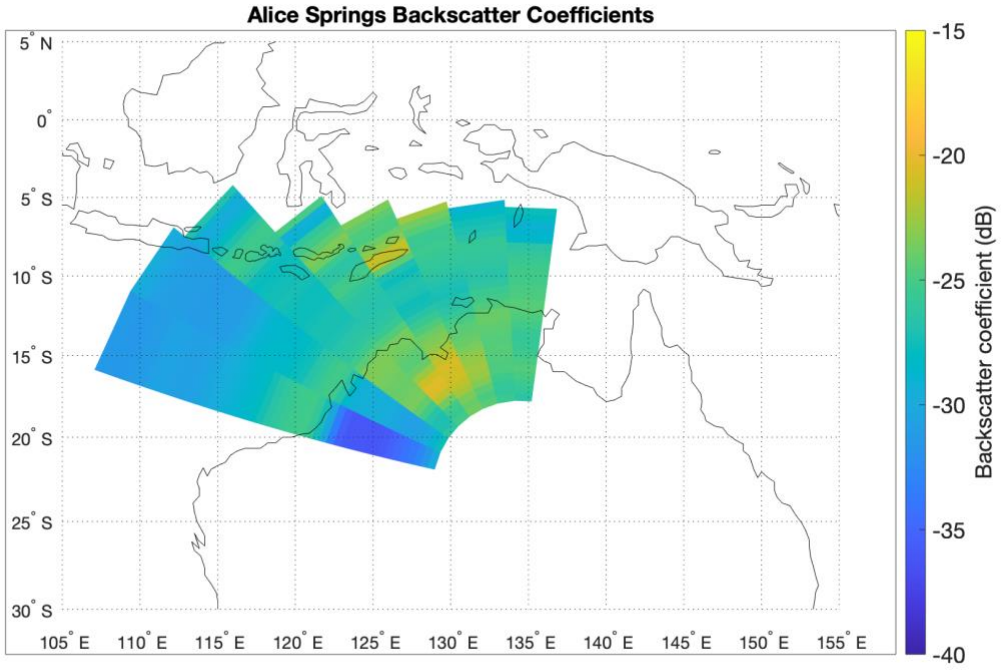

Figure 5.9: Backscatter coefficient map for Alice Springs in March 2016 calculated using the Real Time Ionospheric Model (RTIM).

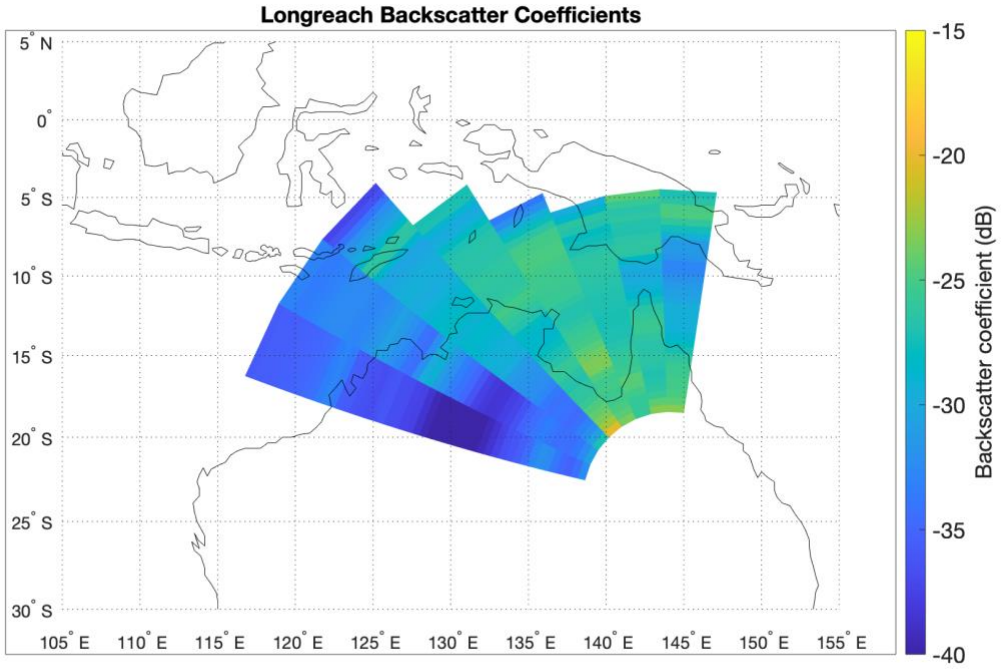

Figure 5.10: Backscatter coefficient map for Longreach in March 2016 calculated using the Real Time Ionospheric Model (RTIM).

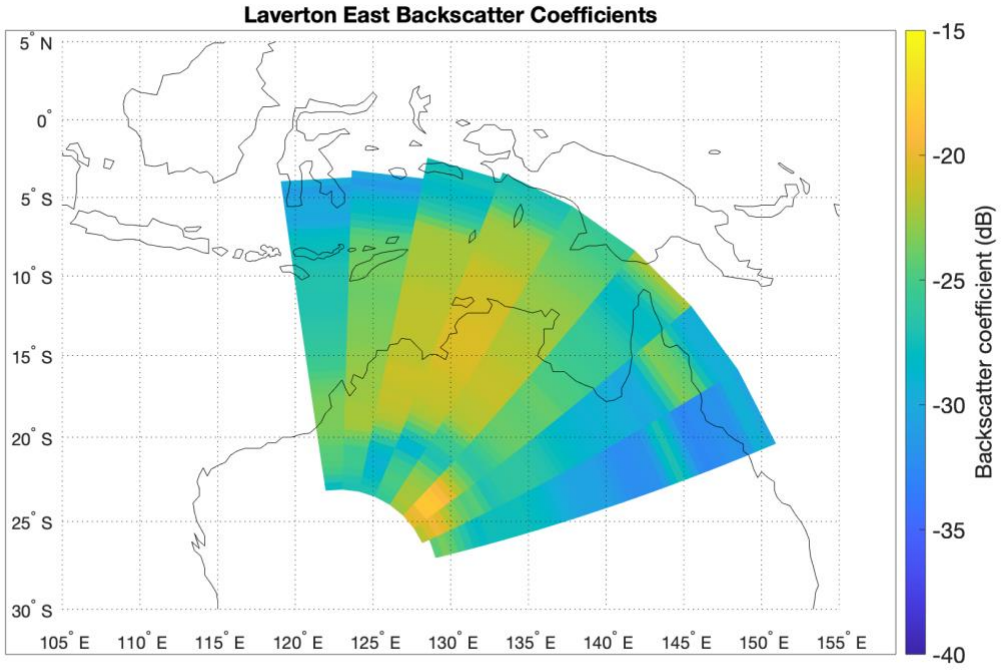

Figure 5.11: Backscatter coefficient map for Laverton East in March 2016 calculated using the Real Time Ionospheric Model (RTIM).

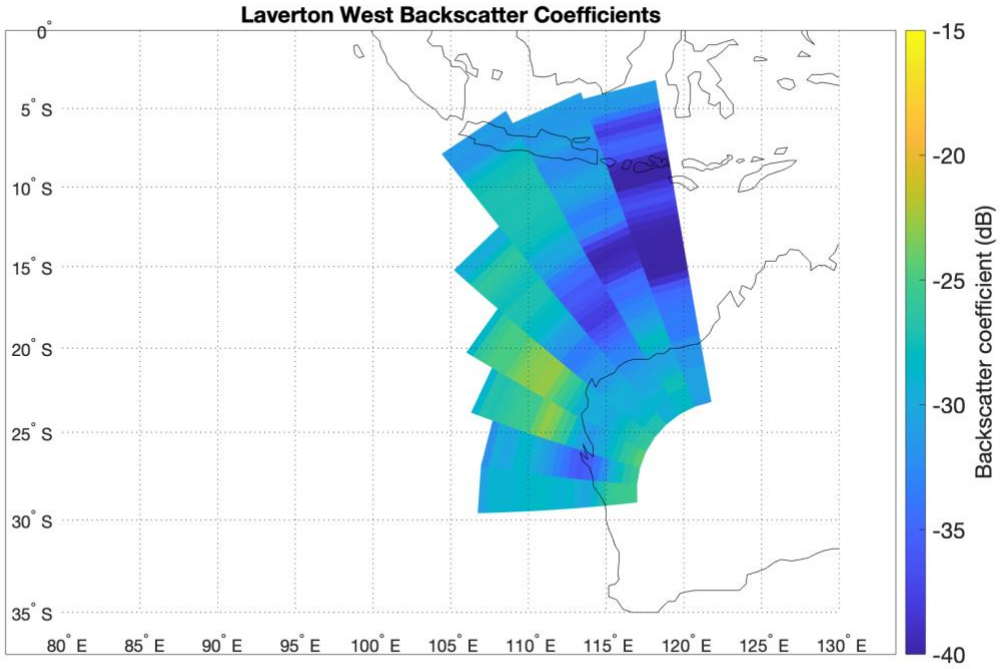

Figure 5.12: Backscatter coefficient map for Laverton West in March 2016 calculated using the Real Time Ionospheric Model (RTIM).

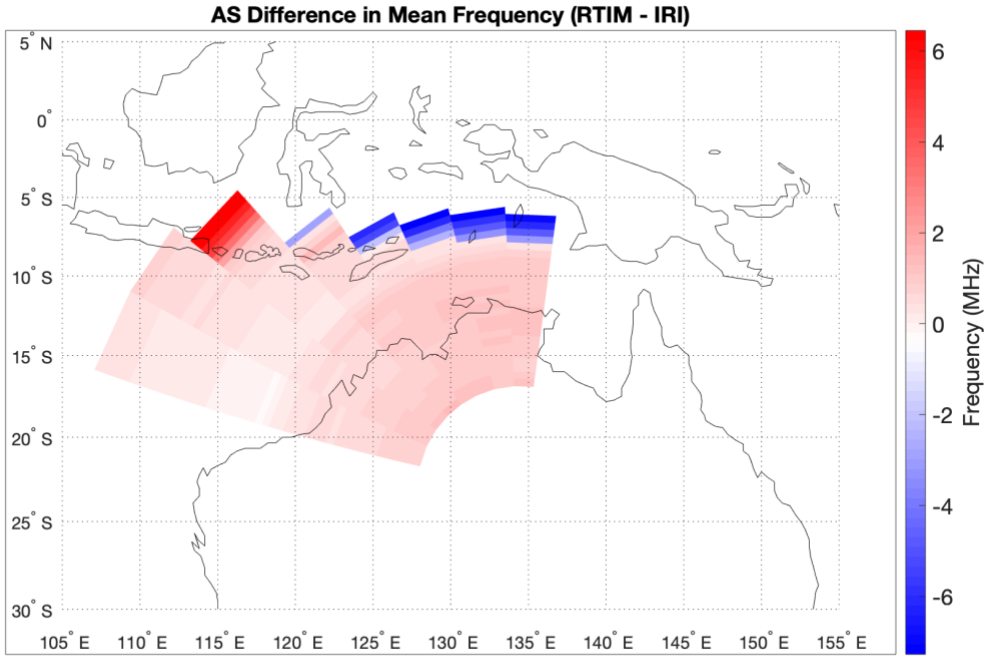

Figure 5.13: Plot of the difference in the mean radio wave frequency contributing to each range-azimuth bin when the raytracing was done through the RTIM and IRI-2016.

5.2.1 Comparison of the IRI-2016 and the RTIM backscatter results

The two different ionospheric models used to synthesise the backscatter ionograms each had their advantages and disadvantages. The IRI-2016 does not incorporate day-to-day variations in the ionosphere as it is a monthly median climatological model. For many times the synthesised ionograms, as expected, did not match well with the observed ionograms. This meant that many of the synthesised ionograms were not used; typically, only around 35% of synthesised ionograms were considered suitable (see Table 5.1). Consequently, less data was available for calculating the backscatter coefficient. However, the geographic region covered by IRI-2016 was greater than the region covered by the RTIM, so backscatter coefficients at greater ranges could be calculated using IRI-2016.

The RTIM did include daily variations in the ionosphere, which meant that the majority of the synthesised ionograms were similar enough to the observed ionograms to be considered suitable. Excluding the Laverton East ionograms, around 80% of synthesised ionograms were used (see Table 5.1). Only around 53% of the Laverton East synthesised ionograms were considered suitable (much fewer than for the other sounders). There was not a seasonal dependence in the number of ionograms rejected, as the level of rejection was similar for both September and March. The Laverton East backscatter sounder faces north-eastward, while the other three sounders face north-westward. Table 5.2 shows that as the direction the beam faces rotates from west to the east (from Beam 1 of Laverton West through to Beam 8 of Laverton East) the percentage of synthesised ionograms that were considered suitable decreases. There was not an obvious time of day dependence on when most of the ionograms were rejected. The method of comparing the leading edges of the observed and synthesised ionograms was sensitive to the slope of the leading edge; small differences in a steeper leading edge would cause larger group range differences. It is possible that the shape of the ionograms differed with the beam direction, causing more of the eastward facing ionograms to be rejected. This will be investigated further in future work. Alternatively, it may be that some aspects of the Laverton East model did not accurately capture the true conditions. The antenna models that were used for Laverton West and Longreach were the same as those used for Laverton East as the antennas are supposed to be identical, which suggests the antenna models were not the cause of the increased number of rejected ionograms in the Laverton East model. Although perhaps there could be an issue with the hardware that could change the beam widths or beam direction. It is unlikely that the RTIM would cause this directionality effect that is seen between the eastward and westward facing beams. There is also some overlap between the areas of the RTIM used by Laverton East, Longreach and Alice Springs so one would expect to see any issues caused by the RTIM in the Alice Springs and Longreach results as well. Currently the cause of reduced number of suitable ionograms for the Laverton East sounder is not clear.

Table 5.1: Number of ionograms synthesised and used for each map.

Sounder		No. Synthesised	No. Kept	% Kept
September 2015 IRI	AS	9602	3167	33.0
	LO	5327	1767	33.2
	LAE	8572	3134	36.6
	LAW	8543	3431	40.2
September 2015 RTIM	AS	9997	7875	78.8
	LO	5349	4562	85.3
	LAE	9346	4925	52.7
	LAW	7608	5968	78.4
March 2016 RTIM	AS	11017	8220	74.6
	LO	8673	8001	92.2
	LAE	12896	6912	53.6
	LAW	11626	9709	83.5

Table 5.2: Percentage of synthesised ionograms kept for each beam of the four backscatter sounders.

	Percentage of ionograms kept (%)							
	Beam 1	**Beam 2**	**Beam 3**	**Beam 4**	**Beam 5**	**Beam 6**	**Beam 7**	**Beam 8**
AS	71	77	79	77	78	77	84	86
LO	64	70	83	88	90	91	90	92
LAE	66	62	59	55	55	50	43	33
LAW	89	87	86	86	83	61	60	67

The interquartile range (IQR) is the difference between the upper and lower quartiles and was used as a measure of the spread in the values of the backscatter coefficient. The IQR of the September 2015 Alice Springs results when using the RTIM and IRI-2016 are shown in Figure 5.14 and Figure 5.15 respectively. For both of these ionospheric models, there was an area with a large IQR over the sea between North Western Australia and Timor. This was due to larger variations in the sea state in this location, which can be seen in the IQR of the wind sea wave height shown in Figure 5.16. The IQR over the land tended to be less than over the sea. This was expected as the land composition has little variability over the time scales of interest unlike the sea state which has a high degree of variability. When the IRI-2016 was used, the IQR increased with distance from the sounder site. This was likely due to differences in the model ionosphere and the true ionospheric conditions having a larger effect when a ray travelled further through the ionosphere. Finally, it is noted that in general, the IQR was less when the RTIM was used. This is because the RTIM captured hourly, minutely and daily

variations in the ionosphere, which IRI is unable to do, and so these calculated backscatter coefficients were a more precise measure. The IQR of the backscatter coefficients when the RTIM was used tended to be around 4 to 5 dB, with the exception of the area of sea between Australia and Timor where the IQR reached 11 dB. In contrast, the IQR of the backscatter coefficients when IRI was used was around 1 - 2dB larger.

The RTIM provided a better representation of the ionosphere, which could be seen in the increased number of suitable synthesised ionograms when compared to the IRI-2016 and was also supported by smaller amounts of variation in the backscatter coefficients as seen in the IQR values. This also meant that more data was available for each location when the RTIM was used, as fewer synthesised ionograms were discarded. For these reasons, from here on, only the RTIM is used to generate backscatter coefficients via the ionogram comparison method for further analysis.

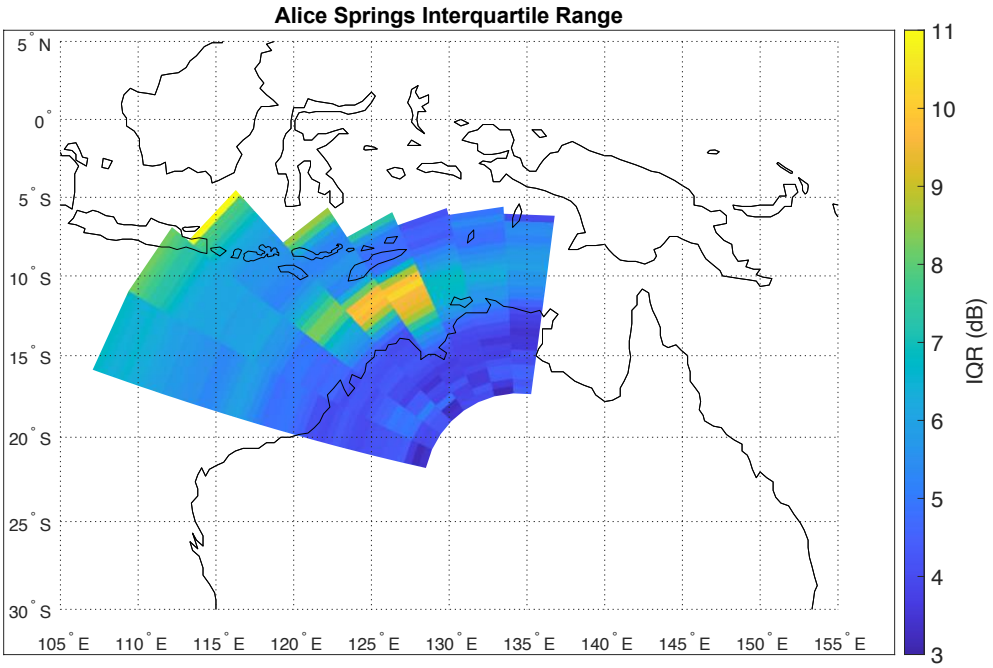

Figure 5.14: Interquartile range of the backscatter coefficient results from Alice Spring in September 2015 when the RTIM was used.

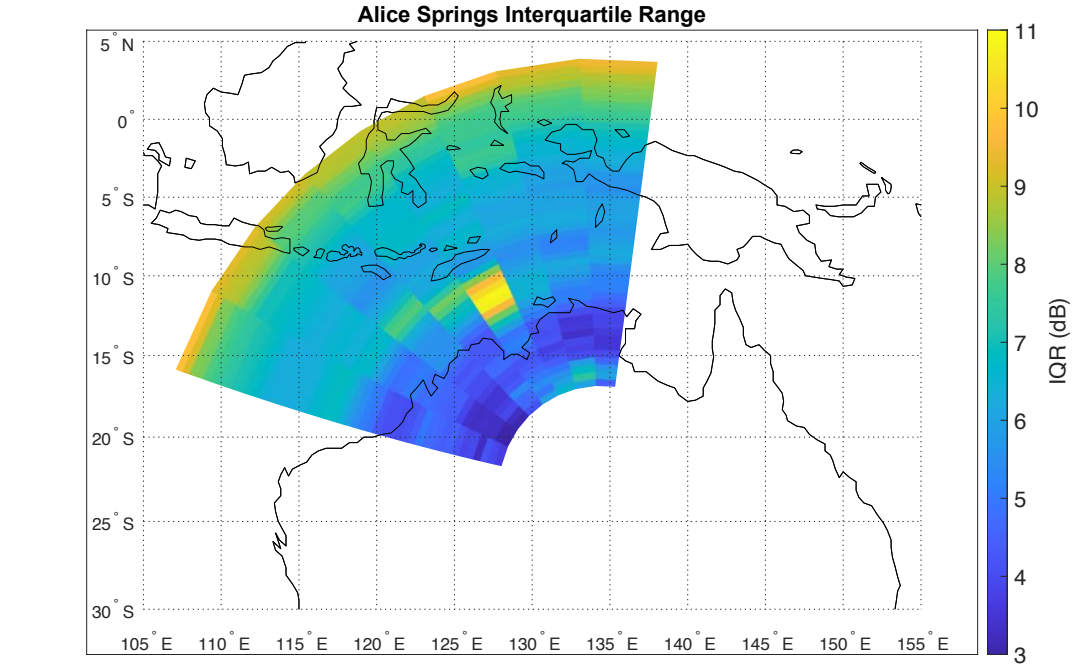

Figure 5.15: Interquartile range of the backscatter coefficient results from Alice Spring in September 2015 when the IRI-2016 was used.

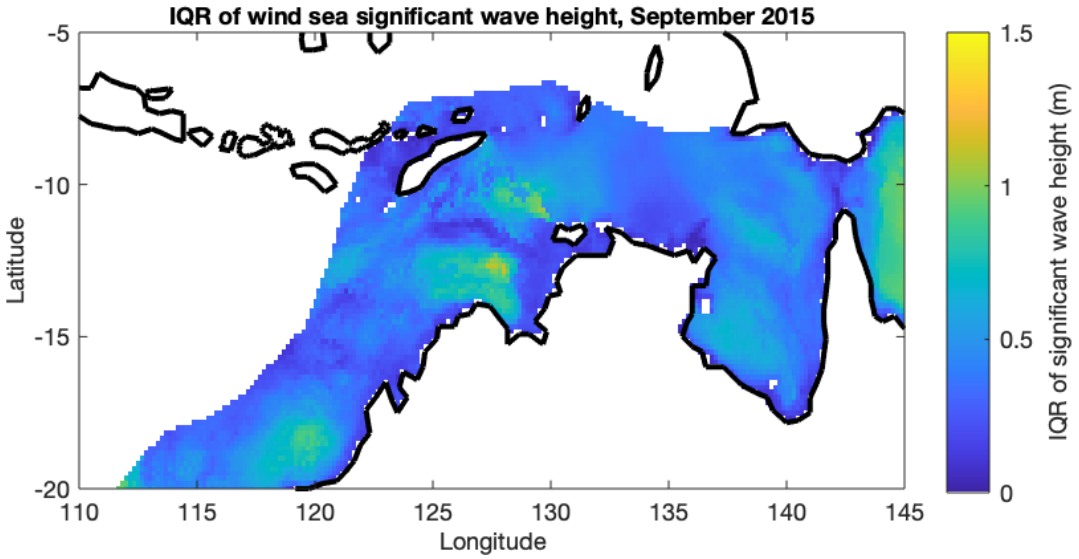

Figure 5.16: Interquartile range of the wind sea significant wave height calculated over the month of September 2015 using sea hindcast data from the Centre for Australian Weather and Climate Research [50]. Wave heights at 0, 2, 4, 6, 8 and 10 UT were used to calculate the IQR.

5.2.2 Data going into the maps

A large amount of data was used in the creation of the backscatter coefficient maps. To further understand these maps, a closer examination of the information used to generate them is required. This section describes only the Alice Springs data; the other sounders were also examined in the same way with similar behaviour. Figure 5.17 shows a histogram of all the

backscatter coefficient values that were used in the Alice Springs September 2015 map. The histogram had a peak at around -24 dB. A one sample Kolmogorov-Smirnov test was conducted to test the null hypothesis that the September 2015 Alice Springs backscatter coefficient results came from a standard normal distribution (i.e., to test if the data is log-normal as the backscatter coefficients are on a logarithmic scale). The null hypothesis was rejected at the 5% significance level with a p-value of 0. It is not surprising that the data was not normally distributed as the backscatter coefficient depends on the surface properties which change with location.

Figure 5.18 displays the number of data points in each range-azimuth bin. It is noted that the number of data points contributing to each cell increases with range. This is due to the method of selecting a suitable area of the ionogram which favoured these greater ranges where the one-hop F2 low propagation path dominated; the E layer propagation paths typically only extended to smaller ranges around 1000 km from the sounder location. A sudden drop in the number of data points in each bin was seen at the most northerly locations near the edge of the geographic limits of the RTIM that was used. Rays that were below 80 km at the edge of the RTIM were kept as they propagated only through the neutral atmosphere, while rays above 80 km at this boundary were discarded. Hence, a ray could only reach these most northerly bins under certain propagation conditions.

The mean radar frequency of the rays reaching each patch of ground increased with distance from the sounder (Figure 5.19). This was because higher frequency rays and those at greater elevations penetrated the ionosphere rather than reflecting down to the close ranges. The mean elevation of the rays contributing to each range bin decreased with increasing distance from the sounder location (Figure 5.20), as expected due to the geometry of the reflections between the ionosphere and the ground.

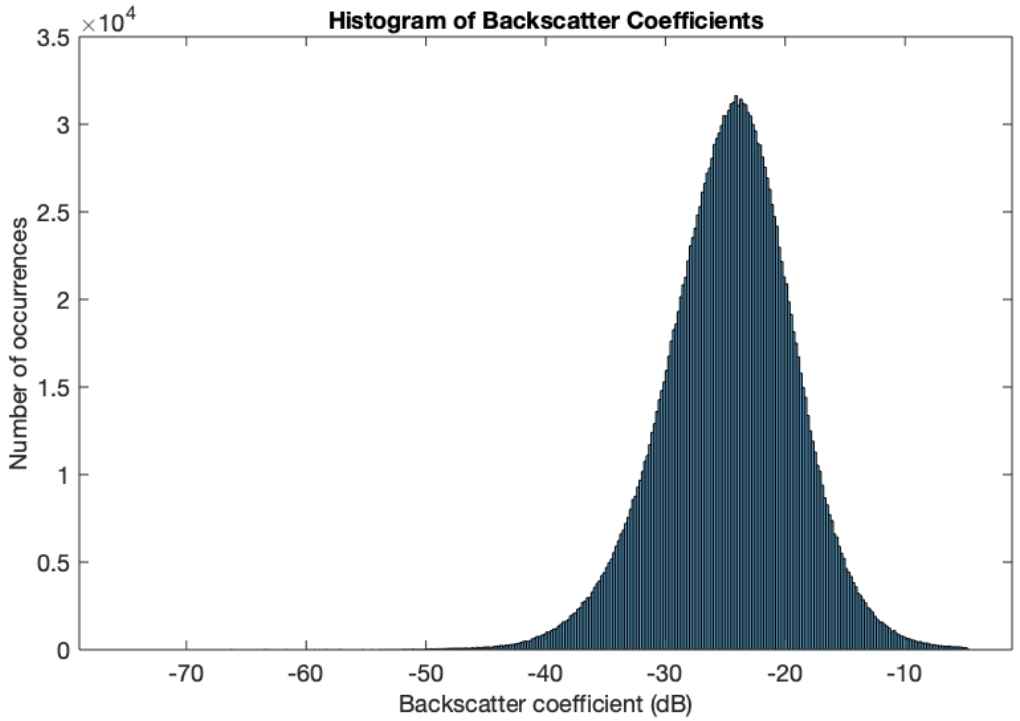

Figure 5.17: A histogram of all the backscatter coefficient data going into the AS September 2015 map.

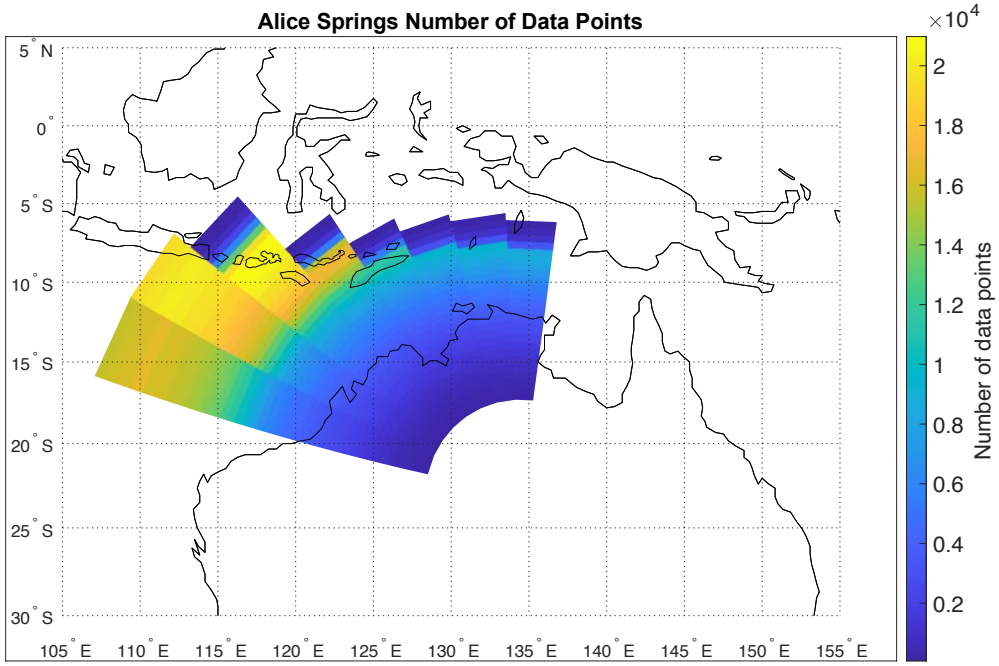

Figure 5.18: The number of data points available for each location in the AS September 2015 map.

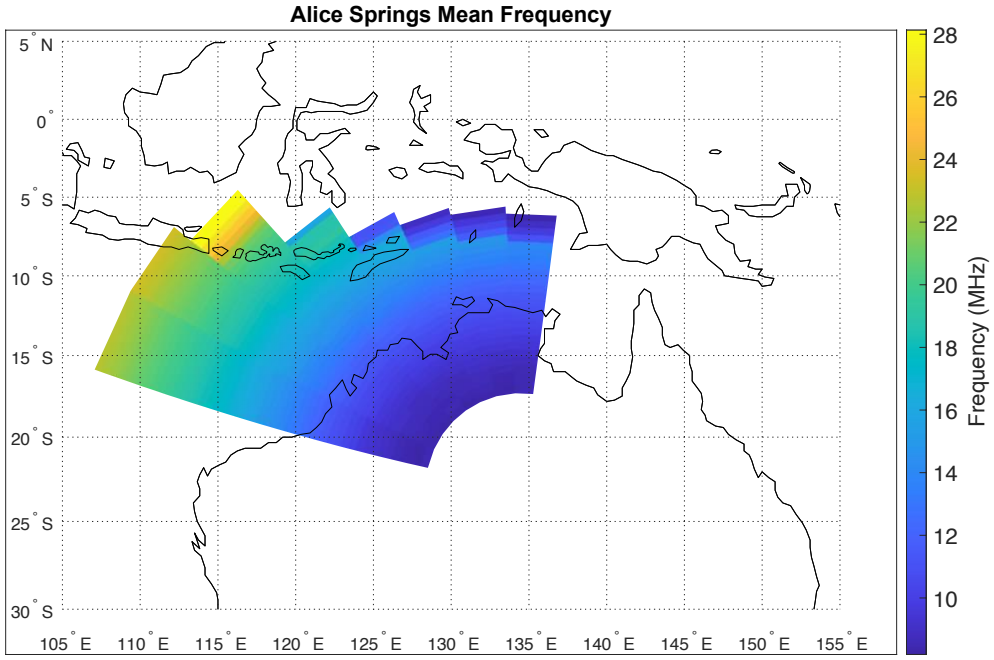

Figure 5.19: The mean frequency of the rays reaching each location in the AS September 2015 map.

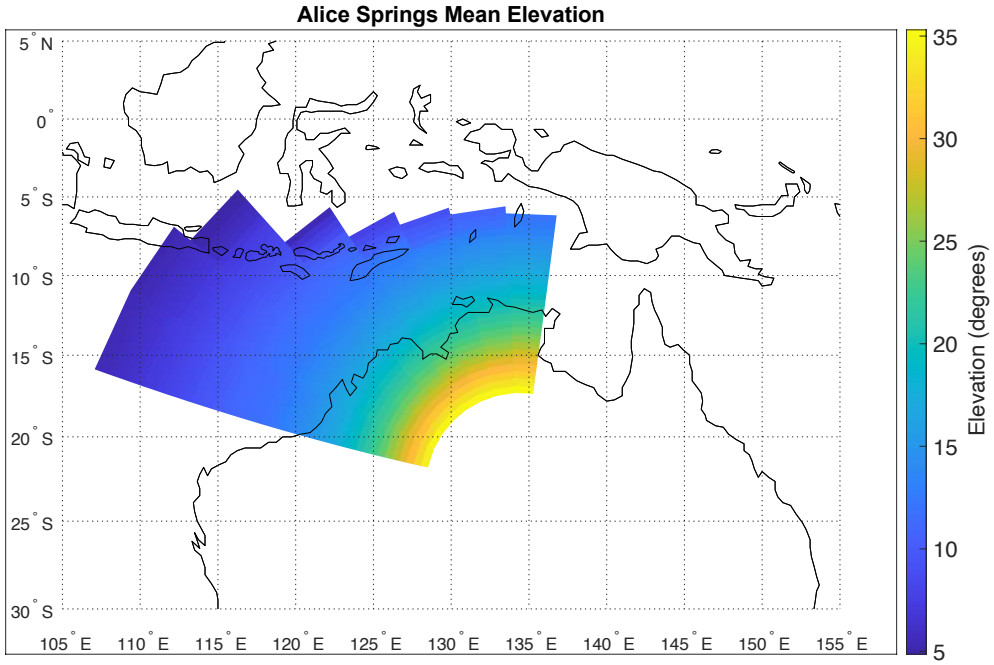

Figure 5.20: The mean elevation of the rays reaching each location in the AS September 2015 map.

5.2.3 Overview of features observed in the backscatter coefficient maps

For each of the maps constructed from the sounder data, consistent areas of high and low backscatter were observed. These distinctive features in the backscatter coefficient maps

aligned with topographic features, such as desert or tropical regions. Differences in the backscatter coefficient of certain areas when viewed from different directions indicated that there was some aspect dependence. Appendix B shows the approximate locations of the places and features discussed.

5.2.3.1 Features in the maps of areas viewed by the Alice Springs backscatter sounder

In the maps of the backscatter coefficient when viewed from the location of the Alice Spring sounder (Figure 5.5, and Figure 5.9), the Great Sandy Desert at around 20˚S, 122˚E stood out as a region of much lower backscatter than the surrounding terrain with a backscatter coefficient of around -35 dB. The Great Sandy Desert is a large, relatively flat area with little vegetation and is covered in sand dunes aligned east to west. The Kimberley region located at around 16˚S, 128˚E had a much larger backscatter coefficient than the surrounding terrain with a backscatter coefficient of around -20 dB; this area is mostly rainforest and consists of large gorges and generally hilly terrain. The mountainous islands of Timor and Indonesia also stood out as areas of high backscatter.

The sea backscatter coefficient differed between September and March. In September the backscatter coefficient was lower between North Western Australia and Timor (around 12˚S, 125˚E) than in the Indian Ocean further west. In March, the backscatter coefficient was more constant over the region of the sea observed, as the backscatter from the Indian Ocean was less than in September. The backscatter coefficient in March of the Indian Ocean was slightly lower than the sea between Timor and North Western Australia. This was due to the different sea states and will be discussed further in Section 5.3.

5.2.3.2 Features in the maps of areas viewed by the Longreach backscatter sounder

The backscatter coefficient maps viewed from the Longreach sounder are shown in Figure 5.6 and Figure 5.10. The March 2016 backscatter coefficients for Longreach were significantly lower than in September 2015, but the general pattern of areas of higher and lower backscatter coefficients was similar between these months. This large difference between the backscatter coefficient over these months was not obvious in the results from the other backscatter sounders. Currently the lower backscatter coefficients in March cannot be explained; the Longreach sounder appeared to be functioning the same way in both September 2015 and March 2016, further investigation was beyond the scope of this thesis.

There was an area of very low backscatter coefficients of around -35 to -40 dB at approximately 18˚S, 132˚E; this corresponded with the location of the Tanami Desert, which is characterised by rocky terrain with small hills. One of the Australian locations with the highest backscatter coefficients when viewed from Longreach was near Cairns (at around 16˚S, 144˚E). This area was mountainous and densely vegetated with tropical rainforest.

The backscatter coefficient through the centre of New Guinea (from 4˚S, 135˚E to 7˚S, 146˚E) was noticeably higher than any other land area at around -20 to -25 dB. This region of high backscatter followed the large mountain chain that runs through the centre of New Guinea. It was expected that this mountainous area would have a larger backscatter coefficient, as is it largely forested and reaches elevations of 4000 m providing a large surface with the normal

directed more towards the backscatter sounder than a flat piece of ground. Timor also stood out as an area with a higher backscatter coefficient than the nearby sea; this was also likely due to the mountainous nature of this island.

The Gulf of Carpentaria and the Arafura Sea had a much higher backscatter coefficient in September 2015 than expected. It was expected that a fully developed sea would have a backscatter coefficient of around -23 dB [30]; however, this area was not out in the open ocean where the sea was likely to be fully developed, yet it had a higher backscatter coefficient of around -20 dB. While this result was unexpected, when the backscatter coefficient of this area was calculated using sea state data from September 2015, a similar result was obtained. This is discussed further in Section 5.3.

5.2.3.3 Features in the maps of areas viewed by the Laverton backscatter sounders

In the maps of the backscatter coefficients when viewed from Laverton East (Figure 5.7 and Figure 5.11) a region of lower backscatter coefficients (around -30 dB) was seen over the Great Sandy Desert (at 22˚S-25˚S, 122-130˚E), which was also seen in the Alice Springs results. However, the Tanami Desert, which appeared with such a low backscatter coefficient in the Longreach results, does not appear as an area of low backscatter in the Laverton East results. This may partly be because this area was closer to the sounder location, meaning higher elevation rays of lower frequency were reaching this area. Alternatively, the backscatter from this region may have a strong aspect dependence. Similar to the Longreach results, the area of tropical rainforest at around 16˚S, 144˚E (near Cairns) had a higher backscatter coefficient than the surrounding areas. The backscatter coefficient at -24˚S, 130˚E over the MacDonnell ranges (near topographical features such as Kings Canyon and Uluru) was quite large, around -20 dB. This may be due to the many uneven features of this terrain. The backscatter coefficient also appeared to be unexpectedly high in the central beams over Northern Australia around Arnhem land, Darwin and surrounds. This area was also characterised by rocky escarpments, gorges, rivers and waterfalls. Beam 8 of the Laverton East sounder viewed the Simpson Desert at around 140˚E. The backscatter coefficient over this desert was around -30 dB, which was similar to the Great Sandy Desert.

The field of view of the Laverton West backscatter sounder was mostly over the Indian Ocean (Figure 5.8 and Figure 5.12). It was expected that this area of ocean would be fully developed, giving an expected backscatter coefficient of around -23 dB. Backscatter coefficients similar to those expected for a fully developed sea were seen in the central beams. However, much lower backscatter coefficients were found for the sea between North Western Australia and Indonesia (seen in beams 7 and 8); this may be because this area of the sea was calmer (see Section 5.3).

5.2.3.4 Summary

In general, the desert regions had much lower backscatter coefficients than the surrounding terrain, while mountainous or tropical regions had much larger backscatter coefficients. This may be due to a number of differences between these kinds of terrain. Deserts tend to be relatively flat expanses of ground with low soil moisture (lower conductivity) and

little vegetation; each of these characteristics would suggest a lower backscatter coefficient. Conversely, mountainous regions have large areas where the normal to the surface is more likely to be oriented in a direction aligned with the direction of propagation of the incident radio waves. This would cause more energy to be scattered back to the sounder. Mountainous and tropical regions also tend to be wetter and more vegetated, which again, is also likely to increase the backscatter coefficient.

The backscatter coefficient of land areas remained similar in both the September and March results (except for the Longreach results which are discussed further in Section 5.4.1.3); however, there were large differences in the calculated sea backscatter coefficients between these months. The sea backscatter coefficient tended to be less in March than in September. This is probably due to the differences in the sea state between the seasons which will be investigated in Section 5.3.

5.3 Sea backscatter coefficients

5.3.1 Sea backscatter coefficients calculated from sea state data

The sea backscatter coefficients were calculated using sea hind cast data from the Centre for Australian Weather and Climate Research, which included the swell period, wave heights and wind speeds. The sea backscatter coefficient was calculated for 15 MHz signals travelling in a direction where the azimuth is radially outwards from each sounder location. A radio wave frequency of 15 MHz was used as this is around the frequency of the radio waves that backscattered from the sea in the model ionograms. The mean daytime sea backscatter coefficients throughout the months of September 2015 and March 2016 as viewed from the Alice Springs, Longreach and Laverton sounders are shown in Figure 5.21, Figure 5.22 and Figure 5.23 respectively. The backscatter coefficient was calculated hourly from 0000 UT to 1000 UT for each day of the month and the mean of these results was taken.

A small aspect dependence between the backscatter sounder sites can be seen in these results; for example, in September 2015 the sea backscatter coefficients in the Gulf of Carpentaria are highest when viewed from the western-most sounder (Laverton) and lowest when viewed from the eastern-most sounder (Longreach). This is caused by the directionality of the ocean swells.

A large difference between the sea backscatter coefficients of September 2015 and March 2016 was also seen. In general, the March sea backscatter coefficients were much lower than the September sea backscatter coefficients. This was likely due to a calmer sea in March, providing less developed wave faces for radio waves to backscatter from. The difference in the sea backscatter coefficient between these months was also seen in the backscatter coefficient results from the ionogram comparison method, indicating there are similarities in the results from these two methods.

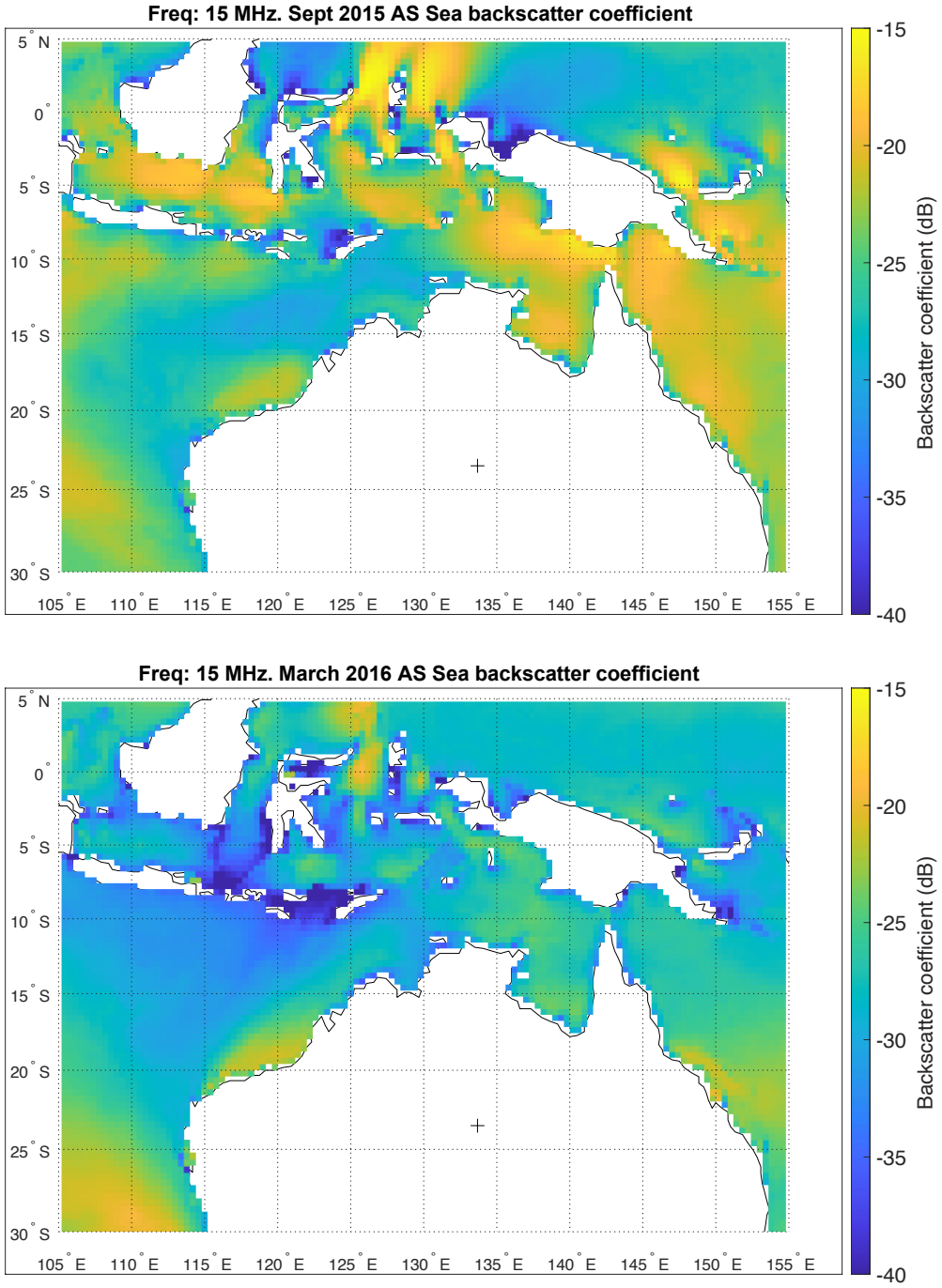

Figure 5.21: Monthly mean sea backscatter coefficient calculated for the Alice Springs sounder (location indicated by +) using the wave spectrum method. Top: September 2015, Bottom: March 2016.

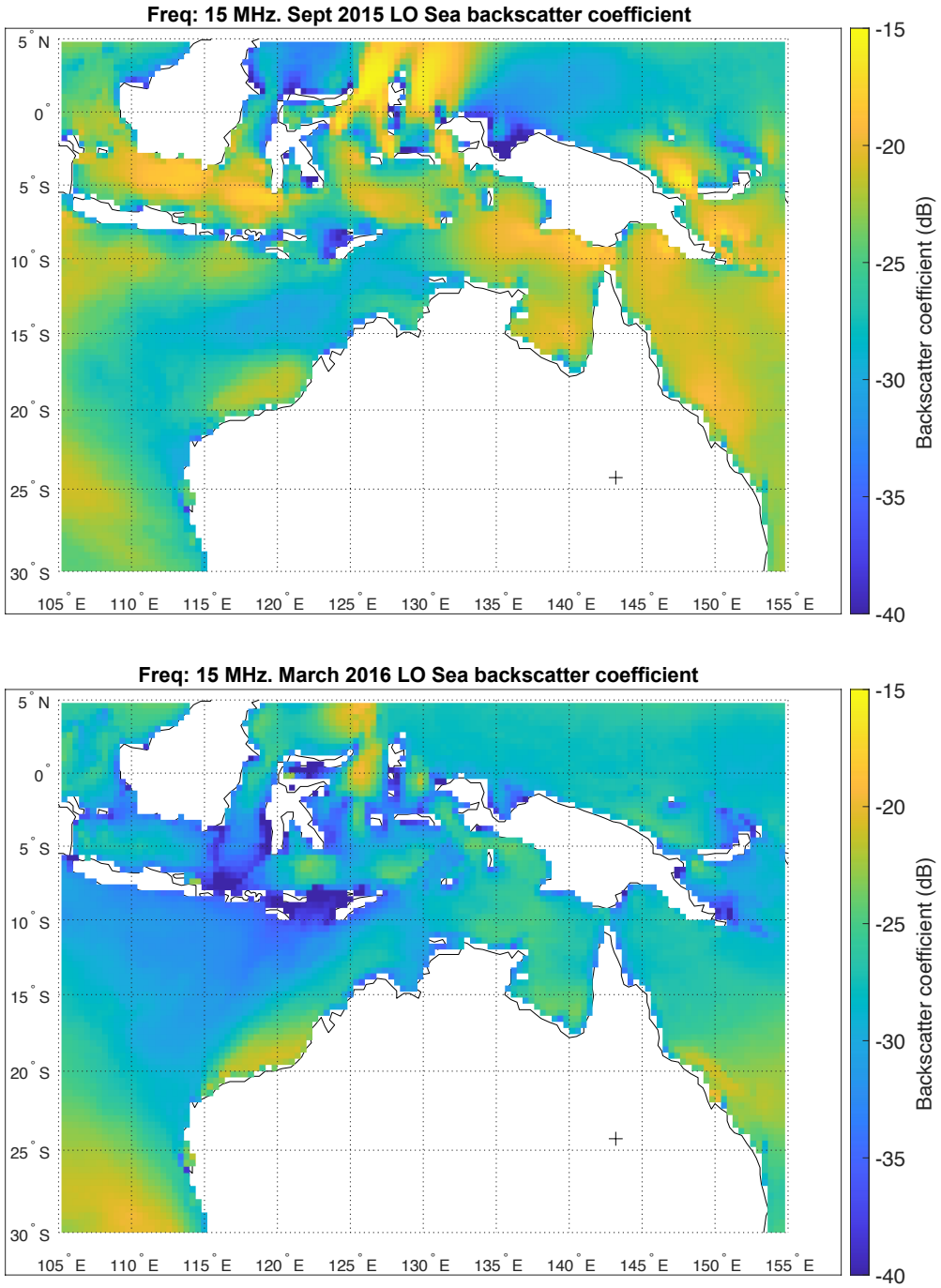

Figure 5.22: Monthly mean sea backscatter coefficient calculated for the Longreach sounder (location indicated by +) using the wave spectrum method. Top: September 2015, Bottom: March 2016.

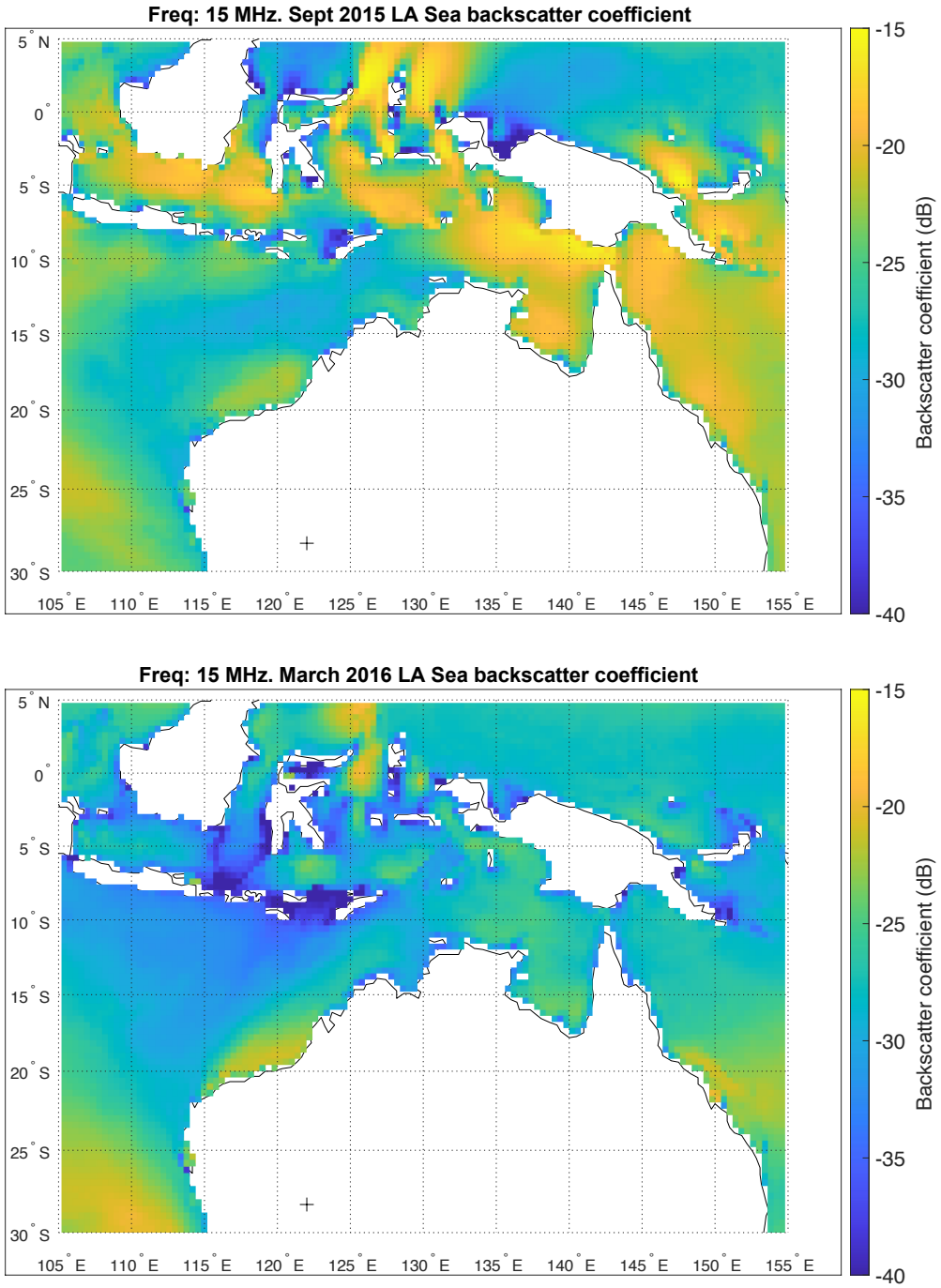

Figure 5.23: Monthly mean sea backscatter coefficients calculated for the Laverton sounder (location indicated by +) using the wave spectrum method. Top: September 2015, Bottom: March 2016.

5.3.2 Comparison of the two methods of calculating the sea backscatter coefficient

The sea backscatter coefficients calculated from the wave spectrum method and the ionogram comparison method were compared to investigate how similar the results from these two methods were.

To investigate the differences in the results between these methods, the sea backscatter coefficients were calculated during the morning (0300 UT) and the afternoon (0700 UT) for each day of the month, for signals with frequencies of 6, 8, 10, 12, 14, 16, 18, 20, 22, 24 and

26 MHz using the wave spectrum method with the 4-arcminute resolution sea state hindcast data. The median morning and afternoon backscatter coefficients calculated using the ionogram comparison method were then compared with these results. For each 100 km range bin of each beam, the mean frequency of rays reaching that bin was calculated from the ionogram comparison method results for each morning and afternoon. The wave spectrum results calculated at the closest frequency to this mean frequency were then used for the comparison. The sea backscatter coefficients were not calculated using the wave spectrum method at the exact value of the mean to decrease the computation time; the small difference in frequency has a negligible effect on the results.

Figure 5.24 shows the wave spectrum sea backscatter coefficient results and the ionogram comparison results for a single 100 km range bin throughout September 2015 (top) and March 2016 (bottom). The two methods appear to agree relatively well, with the trends of lower and higher sea backscatter coefficients agreeing between the two methods. However, while the general trends were similar, there was a period from around the 16th to the 21st March 2016 where the hindcast data sea backscatter coefficient results were around 10 dB larger than the ionogram comparison sea backscatter coefficient results.

The mean difference between the results from the two methods over these times was calculated for each of the range-azimuth bins of each backscatter sounder. The results are displayed in Figure 5.25. A cursory inspection of this figure indicates that while at some locations the two methods agree well, there are other locations where there are significant differences between the two methods.

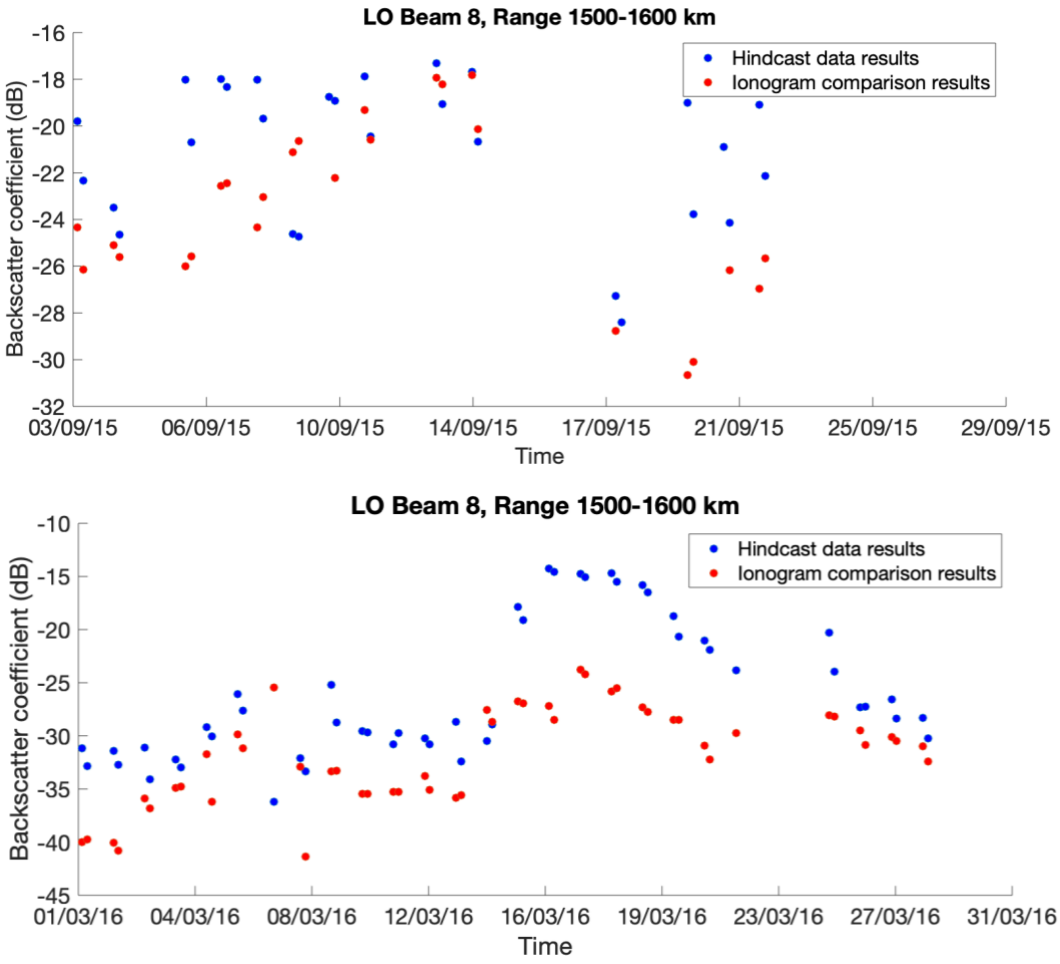

Figure 5.24: Plot of the backscatter coefficient calculated via the hindcast sea state (blue) and the ionogram comparison method (red) for a single location (Longreach beam 8, at a range of 1500-1600 km) throughout the month of September 2015 (top) and March 2016 (bottom).

To initially investigate the difference between the two methods, a mean difference between the backscatter coefficients from the two methods was calculated over all range-azimuth bins for each sounder and month. This mean included data from all of the available range-azimuth cells and so was weighted towards the locations where data was available at more times. The mean difference in the Alice Springs sea backscatter coefficients when the ionogram comparison results were subtracted from the wave spectrum results was -1.7 dB and -2.1 dB in September and March respectively (Figure 5.25 a, b). The backscatter coefficients calculated using the ionogram comparison method for the Alice Springs sounder tended to be around 2 dB larger than those calculated using the hindcast data. The mean difference between these two methods was similar across all beams and ranges investigated, although there did appear to be a slightly larger difference in the central beams than the edge beams. This azimuthal dependence may have been caused by deviations of the real antenna gain patterns from the idealised model antenna gain patterns used in the ionogram synthesis.

The mean difference between the two methods using the data from all of the range-azimuth bins for the Longreach results was -0.8 dB and 2.6 dB in September and March respectively (Figure 5.25 c, d). In September the mean difference for each range-azimuth bin

was relatively constant over all range-azimuth bins; the pattern appeared to be similar to Alice Springs with slightly larger differences in the central beams than the edge beams and again is attributed to possible deviations in the antenna pattern from the idealised model. However, during March the ionogram comparison method produced much lower backscatter coefficients than the wave spectrum method for beams 1 and 2. This is clearly observed when comparing the Longreach sounder derived sea backscatter coefficients (Figure 5.6 and Figure 5.10) and sea state derived sea backscatter coefficients (Figure 5.22, top and Figure 5.22, bottom) for both months. Both the sounder and sea state derived sea backscatter coefficients are significantly reduced in the Arafura Sea and Gulf of Carpentaria (beams 4, 5, and 6) for March versus September. However, while the sounder derived sea backscatter coefficient is reduced in beams 1 and 2 during March, there is very little change in the sea backscatter coefficient derived from the sea state data. This is not currently understood, one possibility is that the sea state data in this region is in error during March 2016.

The mean difference between the sounder and sea state derived backscatter coefficients from Laverton appeared to be similar between September and March; however, there was much more variation in the difference across locations than was seen in the Alice Spring or Longreach results. This is especially the case for the Laverton West results. The larger variation in the difference between the two methods over the field of view suggests that the ionogram comparison method did not work as well for the Laverton sounders than for the other sounders. For Laverton East, the mean differences in September and March using data from all locations was 0.88 dB and -2.1 dB (Figure 5.25 e, f). For Laverton West, the mean differences in September and March using data from all locations was 2.0 dB and 5.2 dB (Figure 5.25 g, h).

(a) Alice Springs (September)

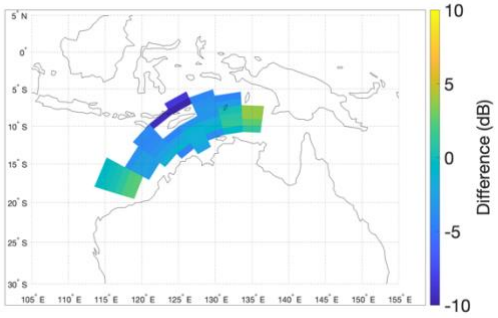

(b) Alice Springs (March)

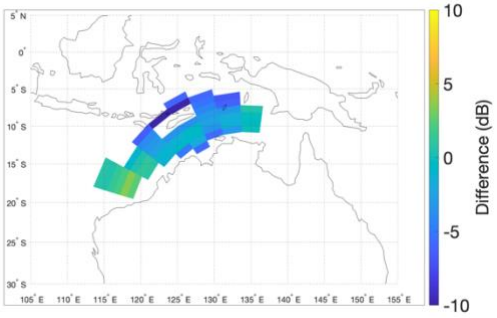

(c) Longreach (September)

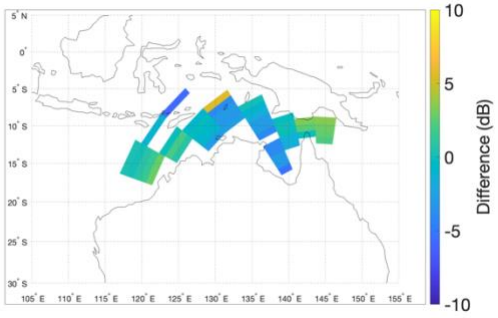

(d) Longreach (March)

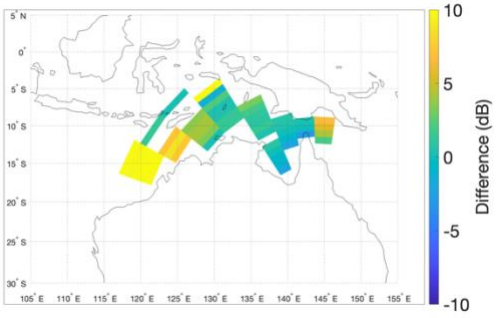

(e) Laverton East (September)

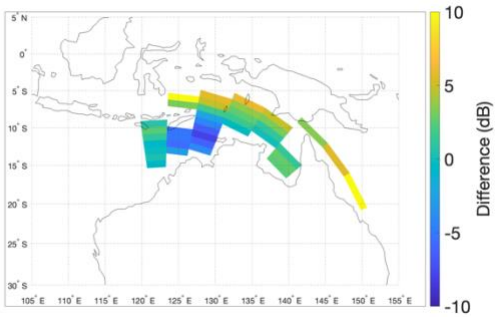

(f) Laverton East (March)

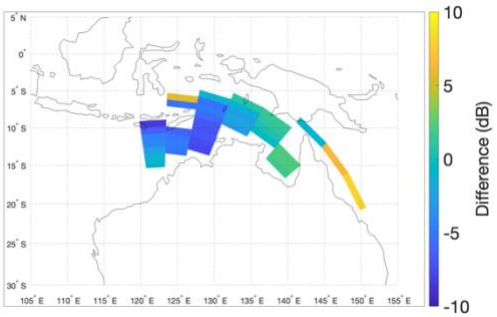

(g) Laverton West (September)

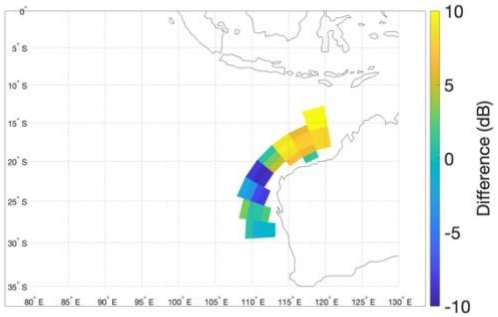

(h) Laverton West (March)

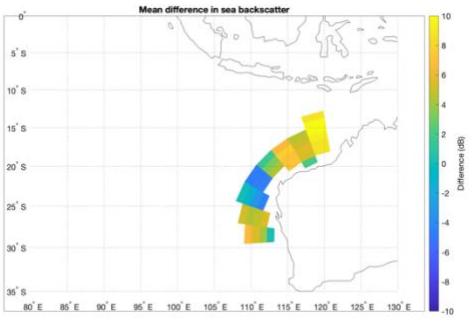

Figure 5.25: Mean difference between the wave spectrum method and the ionogram comparison method backscatter coefficients. The difference between the methods was calculated when data was available throughout a month, then the mean difference was calculated.

To further investigate how well the results from the wave spectrum method and the ionogram comparison method agreed, the backscatter coefficient results for each method from

all times in both September 2015 and March 2016 and all range-azimuth bins were plotted against each other as 2D histograms for each sounder in Figure 5.26. If the two methods produced similar results, it is expected that these 2D histograms would show a linear relationship with a slope of one that passed through the origin. This linear trend could be seen in the Alice Springs and the Longreach results, although the slopes and intercepts did not match the expected results (Figure 5.27 and Figure 5.28). The Laverton West and East results were considerably more scattered. The extra scatter in the Laverton results was expected due to the larger range of differences in the sea backscatter results over the region observed (Figure 5.25). However, the trend in the backscatter coefficient over time between the two methods for a single range-azimuth bin may be similar if the differences were caused by different offsets in the backscatter coefficient over the region observed. The sea backscatter coefficients calculated from the sea state data were rarely greater than around -15 dB. This abrupt cut off in values is due to the sea becoming fully developed.

A Pearson correlation test was conducted to test the linear correlation between the wave spectrum method and the ionogram comparison method results (Table 5.3). This tested the null hypothesis that there was no relationship observed between the results [65]. The strength of the correlation was represented by the absolute value of the correlation coefficient and the direction was represented by the sign of the correlation coefficient. The significance level was given by the P value. For all of these tests the P value was less than 0.05, so the corresponding correlation coefficient was considered significant at the 95% confidence interval. There was a moderate positive correlation for both Alice Springs and Longreach, while the Laverton correlation coefficients indicate very little correlation. This further suggested that the model used in the ionogram comparison method worked better for the Alice Springs and Longreach sounders than for the Laverton sounders.

A line of best fit was fitted to the Alice Springs and Longreach data using an orthogonal least squares linear regression method (Figure 5.27 and Figure 5.28). This method was chosen over a simple linear regression as errors in both the variables are taken into account, rather than using one variable to predict the other. It was expected that the slope of these lines would be 1 with an intercept of 0. However, for both sounders the slope was greater than 1 and the intercept was positive which suggested the backscatter values from the wave spectrum method were different from the ionogram comparison method. The slope of the fitted line in the Alice Springs results was 2.3 which is double what was expected. The slope of the fitted line in the Longreach results was 1.3 which is similar to what was expected. Using these fitted lines, the ionogram comparison method and wave spectrum method produced the same results when the backscatter coefficient was -24.6 dB in the Alice Springs results and -36.7 dB in the Longreach results. The slopes of both fitted lines was greater than one which suggested that the backscatter coefficients calculated from the wave spectrum method had a greater dynamic range than the ionogram comparison method. It is possible this unexpected slope may have been introduced by the different spatial and temporal averaging processes for the different data sets.

A 95% confidence error ellipse was also plotted on the results (Figure 5.27 and Figure 5.28). To create these error ellipses, it was assumed the data was normally distributed. The orientation of the ellipse is determined by the covariance of the data and the magnitude of the axes of the ellipse are determined by the variance in the data (Table 5.4) [66]. The eigenvectors of the covariance data are plotted in green and magenta, these represent the direction of the most spread in the data and are aligned with the semi-major and semi-minor axes of the ellipse, while the eigenvalues define how large this spread is. The centre of the error ellipse for Alice Springs was at (-25.9 dB, -27.9 dB) and the centre of the error ellipse for Longreach was at (-26.9 dB, -25.3 dB). This shows that the two methods had good agreement for the values that were most commonly seen.

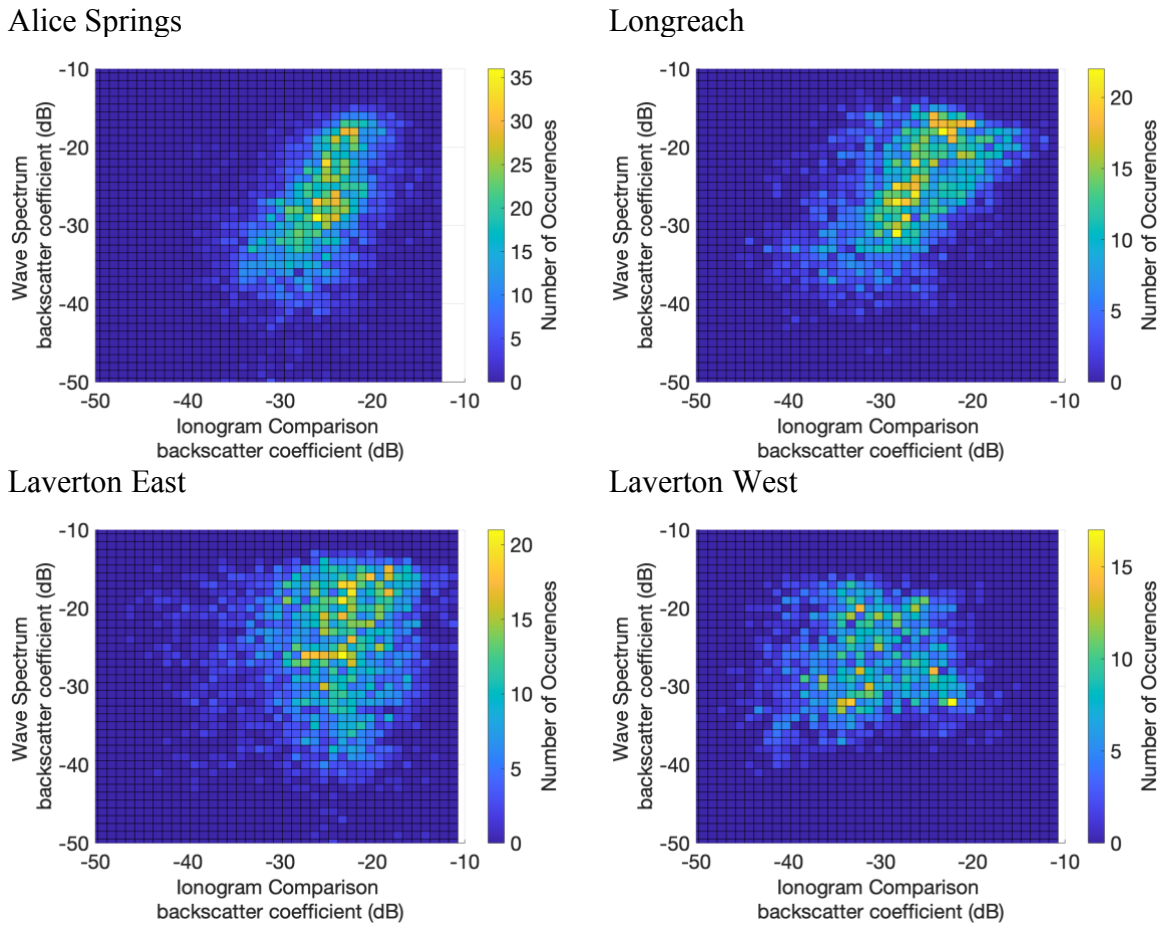

Figure 5.26: 2D histogram of the wave spectrum sea backscatter coefficients vs the ionogram comparison sea backscatter coefficients (Top left: Alice Springs. Top right: Longreach. Bottom left: Laverton East. Bottom right: Laverton West).

Table 5.3: Linear correlation test results for the methods of calculating the sea backscatter coefficients.

Sounder	Correlation Coefficient (R)	P value
AS	0.500	0.000
LO	0.513	0.000
LAE	0.088	0.000
LAW	0.047	0.038

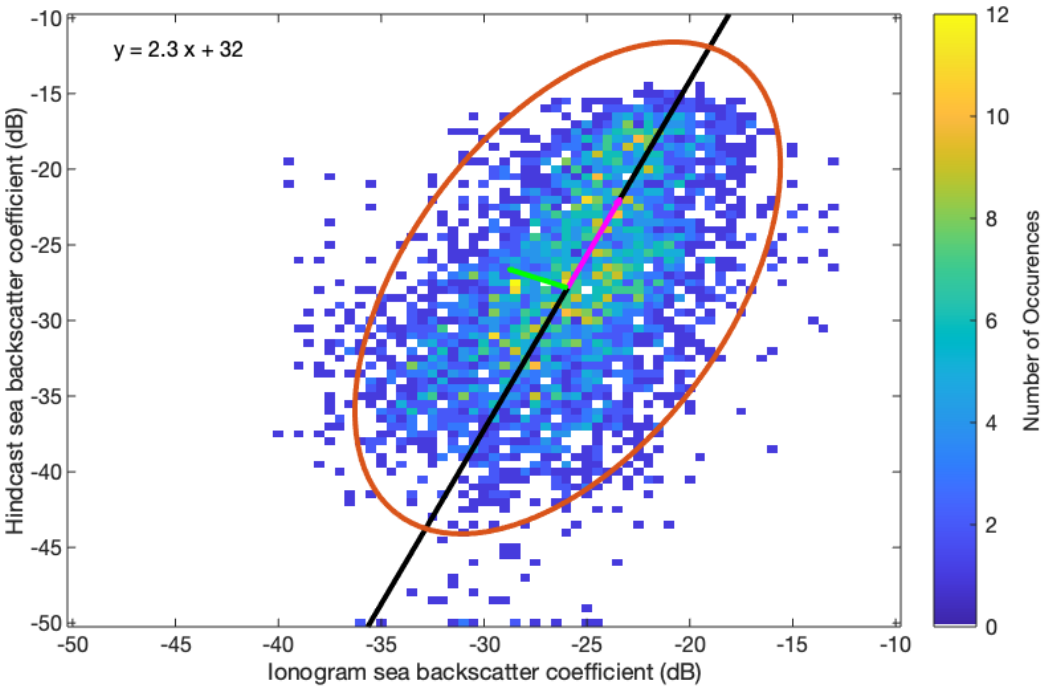

Figure 5.27: Alice Springs sea backscatter coefficients calculated using the wave spectrum method with hindcast data vs sea backscatter coefficients calculated using the ionogram comparison method. A line of best fit is shown in black, with the corresponding equation in the top left corner and a 95% confidence error ellipse shown in red. The eigenvectors of the covariance matrix are shown in green and magenta. The centre of the ellipse is at (-25.9 dB, -27.9 dB).

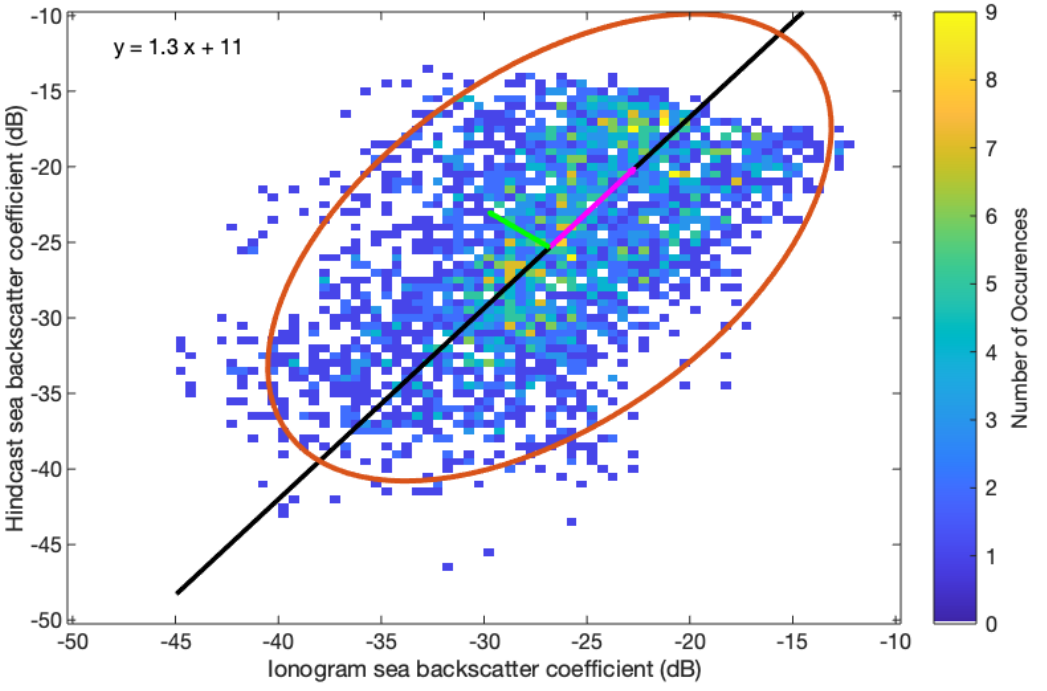

Figure 5.28: Longreach sea backscatter coefficients calculated using the wave spectrum method with hindcast data vs sea backscatter coefficients calculated using the ionogram comparison method. A line of best fit is shown in black, with the corresponding equation in the top left corner and a 95% confidence error ellipse shown in red. The eigenvectors of the covariance matrix are shown in green and magenta. The centre of the ellipse is at (-26.9 dB, -25.3 dB).

Table 5.4: 95% confidence error ellipse results for the comparison of the two methods of calculating sea backscatter coefficients. The orientation of the ellipse is determined by the covariance of the data. The eigenvectors represent the direction of the most spread in the data and the eigenvalues define how large the spread is. The centre of the ellipse is at (X0, Y0).

	Covariance Matrix	**Largest eigenvector**	**Largest eigenvalue**	**Smallest eigenvector**	**Smallest eigenvalue**	**X0**	**Y0**
AS	$\begin{bmatrix}17.85 & 14.04\\14.04 & 44.15\end{bmatrix}$	$\begin{bmatrix}0.40\\0.92\end{bmatrix}$	50.24	$\begin{bmatrix}-0.92\\0.40\end{bmatrix}$	11.77	-25.9	-27.9
LO	$\begin{bmatrix}31.29 & 18.11\\18.11 & 39.88\end{bmatrix}$	$\begin{bmatrix}0.62\\0.78\end{bmatrix}$	54.21	$\begin{bmatrix}-0.78\\0.62\end{bmatrix}$	16.97	-26.9	-25.3

5.3.3 Assumptions and limitations of the sea backscatter coefficient wave spectrum method

The comparison between the wave spectrum method and ionogram comparison method of calculating the sea backscatter coefficients showed agreement between the methods for the Alice Springs and Longreach sounders. The Alice Springs results and Longreach results (except for beams 1 and 2 in March 2016) appeared to agree well. The resolution of the power in the observed backscatter ionograms was 0.5 dBW, so differences in the results no smaller than this were expected. The sea backscatter coefficients calculated using the wave spectrum method with sea state hindcast data were calculated at 0300 UT and 0700 UT, while the sea backscatter coefficients from the ionogram comparison method were calculated as a median of the results from 0000 UT to 0600 UT and 0400 UT to 1000 UT. Thus, for the purpose of this comparison, it was assumed that the sea backscatter coefficient was relatively constant over that period of time (throughout the morning and afternoon). Significant changes in the sea state over these time periods could introduce differences between the two results being compared.

Errors in either the wave spectrum method or the ionogram comparison method may contribute to the differences between the two methods. The limitations of the ionogram comparison method are described in Section 4.3. The model for calculating the sea backscatter coefficient from the wave height spectrum assumed the water was deep, and so may not be valid in coastal regions where ocean waves interact with the ocean floor. Lipa et al. [34] showed that there was increased sea backscatter from shallow water as the radar spectrum saturated at smaller wave heights. It has been suggested that a model of the sea scatter from a sinusoidal diffraction grating rather than a ruled diffraction grating, which was used in this analysis, would better fit the theory and observations of sea backscatter [67, 68]. This is because the wave heights at all points would be considered, rather than only at the wave crests.

The wave spectrum gives the distribution of the wave energy over the different frequencies of ocean waves. The JONSWAP wave spectrum assumed that a wind with a constant velocity had been blowing over the ocean for long periods of time. This allowed a relatively simple spectrum to be calculated. However, it was not necessarily representative of a typical ocean wave spectrum where local winds may create multiple peaks. This could introduce differences between the backscatter coefficients calculated by this model and the

ionogram comparison method. Inaccuracies in the sea state hindcast data would also contribute to the differences in the backscatter coefficient results. Finally, only first order Bragg scatter was considered in the calculation of the sea backscatter coefficient. Higher order scatter was ignored.

5.4 Effects of ray and surface parameters on the backscatter coefficient

In this and subsequent sections only the backscatter coefficients calculated via the ionogram comparison method are considered. In this section various parameters such as the ray frequency and elevation, the time of the year, the surface topography, the ground conductivity and the vegetation are investigated as to how they might affect the backscatter coefficient. Only the Alice Springs and Longreach results were used to investigate the effects of these different parameters. This was because the Laverton results did not appear to be as reliable due to (1) the large variation in the comparison of the two methods of calculating the sea backscatter and (2) the smaller percentage of synthesised ionograms retained for analysis.

5.4.1 Temporal patterns

Diurnal and seasonal patterns in the backscatter coefficient may arise from changes in the surface parameters over these time scales, such as regular patterns in the sea state or regular soil moisture changes throughout the day (e.g., morning dew) or throughout the different wet and dry seasons.

5.4.1.1 Day-to-day variation

The variation of backscatter coefficients over time can be investigated by examining the IQR of the backscatter coefficients. While the variability depicted by the IQR may be partly due to the variance introduced by the assumptions and errors in the model used to calculate the backscatter coefficients, variability can also be introduced by changes in the backscatter coefficient of a region throughout the month. It was expected that the sea backscatter coefficient would show larger day-to-day variation than the land backscatter coefficient due to changes in the sea conditions with different weather conditions. Histograms of the IQR of the backscatter coefficients for sea and land range-azimuth bins calculated using the data from both the Alice Springs and Longreach sounders in September 2015 and March 2016 are shown in Figure 5.29. The median IQR of the backscatter coefficients of the sea was 6.4 dB. This was significantly larger than the median IQR of the backscatter coefficients of the land which was 4.2 dB.

Figure 5.14 showed that the IQR of the backscatter coefficients observed by the Alice Springs sounder throughout September 2015 was location dependent. For example, the sea between North Western Australia and Timor had an IQR of around 10 dB, which was much larger than most other areas such as over the Australian land mass where the IQR was around 4 dB. The Great Sandy Desert and the sea between North Western Australia and Timor were used as a case study to further investigate the day-to-day variation in the backscatter coefficient. Histograms of the backscatter coefficient data for a region of the Great Sandy Desert where the IQR was low (4.0 dB) and a region of ocean between Western Australia and Timor that had a

high IQR (8.5 dB) are shown in Figure 5.30. The histogram of the backscatter coefficients for the Great Sandy Desert appeared log-normally distributed, while the histogram of the backscatter coefficients for the ocean where the IQR was higher had a much larger spread and appeared to be bimodal.

Plots of the backscatter coefficient for these locations over the month are shown in Figure 5.31. Throughout the month the backscatter coefficient over the Great Sandy desert appeared to be relatively constant, while over the ocean there were distinct periods of much higher and lower backscatter coefficients. From the 10th – 13th and the 21st – 25th September 2015, the backscatter coefficients of this area of ocean were much larger than at other times during the month. These times corresponded to times when the significant swell height of the wind sea was largest (Figure 5.32). These distinct periods of low and high backscatter coefficients for this location caused the bimodal appearance of the histogram displayed in Figure 5.30 (right). The sea backscatter changed much more significantly than the land backscatter throughout the month because the roughness of the sea can be easily altered by changes in weather conditions such as the wind speed, while the surface of the land remains much more constant.

In general, it was found that the backscatter coefficient of the ocean varies daily throughout the month, while the backscatter coefficient of the land remains relatively constant from day-to-day.

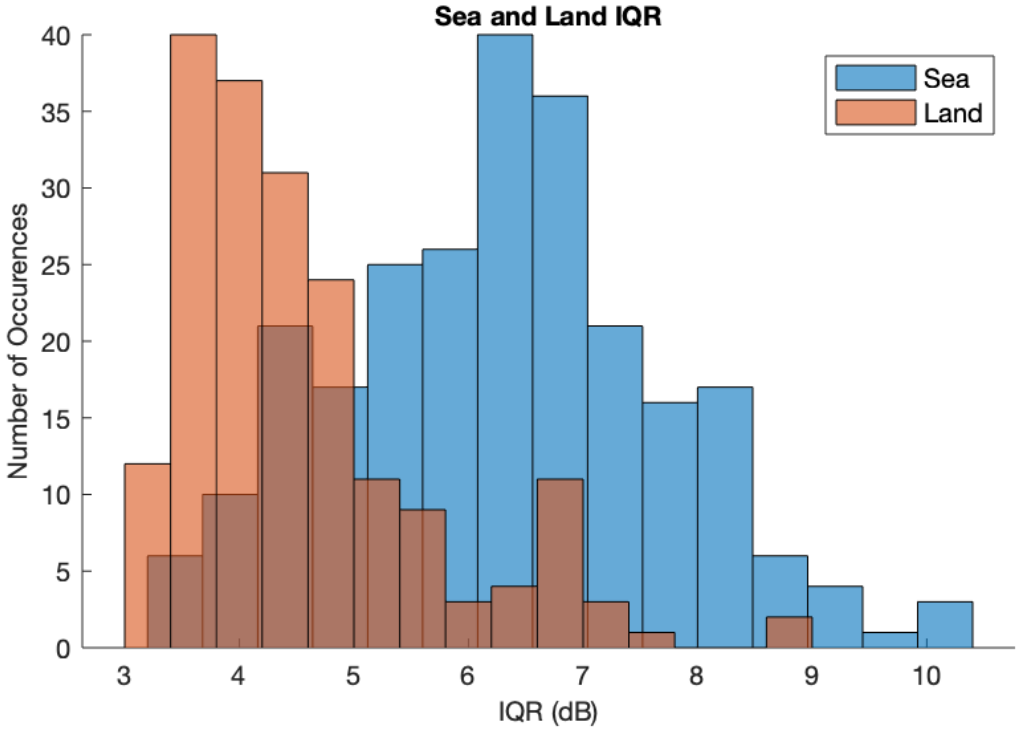

Figure 5.29: Histogram of the interquartile range for the sea (blue) and land (orange) range-azimuth bins. The IQR was calculated for the data in each of the 50 km range-azimuth bins observed by the Alice Springs and Longreach sounders in September 2015 and March 2016.

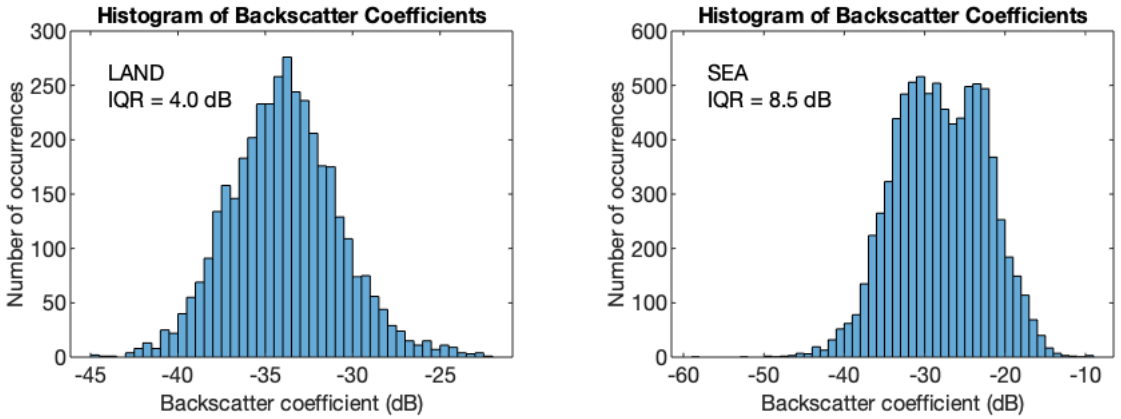

Figure 5.30: Left: Histogram of backscatter coefficients for Alice Springs beam 1 at 1100-1200 km (over the Great Sandy Desert at around 20˚S, 124˚E) from September 2015.

Right: Histogram of backscatter coefficients for Alice Springs beam 5 at 1300-1400 km (over the sea at around 13˚S, 127˚E) from September 2015.

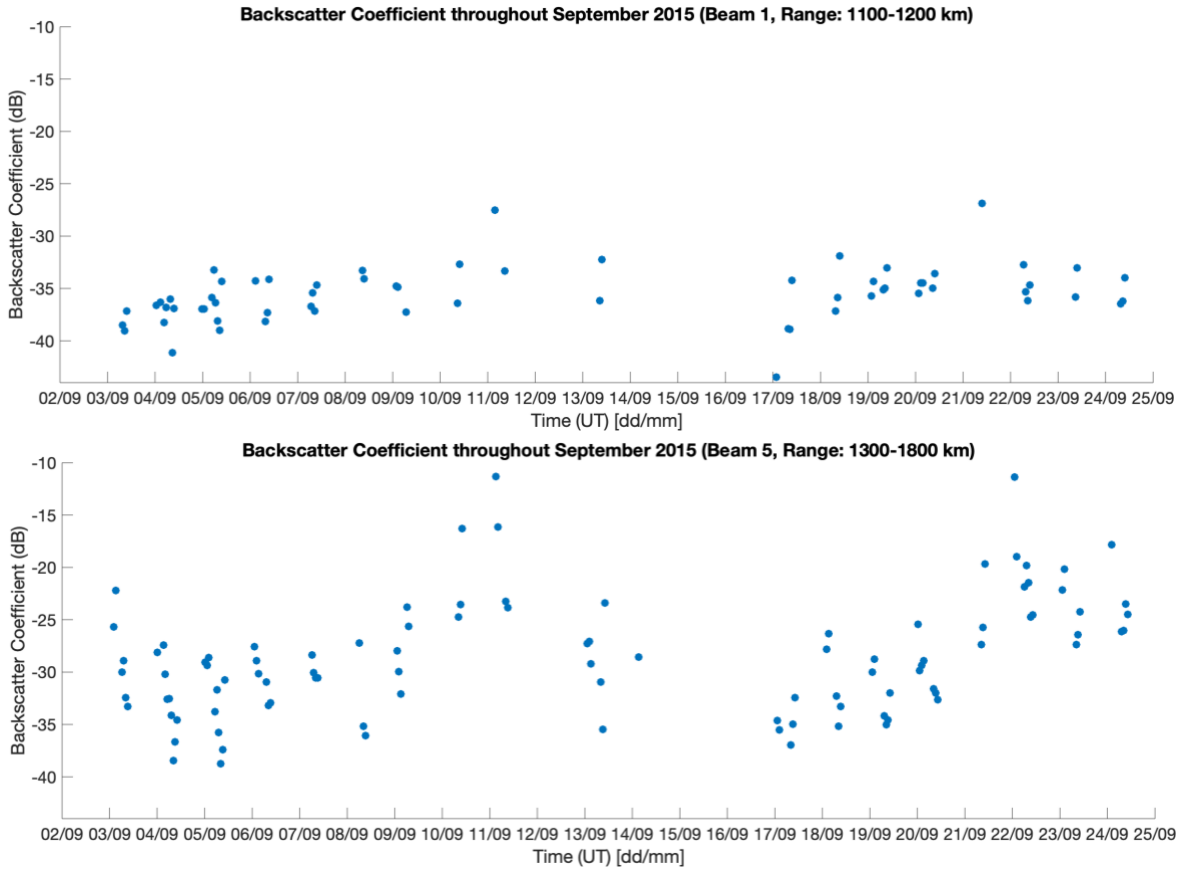

Figure 5.31: Top: Hourly median backscatter coefficients for Alice Springs beam 1 at 1100-1200 km (over the Great Sandy Desert at around 20˚S, 124˚E) throughout the month of September 2015.

Bottom: Hourly median backscatter coefficients for Alice Springs beam 5 at 1300-1400 km (over the sea at around 13˚S, 127˚E) throughout the month of September 2015.

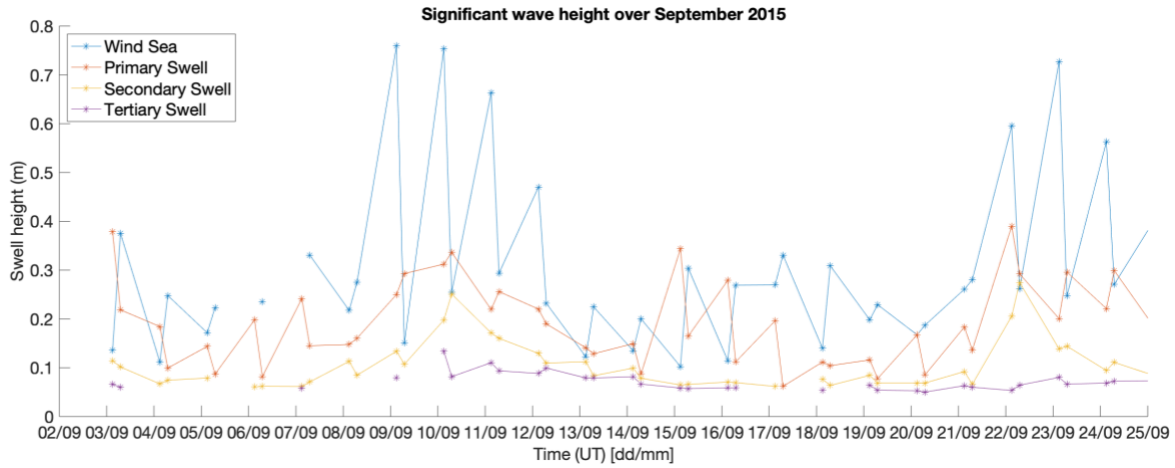

Figure 5.32: Mean significant wave height for the wind sea, primary, secondary and tertiary swells over September 2015 for the range-azimuth bin observed by Alice Springs Beam 5 at a range of 1300-1440 km. Values at 0300 UT and 0700 UT for each day are displayed. Hind cast data from the Centre for Australian Weather and Climate Research [50] was used.

5.4.1.2 Diurnal variation

Diurnal variations in the backscatter coefficient at much larger radio wave frequencies such as in the X-band or Ku-band (8-18 GHz) have been observed in other radar backscatter studies [20]. These diurnal variations were on the order of 1.5 dB. It was suggested that these were due to diurnal temperature changes causing diurnal variations in the soil or vegetation dielectric constant. To investigate any diurnal variations in the backscatter coefficient at HF, the backscatter coefficients from an entire month were superimposed into a single day to create a 2D histogram plot of the backscatter coefficient versus the time of day. Figure 5.33 shows these plots for a single range-azimuth bin over the sea in Beam 1 of the Alice Springs sounder at 1600-1700 km (around 17˚S, 120˚E) and a range-azimuth bin over the land in Beam 1 of the Alice Springs sounder at 1100-1200 km (around 19˚S, 124˚E) for both September 2015 and March 2016. A logarithmic colour scale was used to better visualise the backscatter coefficient variation throughout the day. There did not appear to be a clear diurnal pattern in the backscatter coefficients. It is likely that day-to-day variability, especially over the ocean, would hide any diurnal variation. The absence of night-time data due to the changes in ionospheric propagation conditions meant that only day-time variation in the backscatter coefficient could be investigated.

Over the land in September most of the backscatter coefficients were calculated later in the day due to the ionospheric propagation conditions; this made it difficult to determine any diurnal patterns in the backscatter coefficient as there were few values recorded in the mornings (Figure 5.33 c). In general, most of the backscatter coefficients were calculated using ionograms from around 0600 to 1000 UT; there was better ionospheric propagation conditions in the afternoon so the size of the F2 low region of the backscatter ionograms was larger. In March the backscatter coefficient appeared to slightly decrease in the afternoon, although it was unclear if this was due to the increased number of data points increasing the spread in the results (Figure 5.33 d).

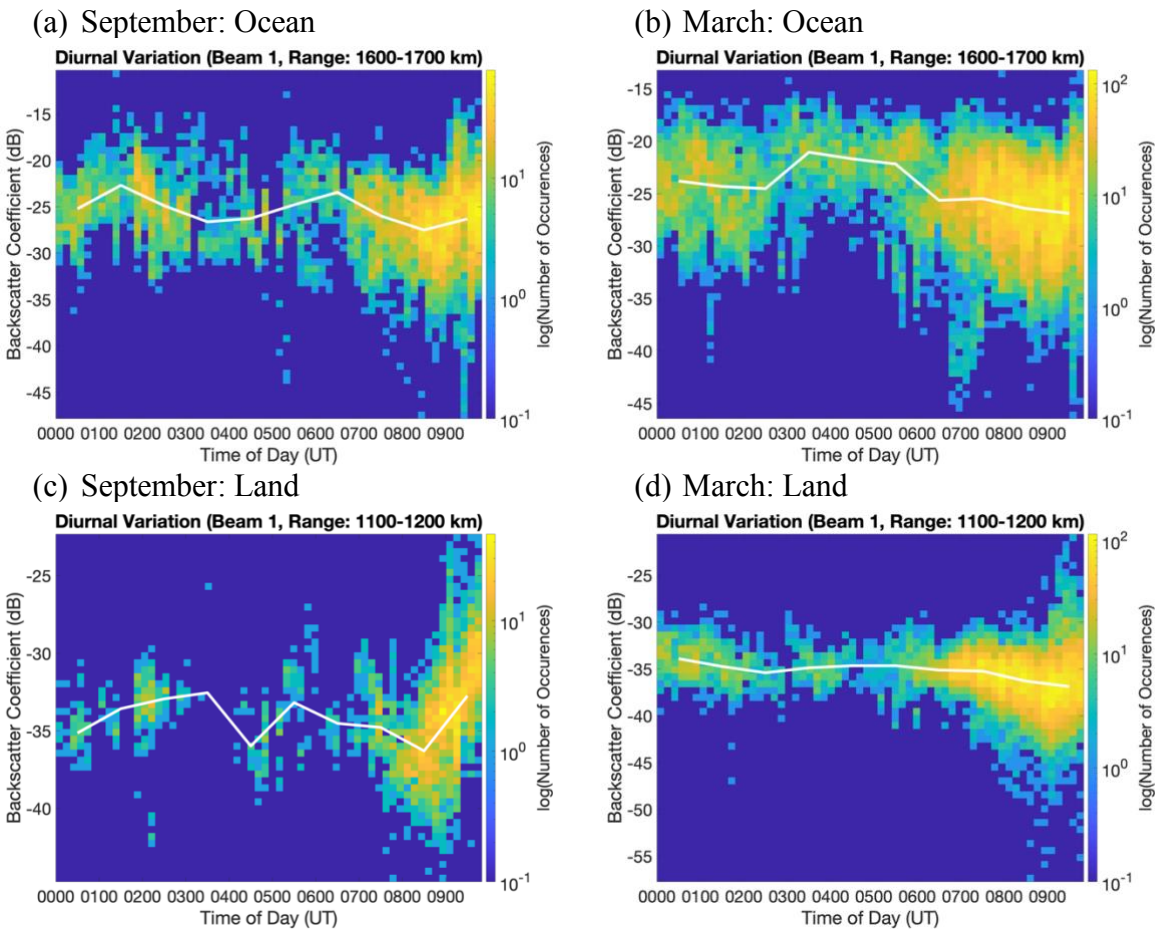

Figure 5.33: 2D histograms of the backscatter coefficient from the Alice Springs results throughout a month, plotted against the time of day. The median backscatter coefficient for each hour is plotted over the top in white. An area of the ocean at around 17˚S, 120˚E in September (a) and March (b) and an area of land at around 19˚S, 124˚E in September (c) and March (d) were investigated. Note: 0000 UT corresponds to approximately 0930 local time.

The median backscatter coefficient for each hour of the day was plotted against the time of day for 16 locations observed by the Alice Springs sounder to investigate the diurnal variation over a representative broad selection of regions (Figure 5.34). Again, a clear diurnal pattern in the backscatter coefficient was not observed; however, there did appear to be a weak peak in the sea backscatter coefficient in March at around 0500 UT which may indicate there was some diurnal pattern in the sea conditions in March (seen in the dashed lines in Figure 5.34, middle panel).

Alice Springs (September)

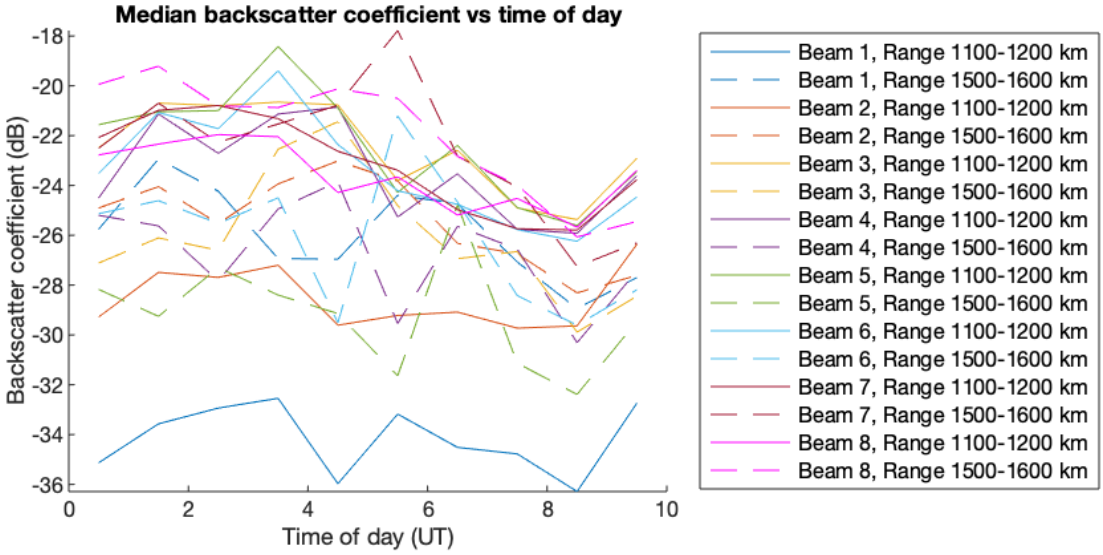

Alice Springs (March)

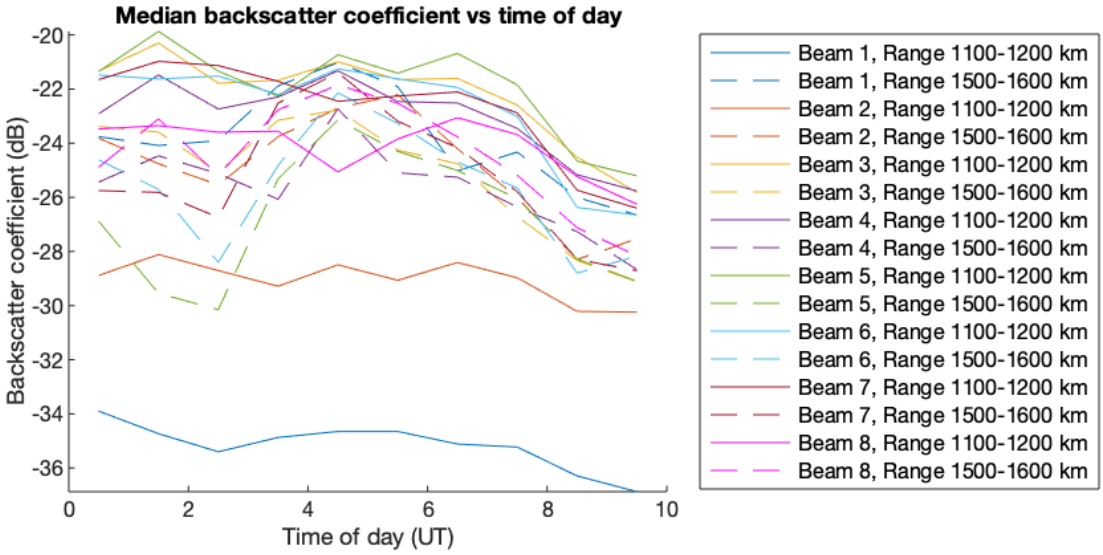

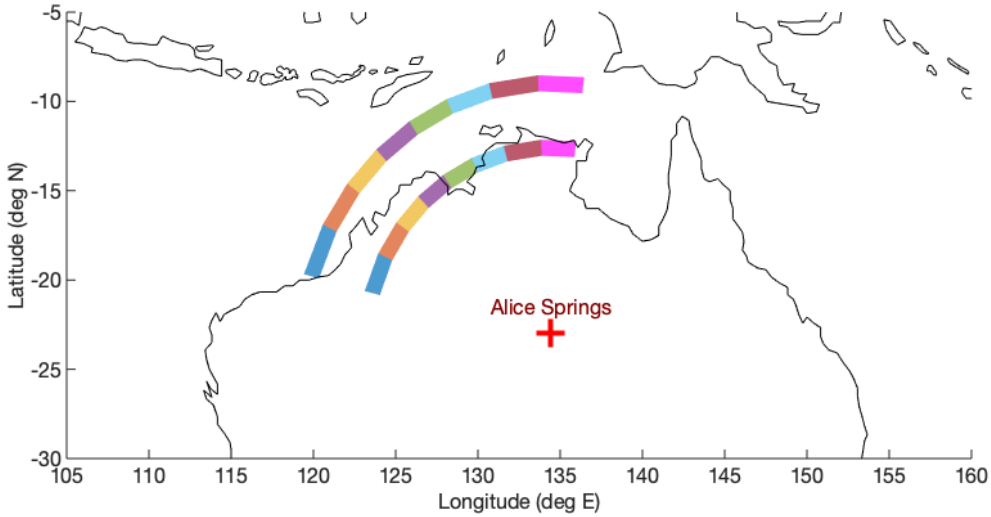

Figure 5.34: Plots of the median backscatter coefficient for each hour versus the time of day for 16 locations viewed by the Alice Springs sounder in September 2015 (top) and March 2016 (middle). The bottom image shows the locations that were used.

5.4.1.3 Seasonal variation

To investigate any seasonal variations in the backscatter coefficients, the monthly median values for each location at the end of the dry season in September 2015 and at the end of the wet season in March 2016 were compared (Figure 5.35). This figure shows that the sea backscatter coefficients changed with the different seasons which was due to the sea state. This figure also shows that there was much less variability in the land backscatter coefficient between seasons.

For the Alice Springs sounder, there was little difference in the land backscatter coefficients of mainland Australia between September 2015 and March 2016; the difference was typically within ±2 dB. However, there were significant differences in the sea backscatter coefficients between these months. In September the backscatter coefficients of the sea along the coast of Australia were around 3 dB higher than in March, but the backscatter coefficients of the Indian Ocean were much lower (around 8 dB lower).

For the Longreach sounder, the differences in the land and the sea backscatter coefficients between these months were not so clear. The September backscatter coefficient results were larger than the March results everywhere; this seasonal difference was not seen in the Alice Springs results for the same patches of ground and it is not obvious why there would be an aspect dependence. An examination of the power in the Longreach observed backscatter ionograms (not shown here) indicates there was a difference in the power in the ionograms between September 2015 and March 2016. This difference could be due to a problem with the Longreach sounder; however, the sounder status logs indicate there was no difference in the power transmitted between September and March, so this seems unlikely. One possible explanation for the lower power in March may be that there was increased ionospheric absorption that was not accurately modelled. However, some of this difference could also be seen when the sea backscatter coefficients were calculated from theory using the wave spectrum method (see Section 5.3.1) which suggests that, at least over the ocean, in beams 4, 5 and 6 this difference between the months could be physical. Over Australia and New Guinea, the difference between the September and March results tended to be around 4 dB with the exception of Cape York, where the September and March values were within around 1-2 dB. The sea values around New Guinea and the Gulf of Carpentaria were much higher in September than in March (around 7 to 8 dB larger), while the sea between Western Australia and Timor was fairly similar for both these months.

To determine if these seasonal differences are regularly seen, a study of the backscatter coefficients over a longer period, preferably a decade, is required.

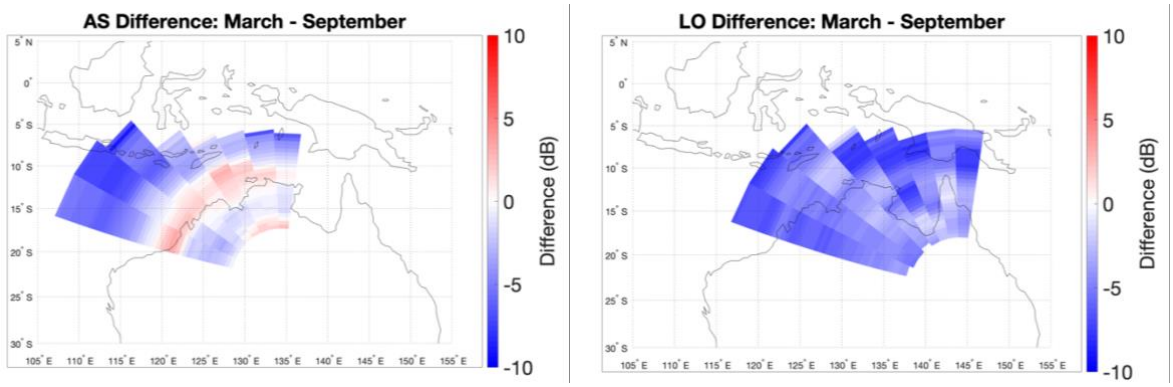

Figure 5.35: Difference in the monthly median backscatter coefficient between the dry and wet seasons (March 2016 – September 2015). Left: Alice Springs, Right: Longreach.

5.4.2 Frequency

The backscatter coefficient is expected to vary with radio wave frequency. This is because the absorption of radio waves at a surface with a given conductivity and permittivity is dependent on the radio wave frequency [69]. The relative roughness of surfaces to radio waves of a particular frequency is also dependent on the frequency; surfaces are considered rough if the structure of the surface has features of a size comparable to the radio wavelength [22]. The relationship between the frequency and the backscatter coefficient was difficult to determine due to the limited number of frequencies used.

To investigate the frequency dependence of the backscatter coefficient, the frequency of the ray reaching each location was plotted against the backscatter coefficient calculated for that location. Figure 5.36 and Figure 5.37 show this plot in the form of a 2D histogram using all of the September 2015 and March 2016 Alice Springs results respectively. Most of the data is in a small frequency band (16 - 22 MHz) as the one-hop F2 low region of the backscatter ionograms was generally largest at this frequency. No clear trend between the backscatter coefficient and the frequency was found. This is not surprising as only a small range of frequencies were able to be used, so the variance in the backscatter from different locations and angles of incidence of the radio waves obscures any relationship.

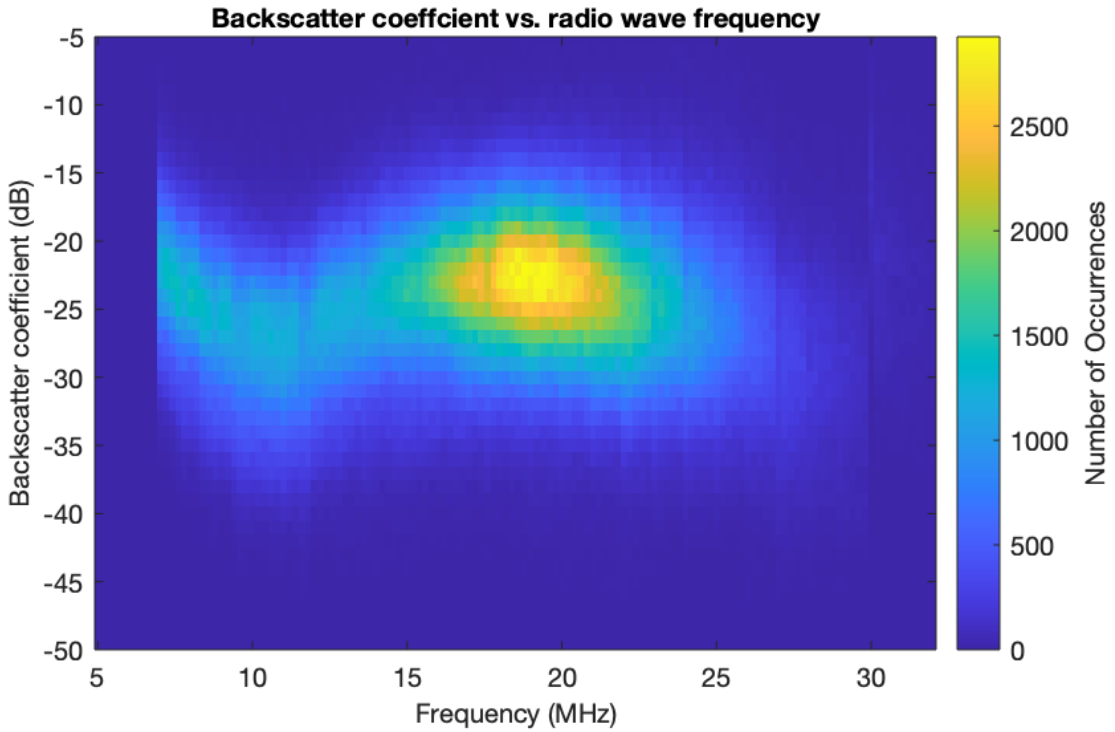

Figure 5.36: Backscatter coefficient vs. radio wave frequency for all of the backscatter values calculated in September 2015 for the Alice Spring sounder.

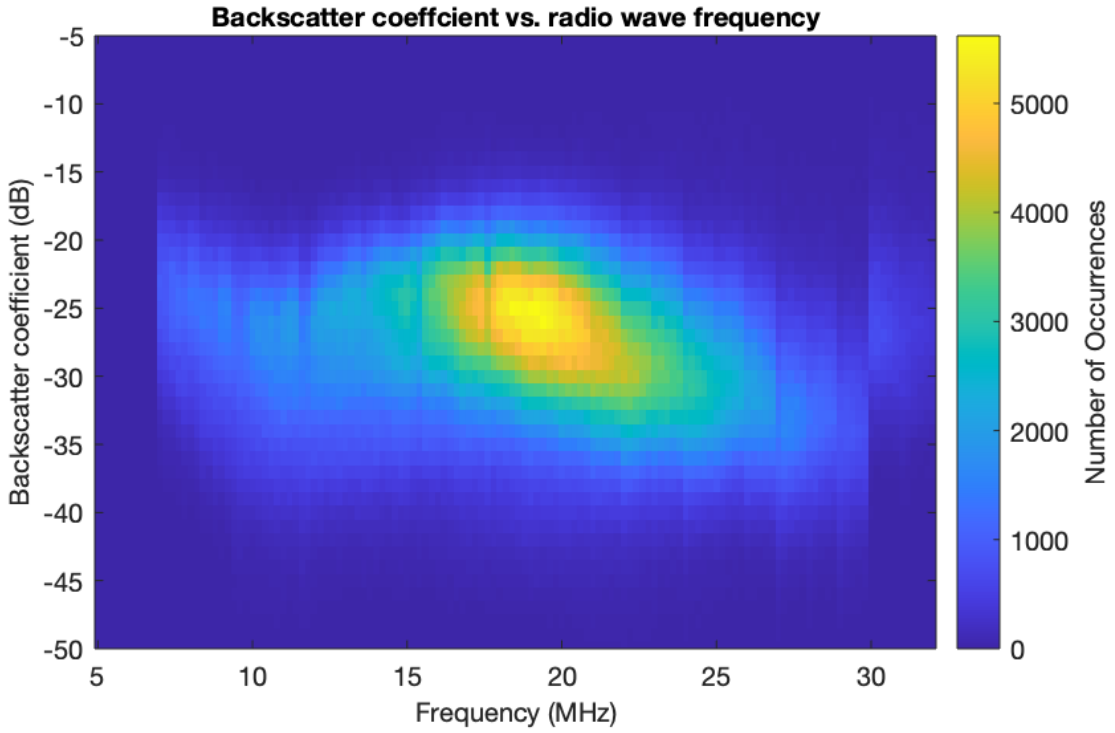

Figure 5.37: Backscatter coefficient vs. radio wave frequency for all of the backscatter values calculated in March 2016 for the Alice Spring sounder.

To ensure that any effect of the frequency on the backscatter coefficient was not being obscured by the differences in the elevations of the rays or the surface properties, the data was

restricted to include only rays with an elevation between 14 and 16 degrees for a single location (the Great Sandy Desert). Figure 5.38 displays the results. A Pearson linear correlation test was conducted to test the null hypothesis that there was no relationship between the radio wave frequency and the backscatter coefficient. A correlation coefficient of -0.66 with a very low p value close to zero was found. The very low p value indicates that the null hypothesis of no correlation was rejected, and the correlation coefficient indicates a moderate negative correlation. It is possible that this negative correlation could indicate a radio wave elevation dependence rather than a frequency dependence, as the elevation of the radio waves decreases as the frequency increases.

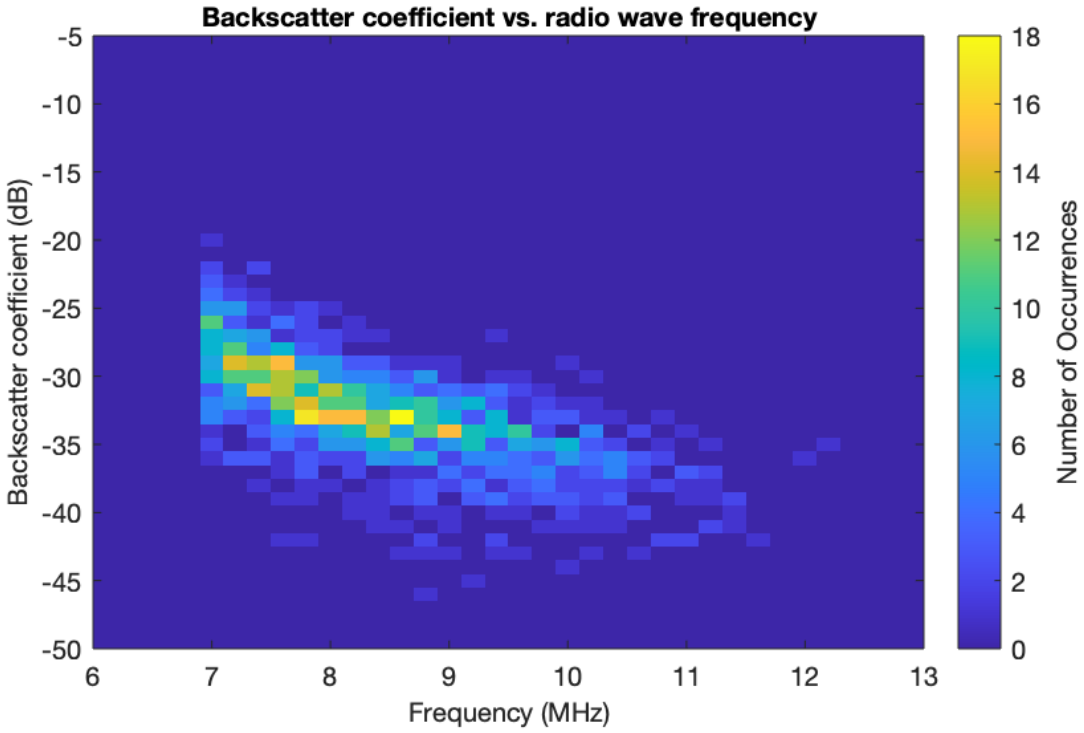

Figure 5.38: Backscatter coefficient vs. radio wave frequency for rays with elevations of 14-16 degrees, scattering from the Great Sandy Desert back to Alice Springs (using the September 2015 results).

5.4.3 Topography

5.4.3.1 Angle of Incidence

The incidence angle of a ray was defined as the angle between the direction of the ray and the normal to the surface. Barrick [23] suggested that the backscattered power from a surface depends on the grazing angle (the angle between the surface and the ray) to the fourth power. Hence, it was expected that the backscatter coefficient would increase as the angle of incidence decreased.

A study on the angular response of the backscatter coefficient at 1-7 GHz over soils of different roughness found that at nadir the backscatter coefficient was strongly dependent on the surface roughness (described by the RMS height) [70]. At the lowest frequency they used (1.1 GHz) the backscatter coefficient varied as a function of the angle of incidence of the radio waves and, furthermore, this variation was dependent on the surface roughness. Over smoother

surfaces, the backscatter coefficient was sensitive to changes in the incidence angle, while changes in the incidence angle over rough surfaces had little effect on the backscatter coefficient. In this section the variation of the backscatter coefficient with incidence angle at HF is investigated.

To calculate the angle of incidence, the ray elevation and the ETOPO1 global relief model [51] were used. The ETOPO1 surface elevation data had a resolution of 1 arcminute (around 2 km). The mean ray elevation reaching a given range and the mean surface normal of that section were used to calculate the angle of incidence. As Australia is relatively flat the angle of incidence was dominated by the ray elevation which decreases with range, rather than changes in the surface normal (Figure 5.39).

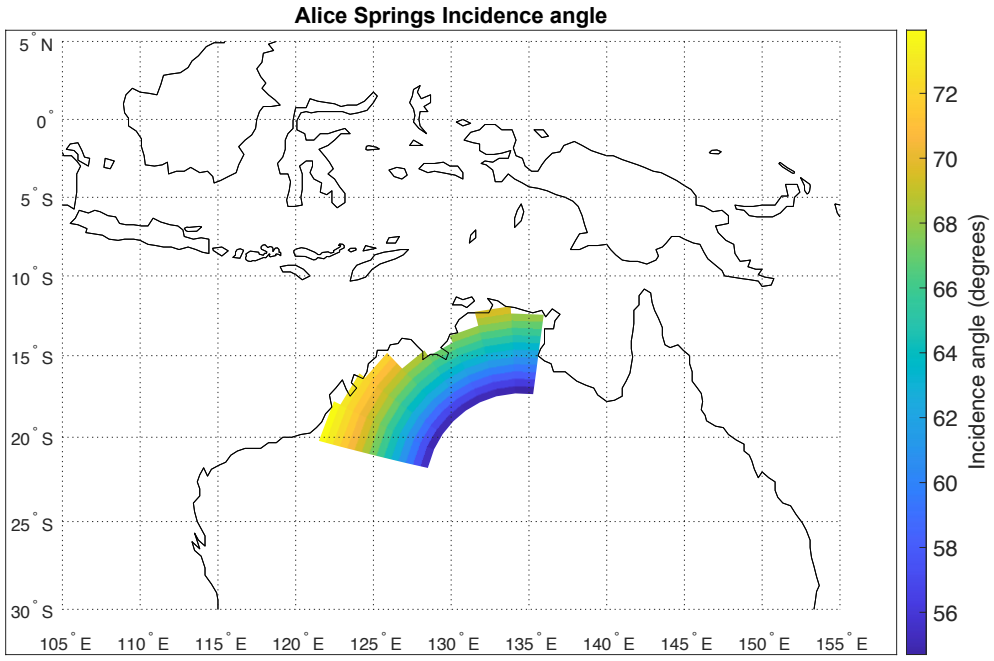

Figure 5.39: Monthly mean incidence angle of rays from Alice Springs, calculated using the ray elevation and land topography.

The backscatter coefficient was plotted against the monthly mean incidence angle for each of the Alice Springs sounder's beams (Figure 5.40). It was expected from Barrick [23] that the backscatter coefficient would increase as the incidence angle decreased. In general, this trend was not observed and is probably due to the other surface parameters that could affect the backscatter coefficient. It is noted this trend was seen in the Beam 1 results over the Great Sandy Desert. The composition of the land viewed by Beam 1 was fairly similar over all ranges, consequently reducing the effects of any differences in the backscattered power due the surface composition. However, the Beam 2 results showed little variation in the backscatter coefficient with changes in the ray elevation and, furthermore, results for other beams show a maximum in the backscatter coefficient for incidence angles around 65 degrees. This could be due to rays at lower incidence angles (closer ranges) backscattering from more desert-like areas which tend

to have low backscatter coefficients, whereas as the high incidence angle rays reach the highly vegetated rain forested regions of Northern Australia. This will be explored in Section 5.4.5. The limited number of angles of incidence (a range of 20 degrees from 55 - 75 degrees) also made it difficult to draw any conclusions on the relationship between the angle of incidence and the backscatter coefficient.

The backscatter coefficient was also plotted against the incidence angle for each of the Longreach sounder's beams (Figure 5.41). Again, it was difficult to draw conclusions on the relationship between the backscatter coefficient and the incidence angle from these results. For beams 1 and 2, a minimum in the backscatter coefficient was observed for incidence angles around 70 to 75 degrees. These incidence angles corresponded to the rays that were scattered back from the Tanami desert. The lower backscatter coefficient usually seen over desert regions likely caused this minimum. There are few data points for beams 4, 5 and 6 because these beams observe little land, they mostly observe the Gulf of Carpentaria and the sea. The backscatter coefficient appears to decrease with increasing incidence angle for beam 7. The higher backscatter values of beam 7 and 8 at an incidence angle of around 78 degrees correspond with the higher backscatter coefficients that were found for the New Guinea mountains.

To remove the effects that different surface properties and rays of different frequencies may have on the backscatter coefficient, the analysis was restricted to only those rays reaching a single ground location for a limited range of frequencies. However, when this was done very few rays remained and it was impossible to draw conclusions about the effect of the angle of incidence on the backscatter coefficient. Overall, due to the limited range of incidence angles for rays reaching each location, a definitive relationship between the angle of incidence and the backscatter coefficient was not able to be determined.

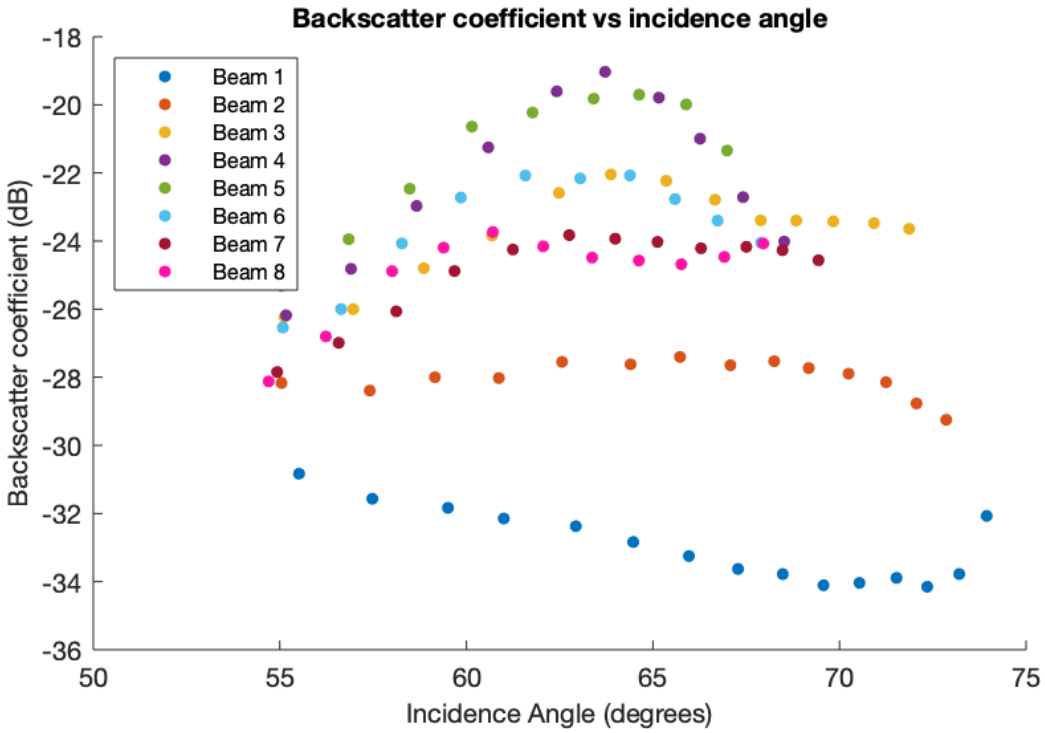

Figure 5.40: Backscatter coefficient versus incidence angle for the Alice Springs September 2015 results.

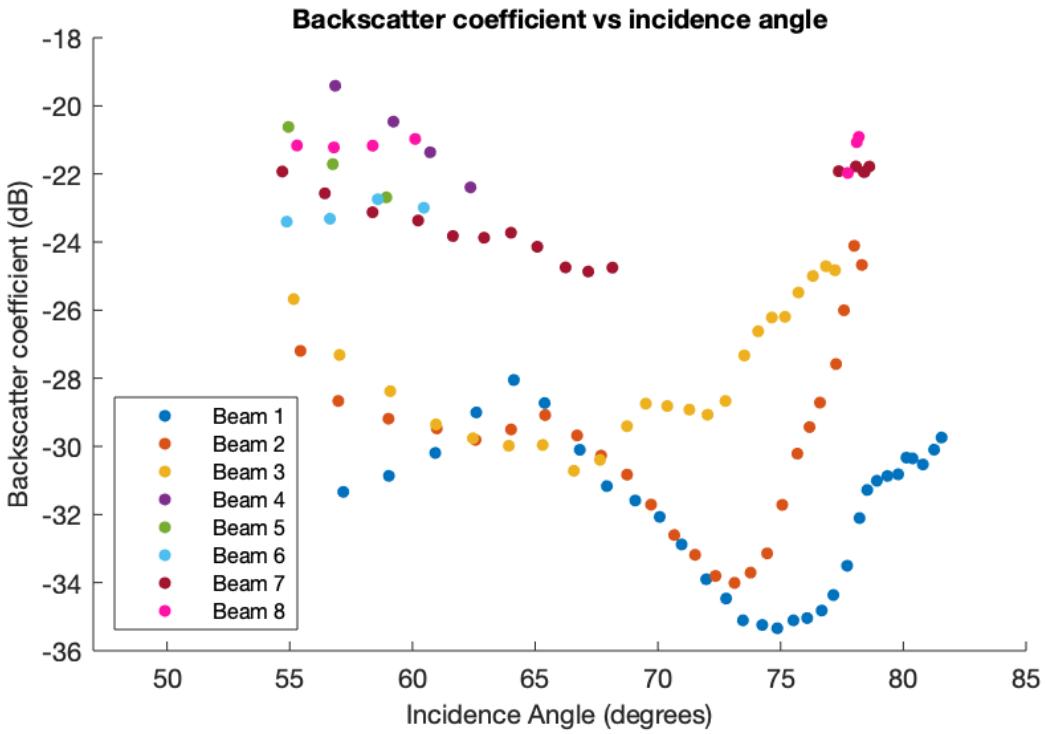

Figure 5.41: Backscatter coefficient versus incidence angle versus for the Longreach September 2015 results.

5.4.3.2 Aspect sensitivity

In general, different backscatter coefficient values were obtained when a location was viewed from different directions, indicating that there was an aspect dependence in the backscatter coefficient. This was expected as there would potentially be different faces of the

surface for the rays to scatter from. For example, it was expected that a mountain range or cliff face oriented perpendicularly to the direction of propagation of the rays would cause more backscatter than if the mountain range was oriented parallel to the direction of propagation of the rays.

Backscatter sounder beams from Alice Springs, Longreach and Laverton East all intersected at 15.7˚S, 130˚E (Figure 5.42). The Laverton data was examined for this case purely for the aspect reasons, even though it was stated earlier that the Laverton data wouldn't be considered further. This location was around 900 km from Alice Springs, 1585 km from Laverton and 1760 km from Longreach. At this location low hills and valleys run northeast to southwest, which is approximately perpendicular to the direction of the Alice Springs and Longreach beams and parallel to the direction of the Laverton East beam (see Figure 5.43). Hence, if topography was the major factor which affects the backscatter coefficient, it would be expected that the backscatter coefficient of this location when viewed from Alice Springs and Longreach would be greater than when viewed from Laverton East.

Histograms of the backscatter coefficient for this location in September 2015 when viewed by each of the sounders is shown in Figure 5.44. The backscatter coefficient was largest when viewed from Alice Springs (median value was -21.6 dB), and lowest when viewed from Longreach (median value was -25.7 dB) with the backscatter coefficient observed by Laverton East (median value of -22.3 dB) falling in between these values. The large spread in the Laverton East histogram is likely due to the issues noted earlier with the Laverton data.

The result displayed in Figure 5.44 was not expected based on the alignment of the terrain. However, the elevations of the features were not large (see Figure 5.43) so the effect of the topography in this case (in contrast to mountain ranges) may not be the largest contributor to the differences in the backscatter coefficient. The range from each sounder to this location was different, which means that rays of different elevation and frequencies from each sounder were backscattering from the terrain. It is also possible that systematic differences between the sounders not captured by the backscatter sounder model could cause an offset in the calculated backscatter coefficient. In order to distinguish particular topographic features and the differences between the features when viewed from different direction, a higher azimuthal resolution and range resolution in the backscatter coefficient results would be useful.

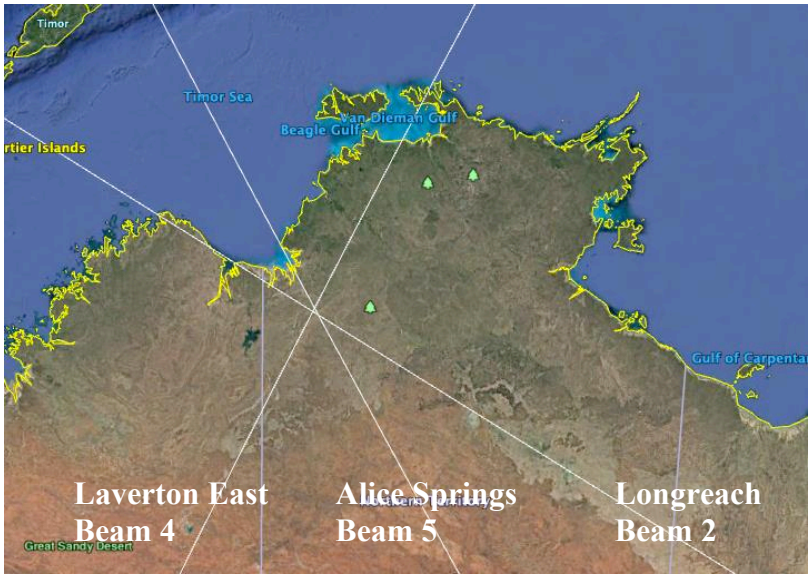

Figure 5.42: The centres of beams from the 3 backscatter sounders intersect near the Auvergne airport in the Northern territory. Image from Google Earth [71].

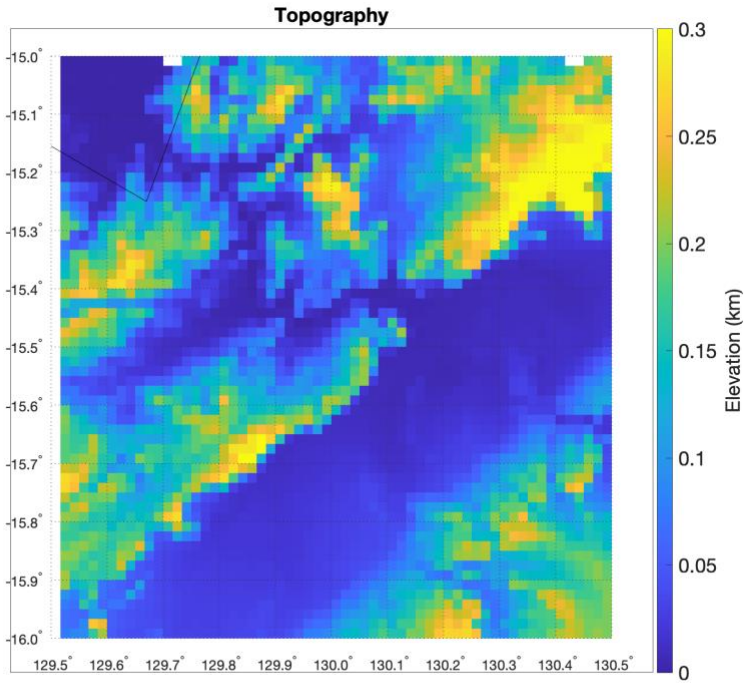

Figure 5.43: Elevation profile of the region where the Alice Springs beam 5, Longreach beam 2 and Laverton East beam 4 intersect.

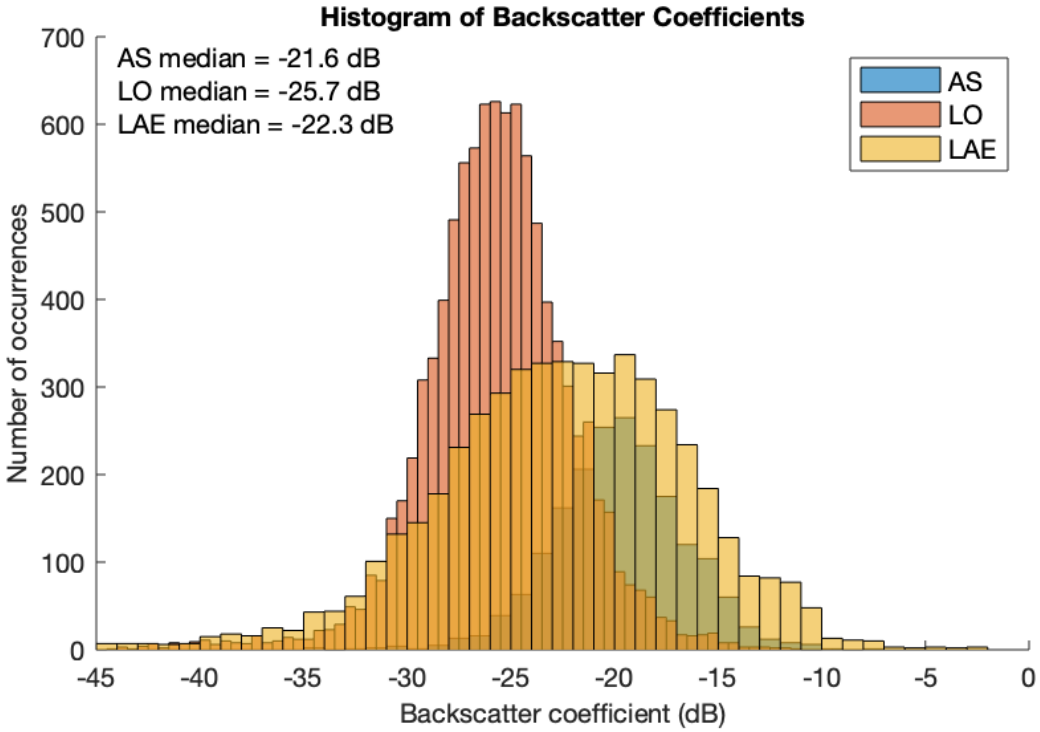

Figure 5.44: Histograms of the backscatter coefficient from each sounder in September 2015 at around 16 ˚S, 130 ˚E, where beams from three sounders intersect in Northern Australia.

The Great Sandy Desert is characterised by sand dunes running from east to west. This region of Australia was observed by the Alice Springs sounder located to the east and the Laverton East sounder located to the south of the desert. The Alice Springs beam 1 and Laverton East beam 2 intersected at around 19˚S, 124˚E (see Figure 5.45). Figure 5.46 shows the elevation profiles for these beams around this location; the Alice Springs elevation profile was a steady downward slope while the Laverton East elevation profile shows the cross section of the sand dunes. This location was a similar distance from each of the sounders; around 1150 km from Alice Springs and around 950 km from Laverton. The elevation profile suggests that the backscatter coefficient of this location would be larger when viewed from Laverton than when viewed from Alice Springs. This was the case, as displayed in Figure 5.47, where the Laverton East backscatter coefficient (median value of -24.5 dB) is around 10 dB higher than the backscatter coefficient measured by the Alice Springs backscatter sounder (median value of -35.7). However, this result must be treated with caution. As discussed earlier the Laverton results may not be accurate as fewer modelled ionograms were retained for analysis and the sea backscatter comparison between the two methods of calculating the backscatter coefficient suggested that there was greater error in the results (see Section 5.3.2).

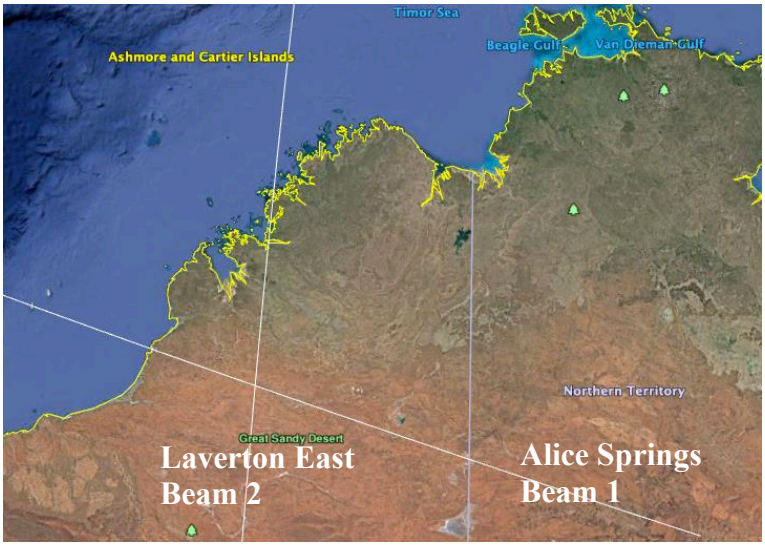

Figure 5.45: The centres of Laverton East Beam 2 and Alice Springs Beam 1 intersect over the Great Sandy Desert. Image from Google Earth [72].

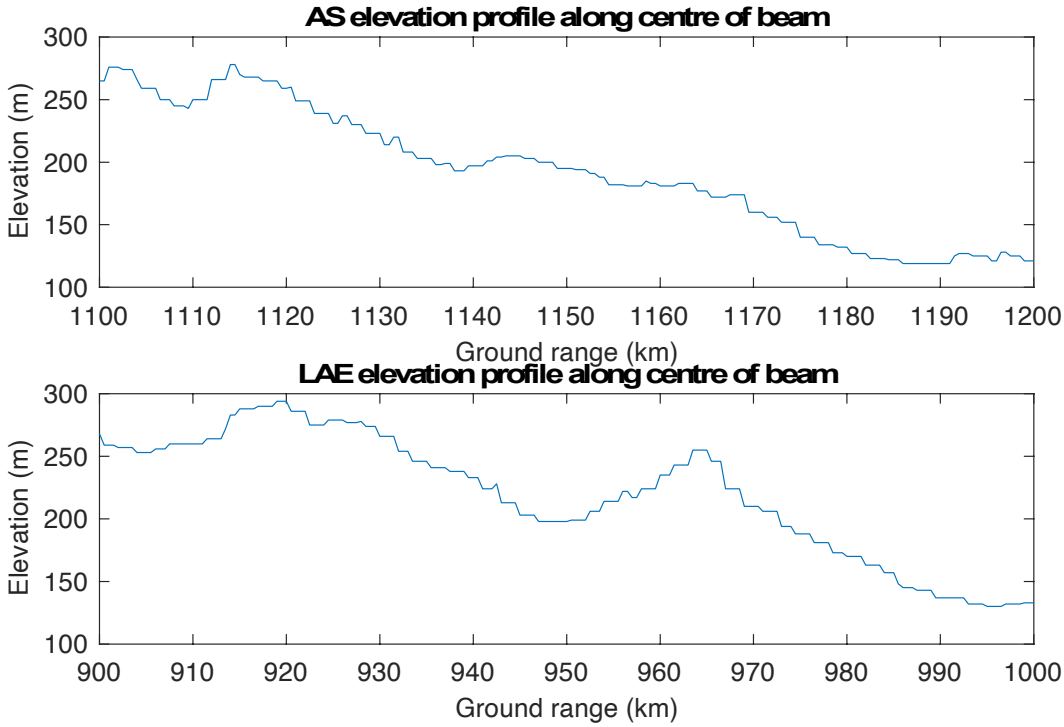

Figure 5.46: Elevation profile along the centre of the Alice Springs beam 1 and Laverton East beam 2 through the area where these beams intersect.

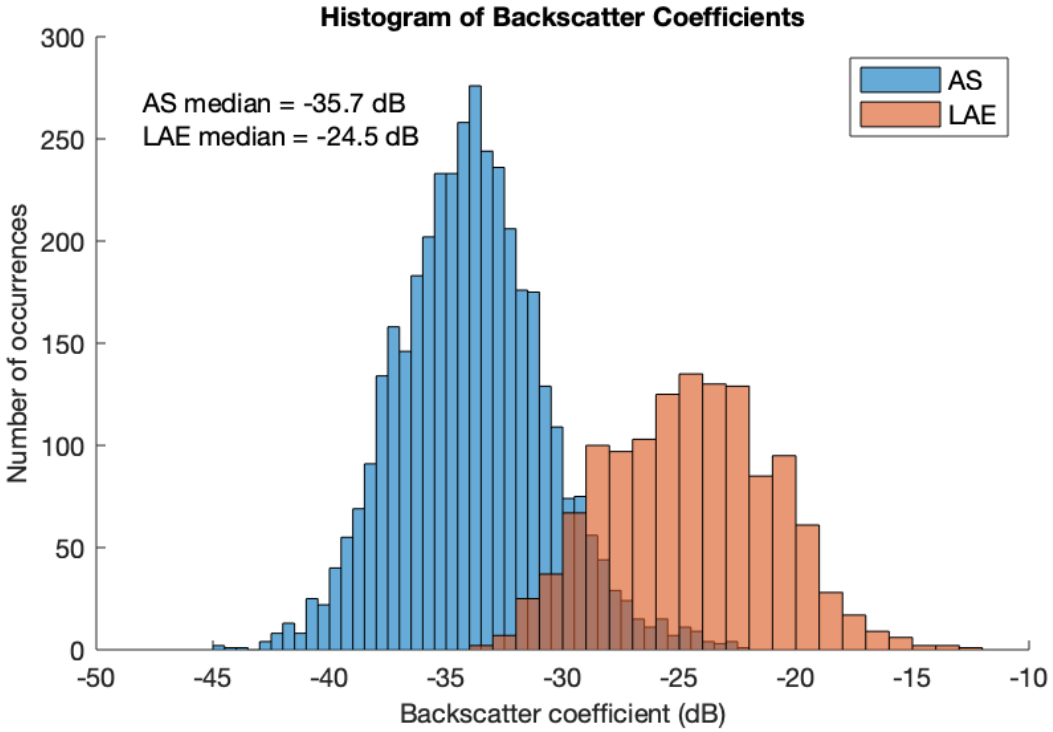

Figure 5.47: Histogram of the backscatter coefficients calculated for a single location (~ 19˚S, 124˚E) viewed by both the Alice Springs and Laverton East sounders in September 2015.

5.4.3.3 Ground Roughness

In the context of radio waves scattering from a surface, the roughness of the surface is dependent on the wavelength of the radiation incident upon it; a surface is considered rough if features of that surface are on the same scale or larger than the radiation wavelength. Barrick and Peake [22] defined surfaces as *very rough* if

$$\frac{2\pi}{\lambda}\zeta \cos\theta_i > 1 \qquad (5.1)$$

and *slightly rough* if

$$\frac{2\pi}{\lambda}\zeta \cos\theta_i < 1 \qquad (5.2)$$

where λ is the signal wavelength, ζ is the mean height of surface variations and θ_i is the angle of incidence of the signal from the mean surface normal. The backscattered power from a very rough surface (primarily due to specular scattering) is strong when radiation is incident near vertical incidence angles but drops off quickly as the angle of incidence approaches grazing [22]. The backscattered power from a slightly rough surface (primarily due to diffuse scattering) is much weaker; however, it does not drop off as rapidly as the angle of incidence approaches grazing [22]. For a composite, which has its roughness defined at two different roughness scales, the backscattered power is dominated by that due to the very rough component of the surface near vertical incidence angles while the scatter due to the slightly rough component is dominant near grazing [22].

Based on Barrick and Peake's work [22], the RMS height of the elevation data was used as a roughness index to characterise the roughness of the scattering surface. This is

commonly used to describe roughness in radar backscatter modelling [73]. While the use of the RMS height in characterising the surface roughness was useful as it provided a single parameter describing a surface, important information about each surface was lost including the slope, shape and regularity of features of the surface.

First, the ETOPO1 global relief model was used to calculate the surface roughness. The RMS height deviation for each location using the available data was then compared to the monthly median backscatter coefficient calculated for each location. Figure 5.48 shows plots of the backscatter coefficient versus the roughness using the Alice Springs and Longreach September and March data. A Pearson correlation test was conducted to test the linear correlation between the roughness and the backscatter coefficient, with the null hypothesis being that there was no relationship between these variables. The results of this test on each of the results are shown in Table 5.5.

The correlation coefficients were in the range 0.27 to 0.37 with P-values from 2.0e-4 to 6.1e-3. Hence, while the null hypothesis that there was no relationship between the roughness and the backscatter coefficient can be rejected, the correlation coefficients indicate that the correlation between the roughness index and the backscatter coefficient is weak. However, this data had a resolution of around 2 km, which was much larger than the wavelengths of interest (10-30 m). To better investigate the effect of the surface roughness on the backscatter coefficient, a roughness index is needed to be calculated at a similar scale size as the radar wavelength. Higher resolution topography data is required for this.

(a) AS September 2015

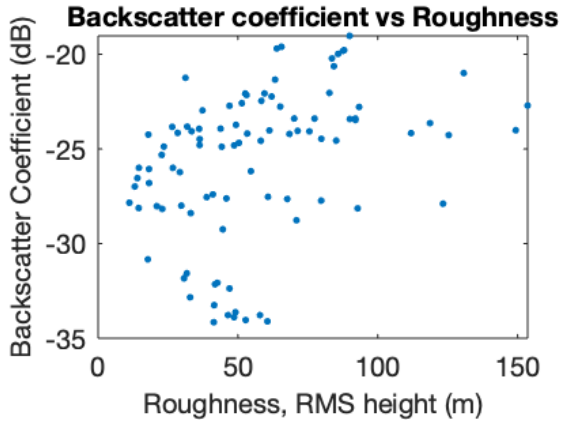

(b) AS March 2016

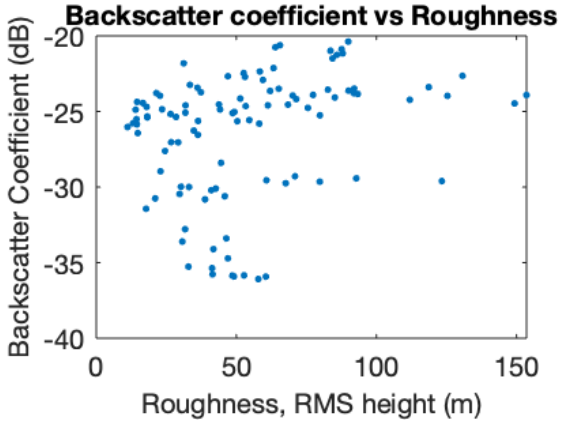

(c) LO September 2015

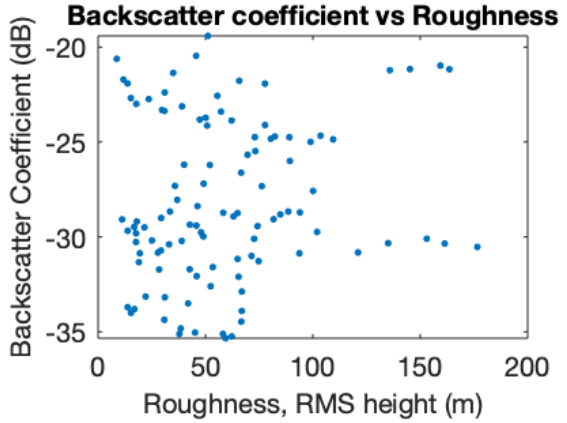

(d) LO March 2016

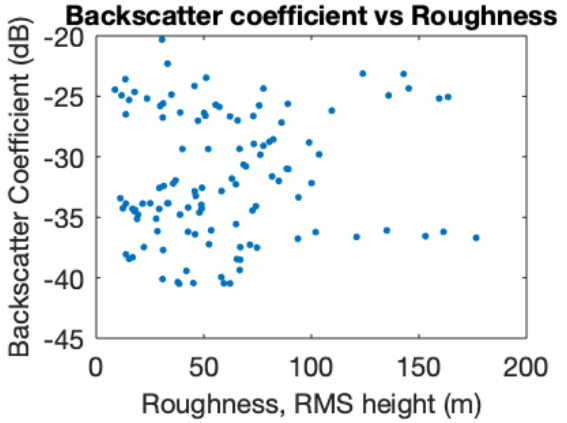

Figure 5.48: Backscatter coefficient versus roughness (RMS height calculated from the ETOPO1 global relief model) from (a) Alice Springs September 2015, (b) Alice Springs March 2016, (c) Longreach September 2015 and (d) Longreach March 2016.

Table 5.5: Roughness (from ETOPO1 data) and backscatter coefficient Pearson correlation test results. The low p values indicate that the null hypothesis of no correlation is rejected for all cases.

	Correlation coefficient	**P value**
Alice Springs Sept 2015	0.37	2.8e-4
Alice Springs March 2016	0.27	6.1e-3
Longreach Sept 2015	0.34	2.0e-4
Longreach March 2016	0.27	2.0e-3

The RMS height was then calculated for each range-azimuth bin using the SRTM 1 arc-second digital elevation model [52]. This data had a resolution of around 30 metres, and so was on a similar scale to the radar wavelengths used. The RMS height for each section was compared to the backscatter coefficient for that range-azimuth bin (Figure 5.49). Again, a Pearson correlation test was conducted to test the null hypothesis that there was no relationship between the roughness and the backscatter coefficient. The results of this test are shown in Table 5.6. The results were very similar to when the lower resolution elevation data was used. However, the Longreach P-values were greater than 0.05 which means that the null hypothesis

that there is no correlation between the roughness and backscatter coefficient cannot be rejected at the 95% confidence level. The correlation test results show that the RMS height was not strongly correlated to the backscatter coefficient.

Mainland Australia is relatively flat; there are no great mountain ranges or other features in the areas observed that could cause large RMS height deviations. This limited range of roughness values may be one reason why little correlation was seen between the RMS height deviation and the backscatter coefficient.

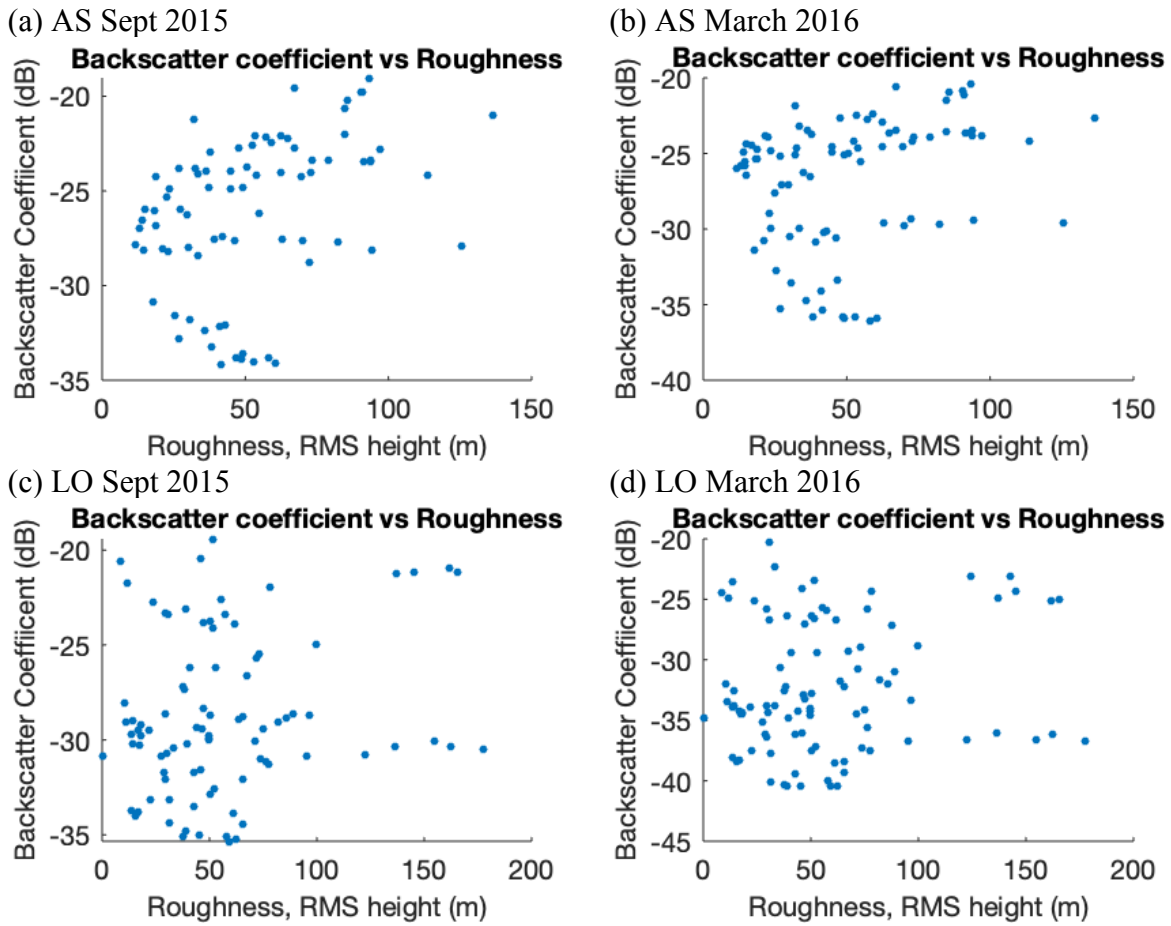

Figure 5.49: Roughness (RMS height calculated from SRTM DEM-H data) versus the backscatter coefficient from (a) Alice Springs September 2015, (b) Alice Springs March 2016, (c) Longreach September 2015 and (d) Longreach March 2016.

Table 5.6: Roughness (from SRTM DEM-H data) and backscatter coefficient Pearson correlation test results. The p values for Longreach indicate that the null hypothesis of no correlation is unable to be rejected at a significance level of 0.05.

	Correlation coefficient	**P value**
Alice Springs Sept 2015	0.38	4.82e-4
Alice Springs March 2016	0.25	0.021
Longreach Sept 2015	0.20	0.067
Longreach March 2016	0.14	0.17

5.4.4 Soil moisture

Changes in soil moisture affect the conductivity and relative permittivity of the land. As the soil moisture increases, the soil becomes more conductive and this affects the radio wave reflectivity of the surface. A surface with an increased conductivity will reflect a greater amount of energy from the incident radio waves. Hence it was expected that increases in the soil moisture would increase the backscatter coefficient.

To investigate the effect of soil moisture on the backscatter coefficient, soil moisture data throughout the months of interest was obtained from the NASA National Snow and Ice Data Centre [53]. There was very little rain over Northern Australia in September 2015 as this was during the dry season, so the soil moisture remained low and relatively constant throughout the month. However, in March 2016 there was a considerable amount of rainfall as this was at the end of the wet season, so the soil moisture was higher than in September 2015 and changed throughout the month. Figure 5.50 and Figure 5.51 show the mean soil moisture in the months of September 2015 and March 2016. The median backscatter coefficient of each range-azimuth bin was plotted against the mean soil moisture of the range-azimuth bin for both months to investigate if there was a correlation between these parameters (Figure 5.52). Differences in the land surfaces across Australia such as the type of material, roughness and vegetation coverage which could also affect the backscatter coefficient are likely to introduce scatter in the backscatter coefficient versus soil moisture plots.

A Pearson linear correlation test was done to test the null hypothesis that the soil moisture and backscatter coefficient were not related. The results of this test are shown in Table 5.7, with correlation coefficients ranging from 0.39 to 0.76. The P-values were less than 0.05, so the null hypothesis for all cases was rejected at the 95% confidence level.

During September 2015 there was a smaller range of soil moisture values than in March because this was during the dry season, so the soil moisture was fairly low across Australia. The higher soil moisture values seen in the Longreach results are from New Guinea. A moderate positive correlation was seen in the September results for both Longreach and Alice Springs. During March 2016 there was a larger range of soil moisture values across Australia because the amount of rainfall varied across regions. A stronger positive correlation was seen in the March results for both Longreach and Alice Springs. The positive correlation that was found between the backscatter coefficient and the soil moisture may simply be due to increasing soil moistures increasing the reflectivity of the ground and hence increasing the backscatter coefficient, or it may be due to areas of higher soil moisture also having an increased surface roughness or providing suitable conditions for vegetation to grow which could affect the backscatter coefficient.

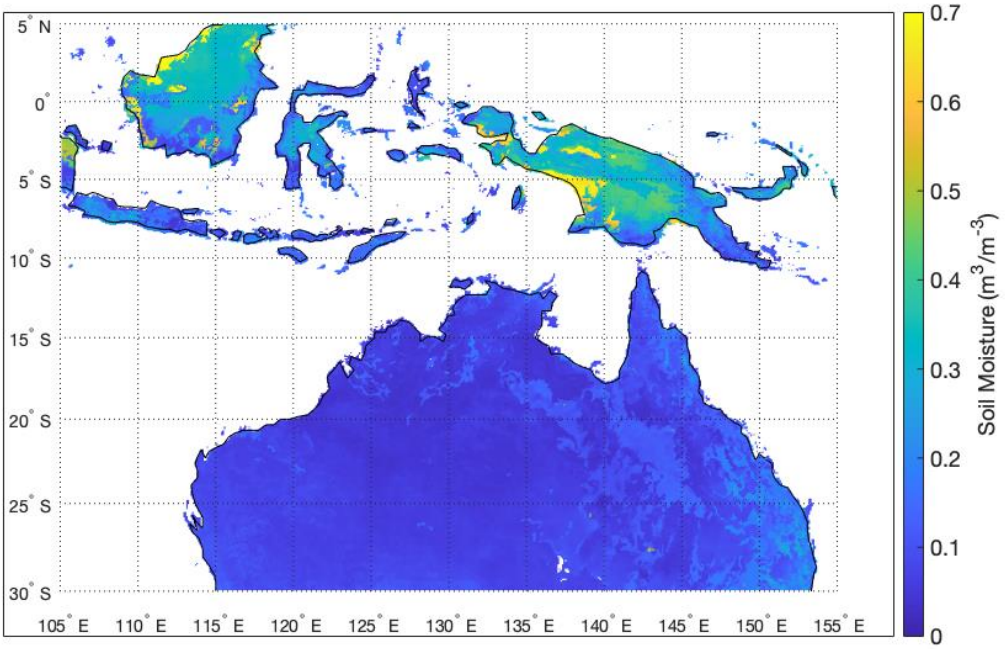

Figure 5.50: Mean soil moisture in September 2015.

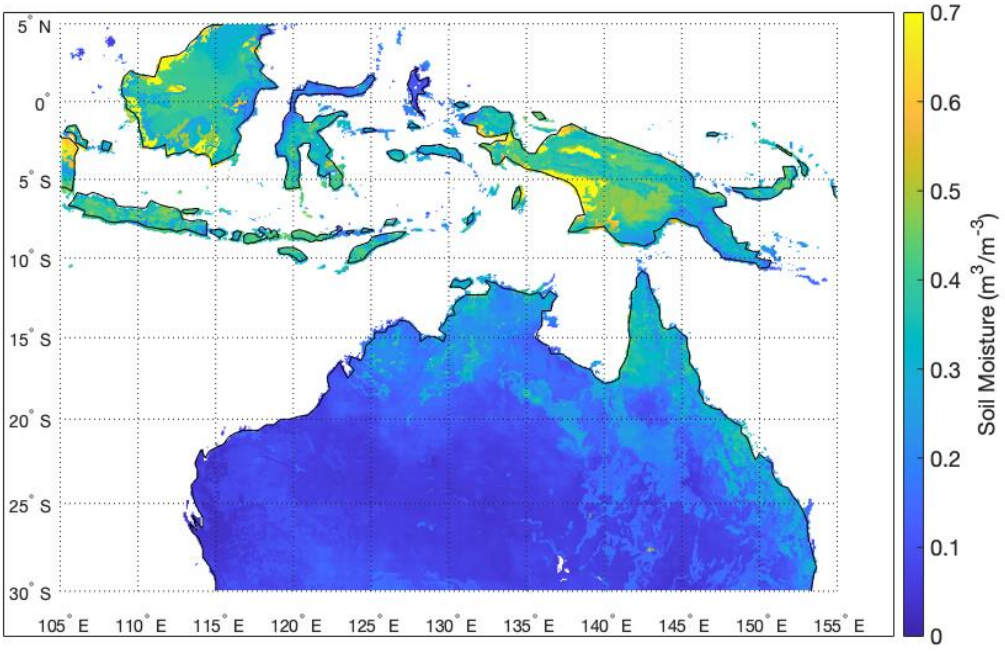

Figure 5.51: Mean soil moisture in March 2016.

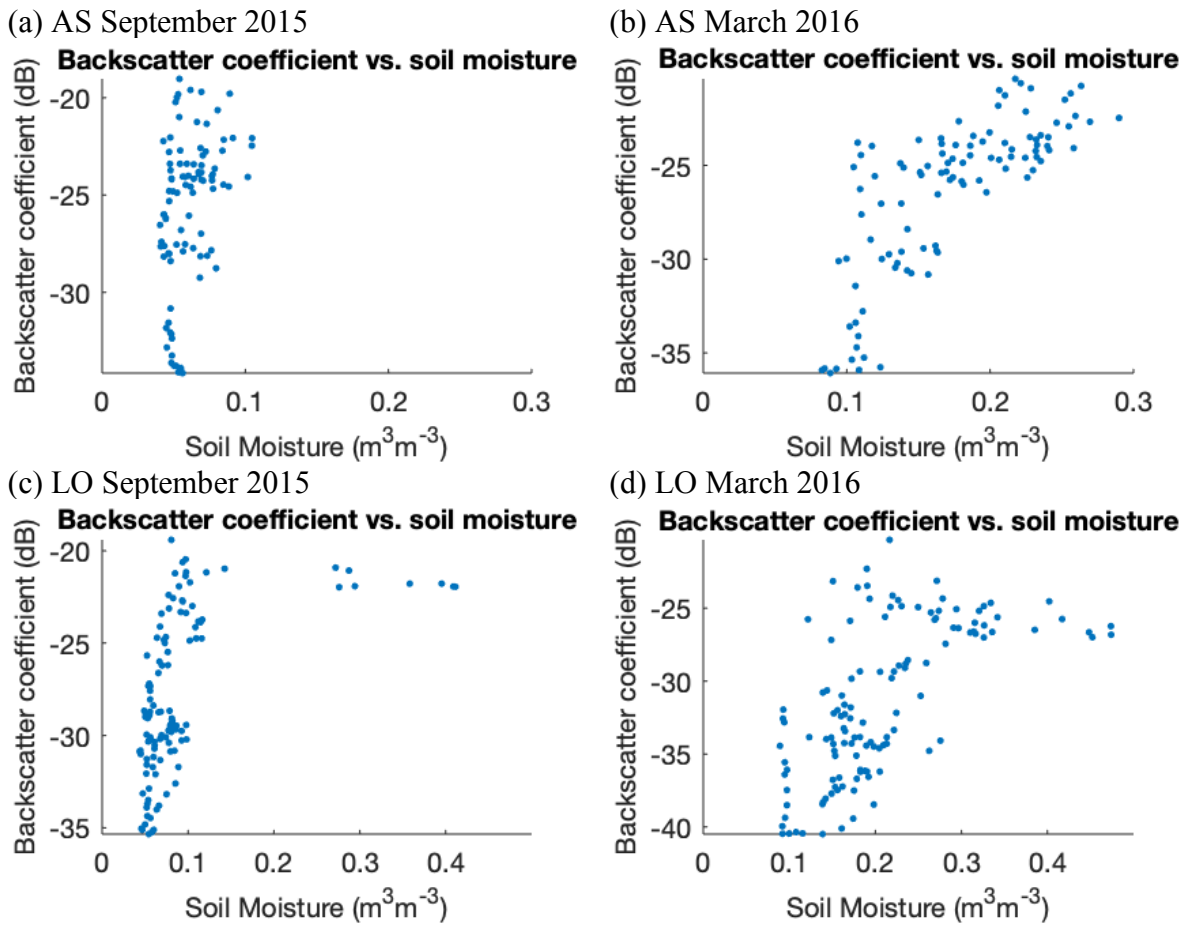

Figure 5.52: Plots of the monthly median backscatter coefficient versus the mean soil moisture for (a) Alice Spring September 2015, (b) Alice Spring March 2016, (c) Longreach September 2015 and (d) Longreach March 2016.

Table 5.7: Soil moisture and backscatter coefficient Pearson correlation test results. The low p values indicate the null hypothesis of no correlation is rejected.

	Correlation coefficient	**P value**
Alice Springs Sept 2015	0.39	1.2e-4
Alice Springs March 2016	0.76	1.3e-20
Longreach Sept 2015	0.53	2.3e-9
Longreach March 2016	0.63	2.3e-15

During March 2016, at the end of the wet season, the soil moisture varied throughout the month due to the appreciable but variable amount of rainfall. Consequently, it was possible to investigate how changes in the soil moisture affected the backscatter coefficient at a single location, thereby reducing the impact of other surface variables on the results. For each 100 km range-azimuth bin, the mean soil moisture and 3-hourly median backscatter coefficient was calculated at three times (0130 UT, 0430 UT and 0730 UT) for each day of the month. A Pearson correlation test was then conducted for each range-azimuth bin, testing the null hypothesis that there was no relationship between the backscatter coefficient and the soil moisture. Plots for two locations have been included as examples; the Great Sandy Desert (around 19˚S, 123˚E) (Figure 5.53) and Arnhem Land (around 13˚S, 135˚E) (Figure 5.54). For

the Great Sandy Desert, the correlation coefficient was 0.35 and the P value was 0.028, while for Arnhem Land, where the soil moisture content had greater variation, the correlation coefficient was -0.036 and the P value was 0.82. In both cases the p-values indicate the null hypothesis cannot be rejected and, further, for Arnhem Land the correlation coefficient was close to zero. Hence, for these two samples, it appears that the backscatter coefficient was not correlated to the soil moisture.

Figure 5.55 displays the Pearson correlation test results for all range-azimuth bins during March 2016 for the Alice Springs and Longreach sounders. A histogram of all the correlation coefficients is shown in Figure 5.56. The median correlation coefficient was 0.13, which indicates the backscatter coefficient does not have a strong relationship with the soil moisture. The P-value was greater than 0.05 for 17 out of 21 of the Alice Springs range-azimuth bins and 30 out of the 36 of the Longreach range azimuth bins. Hence, the null hypothesis that there was no correlation between the soil moisture and the backscatter coefficient was unable to be rejected for most of the range-azimuth bins. Changes in the soil moisture throughout the month within each range-azimuth bin were not large despite the variable amount of rainfall; the median of the spread in the soil moisture values (the difference between the maximum and minimum moisture values for a given range-azimuth bin) for all the Alice Springs and Longreach range-azimuth bins during March 2016 was low at 0.13 m^3m^{-3} (see Figure 5.57). Hence, any affect the change in soil moisture had on the backscatter coefficient may be hidden by the variance in the backscatter coefficient introduced by limitations of the methodology. A stronger positive correlation was seen only once the results from all of the range-azimuth bins were aggregated, as shown in Figure 5.52. However, as stated earlier, it is possible that the correlation seen when all range-azimuth bins were aggregated was due to other features of the surface such as areas of higher soil moisture also having more vegetation.

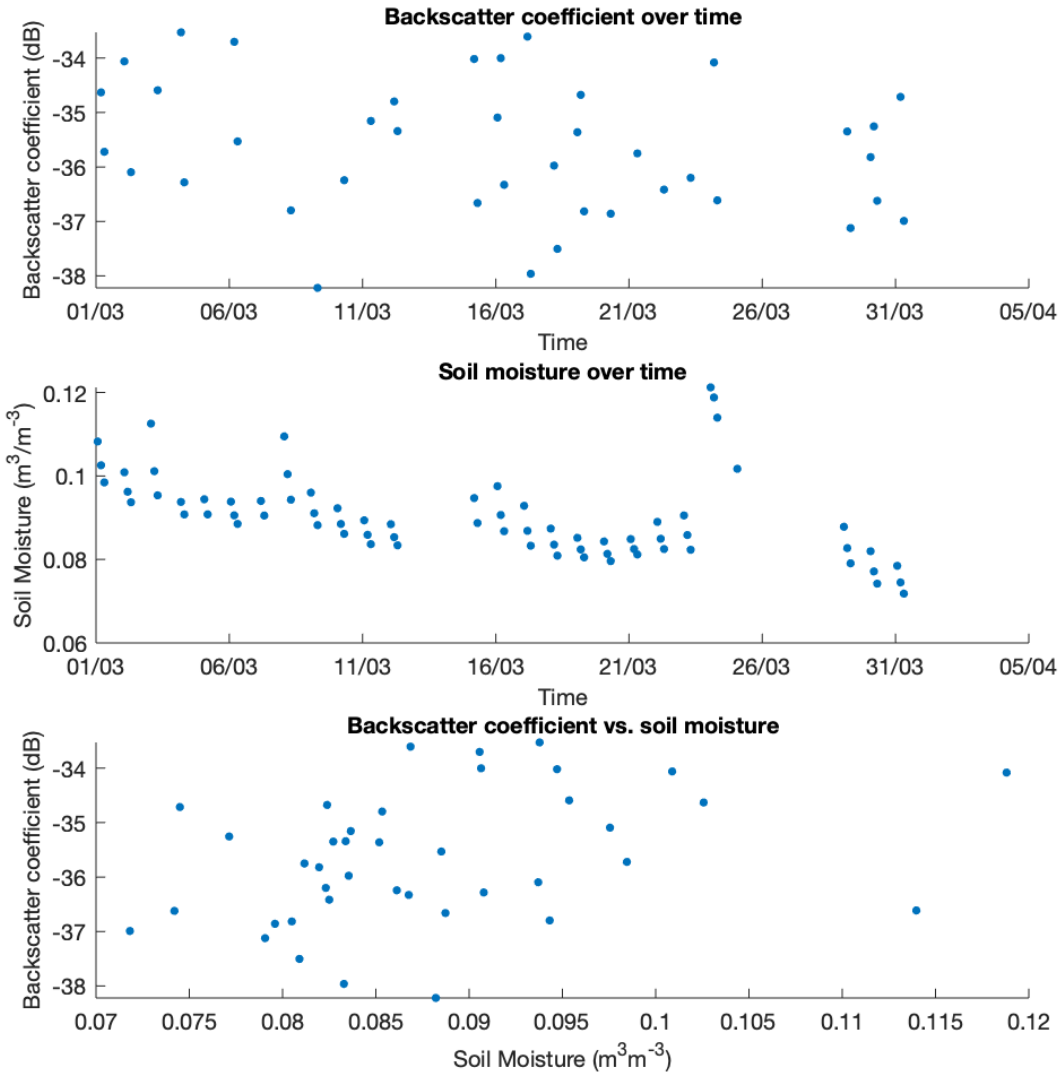

Figure 5.53: Top: The 3-hourly median backscatter coefficient for the Great Sandy Desert throughout March 2016. Middle: The soil moisture over the Great Sandy Desert throughout March 2016. Bottom: A plot of the backscatter coefficient versus the soil moisture using the data from March 2016 over the Great Sandy Desert.

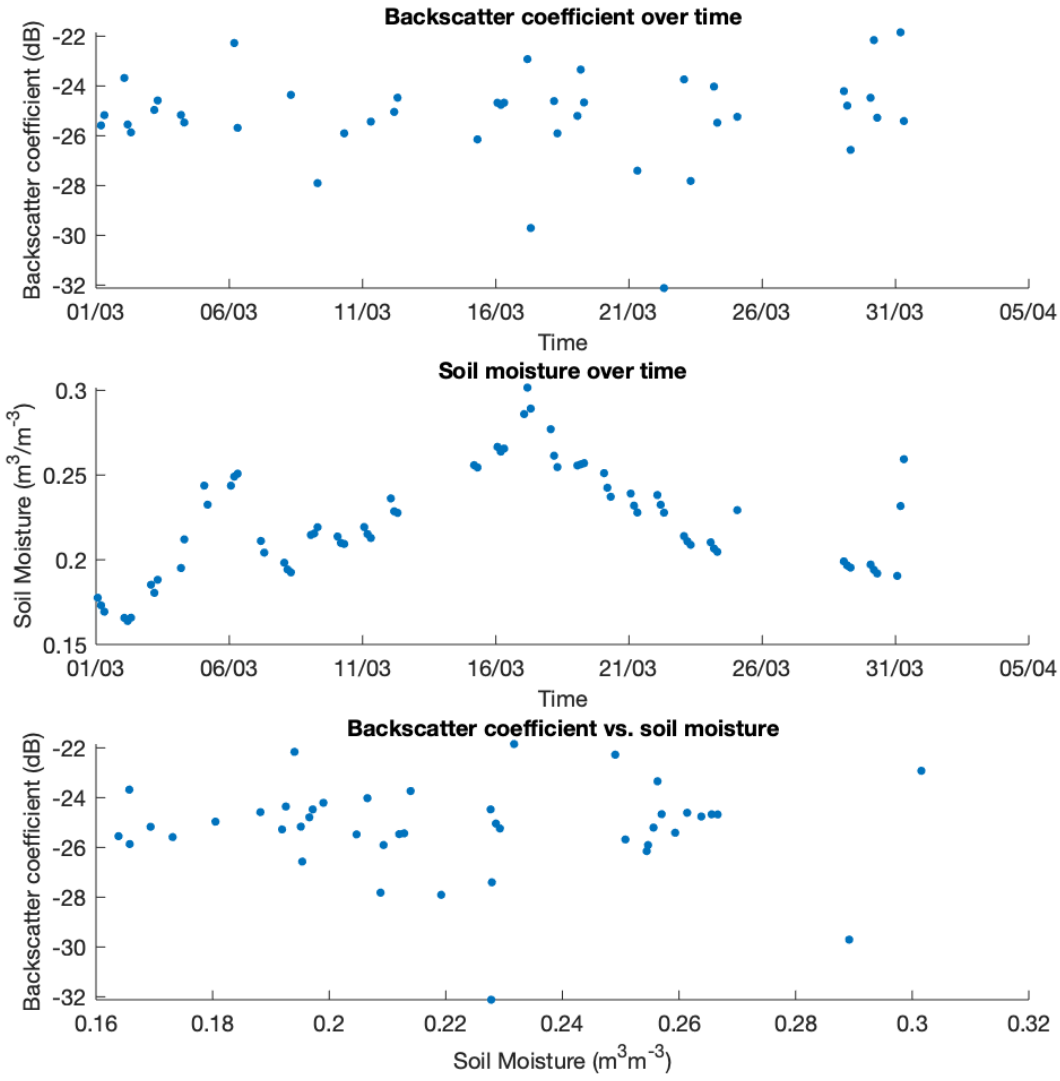

Figure 5.54: Top: The 3-hourly median backscatter coefficient over Arnhem Land throughout March 2016. Middle: The soil moisture over Arnhem Land throughout March 2016. Bottom: A plot of the backscatter coefficient versus the soil moisture using the data from March 2016 over Arnhem Land.

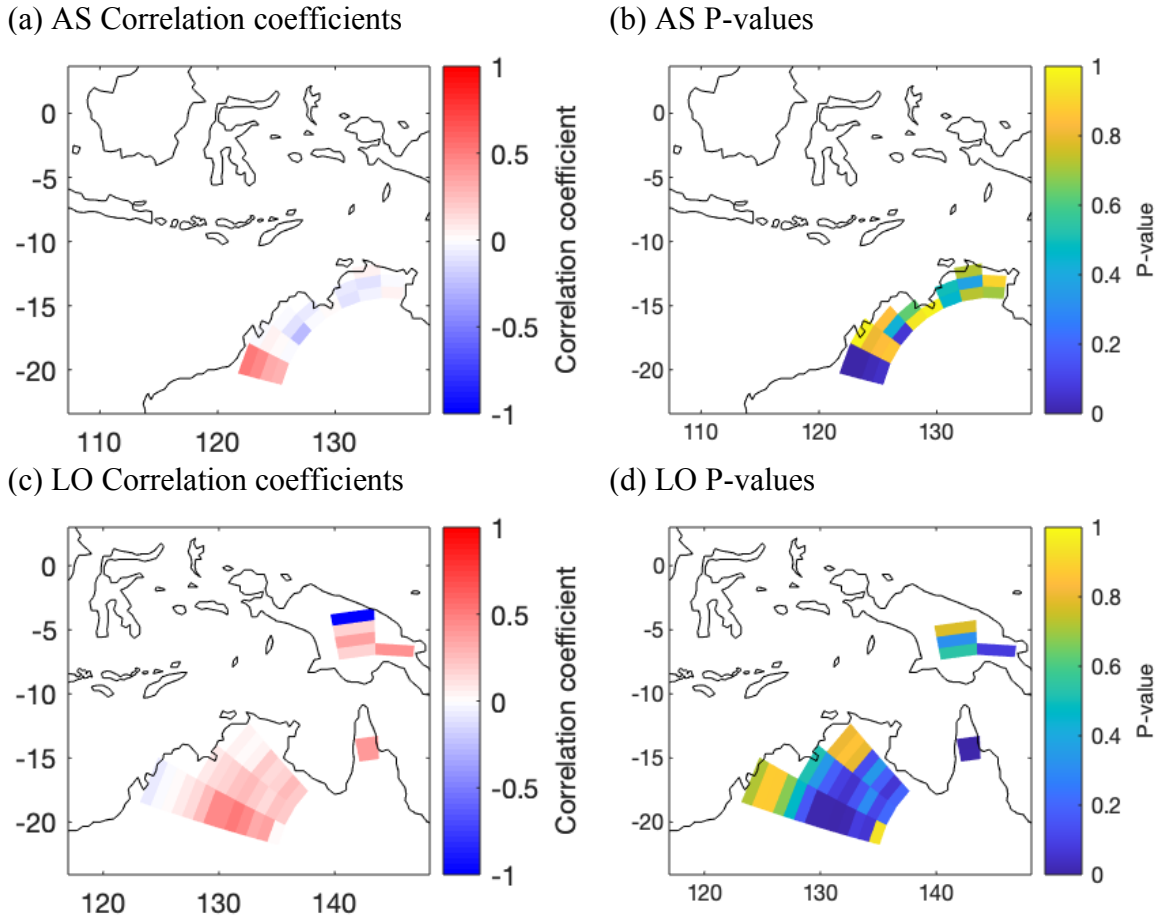

Figure 5.55: Pearson correlation test results for each range-azimuth bin, testing the null hypothesis that the backscatter coefficient and the soil moisture are uncorrelated. The correlation coefficients (a) and P-values (b) for the Alice Springs sounder and the correlation coefficients (c) and P-values (d) for the Longreach sounder are shown.

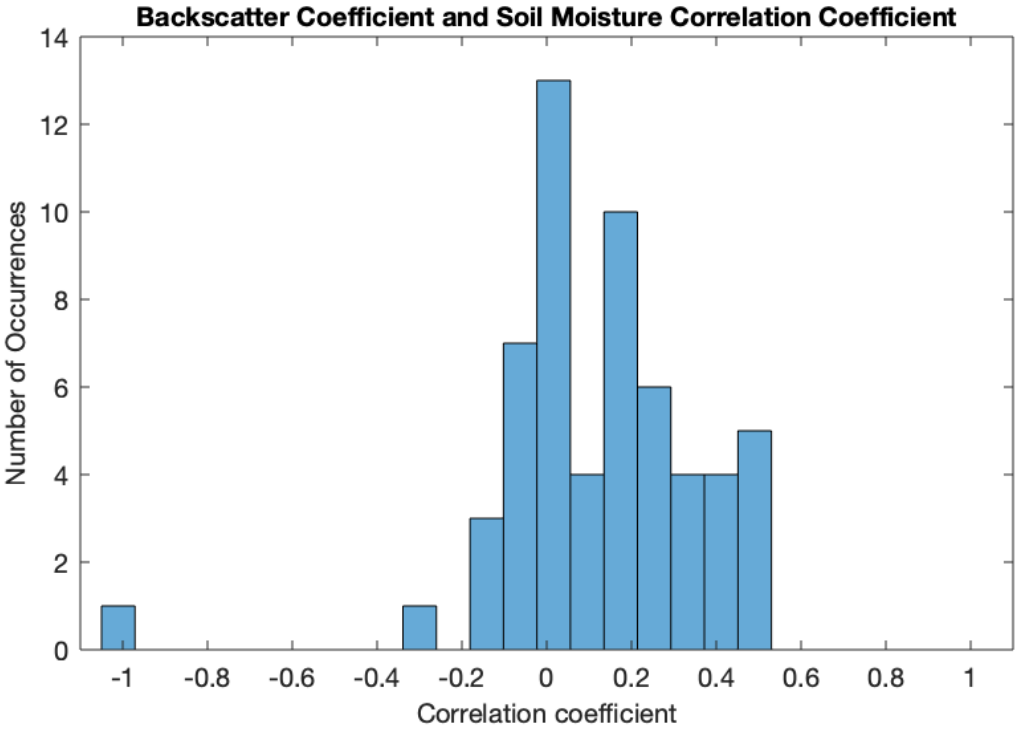

Figure 5.56: Histogram of Pearson correlation coefficients testing the correlation between the backscatter coefficient and soil moisture using both the Alice Spring and Longreach March 2016 data. The median correlation coefficient is 0.13.

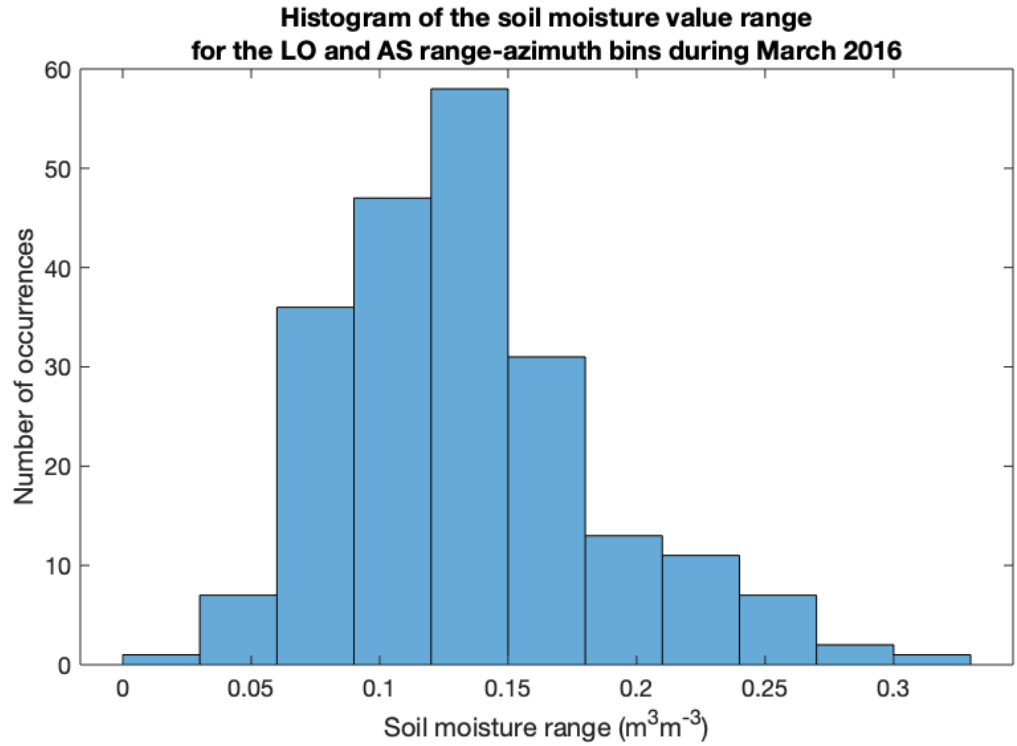

Figure 5.57: Histogram of the spread of soil moisture value from all of the Alice Springs and Longreach range-azimuth bins during March 2016. The spread of soil moisture values for a given range-azimuth bin is the difference between the maximum and minimum soil moisture values for that bin.

5.4.5 Vegetation

It has been suggested by Steele [39] that trees may act as dipoles, absorbing and reradiating HF signals back towards the receiver antenna. While the JORN backscatter sounders transmit vertically polarised waves, the polarisation of the signals changes as they propagate through the ionosphere. The vertically oriented trees will have a backscatter radar cross-section which is maximum to vertically polarised radio waves and at a minimum to horizontal polarisation. This resultant polarisation mismatch of the incident radio waves with respect to the trees is similar to the vertically polarised receive antennas. In general, we can assume the scattering cross section will be 3 dB less than that for vertically polarised incident radio waves.

Vegetation data describing the density and height of trees across the Australian continent was used to investigate if there was a correlation between the vegetation structure and the land backscatter coefficient. Figure 5.58 shows a map of the vegetation structure across Australia. Most of the trees had heights of the order of half to a full radar wavelength (10-30 m) and so would be near the resonance length of integer multiples of a half-wavelength. The mean vegetation structure code, which increases with increasing tree densities and heights (Table 3.2) was compared against the backscatter coefficient calculated for each range-azimuth bin.

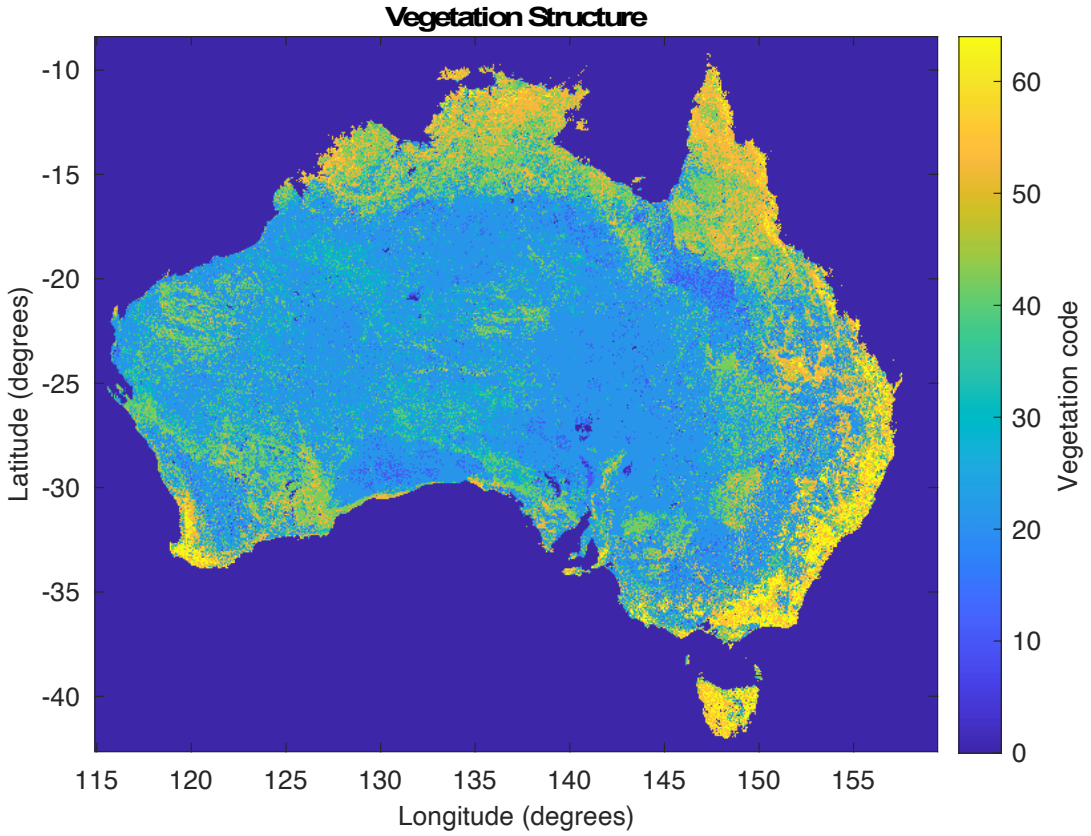

Figure 5.58: Vegetation structure code across Australia.

Figure 5.59 and Figure 5.60 show plots of the backscatter coefficients versus the vegetation code when viewed by the Longreach and Alice Springs sounders using the September 2015 and March 2016 backscatter coefficient results. A Pearson linear correlation test was conducted to test the null hypothesis that there was no relationship between the backscatter coefficient and the vegetation structure code. A strong correlation between the backscatter coefficient and the vegetation code was seen with the backscatter coefficient increasing with increasing vegetation density and height (Table 5.8). The correlation coefficients ranged from 0.79 to 0.88. The very low p values indicate that in each case the null hypothesis of no correlation was rejected.

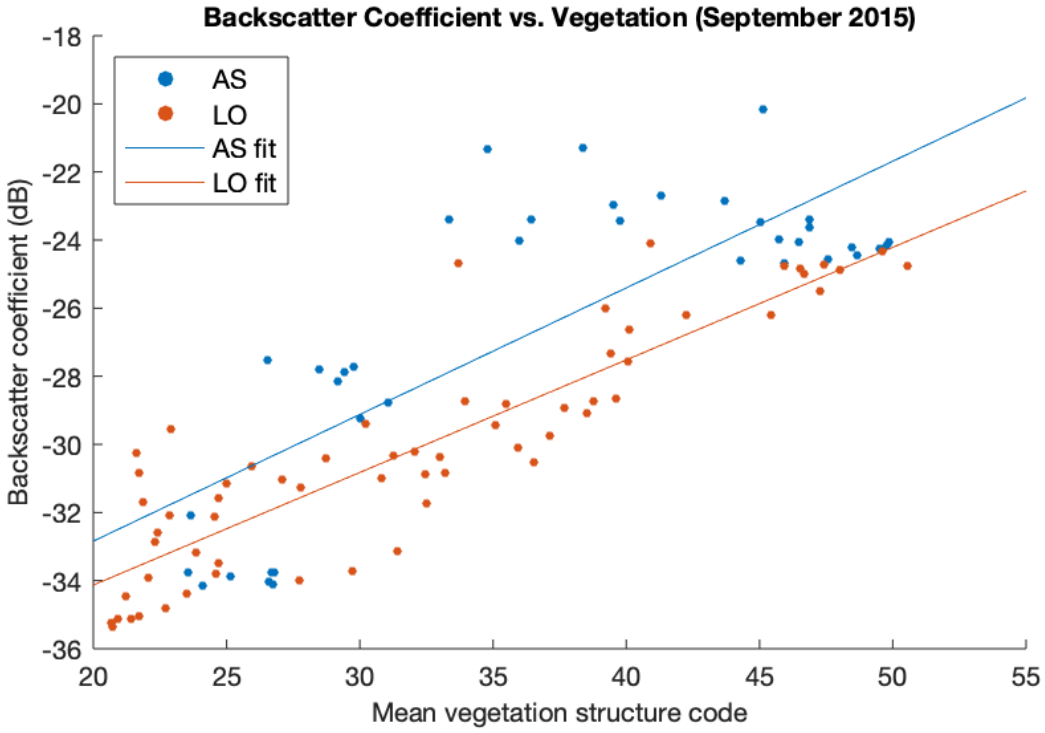

Figure 5.59: Backscatter coefficient versus the mean vegetation structure code calculated for each range-azimuth bin for the Alice Springs sounder (blue) and the Longreach sounder (red) during September 2015. Also shown are lines of best fit to the data.

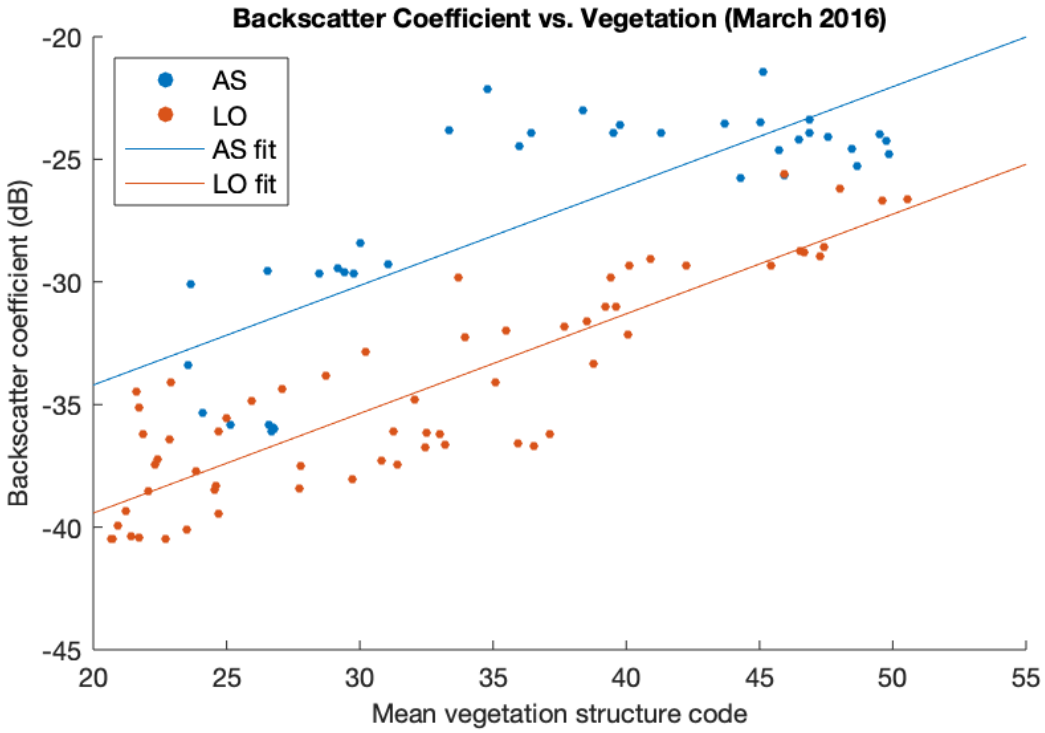

Figure 5.60: Backscatter coefficient versus the mean vegetation structure code calculated for each range-azimuth bin for the Alice Spring sounder (blue) and the Longreach sounder (red) during March 2016. Also shown are lines of best fit to the data.

Table 5.8: Backscatter coefficients and vegetation Pearson correlation test results

	Correlation coefficient	**P-value**
AS September	0.79	2.71E-09
AS March	0.81	1.04E-09
LO September	0.89	1.24E-22
LO March	0.88	6.41E-21

A line of best fit was fitted to the results using linear regression (Table 5.9). The lines of best fit for the Alice Springs results appear to be offset from the lines of best fit for the Longreach results, with the Alice Spring backscatter coefficients being larger than the Longreach backscatter coefficient for the same vegetation structure. However, during September 2015, the offset between the lines is within the standard errors in the fits as shown in Table 5.9.

Table 5.9: Line of best fit results for the backscatter coefficient versus the vegetation structure.

	Linear Fit		**Standard error**
Alice Springs September 2015	Intercept (dB)	-40.3	1.8
	Slope	0.37	0.05
Alice Springs March 2016	Intercept (dB)	-42.3	1.9
	Slope	0.41	0.05
Longreach September 2015	Intercept (dB)	-40.7	0.7
	Slope	0.33	0.02
Longreach March 2016	Intercept (dB)	-47.5	0.96
	Slope	0.41	0.03

A closer inspection of the Alice Springs results displayed in Figure 5.59 and Figure 5.60 indicates that the relationship between the vegetation and backscatter coefficient flattens out once a vegetation structural code of around 35 is reached. However, with the Longreach results the backscatter coefficient increased with increasing vegetation through to the maximum vegetation code observed of 53. This difference in behaviour may be due to the way in which the vegetation structure code is defined; codes of 31-33 imply a coverage of 6-11%, codes of 41-44 imply a coverage of 11-30% and codes from 51-53 imply a coverage of 30-70%. Values between these codes were created through the process of averaging the vegetation code data within each region. There were large ranges in the fraction of coverage for a single vegetation code, so it may be that with the Alice Springs results the regions with codes from 35 to 50 had a similar fraction of vegetation coverage, whereas in the Longreach results there could be a larger range of values in the vegetation coverage. Regions with a vegetation code >50 were in the Longreach sounder field of regard, but not the Alice Springs sounder. As the Alice Springs sounder was located in central Australia, all regions close to the sounder had little vegetation while the regions further away had much more vegetation. There was not a variety of different vegetation structures at similar ranges from the sounder. However, in contrast, the Longreach sounder field of regard covered regions of different levels of vegetation at many different range bins. This makes it a better system for investigating the relationship between the vegetation and the backscatter coefficient as the effects on the backscatter coefficient due to different frequencies and elevations associated with different ranges should be smoothed out.

While the increase in the backscatter coefficient with increased vegetation structure code is probably due to the effect of the trees on the signals it may also have been related to the fact that trees tend to grow in areas of higher moisture or rougher terrain. For example, over the desert where the terrain tends to be relatively smooth and dry there are few trees, while in tropical regions the land is often wetter, rougher and highly vegetated. However, due to the little impact seen on the backscatter coefficient from soil moisture or roughness as discussed in Section 5.4.4 and Section 5.4.3.3, it appears likely that the increase in the backscatter coefficient with vegetation structure code was due to the vegetation alone.

To further investigate how the surface roughness and vegetation affected the backscatter coefficient, the backscatter coefficient was plotted against both the roughness and the vegetation structure in Figure 5.61. This figure shows how the backscatter coefficient changes for flat and rough locations with little vegetation and high vegetation. Unfortunately, there were few areas with both high roughness and little vegetation making it difficult to fully investigate the effects of these parameters on the backscatter coefficient. Nevertheless, this figure clearly shows that the vegetation has a much larger effect than the surface roughness.

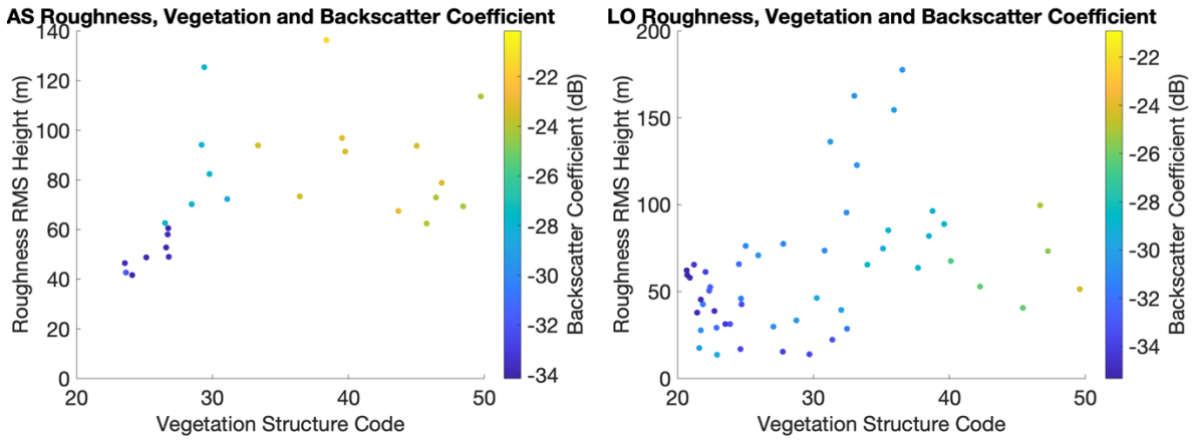

Figure 5.61: Effect of different roughness and vegetation values on the backscatter coefficient. Left: Alice Springs September 2015. Right: Longreach September 2015.

The September 2015 Alice Springs and Longreach backscatter coefficients were plotted against the vegetation structure for locations with an RMS height less than 50 m, between 50-80 m and greater than 80 m (Figure 5.62). There was the widest range of vegetation structure values observed for RMS heights between 50-80 m. For this range of RMS heights there was a very clear trend of increasing backscatter coefficients with increasing vegetation in the Longreach results; the difference in the backscatter coefficient between areas with the highest and lowest vegetation values was over 10 dB. In each plot a general trend of increasing backscatter coefficient with increasing vegetation can be seen, except for in the Alice Springs results with RMS height values less than 50 m. However, there were very few data points for RMS height values less than 50 m for Alice Springs, so the vegetation structure only ranged from 23 to 27, and the backscatter coefficient only varied by around 2 dB.

The September 2015 Alice Springs and Longreach backscatter coefficients were also plotted against the RMS height for vegetation structure values less than 30, between 30-35 and greater than 35 (Figure 5.63). No clear trend in the backscatter coefficient versus the roughness was seen, and the range in the backscatter coefficient was much smaller compared to when the backscatter coefficient was plotted against a wide range of vegetation structures for a small range of roughness values. Figure 5.62 and Figure 5.63 demonstrate that the ground backscatter coefficient is dominated by the vegetation.

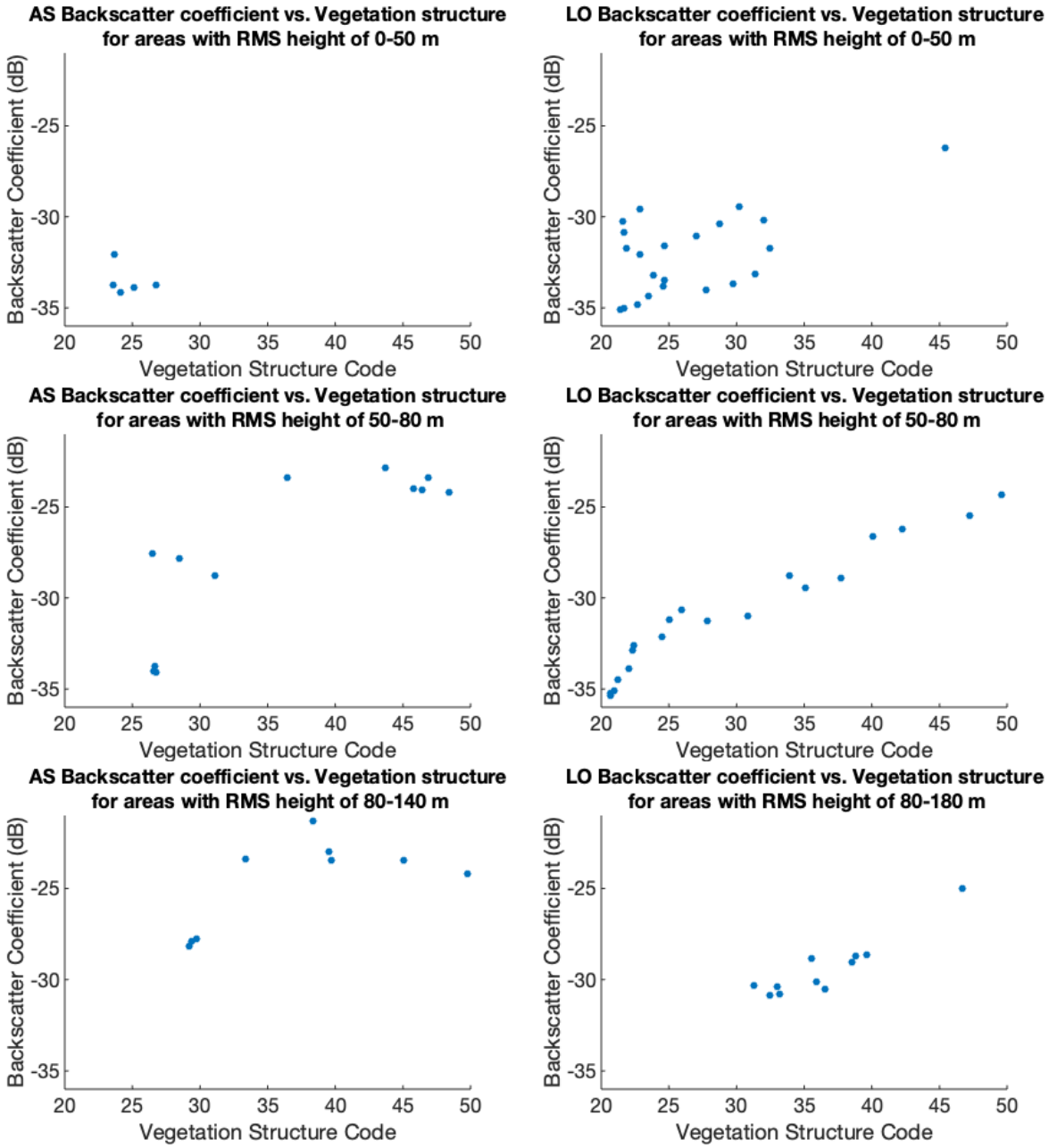

Figure 5.62: Backscatter coefficient from September 2015 versus vegetation structure for range-azimuth bins with a mean RMS height less than 50 m (top), between 50-80 m (middle), greater than 80 m (bottom).

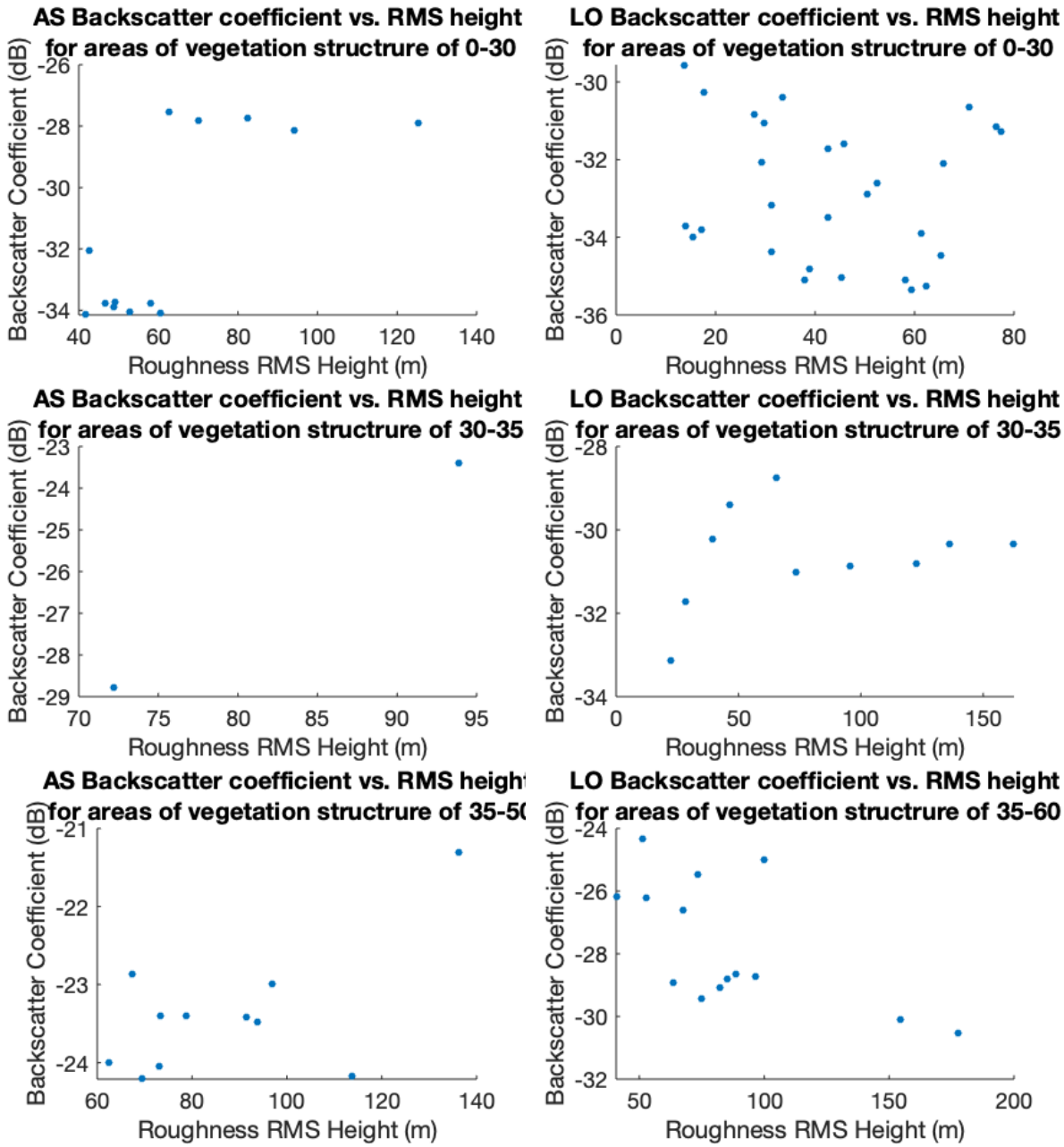

Figure 5.63: Backscatter coefficient from September 2015 versus RMS height for range-azimuth bins with a mean vegetation structure code less than 30 (top), between 30-35 (middle), greater than 35 (bottom).

5.5 Summary

Maps of the backscatter coefficient across Northern Australia were constructed for September 2015 and March 2016 for the areas viewed by each of the four JORN FMS backscatter sounders. Land and sea boundaries could be seen in the backscatter coefficient maps, along with topographic features such as deserts and mountain ranges. It was found that the method did not work as well for the Laverton sounder as it did for the others, as fewer synthesised ionograms matched the observed ionograms. The reason why is not yet understood and warrants further investigation which was beyond the scope of this thesis.

The backscatter coefficient results from the ionogram comparison method were compared to sea backscatter coefficients calculated using a wave height spectrum from sea

state hind cast data, from which the backscatter coefficient could be calculated from theory. These two methods of calculating the backscatter coefficient yielded similar results, with regions of high and low sea backscatter in agreement. Again, the Laverton results were the most dissimilar while the other two sounders showed similar results between the two methods. This further suggested that the method for calculating backscatter coefficients from backscatter sounder data worked best for the Alice Springs and Longreach sounders, rather than for the Laverton sounders.

The effects of different ray and surface parameters were investigated. However, due to the large variance in the backscatter coefficient results, many of the comparisons were inconclusive. It was found that the sea backscatter coefficients changed over time as the sea state changed, while the land backscatter coefficients remained more constant. Due to the limited frequencies and elevations able to be propagated via the ionosphere, any effect of the frequency and angle of incidence on the backscatter coefficient was not apparent. An aspect dependence of the backscatter coefficient was seen in the different backscatter coefficient values for a single location when viewed by different sounders. A weak positive correlation between the backscatter coefficient and the surface roughness and between the backscatter coefficient and the soil moisture was also found. The parameter that was most strongly correlated with the backscatter coefficient was the vegetation structure. The backscatter coefficient increased with increasing vegetation density and height and is likely due to trees acting as vertical dipoles. The correlation coefficient was in the range 0.79 – 0.89.

Chapter 6 Conclusion

6.1 Conclusion

A model of backscatter coefficients is important for assessing the performance of over-the-horizon radars. The backscatter coefficient of the sea has been well defined, but the land backscatter coefficients are not well understood. This thesis presented a method of calculating land and sea backscatter coefficients by comparing observed backscatter ionograms to synthesised backscatter ionograms where all other losses had been accounted for. The difference in the power of the one-hop F2 low region of the synthesised and observed ionograms was calculated. This difference in power gave the backscatter coefficient, as all other losses were accounted for. Maps of the backscatter coefficients over Northern Australia in September 2015 and March 2016 when observed by the four JORN FMS backscatter sounders were produced. In these maps, topographic features such as desert regions and mountain ranges could be identified along with land sea boundaries.

Another method of calculating sea backscatter coefficients using a perturbation approach with a sea wave height spectrum calculated from sea state data was used. The sea backscatter coefficients from this method were compared to those from the ionogram comparison method. The trends and variations between the two methods of calculating the sea backscatter coefficient were similar. The average values obtained from the two methods show good agreement for both the Alice Springs and Longreach sounders; however, for Alice Springs the dynamic range of the results from the wave spectrum method was larger than the ionogram comparison method.

The effects of various ray and surface parameters on the backscatter coefficient were investigated. These included the time of day and year, radio wave frequency, angle of incidence, aspect, surface roughness, soil moisture and vegetation. It was difficult to determine how the backscatter coefficient was affected by many of these parameters due to the variance in the calculated backscatter coefficients introduced by the limitations of the method, and the limited range of values for the surface parameters and ray properties. The backscatter coefficient of the sea varied from day-to-day much more than the backscatter coefficient of the land. This was because the sea conditions such as the wave height and period changed with weather conditions while the land composition remained relatively constant over the period for which data was available. A conclusive relationship between the backscatter coefficient and the radio wave frequency or angle of incidence was not found due to the ionospheric propagation conditions limiting the range of frequencies and incidence angles able to be used by the backscatter sounders. A weak positive correlation between the backscatter coefficient and the surface roughness and soil moisture was observed. Finally, it was found that the backscatter coefficient was highly correlated with the vegetation structure. The backscatter coefficient increased with increasing density of vegetation. One explanation for this effect was that the trees were acting as antennas, reradiating the power back towards the receiver.

6.2 Future Work

The assumptions and limitations of the method used to calculate the backscatter coefficient introduced variance in the backscatter coefficient results. To increase the accuracy of the results, 3D numerical ray tracing could be used. This would improve the model of where the rays reached the ground by including out of plane propagation and the splitting of the ray into the ordinary and extraordinary modes. The ionospheric absorption model did not include day-to-day variations in the ionosphere as it was based on a climatological model. The absorption could be calculated along the ray path if a model of the D layer was included in the ionospheric model. Future work would involve updating the ionogram synthesis to use 3D numerical ray tracing and including a D layer in the ionospheric model for absorption calculations.

To further understand how the backscatter coefficient changes over time and how changes in the surface parameters affect the backscatter coefficient, a study over a longer period of time needs to be conducted. Backscatter ionograms observed over a decade could be used to investigate seasonal trends in the backscatter coefficient. This would provide further insight into the differences in the backscatter coefficients from the Longreach sounder in September 2015 and March 2016.

Further work could also include an investigation into why the ionogram comparison method of calculating the backscatter coefficients from the Laverton backscatter sounders was not as successful, and why more of the modelled backscatter ionograms were rejected. This would involve examining the differences between the leading edges of the east facing beams and the west facing beams for the model and the observed ionograms.

A larger data set combined with a more detailed investigation into the differences in the sea backscatter coefficients calculated by the method developed in this thesis and that from Barrick's theory could provide insight into whether there were particular sea conditions that contributed to the observed differences between these methods. This may help answer why there was a bias seen in the backscatter coefficients from the two methods. Insight may also be gained with respect to the physics of the scattering of HF radio waves from the sea surface and whether alternative scattering models may be more appropriate.

Data with a higher azimuthal resolution, such as from the JORN main receive array, could be used to calculate the land backscatter coefficients at a higher resolution. Topographic features would then be easier to identify and hence the effects of these features could be further investigated. The area of land viewed would be smaller so less variance in the backscatter results from differences in the backscatter coefficient over the area viewed could be expected.

Finally, future work could include the incorporation of the backscatter coefficients into the JORN FMS system to improve the assessment of ionospheric propagation conditions.

Appendix A Backscatter ionogram comparison codes

A.1 Code to obtain synthesised and observed ionograms for specified times

```
% Name :
%   compare_synth_to_obs_function
%
% Purpose :
%   Synthesises ionograms and finds the observed ionograms for the same
%   location and time for comparison. Results are saved for each time and
%   location in a file that contains both the synthesised ionogram and the
%   matching observed ionogram.
%
% Calling sequence :
%   compare_synth_to_obs_function(bss_id, year, month, day_vect, time_vect,
min_vect)
%
% Inputs :
%    bss_id = 'LAE';  % Sounder of interest.
%         'LAE' - Laverton East
%         'LO' - Longreach
%         'LAW' - Laverton West
%         'AS' - Alice Springs
%    year
%    month
%    day_vect: Vector of days to synthesise ionograms for
%    time_vect: Vector of times (hour of day) to synthesise ionograms for
%    min_vect: Vector of times (minute of hour) to synthesise ionograms for
%
% Outputs :
%    Saves synthesised and observed ionograms to a file

function compare_synth_to_obs_function(bss_id, year, month, day_vect,
time_vect, min_vect)

UT = [year, month, 1, 0, 0];

% Loop over bss, times and beams
for day_loop = day_vect % day of month
UT(3) = day_loop;

% Open file containing observed ionograms from this day
day_num = day(datetime(UT(1), UT(2), UT(3)), 'dayofyear');
bss_filename = sprintf('bss_records_%03d_%d', day_num, UT(1));
load(bss_filename)

for time = time_vect % hour, UTC time
UT(4) = time;
for min = min_vect
UT(5) = min;

% Find the index for the observed results from this time
bss_index = find_bss_record(bss_id, UT);
if isnan(bss_index) % if data from this time doesn't exist move onto next
time
fprintf('%s_%d%02d%02d_%02d%02d Observed ionogram not availble, moved onto
next time\n', bss_id, UT(1), UT(2), UT(3), UT(4), UT(5));
```

```
continue
end
raw_bss = bss_records(bss_index);
bss = get_scaled_bss( bss_records(bss_index) );

for beam = 1:8 % beam (1 to 8)

obs_bss = bss(:,:,beam);

% Only synthesise ionograms if the observed ionograms
% contains enough power to be useful.
power_check = obs_bss >= -125;
if numel( power_check( power_check > 0 ) ) > 75 %100

% Generate synthesised results
[xrange, yrange, pow_tot_dB, elevation_dom, num_hops_dom, gnd_range_km,
E_or_F2high_flag] = bss_synth_2D(bss_id, beam, UT);

% Save synthesised results in structure
synth.xrange = xrange;
synth.yrange = yrange;
synth.pow_tot_dB = pow_tot_dB;
synth.elevation_dom = elevation_dom;
synth.num_hops_dom = num_hops_dom;
synth.gnd_rng_km = gnd_range_km;
synth.E_or_F2high_flag = E_or_F2high_flag;

% Save synthesised and observed results in a single file
% save to folder
filename = sprintf('%s_Beam%d_%d%02d%02d_%02d%02d', bss_id, beam, UT(1),
UT(2), UT(3), UT(4), UT(5));
save(filename, 'synth', 'obs_bss', 'raw_bss')

end % end of power check

end % beam
end %min
end % time
end % day

end
```

A.2 Code to synthesise backscatter ionograms using 2D raytracing

```
% Name :
%   bss_synth_2D.m
%
% Purpose :
%   Function for synthesising a backscatter ionogram using 2D ray tracing
%   through the RTIM or IRI-2016. All losses are included other than the
%   backscatter. The backscatter coefficient has been set to 0 dB. Based on
%   bss_synth from PHaRLAP.
%
% Calling sequence :
%   bss_synth(bss_id, beam, UT)
%
% Inputs :
%    bss_id = 'LAE';  % Sounder of interest.
%         'LAE' - Laverton East
%         'LO' - Longreach
```

```
%         'LAW' - Laverton West
%         'AS' - Alice Springs
%    beam = 8;   % Beam, used to specify which FMS beam (1 to 8 clockwise)
%    UT = [2015, 9, 3, 4, 00];   % Universal time [YYYY,M,D,H,mm]
%
% Outputs :
%    xrange = [freq_min freq_max]; % Minimum and maximum frequencies (MHz)
%    yrange = [0 group_max]; % Minimum and maximum group range (km)
%    pow_tot_dB: Matrix of power (dBW) in the ionogram elevation_dom:
%       Matrix of the dominant elevation of rays contributing to each cell
%       in the ionograms
%    num_hops_dom: Matrix of the dominant number of hops of the rays
%       contributing to each cell in the ionograms
%    gnd_range_km: Matrix of the ground range of the rays for each cell in
%       the ionogram
%    E_or_F2high_flag: Matrix flagging if a cell in the ionogram had E or
%       F2 high rays contributing
%
% Note: environment variables need to be set by for PHaRLAP
%    setenv('DIR_MODELS_REF_DAT', '.../pharlap_4.3.1/dat/')
%
function [xrange, yrange, pow_tot_dB, elevation_dom, num_hops_dom,
gnd_range_km, E_or_F2high_flag] = bss_synth_2D(bss_id, beam, UT)

% Setup physical constants and parameters
radius_earth_km = 6371;       % Mean radius of the Earth (km)
light_speed = 299792459.0;    % speed of light (m/s)
% Set sunspot number
if UT(1) == 2015 && UT(2) == 9
R12 = 46;    % yearly smoothed sunspot number for Sep 2015
elseif UT(1) == 2016 && UT(2) == 3
R12 = 35.3;  % yearly smoothed sunspot number for March 2016.
else
disp('sunspot number not available')
end

% Select radar specific variables
[~, ~, rx_bore, tx_lat, tx_long, tx_bore, ~, sector_bearings] =
get_site_values (bss_id);

if strcmp(bss_id, 'LAE') || strcmp(bss_id, 'LAW') || strcmp(bss_id, 'LO')
% Note: these values are for LO, LAE, LAW radars at frequencies below 32
MHz
num_elem_rx_array = 32;       % no. of antenna elements in rx. array
rx_arr_space = 6.2;           % spacing between antenna elements
arr_length = (num_elem_rx_array - 1) .* rx_arr_space;
crossover_frequency = 32;     % MHz
elseif strcmp(bss_id, 'AS')
num_elem_rx_array = 28;       % no. of antenna elements in rx. array
rx_arr_space = 6.0;           % spacing between antenna elements
arr_length = (num_elem_rx_array - 1) .* rx_arr_space;
crossover_frequency = 30;     % MHz
else
disp('ERROR: bss_id not valid');
return % stop execution
end

ray_bearing = sector_bearings(beam); % direction (degrees) of the beam
relative to true north
% bore bearings definition
```

```
tx_bore_bearing = sector_bearings(beam)-tx_bore;
rx_bore_bearing = sector_bearings(beam)-rx_bore;

% Select absorption model to use
GB_abso_flag = 1;             % use George and Bradley absorption
% set GB_abso_flag = 0 for SiMIAN absorption
if GB_abso_flag
fprintf('Generating the model BSS using George and Bradley absorption... ')
else
fprintf('Generating the model BSS usinig SiMIAN absorption... ')
end

tx_pow = 20e3;                % transmitter power (Watts)
tx_pow_db = 10 .* log10(tx_pow); % transmitter power (dBW)

% Obtain ionosphere model to use for raytracing
% Get more information about the ionosphere using the IRI
doppler_flag = 0;       % not interested in Doppler shift and spread
kp = 0;                 % kp not used as doppler_flag = 0. Set it to a
dummy value

clear iri_options
iri_options.Ne_B0B1_model = 'Bil-2000';

RTIM = 1; % If RTIM = 1 use RTIM, if RTIM = 0 use IRI.

if RTIM == 1
% Get the ionosphere slice from the RTIM
[iono_en_grid2, range_max, range_max_RTIM, height_info] =
get_2D_iono_slice_interp(bss_id, UT, beam);

% Get information about the RTIM
start_height = height_info.start_height; % 80 km
height_inc = height_info.height_inc; % 1 km
num_heights = height_info.num_heights;

max_range_km = range_max * 10^-3;
num_range = length(iono_en_grid2(1,:));
range_inc = max_range_km ./ (num_range - 1);

% Convert plasma frequency to electron density
iono_en_grid = iono_en_grid2;
iono_en_grid_5 = iono_en_grid2;

% this part is used to determine the collision_freq
fprintf('Generating ionospheric grid... ')
tic
[iono_pf_grid, iono_pf_grid_5, collision_freq, irreg] = ...
gen_iono_grid_2d(tx_lat, tx_long, R12, UT, ray_bearing, ...
max_range_km, num_range, range_inc, start_height, ...
height_inc, num_heights, kp, doppler_flag, 'iri2016', ...
iri_options);
toc
collision_freq(isnan(collision_freq)) = 0; % remove nans

elseif RTIM == 0
% Set information about IRI ionosphere to generate (when not using RTIM)
start_height = 80; % 80 km
height_inc = 1; % 1 km
```

```
num_heights = 321; %

max_range_km = 3200;
range_max_RTIM = max_range_km.*10^3; % Don't need to ignore values beyond
end of RTIM as using IRI.
range_inc = 50;
num_range = (max_range_km/(range_inc)+1);

% this part is used to determine the collision_freq
fprintf('Generating ionospheric grid... ')
tic
[iono_pf_grid, iono_pf_grid_5, collision_freq, irreg] = ...
gen_iono_grid_2d(tx_lat, tx_long, R12, UT, ray_bearing, ...
max_range_km, num_range, range_inc, start_height, ...
height_inc, num_heights, kp, doppler_flag, 'iri2016', ...
iri_options);
toc
collision_freq(isnan(collision_freq)) = 0; % remove nans

% convert plasma frequency grid to electron density in electrons/cm^3
% Using IRI
iono_en_grid = iono_pf_grid.^2 / 80.6164e-6;
iono_en_grid_5 = iono_pf_grid_5.^2 / 80.6164e-6;

end

% Set up necessary parameters for the raytacing
irregs_flag = 0;     % no irregularities
num_hops = 4;        % number of hops %4
tol = 1e-7;          % rkf tolerance

freq_min = 5; % MHz
freq_max = 32; % MHz
freq_step = 0.2; % MHz

elev_step = 0.2; % degrees
elev_min = 2; % degrees
elev_max = 50; % degrees

freqs_range = (freq_min: freq_step: freq_max);
num_freqs = length(freqs_range);
elevs = (elev_min : elev_step : elev_max);
num_elevs = length(elevs);

group_step = 50; % km
group_max = 4000; % km
groups = (0: group_step : group_max);
num_groups = length(groups);

group_range_res = group_step;

% Initialise arrays
power_total = zeros(num_groups, num_freqs) + 1e-200;
power_dominant = zeros(num_groups, num_freqs);
phase_path_dom = zeros(num_groups, num_freqs);
elevation_dom = zeros(num_groups, num_freqs);
num_hops_dom = zeros(num_groups, num_freqs);
gnd_range_km = zeros(num_groups, num_freqs);
```

```
% Initialise arrays for selecting the cells to flag with large E
% or F2 high contributions to the power.
power_E_tot = zeros(num_groups, num_freqs) + 1e-200; % E layer rays. Rays
with an apogee (heighest altitude) of 150 km
power_high_tot = zeros(num_groups, num_freqs) + 1e-200; % F2 high rays.
Rays with change in ground range wrt elevation greater than zero
power_below80_tot = zeros(num_groups, num_freqs) + 1e-200; % Rays below 80
km at end of inosphere model

% For testing how much power was contributed by these rays
power_above80_tot = zeros(num_groups, num_freqs) + 1e-200;
num_hops_E_rays = zeros(num_groups, num_freqs);
num_hops_F2high_rays = zeros(num_groups, num_freqs);

% first call to raytrace so pass in the ionospheric and geomagnetic grids
[ray_data, ray_path_data] = ...
raytrace_2d(tx_lat, tx_long, elevs(1), ray_bearing, freq_min, ...
num_hops, tol, irregs_flag, iono_en_grid, iono_en_grid_5, ...
collision_freq, start_height, height_inc, range_inc, irreg);

disp('first call to raytracing complete')

% Get the gain information for the transmitter and receiver
% Calling gain function
if strcmp(bss_id, 'LO') || strcmp(bss_id, 'LAE') || strcmp(bss_id, 'LAW')
radar_type = 'jorn';
elseif strcmp(bss_id, 'AS') % alice springs
radar_type = 'jfas';
end

rx_tx = 'tx';
% crossover_frequency = 30; %MHz %true for both rx and tx
clamp = true;
mismatch_flag = true;
% Get transmitter gains
[frequency_array, elevation_array] = meshgrid(freqs_range, elevs);
azimuth_array = tx_bore_bearing.*ones(size(frequency_array));
[gain_freq_elev_tx, ~, ~] = bss_antenna_gain(frequency_array,
azimuth_array, elevation_array, radar_type, rx_tx, crossover_frequency,
clamp, mismatch_flag);
% Now consider receiver
rx_tx = 'rx';
return_elev = elev_min: (elev_step/10): elev_max; % increase resolution of
elevations
azimuth_array = asind(sind(rx_bore_bearing)./cosd(return_elev));
gain_freq_elev_rx = zeros(1,length(return_elev),length(freqs_range)); %
initialise array
gain_freq_elev_rx(:,:,:) = bss_beam_gain_for_bss_synth(bss_id, beam,
azimuth_array, return_elev, freqs_range);

% Loop over ray frequency
for freq = freq_min:freq_step:freq_max
% Change antenna array info to VHF when frequency greater than
% crossover frequency
if freq >= crossover_frequency
if strcmp(bss_id, 'LAE') || strcmp(bss_id, 'LAW') || strcmp(bss_id, 'LO')
num_elem_rx_array = 16;       % no. of antenna elements in rx. array
rx_arr_space = 3.7;           % spacing between antenna elements
arr_length = (num_elem_rx_array - 1) .* rx_arr_space;
elseif strcmp(bss_id, 'AS')
```

```
num_elem_rx_array = 12;       % no. of antenna elements in rx. array
rx_arr_space = 3.9;           % spacing between antenna elements
arr_length = (num_elem_rx_array - 1) .* rx_arr_space;
end
end

freq_bin = round((freq - freq_min) ./ freq_step + 1);

latitude_hop = zeros(num_elevs, num_hops) * nan;
longitude_hop = zeros(num_elevs, num_hops) * nan;
gnd_range = zeros(num_elevs, num_hops) * nan;
grp_range = zeros(num_elevs, num_hops) * nan;
elev_init = zeros(num_elevs, num_hops) * nan;
elev_fin = zeros(num_elevs, num_hops) * nan;
elevation_tx = zeros(num_elevs, num_hops) * nan;
effective_range = zeros(num_elevs, num_hops) * nan;
dev_absorption = zeros(num_elevs, num_hops) * nan;    % deviative
absorption
gb_absorption = zeros(num_elevs, num_hops) * nan;     % George and Bradley
absorption = zeros(num_elevs, num_hops) * nan;        % SiMIAN absorption
forward_scatt_loss = zeros(num_elevs, num_hops) * nan;
phase_path = zeros(num_elevs, num_hops) * nan;
labels = zeros(num_elevs, num_hops) * nan;
num_hops_done = zeros(num_elevs, 1);

labels_above_80 = zeros(num_elevs, num_hops) * nan; % Flag rays above 80 km
at max range of ionosphere model
apogee_height = zeros(num_elevs, num_hops) * nan;

% calculate the azimuthal beam width
wave_length = light_speed ./ (freq *1e6);             % wave length in m
%     beam_az_width = wave_length ./ arr_length;            % azimuthal
beam width
beam_az_width = wave_length ./ ( arr_length * cosd(rx_bore_bearing) );
% azimuthal beam width

% call 2D raytrace - multi-thread over elevation
freqs = freq .* ones(size(elevs));
[ray_data, ray_path_data] = ...
raytrace_2d(tx_lat, tx_long, elevs, ray_bearing, freqs, ...
num_hops, tol, irregs_flag);

% loop over ray elevation and calculate various quantites
for elev_idx = 1:num_elevs
nhops_done = ray_data(elev_idx).nhops_attempted;

% obtain the ground and group range, initial and final elevation,
% effective range, deviative absorption, phase path, O-X mode correction,
% number of hops done and hop label.
latitude_hop(elev_idx, 1:nhops_done) = ray_data(elev_idx).lat;
longitude_hop(elev_idx, 1:nhops_done) = ray_data(elev_idx).lon;
gnd_range(elev_idx, 1:nhops_done) = ray_data(elev_idx).ground_range;
grp_range(elev_idx, 1:nhops_done) = ray_data(elev_idx).group_range;
elev_init(elev_idx, 1:nhops_done) = ray_data(elev_idx).initial_elev;
elev_fin(elev_idx, 1:nhops_done) = ray_data(elev_idx).final_elev;
elevation_tx(elev_idx, 1:nhops_done) = elevs(elev_idx);
effective_range(elev_idx, 1:nhops_done) = ...
ray_data(elev_idx).effective_range;
dev_absorption(elev_idx, 1:nhops_done) = ...
ray_data(elev_idx).deviative_absorption;
```

```
absorption(elev_idx, 1:nhops_done) = ...
ray_data(elev_idx).total_absorption;
phase_path(elev_idx, 1:nhops_done) = ray_data(elev_idx).phase_path;
num_hops_done(elev_idx) = ray_data(elev_idx).nhops_attempted;
labels(elev_idx, 1:nhops_done) = ray_data(elev_idx).ray_label;

apogee_height(elev_idx, 1:nhops_done) = ray_data(elev_idx).apogee;

% find ray_data at max range of ionosphere model
% exclude if it is above 80km
labels_above_80(elev_idx, 1:nhops_done) = ray_data(elev_idx).ray_label;
elem_maxRange = find(ray_path_data(elev_idx).ground_range >
range_max_RTIM*10^-3,1); % find the first index greater than max_range

if ~isempty(elem_maxRange)
% If the ray is above a height of 80 km beyond the max range of the
% RTIM, flag this ray (by setting the label to -10).
if  max(ray_path_data(elev_idx).height(elem_maxRange:end) > 80) == 1
% Find the first index beyond the RTIM where the ray is above 80 km
idx_max = (elem_maxRange-1) +
find(ray_path_data(elev_idx).height(elem_maxRange:end) > 80,1);
% Calculate which hops to set to -10
good_hops = nnz(~ray_path_data(elev_idx).height(1:idx_max)) - 1;
labels_above_80(elev_idx, good_hops+1:nhops_done) = -10;
end
end

% Calculate the cumulative-hop forward scattering loss and the absorption
% loss (O mode only) via the George and Bradley model
O_mode = 1;
fsloss_hop_cumu = 0;
absorp_cumu = 0;
lat_hop_start = tx_lat;
lon_hop_start = tx_long;
elev_hop_start = elevs(elev_idx);
forward_scatt_loss(elev_idx, 1) = 0;
for hop_idx = 1:nhops_done-1
lat_hop_end = ray_data(elev_idx).lat(hop_idx);
lon_hop_end = ray_data(elev_idx).lon(hop_idx);
elev_hop_end = elev_fin(elev_idx, hop_idx);

% forward scattering loss
fsloss_hop_cumu = fsloss_hop_cumu + ...
ground_fs_loss(lat_hop_end, lon_hop_end, elev_hop_end, freq);
forward_scatt_loss(elev_idx, hop_idx+1) = fsloss_hop_cumu;
frontscatter = ground_fs_loss(lat_hop_end, lon_hop_end, elev_hop_end,
freq);
% calculate absorption loss via George and Bradley model
apogee_gndr = ray_data(elev_idx).gnd_rng_to_apogee(hop_idx);
[lat_hop_mp, lon_hop_mp] = raz2latlon(apogee_gndr*1000, ray_bearing, ...
tx_lat, tx_long);
absorp_thishop = abso_bg(lat_hop_mp, lon_hop_mp, elev_hop_start, ...
freq, UT, R12, O_mode);
absorp_cumu = absorp_cumu + absorp_thishop;
gb_absorption(elev_idx, hop_idx) = absorp_cumu;

lat_hop_start = lat_hop_end;
lon_hop_start = lon_hop_end;
elev_hop_start = elev_hop_end;
end
```

```
% George and Bradley absorption loss for the last hop
if isempty(hop_idx), hop_idx = 0; end
hop_idx = hop_idx + 1;
if labels(elev_idx, hop_idx) == 1
apogee_gndr = ray_data(elev_idx).gnd_rng_to_apogee(hop_idx);
[lat_hop_mp, lon_hop_mp] = raz2latlon(apogee_gndr*1000, ray_bearing, ...
tx_lat, tx_long);
absorp_lasthop = abso_bg(lat_hop_mp, lon_hop_mp, elev_hop_start, ...
freq, UT, R12, O_mode);
absorp_cumu = absorp_cumu + absorp_lasthop;
gb_absorption(elev_idx, hop_idx) = absorp_cumu;
end

end   % for elev_idx = 1:num_elevs

% add the George and Bradley absorption and deviative absorption to give
% the total ionospheric absorption
absorption_gb_dev = gb_absorption + dev_absorption;

% Calculate rate of change of group-range wrt elevation and rate of change
% of ground-range wrt group-range
dgrp_dels = zeros(size(grp_range)) .* NaN;
dgnd_dgrp = zeros(size(grp_range)) .* NaN;
dgnd_dels = zeros(size(grp_range)) .* NaN;

for ii = 1:num_hops
good_ray = find(labels(:,ii) > -2);  % these rays have not penetrated
if length(good_ray) > 2
dgrp_dels(good_ray, ii) = deriv(grp_range(good_ray, ii)', ...
elev_init(good_ray, ii)');
dgnd_dgrp(good_ray, ii) = deriv(gnd_range(good_ray, ii)', ...
grp_range(good_ray, ii)');
dgnd_dels(good_ray, ii) = deriv(gnd_range(good_ray, ii)', ...
elev_init(good_ray, ii)');
end
end

% Find the the rays which return to ground. Ignore the other rays as they
% don't propogate back to the receiver. Remove rays whose rate of change of
% range with elevation is too large as this indicates we are too far into a
% cusp region to be reliable.
idx_raygnd = find(labels == 1 & grp_range < group_max & abs(dgrp_dels) <
400);
idx_reflect = find(labels == 0 & grp_range < group_max);
idx_fai = find(labels == -1 & grp_range < group_max);

lat_hop = latitude_hop(idx_raygnd);
lon_hop = longitude_hop(idx_raygnd);
gnd_rng = gnd_range(idx_raygnd);
grp_rng = grp_range(idx_raygnd);
dgrp_dels = dgrp_dels(idx_raygnd);
dgnd_dgrp = dgnd_dgrp(idx_raygnd);
dgnd_dels = dgnd_dels(idx_raygnd);
elev_tx = elevation_tx(idx_raygnd);
phase = phase_path(idx_raygnd);
fs_loss = forward_scatt_loss(idx_raygnd);
eff_range = effective_range(idx_raygnd);
absorp_gb_dev = absorption_gb_dev(idx_raygnd);    % G-B + dev absorption
model
```

```
absorp_simian = absorption(idx_raygnd);          % SiMIAN absorption model
hop_num_array = repmat((1:num_hops),num_elevs,1);
hop_num = hop_num_array(idx_raygnd);

apogee_ht = apogee_height(idx_raygnd); % For finding F2 high rays
label_above_80 = labels_above_80(idx_raygnd); % For finding rays above 80
km at edge of ionosphere model

% Loop over all the out-bound rays - find matching in-bound rays (same
% ground range) and use the radar equation to calculate backscattered
% power. Bin according to group-range and frequency.
for ray_out = 1:length(gnd_rng)
this_gnd_rng = gnd_rng(ray_out);

% various out-bound quantities
lat_hop_out = lat_hop(ray_out);
lon_hop_out = (ray_out);
grp_out = grp_rng(ray_out);
elev_out = elev_tx(ray_out);
fs_loss_out = fs_loss(ray_out);
eff_range_out = eff_range(ray_out);
absorp_gb_dev_out = absorp_gb_dev(ray_out);   % G-B + dev absorption model
absorp_simian_out = absorp_simian(ray_out);   % SiMIAN absorption model
dgnd_dgrp_out = dgnd_dgrp(ray_out);
dgrp_dels_out = dgrp_dels(ray_out);
dgnd_dels_out = dgnd_dels(ray_out);
apogee_out = apogee_ht(ray_out);

label_remove_above_80 = label_above_80(ray_out); % ray above 80 km beyond
ionsphere model

% for this out-bound ray find the matching in-bound rays ie. those which
% have the same ground range - we need to find the bracketing rays but
% ignore those whose rate of change of range with elevation is too large
% as this indicates we are too far into a cusp region to be reliable
for ray_in=1:length(gnd_rng)-1

if ( ( (gnd_rng(ray_in) >= this_gnd_rng && ...
gnd_rng(ray_in+1) <= this_gnd_rng) || ...
(gnd_rng(ray_in) <= this_gnd_rng && ...
gnd_rng(ray_in+1) >= this_gnd_rng)) && ...
(hop_num(ray_in) == hop_num(ray_in+1)) )

idx = [ray_in ray_in+1];
grp_in = ...
interp1(gnd_rng(idx), grp_rng(idx), this_gnd_rng);
elev_in = ...
interp1(gnd_rng(idx), elev_tx(idx), this_gnd_rng);
phase_in = ...
interp1(gnd_rng(idx), phase(idx), this_gnd_rng);
absorp_gb_dev_in = ...
interp1(gnd_rng(idx), absorp_gb_dev(idx), this_gnd_rng);
absorp_simian_in = ...
interp1(gnd_rng(idx), absorp_simian(idx), this_gnd_rng);
eff_range_in = ...
interp1(gnd_rng(idx), eff_range(idx), this_gnd_rng);
fs_loss_in = ...
interp1(gnd_rng(idx), fs_loss(idx), this_gnd_rng);
dgrp_dels_in = ...
interp1(gnd_rng(idx), dgrp_dels(idx), this_gnd_rng);
```

```
num_hops_in = hop_num(ray_in);

group_bin = round((grp_out + grp_in) ./ 2 ./ group_range_res) + 1;

% choose the absoprion model to use, either :
%   1. George and Bradley + deviative absorption
%   2. SiMIAN
if GB_abso_flag
absorp_in = absorp_gb_dev_in;
absorp_out = absorp_gb_dev_out;
else
absorp_in = absorp_simian_in;
absorp_out = absorp_simian_out;
end

% Calculate the area of ground illuminated by the ray - note that
% dgnd_dgrp -> inf at the "time-caustic" which means that geometrical
% optics breaks down and the equation used for area is no longer
% valid. Apply a limit to dgnd_dgrp to account for this. See Ong,
% Dyson and Bennet, RS, 1173-1186, 1998 for a better solution at the
% time-caustic.
area = radius_earth_km .* sin(this_gnd_rng ./ radius_earth_km) .* ...
elev_step .* abs(dgnd_dels_out) .* beam_az_width;

area = area * 1e6;     % convert units from km^2 to m^2

% need antenna gains and receiver mis-match loss
freq_ndx = find(abs(freqs_range - freq)<1e-7);
elev_ndx = find(elevs == elev_out);
gain_tx = gain_freq_elev_tx(elev_ndx, freq_ndx);

% finding nearest elevation to the incoming elevation
elevs_diff = abs(elev_in - return_elev);
min_elevs_diff = min(elevs_diff);
return_elev_ndx = find(elevs_diff == min_elevs_diff);
return_elev_angle = return_elev(return_elev_ndx);

gain_rx = gain_freq_elev_rx(1, return_elev_ndx, freq_ndx);
rx_mis_match_loss = 0;  % dB (included in gain)
pol_mis_match_loss = 3; % dB (polarisation mis match)

% basic two-way radar equation for ground backscatter of flux-tube

pow = tx_pow .* (wave_length.^2 ./ (4.*pi)) .* ...
area ./ (16.*pi.^2 .* eff_range_in.^2  * eff_range_out.^2);

% pow_dB = 10 .* log10(pow) - bs_loss + gain_tx + gain_rx;
pow_dB = 10 .* log10(pow) + gain_tx + gain_rx - pol_mis_match_loss;

% include forward scattering, ionospheric absorption, receiver
% mis-match, and cone-effect spreading losses
ray_power_dB = pow_dB - fs_loss_out - fs_loss_in - ...
absorp_out - absorp_in;

% calculate group range of mode and the group-range extent of flux-tube
% represented by the ray
group = (grp_out + grp_in) ./ 2;
del_elev_out = elev_step;
delta_group = del_elev_out .* (abs(dgrp_dels_in) + abs(dgrp_dels_out))./2;
```

```
group_start = group - delta_group ./ 2;
group_start = max([1, group_start]);
group_end = group + delta_group ./ 2;
group_end = min([group_end group_max]);

% determine the group range bins to which the mode contributes energy
group_start_bin = fix(group_start ./ group_step) + 1;
group_end_bin = fix(group_end ./ group_step) + 1;
grp_bin_idx = (group_start_bin : 1 : group_end_bin);
num_bins = length(grp_bin_idx);

% determine scaling factor for power in each group bin - will be
% 1/numbins for each bin except at the ends where it is give by the
% fractional conrtibution and is < 1/numbins
bin_scale = ones(size(grp_bin_idx));
if length(bin_scale) > 1
bin_scale(1) = group_start_bin - group_start ./ group_step;
bin_scale(num_bins) = group_end  ./ group_step - (group_end_bin - 1);
bin_scale = bin_scale ./ sum(bin_scale);
else
bin_scale = 1;
end
bin_scale = bin_scale';

% populate the ionogram range-frequency grid
ray_power = 10.^(ray_power_dB ./ 10);
power_total(grp_bin_idx, freq_bin) = ...
power_total(grp_bin_idx, freq_bin) + ray_power.* bin_scale;

for ii = 1:length(bin_scale)
if ray_power.*bin_scale(ii) > power_dominant(grp_bin_idx(ii),freq_bin)
power_dominant(grp_bin_idx(ii), freq_bin) =ray_power.*bin_scale(ii);
phase_path_dom(grp_bin_idx(ii), freq_bin) = phase_in;
elevation_dom(grp_bin_idx(ii), freq_bin) = elev_in;
num_hops_dom(grp_bin_idx(ii), freq_bin) = num_hops_in;

% Save the ground ranges corresponding to the group ranges
gnd_range_km(grp_bin_idx(ii),freq_bin) = this_gnd_rng;
end
end

% Check E and F2 high contributions to cell

% check F2 high rays
if dgnd_dels_out > 0
pow_high = tx_pow .* (wave_length.^2 ./ (4.*pi)) .* area ./ (16.*pi.^2 .*
eff_range_in.^2  * eff_range_out.^2);
pow_high_dB = 10 .* log10(pow_high) + gain_tx + gain_rx;
ray_power_dB_high = pow_high_dB - fs_loss_out - fs_loss_in - absorp_out -
absorp_in;
ray_power_high = 10.^(ray_power_dB_high ./ 10);
power_high_tot(grp_bin_idx, freq_bin) = power_high_tot(grp_bin_idx,
freq_bin) + ray_power_high.* bin_scale;
% for testing
for ii = 1:length(bin_scale)
num_hops_F2high_rays(grp_bin_idx(ii), freq_bin) = num_hops_in;
end
end

% check E rays
```

```
if apogee_out < 110 % previously set 150 km
pow_E = tx_pow .* (wave_length.^2 ./ (4.*pi)) .* area ./ (16.*pi.^2 .*
eff_range_in.^2  * eff_range_out.^2);
pow_E_dB = 10 .* log10(pow_E) + gain_tx + gain_rx;
ray_power_dB_E = pow_E_dB - fs_loss_out - fs_loss_in - absorp_out -
absorp_in;
ray_power_E = 10.^(ray_power_dB_E ./ 10);
power_E_tot(grp_bin_idx, freq_bin) = power_E_tot(grp_bin_idx, freq_bin) +
ray_power_E.* bin_scale;
% for testing
for ii = 1:length(bin_scale)
num_hops_E_rays(grp_bin_idx(ii), freq_bin) = num_hops_in;
end
end

% Flag rays above 80 km at end of ionosphere model
% Keep track of power from rays below 80 km at max range of
% ionosohere model
if label_remove_above_80 ~= -10
power_below80_tot(grp_bin_idx, freq_bin) = power_below80_tot(grp_bin_idx,
...
freq_bin) + ray_power.*bin_scale;
end

% Testing: Calculate total power from rays above 80 km at
% edge of RTIM
if label_remove_above_80 == -10
power_above80_tot(grp_bin_idx, freq_bin) = power_above80_tot(grp_bin_idx,
...
freq_bin) + ray_power.*bin_scale;
end

end

end

end

end   % of frequency loop

% Get power in decibels
pow_tot_dB = 10.*log10(power_total);
pow_dom_dB = 10.*log10(power_dominant);

% Flag cells with large E and F2 high contributions (within 10 dB of other
% contribution)
pow_tot_dB_high = 10.*log10(power_high_tot);
pow_tot_dB_E = 10.*log10(power_E_tot);
% Total for F2 and E
pow_tot_dB_high_or_E = 10.*log10( 10.^(pow_tot_dB_high/10) +
10.^(pow_tot_dB_E/10) );
E_or_F2high_flag = abs(pow_tot_dB - pow_tot_dB_high_or_E) < 10;
% % For testing: show which flagged cells were E and which were F2 high
% E_flag_testing = abs(pow_tot_dB - pow_tot_dB_E) < 10;
% F_flag_testing = abs(pow_tot_dB - pow_tot_dB_high) < 10;

% If the difference in power from rays below 80 km and the total power is
greater than 1 dB, remove cell
pow_tot_dB_80 = 10.*log10(power_below80_tot);
```

```
height_80_flag = (abs(pow_tot_dB - pow_tot_dB_80) > 1);

pow_tot_dB = pow_tot_dB .* ~height_80_flag;
pow_tot_dB(pow_tot_dB==0) = -2000;

xrange = [freq_min freq_max];
yrange = [0 group_max];

end
```

A.3 Code to automatically select area an area of the ionograms to use for calculating the backscatter coefficient

```
% Name :
%   get_bss_coeff_auto
%
% Purpose :
%   Auto selects the area of the observed and syntehsized backscatter
%   ionograms to compare to get the backscatter coefficient using the
number
%   of hops from the synthezised ionograms, the leading edges and the ray
%   information.
%   This requires files that have been saved with both the
%   synthesised ionogram, the observed ionogram and the raw ionogram data
%   (the raw data is needed for the leadin edge detction). The script
%   compare_synth_to_obs_function.m outputs these.
%   After using
%   get_bss_coeff_auto.m, use save_all_result.m to save results into a
single
%   file.
%
% Calling sequence :
%   get_bss_coeff_auto
%
% Inputs :
%
% Outputs :
%    Saves backscatter coefficient data to file in an array that contains
%    the time, beam number, range (km), backscatter coefficient, dominant
%    elevation and frequency.

clear all

bss_id = ["LO","LAE","AS","LAW"];
year = 2016; % 2015 or 2016
month = 3; % 9 or 3

beam_vect = [1:8];
%date_vect = [3:30]; % date (day of September 2015)
date_vect = [1:31]; % date (day of March 2016)
hour_vect = [0,1,2,3,4,5,6,7,8,9]; % hour of day (UT)
min_vect = [0,10,20,30,40,50]; % minutes

for radar = 1:length(bss_id)
for date = date_vect
disp(date)
for hour = hour_vect
for minute = min_vect
```

```
time = sprintf('%02d%02d',hour, minute);

for beam = beam_vect

file = sprintf('%s_Beam%d_%d%02d%02d_%s.mat', bss_id(radar), beam, year,
month, date, time);
date_str = sprintf('%d%02d%02d %s', year, month, date, time);

if isfile(file)
load(file);

% Check the ionogram is usable (only use ionograms with
% an arbitrary amount of power). (e.g. 100 cells with power
% > -125)
power_check = obs_bss >= -125;
if numel( power_check( power_check > 0 ) ) < 50 %100 was 50

else % Select a good area of the ionogram to calculate backscatter from

% Calculate ionogram info
num_freqs = length(synth.pow_tot_dB(1,:));
num_ranges = length(synth.pow_tot_dB(:,1));
freq_synth = linspace(synth.xrange(1), synth.xrange(2), num_freqs);
range_synth = linspace(synth.yrange(1), synth.yrange(2), num_ranges);

% Only look at the one hop values
mask_hops = synth.num_hops_dom == 1;
mask_good_iono = synth.pow_tot_dB > -1000; % remove unwanted area due to
extended ionosphere
mask_hops = mask_good_iono.*mask_hops;

% Compare leading edges
% Find the synthesised leading edge.
LE_range_synth = zeros(1, num_freqs);

for freq = 1:num_freqs
if max(mask_hops(:,freq)) > 0
LE_range_synth(freq) = find(mask_hops(:,freq), 1); % find first non zero
elements for each frequency
LE_range_synth(freq) = range_synth(LE_range_synth(freq)); % find the ranges
that these values correspond to
% Don't include point too close to leading edge
points_near_edge = find(mask_hops(:,freq), 3); % find last 3 non zero
elements for each frequency
mask_hops(points_near_edge,freq) = 0;
end
end

[~, freq_index, ~] = find(LE_range_synth); % remove frequencies where the
range is zero
max_idx = max(freq_index);
for idx = 1:length(freq_index)-1 % remove extra values after a break in the
leading edge
if freq_index(idx) - freq_index(idx+1) ~= 1 % if there is a break in the
leading edge
max_idx = idx;
end
end
LE_freq_synth = freq_synth(freq_index <= max_idx);
```

```
% Get the observed leading edge
LE_data_obs = LE_get_leading_edge(raw_bss);
LE_range_obs = LE_data_obs.beam(beam).le_smoothed_trace.range; % km
LE_freq_obs = LE_data_obs.beam(beam).le_smoothed_trace.frequency; % MHz

if ~isempty(LE_range_obs) && ~isempty(LE_freq_obs) % if leading edgde data
is found

% Compare the synth and obs leading edges

% Calculate the min and max freqs that are covered
% by both the synth and obs leading edge
LE_min_freq = max(min(LE_freq_obs), min(LE_freq_synth));
LE_max_freq = min(max(LE_freq_obs), max(LE_freq_synth));

% Get the frequnecies and the ranges that are covered
% by both the synth and obs leading edge
LE_freq = freq_synth((freq_synth >= LE_min_freq) & (freq_synth <=
LE_max_freq));
LE_range_synth = LE_range_synth((freq_synth >= LE_min_freq) & (freq_synth
<= LE_max_freq));

if ~isempty(LE_freq) % if observed and synthesised leading edges cover the
same area

% Interpolate obs leading edge values to get ranges
% for the same freqs as synth
LE_range_obs = interp1(LE_freq_obs, LE_range_obs, LE_freq);

% calculate the RMS difference between the curves
LE_difference = ( mean( (LE_range_synth - LE_range_obs).^2 ) )^(1/2);

% If the difference between the leading edges is
% less than an arbitrary value, continue getting
% the backscatter coeffcients. (if it is greater
% the BS results are not saved)
if LE_difference < 300 % km

% Calculate backscatter values
bss_value = obs_bss - synth.pow_tot_dB;

% Leading edge mask (remove values for ranges
% less than observed leading edge ranges.
% Initialise leading edge mask
mask_edge = true(size(synth.pow_tot_dB));
% Find index of frequencies in leading edge
[~, freq_index, LE_freq_index] = intersect(freq_synth, LE_freq);
for i = 1:length(freq_index)
    % Find index of ranges less than obs
    % leading edge (+ 100 km to get away from edge)
    [~,col] = find( range_synth <= LE_range_obs(LE_freq_index(i)) + 100 );
    % Set these ranges to zero
    mask_edge(col,freq_index(i)) = 0;
end

% Remove points from around trailing edge
% (as the trailing edges do not always
% match)
```

```
% Remove points along each range (acroos
% ionogram).
for range = 1:num_ranges
    trailingEdge = find(mask_hops(range,:), 10); % find last 3 non zero
elements for each frequency
    mask_hops(range,trailingEdge) = 0;
end

% Remove cells with large E or F2 high contributions
mask_good_rays = ~synth.E_or_F2high_flag;

% Remove points where the bs coefficient is greater than zero
% or less than -100 dB
mask_outlier = bss_value < 0 & bss_value > -100;

% Remove nans
bss_value(isnan(bss_value)) = 0;

% Calculate the entire mask and apply to the
% backscatter values
mask_full = mask_hops .* mask_edge .* mask_outlier .* mask_good_rays;
bss_value = bss_value .* mask_full;

ranges = mask_full .* synth.gnd_rng_km;
elevs_dom = mask_full .* synth.elevation_dom;
coeffs = nonzeros(bss_value);

% Create a matrix of the frequency for each cell
frequencies = linspace(synth.xrange(1), synth.xrange(2), num_freqs);
frequencies = mask_full .* repmat(frequencies, num_ranges, 1);

% Save the results in an array (columns containing time, beam,
% range, coefficient, elevation, frequency)
results = zeros(length(coeffs), 6);

results(:,1) = datenum( datetime(date_str, 'InputFormat', 'yyyyMMdd HHmm')
);
results(:,2) = beam;
results(:,3) = nonzeros(ranges);
results(:,4) = coeffs;
results(:,5) = nonzeros(elevs_dom);
results(:,6) = nonzeros(frequencies);

% Save results
save_name = sprintf('%s_Beam%d_%d%02d%02d_%s_results_auto.mat',
bss_id(radar), beam, year, month, date, time);
save(save_name, 'results')

end % Leading edge difference check
end % Check leading edges overlap
end % Leading edge data found check
end % Observed ionogram power check

else
message = sprintf("%s file not found", file);
disp(message)
end % File exists check

end % beam
```

```
end % minute
end % hour
end % date
end % radar
```

Appendix B Locations of places mentioned

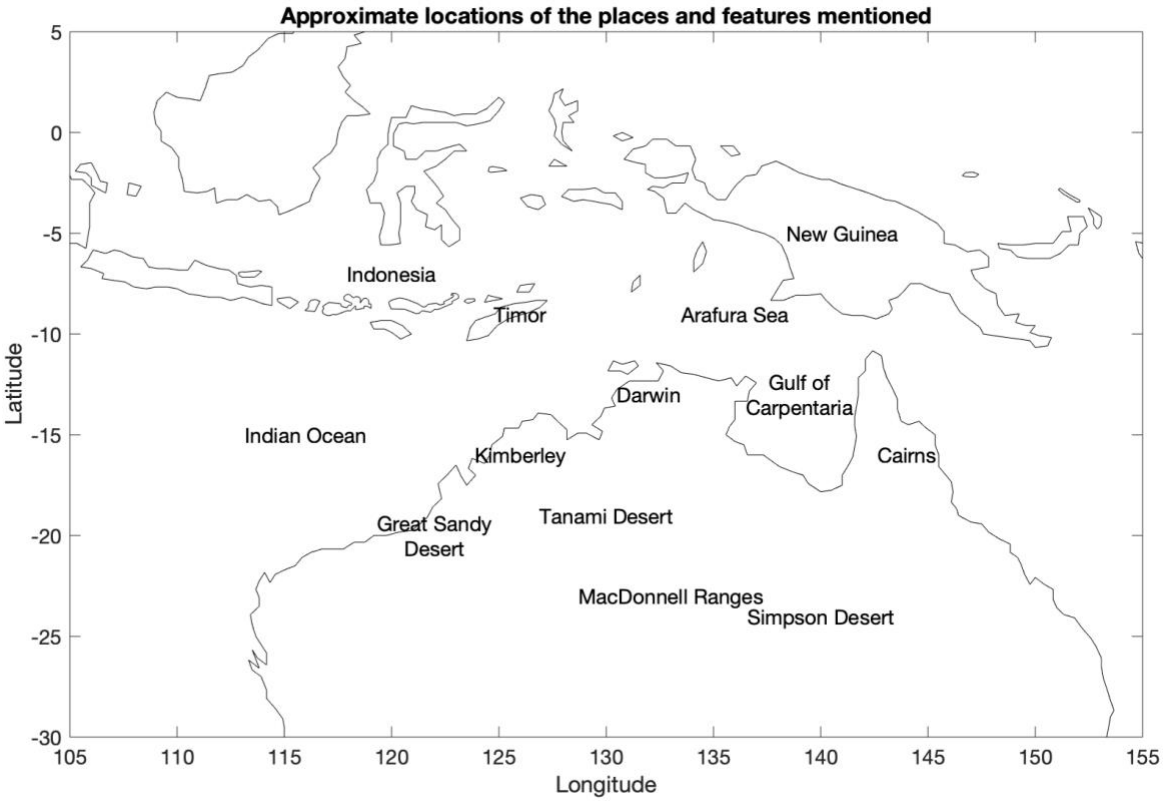

Figure 6.1: Approximate locations of the places and features mentioned in this thesis.

References

1. Cervera, M.A. and Harris, T.J., *Modeling ionospheric disturbance features in quasi-vertically incident ionograms using 3-D magnetoionic ray tracing and atmospheric gravity waves.* Journal of Geophysical Research: Space Physics, 2014. **119**(1): p. 431-440.

2. Cameron, A., *The Jindalee operational radar network: its architecture and surveillance capability*, in *Proceedings International Radar Conference*. 1995: Alexandria, VA, USA. p. 692-697.

3. Earl, G.F. and Ward, B.D., *The frequency management system of the Jindalee over-the-horizon backscatter HF radar.* Radio Science, 1987. **22**(2): p. 275-291.

4. Croft, T.A., *Sky-wave backscatter: A means for observing our environment at great distances.* Reviews of Geophysics, 1972. **10**(1): p. 73.

5. McNamara, L.F., *The Ionosphere: Communications, Surveillance, and Direction Finding*. 1991, Florida: Kriega Publishing Company.

6. Holdsworth, D.A., *Skywave over-the-horizon radar track registration using earth surface and infrastructure backscatter*, in *IEEE Radar Conference*. 2017: Seattle, WA. p. 0986-0991.

7. Davies, K., *Ionospheric radio*. 2008: Institution of Engineering and Technology.

8. Netherway, D.J., Whitingham, M.J., and Gardiner-Garden, R.S., *High Range Resolution Backscatter Sounder Ionograms*. 2018, DST Group, DST-Group-TR-3477

9. Coleman, C.J., *A ray tracing formulation and its application to some problems in over-the-horizon radar.* Radio Science, 1998. **33**(4): p. 1187-1197.

10. Ong, C.Y., Bennett, J.A., and Dyson, P.L., *An improved method of synthesizing ground backscatter ionograms for spherical ionospheres.* Radio Science, 1998. **33**(4): p. 1173-1185.

11. Russell, C., Dyson, P., Houminer, Z., and Bennett, J., *The effect of large-scale ionospheric gradients on backscatter ionograms.* Radio Science, Washington, DC, 1997. **32**(5): p. 1881-1897.

12. Coleman, C.J., *On the simulation of backscatter ionograms.* Journal of Atmospheric and Solar-Terrestrial Physics, 1997. **59**(16): p. 2089-2099.

13. Croft, T.A., *The influence of ionospheric irregularities on sweep-frequency backscatter.* Journal of Atmospheric and Terrestrial Physics, 1968. **30**(5): p. 1051,IN15,1053-1052,IN17,1063.

14. Sales, G.S., *High Frequency (HF) Radiowave Propagation*. 1992, Massachusetts University, Center for Atmospheric Research, PL-TR-92-2123

15. Cervera, M.A., Francis, D.B., and Frazer, G.J., *Climatological Model of Over-the-Horizon Radar.* Radio Science, 2018. **53**(9): p. 988-1001.

16. Coleman, C.J., *A General Purpose Ionospheric Ray Tracing Procedure*. 1993, DSTO, SRL-0131-TR

17. Haselgrove, J., *The Hamiltonian ray path equations.* Journal of atmospheric and terrestrial physics, 1963. **25**(7): p. 397-399.

18. Haselgrove, C.B. and Haselgrove, J., *Twisted Ray Paths in the Ionosphere.* Proceedings of the Physical Society, 1960. **75**(3): p. 357-363.

19. Jones, R.M. and Stephenson, J.J., *A versatile three-dimensional ray tracing computer program for radio waves in the ionosphere*. 1975, U.S. Department of Commerce, Office of Telecommunications, OT Report 75-76

20. Ridley, J., Strawbridge, F., Card, R., and Phillips, H., *Radar backscatter characteristics of a desert surface.* Remote Sensing of Environment, 1996. **57**(2): p. 63-78.

21. Peake, W., *Theory of radar return from terrain*, in *1958 IRE International Convention Record*. 1959: New York, NY, USA. p. 27-41.

22. Barrick, D.E. and Peake, W.H., *A Review of Scattering From Surfaces With Different Roughness Scales.* Radio Science, 1968. **3**(8): p. 865-868.

23. Barrick, D.E., *Grazing behavior of scatter and propagation above any rough surface.* IEEE Transactions on Antennas and Propagation, 1998. **46**(1): p. 73-83.

24. Barrick, D., *First-order theory and analysis of MF/HF/VHF scatter from the sea.* IEEE Transactions on Antennas and Propagation, 1972. **20**(1): p. 2-10.

25. Peake, W.H. and Barrick, D.E., *Scattering from surfaces with different roughness scales, analysis and interpretation*. 1967, NASA, NASA-CR-89320

26. Barrick, D. and Bahar, E., *Rough surface scattering using specular point theory.* IEEE Transactions on Antennas and Propagation, 1981. **29**(5): p. 798-800.

27. Barrick, D.E., *Near-grazing illumination and shadowing of rough surfaces.* Radio Science, 1995. **30**(3): p. 563-580.

28. Crombie, D.D. and Watts, J.M., *Observations of coherent backscatter of 2–10 MHz radio surface waves from the sea.* Deep-Sea Research and Oceanographic Abstracts, 1968. **15**(1): p. 81-87.

29. Lipa, B.J. and Barrick, D.E., *Extraction of sea state from HF radar sea echo: Mathematical theory and modeling.* Radio Science, 1986. **21**(1): p. 81-100.

30. Munk, W.H. and Nierenberg, W.A., *High Frequency Radar Sea Return and the Phillips Saturation Constant.* Nature, 1969. **224**(5226): p. 1285.

31. Barrick, D.E., Headrick, J.M., Bogle, R.W., and Crombie, D.D., *Sea backscatter at HF: Interpretation and utilization of the echo.* Proceedings of the IEEE, 1974. **62**(6): p. 673-680.

32. Barrick, D. and Snider, J., *The statistics of HF sea-echo Doppler spectra.* IEEE Journal of Oceanic Engineering, 1977. **2**(1): p. 19-28.

33. Parkinson, M.L., *Advanced directional sea spectrum studies with the Bribie Island MF/lower HF surface-wave radar.* Radio Science, 1994. **29**(4): p. 815-830.

34. Lipa, B., Nyden, B., Barrick, D., and Kohut, J., *HF Radar Sea-echo from Shallow Water.* Sensors, 2008. **8**(8): p. 4611-4635.

35. Hasselmann, K., Barnett, T., Bouws, E., Carlson, H., Cartwright, D., Enke, K., Ewing, J., Gienapp, H., Hasselmann, D., Kruseman, P., Meerburg, A., Muller, P., Olbers, D., Richter, K., Sell, W., and Walden, H., *Measurements of wind-wave growth and swell decay during the Joint North Sea Wave Project (JONSWAP).* Deut. Hydrogr. Z., 1973. **8**: p. 1-95.

36. Neller, C., *Over-the-Horizon Radar Sea-State Parameter Estimation using Bureau of Meteorology Interactive Weather and Wave Forecast Data*. 2014, NSID, DST Group DSTO-DP-1266

37. Barnum, J.R. and Simpson, E.E., *Over-the-horizon radar target registration improvement by terrain feature localization.* Radio Science, 1998. **33**(4): p. 1077-1093.

38. Balser, R.P. and Scott, T.D., *Ground Backscatter Observed With High Resolution Oblique Sounders.* Radio Science, 1972. **7**(2): p. 239-243.

39. Steele, J.G., *High-frequency backscatter from terrain with trees.* Proceedings of the IEEE, 1967. **55**(9): p. 1583-1590.

40. Barnum, J., *High-frequency backscatter from terrain with cement-block walls.* IEEE Transactions on Antennas and Propagation, 1971. **19**(3): p. 343-347.

41. Li, L.-W., *High-frequency over-the-horizon radar and ionospheric backscatter studies in China.* Radio Science, Washington, DC, 1998. **33**(5): p. 1445-1458.

42. Slimming, B. and Cervera, M., *Calculation of High Frequency Land Backscatter Coefficients*. 2019, NSID, DST Group, DST-Group-TR-3613

43. Turley, M.D.E., Gardiner-Garden, R.S., and Holdsworth, D.A., *High-resolution wide area remote sensing for HF radar track registration*, in *2013 International Conference on Radar*. 2013: Adelaide, SA. p. 128-133.

44. Jin, Z., Pan, Q., Zhao, C., and Zhou, W., *SVM Based Land/Sea Clutter Classification Algorithm.* Applied Mechanics and Materials, 2012. **236-237**: p. 1156.

45. Gardiner-Garden, R., Cervera, M., Debnam, R., Harris, T., Heitmann, A., Holdsworth, D., Netherway, D., Northey, B., Pederick, L., Praschifka, J., Quinn, A., Turley, M., Unewisse, A., Ward, B., and Warne, G., *A description of the Elevation*

sensitive Oblique Incidence Sounder Experiment (ELOISE). Advances in Space Research, 2019. **64**(10): p. 1887-1914.

46. Barnes, R., Gardiner-Garden, R., and Harris, T., *Real time ionospheric models for the Australian Defence Force.* Proc. WARS-2000, 2000. **122135**.

47. Harris, T.J., Quinn, A.D., and Pederick, L.H., *The DST group ionospheric sounder replacement for JORN.* Radio Science, 2016. **51**(6): p. 563-572.

48. Dyson, P.L. and Bennett, J.A., *A model of the vertical distribution of the electron concentration in the ionosphere and its application to oblique propagation studies.* Journal of atmospheric and terrestrial physics, 1988. **50**(3): p. 251-262.

49. Barnes, R.I., Braendler, S.A., Coleman, C.J., Gardiner-Garden, R.S., and Hoang, T.V., *Analysis of data-driven parametric models of the vertical ionospheric profile for use in oblique propagation studies.* Radio science, 1998. **33**(4): p. 1215-1226.

50. Durrant, T.H., *A global wave hindcast focussed on the Central and South Pacific*, ed. D.J.M.a. Greenslade, et al. 2014: Centre for Australian Weather and Climate Research.

51. Amante, C. and Eakins, B.W., *ETOPO1 1 Arc-Minute Global Relief Model: Procedures, Data Sources and Analysis*. 2009, NOAA Technical Memorandum NESDIS NGDC-24: National Geophysical Data Center, NOAA.

52. Gallant, J., Wilson, N., Dowling, T., Read, A., and Inskeep, C., *SRTM-derived 1 Second Digital Elevation Models Version 1.0. Record 1.* 2011, Geoscience Australia: Canberra.

53. Reichle, R., De Lannoy, G., Koster, R.D., Crow, W.T., Kimball, J.S., and Liu, Q., *SMAP L4 Global 3-hourly 9 km EASE-Grid Surface and Root Zone Soil Moisture Geophysical Data, Version 4.* 2018, NASA National Snow and Ice Data Center Distributed Active Archive Center: Boulder, Colorado USA.

54. Scarth, P., Armston, J., Lucas, R., and Bunting, P., *A Structural Classification of Australian Vegetation Using ICESat/GLAS, ALOS PALSAR, and Landsat Sensor Data.* Remote Sensing, 2019. **11**(2).

55. *MATLAB version 2019b*. 2019, The MathsWorks Inc.: Natick, Massachusetts.

56. Cervera, M.A. and Harris, T.J., *A Model of Backscatter Ionograms*, in *Workshop on the Application of Radio Science*. 2004: Hobart.

57. George, P.L. and Bradley, P.A., *A new method of predicting the ionospheric absorption of high frequency waves at oblique incidence.* Telecommunication Journal, 1974. **41**: p. 307-312.

58. Bilitza, D., Altadill, D., Truhlik, V., Shubin, V., Galkin, I., Reinisch, B., and Huang, X., *International Reference Ionosphere 2016: From ionospheric climate to real-time weather predictions.* Space Weather, 2017. **15**(2): p. 418-429.

59. Pederick, L.H. and Cervera, M.A., *Semiempirical Model for Ionospheric Absorption based on the NRLMSISE-00 atmospheric model.* Radio Science, 2014. **49**(2): p. 81-93.

60. George, P.L. and Bradley, P.A., *Relationship between H.F. absorption at vertical and oblique incidence.* Proceedings of the Institution of Electrical Engineers, 1973. **120**(11): p. 1355-1361.

61. Burke, G., Poggio, A., Logan, J., and Rockway, J., *NEC - Numerical electromagnetics code for antennas and scattering*, in *1979 Antennas and Propagation Society International Symposium*. 1979, IEEE: Seatlle, WA, USA. p. 147-150.

62. Netherway, D., *Private communication*. 2020.

63. Gardiner-Garden, R.S. and Pincombe, A.H., *A study of the seasonal pattern of variability in the HF radar cross-section of the sea*. 1996, Intelligence, Surveillance and Space Division, DST Group, DSTO-DPP-0261

64. Brodtkorb, P.A., Johannesson, P., Lindgren, G., Rychlik, I., Rydén, J., and Sjö, E., *WAFO - A Matlab Toolbox For Analysis of Random Waves And Loads*. 2011.

65. MathsWorks, *Data Analysis (R2020a)*. 2020,

66. Ogundare, J.O., *Understanding Least Squares Estimation and Geomatics Data Analysis*. 2018, Newark: John Wiley & Sons, Incorporated.

67. Naylor, G. and Robson, R., *Interpretation of Backscattered HF Radio Waves from the Sea.* Australian Journal of Physics, 1986. **39**(3): p. 395.

68. Jordan, A.K. and Lang, R.H., *Electromagnetic scattering patterns from sinusoidal surfaces.* Radio Science, 1979. **14**(6): p. 1077-1088.

69. Jackson, J.D., *Classical electrodynamics*. 2d ed. ed. 1975, New York: Wiley.

70. Ulaby, F.T., Batlivala, P.P., and Dobson, M.C., *Microwave Backscatter Dependence on Surface Roughness, Soil Moisture, and Soil Texture: Part I-Bare Soil.* IEEE Transactions on Geoscience Electronics, 1978. **16**(4): p. 286-295.

71. Google Earth Pro v7.3.3.7786, *Northern Territory, Australia, 17˚56'44.06" S, 132˚29'18.62" E*. 2015.

72. Google Earth Pro v7.3.3.7786, *Great Sandy Desert, Australia, 20˚19'22.28" S, 124˚29'38.80" E*. 2015.

73. Hollaus, M., *A Review of Surface Roughness Concepts, Indices and Applications*. 2014, European Territorial Coorperation Alpine Space Programme, 2-3-2-FR